

**UCLA**

**UCLA Electronic Theses and Dissertations**

**Title**

Novel microfluidic technologies for the concentration of radionuclides and radiotracers for positron emission tomography

**Permalink**

<https://escholarship.org/uc/item/7qb3p6x1>

**Author**

Chao, Philip Hong-Sean

**Publication Date**

2019

Peer reviewed|Thesis/dissertation

UNIVERSITY OF CALIFORNIA

Los Angeles

Novel microfluidic technologies for the  
concentration of radionuclides and radiotracers  
for positron emission tomography

A dissertation submitted in partial satisfaction of the  
requirements for the degree Doctor of Philosophy in  
Bioengineering

by

Philip Hong-Sean Chao

2019

© Copyright by

Philp Hong-Sean Chao

2019

## ABSTRACT OF THE DISSERTATION

Novel microfluidic technologies for the  
concentration of radionuclides and radiotracers  
for positron emission tomography

by

Philip Hong-Sean Chao

Doctor of Philosophy in Bioengineering

University of California, Los Angeles, 2019

Professor Pei-Yu Chiou, Co-Chair

Professor Robert Michael van Dam, Co-Chair

Positron emission tomography (PET) is an imaging modality capable of visualizing biomolecules *in vivo* and can be used to aid in disease diagnosis, staging of disease severity, and monitoring of disease response to treatment. PET relies on the use of tracers (i.e. biomolecules labeled with radionuclides) for imaging. Due to the short half-life of the radionuclides used, PET tracer production is typically performed right before an imaging event. Production of a PET tracer can be broken down into three major parts: production of the radionuclide, radiochemical synthesis of the tracer, and, lastly, purification, formulation and quality control testing of the tracer.

Several groups, including our own, have looked into leveraging the benefits of microfluidics (reduced system size, finer control of reaction parameters, reduced reagent consumption) towards the production of PET tracers. These microfluidic versions of commonly-used PET tracer production equipment enable users to scale up or down the amount of tracer

that is produced at a given time. Compared to current commercial systems which are designed to synthesize large batches of PET tracers for clinical applications, these microfluidic systems can offer substantial cost savings by enabling production of smaller batches based on user needs.

Microfluidic approaches have already been applied successfully towards radiochemical synthesis, purification, and quality control testing of tracers. There, however, still exists several steps in tracer production that could benefit from microfluidic technologies. Evaporation of solvent during the concentration and formulation steps following tracer purification is currently performed on slow and bulky rotary evaporators. Microfluidic technology could aid in size reduction while also leveraging microfluidic advantages such as faster heat transfer to increase evaporation rates. Part of this dissertation is focused on applying microfluidic technologies towards the concentration and formulation of PET tracers following purification.

Despite successful design and operation of microfluidic radiosynthesizers, one main limitation that microfluidic radiosynthesizers face is differences between radionuclide volumes (mL) and microfluidic reactor volumes ( $\mu\text{L}$ ). This disconnect limits the amount of starting radioactivity that can be loaded into microscale reactors for radiosyntheses. To address this need, work presented in this dissertation also focuses on the design, fabrication, and testing of an automated microfluidic radionuclide concentrator based on miniaturized anion and cation exchange cartridges enabling the concentration of various types of radionuclides (e.g. fluorine-18 and gallium-68). Concentrated radionuclides in microliter volumes enables microfluidic synthesis of a diverse range of PET tracers in large quantities.

We have also pursued further development of microreactors leading to new advancements to improve the radiosynthesis step during tracer production. Previously our group has demonstrated synthesis of a diverse range of PET tracers using a microfluidic radiosynthesizer based on electrowetting on dielectric (EWOD). Despite advantages of compact size and reduced reagent consumption, a limitation was the cost and complexity of the single-

use EWOD chips used during production. In this dissertation, we combat these limitations through the design and fabrication of an automated microfluidic radiosynthesizer based on patterned wettability. This new platform uses reaction chips that are easier to fabricate (compared to EWOD), are a fraction of the cost, and are significantly easier to operate.

Lastly, in this dissertation we demonstrate successful integration of our radionuclide concentrator with our newly design radiosynthesizer. We perform synthesis of [ $^{18}\text{F}$ ]fallypride using high starting activities and demonstrate the ability to produce tracers in high quantities. This integrated platform thus enables both production of low and high quantities of tracer depending on user needs.

The developments presented in this dissertation represent tools for performing portions of the whole PET tracer production process in a more cost effective and efficient manner. Future work will be focused on the successful integration of all components (both microfluidic and conventional) necessary for PET tracer production to enable automated, reliable, high yielding radiosyntheses of clinical grade PET tracers.

The dissertation of Philip Hong-Sean Chao is approved.

Seyed Sam Sadeghi Hosseini

Jennifer M. Murphy

Pei-Yu Chiou, Co-Chair

Robert Michael van Dam, Co-Chair

University of California, Los Angeles

2019

*Dedicated to my loving and supporting parents*

## TABLE OF CONTENTS

<u>LIST OF FIGURES</u> .....	xi
<u>LIST OF TABLES</u> .....	xiii
<u>ACKNOWLEDGEMENTS</u> .....	xv
<u>VITA</u> .....	xx
<u>1 Chapter 1: Introduction</u> .....	1
<u>1.1 Positron emission tomography</u> .....	1
<u>1.2 Production of PET tracers</u> .....	7
<u>1.2.1 General production scheme of PET tracers</u> .....	7
<u>1.3 Microfluidic production of PET tracers</u> .....	16
<u>1.3.1 Benefits of microfluidics for PET tracer production</u> .....	18
<u>1.3.2 Limitations of current microfluidic technologies</u> .....	22
<u>1.4 Focus of this dissertation</u> .....	23
<u>2 Chapter 2: Microfluidic Membrane Concentration of Purified Tracers</u> .....	27
<u>2.1 Introduction</u> .....	27
<u>2.2 Materials and Methods</u> .....	29
<u>2.2.1 Microfluidic concentrator design and fabrication</u> .....	29
<u>2.2.2 Automated concentrator system</u> .....	32
<u>2.2.3 Concentrator operation</u> .....	35
<u>2.2.4 Measuring evaporation rate</u> .....	38
<u>2.2.5 Reagents</u> .....	38
<u>2.2.6 Determining Operating Conditions</u> .....	39
<u>2.2.7 Determining Sample Recovery Efficiency</u> .....	44
<u>2.2.8 Assessing thermal stability of tracers</u> .....	45
<u>2.2.9 Determining residual organic solvent content</u> .....	48
<u>2.2.10 Theoretical vapor pressures that may affect BTP measurements</u> .....	49
<u>2.2.11 Evaporation rate of rotary evaporator</u> .....	50
<u>2.2.12 Additional designs considered for optimization of heating</u> .....	51
<u>2.2.13 Comparison of surface temperatures</u> .....	53
<u>2.2.14 Surface roughness characterization</u> .....	54
<u>2.2.15 Total operating time</u> .....	55
<u>2.2.16 In vivo mouse imaging of [<sup>18</sup>F]D-FAC</u> .....	56
<u>2.3 Results and Discussion</u> .....	58
<u>2.3.1 Scope of HPLC mobile phases</u> .....	58
<u>2.3.2 Operating conditions</u> .....	61

2.3.3	<u>Evaporation rate</u> .....	63
2.3.4	<u>Effect of solutes and solvents on evaporation rate</u> .....	68
2.3.5	<u>Sample recovery</u> .....	71
2.3.6	<u>In-chip measurements of breakthrough</u> .....	73
2.3.7	<u>Concentration of PET tracers</u> .....	75
2.4	<u>Conclusion</u> .....	81
3	<u>Chapter 3: Concentration of [<sup>18</sup>F]fluoride</u> .....	84
3.1	<u>Introduction</u> .....	84
3.2	<u>Materials and Methods</u> .....	89
3.2.1	<u>Reagents</u> .....	89
3.2.2	<u>Miniature anion exchange cartridge</u> .....	89
3.2.3	<u>System design</u> .....	90
3.2.4	<u>Concentration process</u> .....	100
3.2.5	<u>Characterization of trapping and elution efficiency</u> .....	105
3.2.6	<u>Synthesis of N-boc-5-[<sup>18</sup>F]Fluoroindole</u> .....	106
3.2.7	<u>Duration of concentration process</u> .....	109
3.3	<u>Results and Discussion</u> .....	110
3.3.1	<u>Duration of concentration process</u> .....	110
3.3.2	<u>Trapping efficiency</u> .....	112
3.3.3	<u>Effect of initial volume of radionuclide solution</u> .....	113
3.3.4	<u>Effect of number of eluent plugs</u> .....	115
3.3.5	<u>Elution efficiency</u> .....	116
3.3.6	<u>Elution with organic solvent containing eluent</u> .....	117
3.3.7	<u>Synthesis of N-boc-5-[<sup>18</sup>F]fluoroindole</u> .....	118
3.3.8	<u>Comparison of operational differences between concentration system architectures</u> .....	120
3.3.9	<u>Concentration of other radionuclides</u> .....	121
3.4	<u>Conclusion</u> .....	122
4	<u>Chapter 4: Concentration of Radiometals</u> .....	124
4.1	<u>Introduction</u> .....	124
4.2	<u>Methods</u> .....	128
4.2.1	<u>Materials</u> .....	128
4.2.2	<u>Radionuclide concentrator</u> .....	128
4.2.3	<u>Cartridge fabrication</u> .....	129
4.2.4	<u>Trapping and elution testing</u> .....	132
4.3	<u>Results and discussion</u> .....	134
4.3.1	<u>Radiometal concentrator cartridge optimization</u> .....	134

4.3.2	<u>Trapping and elution optimization</u> .....	135
4.3.3	<u>Integration with synthesis platform to explore radiometal labeling</u> .....	139
4.4	<u>Conclusion and Future Work</u> .....	140
5	<u>Chapter 5: Design of a simple and reliable microfluidic radiosynthesizer</u> .....	143
5.1	<u>Introduction</u> .....	143
5.2	<u>Materials and Methods</u> .....	147
5.2.1	<u>Materials</u> .....	147
5.2.2	<u>Design and fabrication of microfluidic droplet reactor</u> .....	148
5.2.3	<u>Automation of microdroplet reactions</u> .....	151
5.2.4	<u>On-chip radiosynthesis of [<sup>18</sup>F]fallypride</u> .....	156
5.2.5	<u>Analytical methods</u> .....	158
5.2.6	<u>Micro PET/CT imaging protocol</u> .....	161
5.3	<u>Results and Discussion</u> .....	162
5.3.1	<u>Development of fabrication method</u> .....	162
5.3.2	<u>Feasibility studies and characterization</u> .....	163
5.3.3	<u>Mock radiosynthesis</u> .....	165
5.3.4	<u>Multi-step radiosyntheses</u> .....	166
5.3.5	<u>Scaling up the amount of radioactivity</u> .....	168
5.3.6	<u>Preclinical imaging</u> .....	169
5.4	<u>Conclusion</u> .....	171
6	<u>Chapter 6: Combined radionuclide concentration and PET tracer synthesis</u> .....	172
6.1	<u>Introduction</u> .....	172
6.2	<u>Materials and Methods</u> .....	174
6.2.1	<u>Materials</u> .....	174
6.2.2	<u>Apparatus</u> .....	175
6.2.3	<u>Micro-cartridge fabrication</u> .....	178
6.2.4	<u>Optimization and evaluation of concentrator performance</u> .....	180
6.2.5	<u>Interface between concentrator and droplet synthesizer</u> .....	183
6.2.6	<u>[<sup>18</sup>F]fallypride synthesis on chip</u> .....	185
6.2.7	<u>Evaluation of synthesis performance</u> .....	187
6.2.8	<u>Purification, formulation, and quality control testing</u> .....	188
6.3	<u>Results and Discussion</u> .....	188
6.3.1	<u>[<sup>18</sup>F]fluoride concentrator cartridge optimization</u> .....	188
6.3.2	<u>Optimization of [<sup>18</sup>F]fluoride concentration process</u> .....	190
6.3.3	<u>Optimization of [<sup>18</sup>F]fallypride synthesis conditions</u> .....	192
6.3.4	<u>Performance of transfer method between systems</u> .....	195

6.3.5	<u>Low activity [<sup>18</sup>F]fallypride synthesis</u> .....	196
6.3.6	<u>High activity [<sup>18</sup>F]fallypride synthesis</u> .....	198
6.4	<u>Conclusion and Future Work</u> .....	202
7	<u>Future outlook</u> .....	203
8	<u>Appendix</u> .....	206
8.1	<u>Droplet merging methods at interface of radionuclide concentrator and droplet synthesizer</u> .....	206
8.1.1	<u>Overview</u> .....	206
8.1.2	<u>Intermediate vial approach</u> .....	207
8.1.3	<u>Microfluidic chip approach</u> .....	208
8.2	<u>Simulating higher activity levels in [<sup>18</sup>F]fluoride concentrator</u> .....	211
8.2.1	<u>KF spiking</u> .....	211
8.2.2	<u>Decayed, bombarded [<sup>18</sup>O]H<sub>2</sub>O spiking</u> .....	213
8.3	<u>Performance of higher resin mass in [<sup>18</sup>F]fluoride concentrator</u> .....	214
8.4	<u>SCX filtration upstream of [<sup>18</sup>F]fluoride concentrator</u> .....	215
8.4.1	<u>[<sup>18</sup>F]fluoride filtering testing</u> .....	215
9	<u>References</u> .....	218

## LIST OF FIGURES

<u>Figure 1-1: Mechanism of action during PET</u> .....	2
<u>Figure 1-2: The typical process flow for production of PET tracers for patient imaging</u> .....	7
<u>Figure 1-3: Chemical scheme for the synthesis of [<sup>18</sup>F]fallypride [35].</u> .....	11
<u>Figure 1-4: Different production schemes of PET tracers</u> .....	15
<u>Figure 2-1: Schematic of the microfluidic concentrator chip</u> .....	30
<u>Figure 2-2: Fluidic and electronic wiring diagram of the automated microfluidic concentration system</u> .....	32
<u>Figure 2-3: Photographs showing system operation during the concentration process for a sample of diluted food dye</u> .....	35
<u>Figure 2-4: Contact angle measurements for (A) EtOH and (B) MeCN mixtures with water at different temperatures</u> .....	41
<u>Figure 2-5: Determination of BTP</u> .....	42
<u>Figure 2-6: Breakthrough pressure testing rig and testing setup</u> .....	44
<u>Figure 2-7: Radio-chromatograms to assess radiochemical purity of PET tracers before and after microfluidic concentration</u> .....	47
<u>Figure 2-8: Standard curve comparing AUC and organic solvent composition</u> .....	49
<u>Figure 2-9: Schematic of setup to measure speed of rotary evaporation</u> .....	51
<u>Figure 2-10: Alternative heating designs</u> .....	53
<u>Figure 2-11: Sample IR thermal images of a (A) gas flow layer, and a (B) sample layer</u> .....	54
<u>Figure 2-12: PET/CT maximum intensity projection (MIP) image of mouse one hour after injection with [<sup>18</sup>F]D-FAC</u> .....	57
<u>Figure 2-13: Evaporation rates as a function of different operating parameters</u> .....	62
<u>Figure 2-14: Evaporation rate comparison between microfluidic and rotary evaporator</u> .....	63
<u>Figure 2-15: Evaporation rates of deionized water as a function of temperature for different chip materials</u> .....	64
<u>Figure 2-16: Evaporation rates of deionized water for different designs</u> .....	67
<u>Figure 2-17: Dynamic evaporation rates of different solvents</u> .....	70
<u>Figure 2-18: Sample recovery measurements using [<sup>18</sup>F]fluoride solutions</u> .....	72
<u>Figure 2-19: In-chip measurement of the effects of sample breakthrough</u> .....	74
<u>Figure 2-20: Percent recovery of different tracers on different sample layer materials concentrated with both partial and complete evaporation modes</u> .....	76
<u>Figure 2-21: Contour plots of % residual solvent after concentration by partial evaporation</u> .....	78
<u>Figure 3-1: Concept image illustrating the role of radionuclide concentration</u> .....	86
<u>Figure 3-2: Fluidic and pneumatic diagram for micro-cartridge and associated valve</u> .....	91
<u>Figure 3-3: Fluidic and pneumatic diagram for the eluent metering subsystem</u> .....	92
<u>Figure 3-4: Fluidic and pneumatic diagram for the reagent delivery subsystem</u> .....	94
<u>Figure 3-5: Contour plots of volume loaded into the intermediate vial as a function of vacuum pressure and flow time for (A) MeCN and (B) DI water</u> .....	96
<u>Figure 3-6: Fluidic and pneumatic diagram for the complete direct loading system (left), and a photograph of the direct loading system (right)</u> .....	97
<u>Figure 3-7: Electronic wiring diagram of the intermediate vial system of the concentrator</u> .....	99
<u>Figure 3-8: Electronic wiring diagram of the direct loading system of the concentrator</u> .....	99
<u>Figure 3-9: Process flow for concentration of a radionuclide</u> .....	100
<u>Figure 3-10: Fluidic and pneumatic diagram of the eluent valve during MeCN rinse of the eluent line (A), eluent line purge (B), and DI water rinse of the eluent line (C)</u> .....	104
<u>Figure 3-11: Fluidic and pneumatic diagram of the cartridge valve during DI water rinse of the reagent loading system</u> .....	105

Figure 3-12: (A) Reaction scheme for synthesis of N-boc-5- <sup>18</sup> Ffluoroindole from Ni-indole complex. (B) System configuration for production of N-boc-5- <sup>18</sup> Ffluoroindole.....	106
Figure 3-13: A model radio-TLC chromatogram of the crude N-boc-5- <sup>18</sup> Ffluoroindole synthesized using concentrated <sup>18</sup> Ffluoride .....	109
Figure 3-14: Trapping efficiency on the cartridge as a function of the starting volume of <sup>18</sup> Ffluoride .....	114
Figure 5-1 Photograph and schematic of the passive microfluidic chip.....	145
Figure 5-2: Schematic of microfluidic chip fabrication process .....	148
Figure 5-3: Droplet dispensing and movement on simple passive microfluidic chips .....	150
Figure 5-4: Behavior of solvents droplets of different volumes after reaching the reaction site .....	151
Figure 5-5: Calibration curves for dispensed droplet volume .....	154
Figure 5-6: Schematic and photograph of microreactor system.....	155
Figure 5-7: Radiosynthesis scheme of <sup>18</sup> Ffallypride.....	157
Figure 5-8: Schematic of <sup>18</sup> Ffallypride synthesis on the passive microfluidic chip.....	158
Figure 5-9: Examples of radio-HPLC chromatograms of <sup>18</sup> Ffallypride synthesis on the microfluidic reaction chip.....	160
Figure 5-10: Moving rate of different solvents as a function of taper angle of the reagent delivery pathway .....	163
Figure 5-11: Sequence of photographs of the microfluidic chip during the mock synthesis of <sup>18</sup> Ffallypride.....	165
Figure 5-12: Distribution of radioactivity visualized using Cerenkov imaging after different steps of radiosyntheses. (A) after <sup>18</sup> Ffluoride drying step; (B) after fluorination reaction; (C) residual radioactivity on chip after collection of product. ....	166
Figure 5-13: Small-animal PET/CT images from the static scan after 60 min uptake of <sup>18</sup> Ffallypride.....	170
Figure 6-1: Tracer production scheme using the integrated radionuclide concentrator and microfluidic radiosynthesizer .....	174
Figure 6-2: Photographs of subcomponents used in the integration platform .....	175
Figure 6-3: Schematic of the SCX filtration module .....	177
Figure 6-4: Two different designs of the interface between the radionuclide concentrator and the droplet-based radiochemistry chip.....	184
Figure 6-5: Microdroplet synthesis of <sup>18</sup> Ffallypride.....	185
Figure 6-6: Distribution of radioactivity on the chip after evaporation following initial <sup>18</sup> Ffluoride loading and drying, visualized using Cerenkov imaging .....	195
Figure 6-7: Performance of synthesis on integrated system at higher activity levels (3.7 – 41 GBq [0.10 – 1.1 Ci]) .....	199
Figure 6-8: Examples of HPLC purification (crude) chromatograms of syntheses .....	201
Figure 8-1: Illustration of droplet merging methods used between the radionuclide concentrator and downstream dispenser .....	206
Figure 8-2: Droplet merging chip.....	209
Figure 8-3: Activity recovery from the droplet merging chip as a function of number of eluent plugs (each 6.2 $\mu$ L) loaded into the chip.....	211
Figure 8-4: Trapping efficiency of a solution containing 1.0 mL KF of various concentrations spiked with a small amount of <sup>18</sup> Ffluoride .....	212

## LIST OF TABLES

<u>Table 2-1: Semi-preparative HPLC conditions used for the purification of example PET tracers [<sup>18</sup>F]D-FAC and [<sup>18</sup>F]FHBG were purified using Phenomenex Gemini-NX column (10mm x 250mm); others used a Phenomenex Luna column (10mm x 250mm).....</u>	45
<u>Table 2-2: Analytical HPLC conditions for PET tracers and prosthetic groups.....</u>	46
<u>Table 2-3: Desired and actual operating parameters for the rotary evaporator.....</u>	51
<u>Table 2-4: Comparison of biodistribution showing similar uptake in key organs.....</u>	57
<u>Table 2-5: Breakthrough pressures measured with the membrane test rig.....</u>	59
<u>Table 2-6: Vapor pressure as a function of temperature for various mobile phase compositions based on (A) MeCN and (B) EtOH.....</u>	61
<u>Table 2-7: Unpaired t-test of evaporation rates.....</u>	71
<u>Table 3-1: Parameters used to load the specified volumes from reagent reservoirs into the intermediate vial.....</u>	96
<u>Table 3-2: Duration for each low-level step of the concentration process (intermediate vial system).....</u>	110
<u>Table 3-3: Duration for each low-level step of the concentration process (direct loading system).....</u>	111
<u>Table 3-4: Efficiencies of [<sup>18</sup>F]fluoride trapping after preconditioning with various solutions measured in the intermediate vial system.....</u>	113
<u>Table 3-5: Performance as a function of number of eluent and rinse plugs.....</u>	115
<u>Table 3-6: Efficiencies of [<sup>18</sup>F]fluoride elution using different eluent solutions measured in the intermediate vial system.....</u>	117
<u>Table 3-7: Recovery of [<sup>18</sup>F]fluoride (with respect to trapped activity) with the intermediate vial system as a function of eluent with varying compositions of MeCN.....</u>	118
<u>Table 3-8: Reaction conditions and radiochemical yield (RCY; decay-corrected) for synthesis of N-boc-5-[<sup>18</sup>F]fluoroindole using concentrated [<sup>18</sup>F]fluoride.....</u>	119
<u>Table 4-1: Flow rates of cartridges fabricated with different resin, resin mass, and tubing inner diameter (ID).....</u>	134
<u>Table 4-2: Trapping and elution data for various sized cartridges packed with Oasis MCX resin.....</u>	136
<u>Table 4-3: Performance of automated trapping and elution with different cartridges (resin type and resin mass) and different eluent solutions.....</u>	137
<u>Table 4-4: Trap and elution performance of gallium-68 for straight tubing cartridges with 9 grams of Chromafix PS-H<sup>+</sup> resin and 0.05N HCL in 98% (v/v) acetone/H<sub>2</sub>O as an eluent solution.....</u>	139
<u>Table 5-1: Contact angle measurements of a droplet of DI water (~2 μL) on the microfluidic chip at different stages during the fabrication process.....</u>	163
<u>Table 5-2: Performance of [<sup>18</sup>F]fallypride synthesis using manual or automated reagent loading and product collection.....</u>	167
<u>Table 5-3: Performance of [<sup>18</sup>F]fallypride synthesis with scaled-up starting radioactivity.....</u>	169
<u>Table 6-1: Trapping efficiency of [<sup>18</sup>F]fluoride in cartridges with 3mg of varying resin as a function of volume of DI water rinse used during preconditioning.....</u>	181
<u>Table 6-2: Flow rates of water (driven at 20 psi) through different SAX cartridges (resin type and mass).....</u>	189
<u>Table 6-3: Effect of resin type on trapping and elution performance (for 3 mg cartridges).....</u>	190
<u>Table 6-4: Effect of eluent concentration on trapping and elution performance (for 3 mg Sep-Pak QMA cartridges).....</u>	192
<u>Table 6-5: Effect of different TBAHCO<sub>3</sub> concentrations (mixed with [<sup>18</sup>F]fluoride source) on the performance of the droplet synthesis of [<sup>18</sup>F]fallypride (n=1).....</u>	193
<u>Table 6-6: Optimization of precursor volume for [<sup>18</sup>F]fallypride synthesis.....</u>	194

Table 6-7: Activity loss in various locations within the integrated system during [<sup>18</sup>F]fluoride transfer and dispensing ..... 196

Table 6-8: Detailed performance of integrated process of radionuclide concentration and droplet synthesis of [<sup>18</sup>F]fallypride ..... 198

Table 8-1: Trapping and elution performance of a [<sup>18</sup>F]fluoride solution spiked with 1mM KF using cartridges with increased resin mass .....215

Table 8-2: Trapping performance of [<sup>18</sup>F]fluoride spiked into a solution of decayed [<sup>18</sup>O]H<sub>2</sub>O that was filtered through an SCX cartridge or not filtered .....217

## ACKNOWLEDGEMENTS

I wanted to first start off by thanking the funding sources that supported all of my doctoral work: the National Institute on Aging (R21 AG049918), the National Institute of Mental Health (R44MH097271), the National Cancer Institute (R21 CA212718, U54 CA151819, R21CA174611), and the UCLA Foundation from a donation made by Ralph and Marjorie Crump for the Crump Institute for Molecular Imaging.

I want to thank all of my fellow lab members in the van Dam lab, both past and present. I want to thank Dr. Tim Tseng for welcoming me into the lab and helping me get started on my first project. I want to sincerely thank Dr. Mark Lazari whom of which went above and beyond to help make sure the van Dam lab was the right fit and then for always making sure I got the help I needed to perform my research. Dr. Lazari's work ethic and mindset is something I strive to achieve. Furthermore, I also want to thank Dr. Jimmy Ly for helping me both in academics and in life by keeping me focused on school and research while also reminding me to destress and take care of my health. I want to also thank Dr. Maxim Sergeev, for all of his help with radiochemistry and for his input on my projects. Thank you to Jia Wang for her friendship and help on various projects. It's been a pleasure to work with you, and I know for certain I couldn't have accomplished as much as I have without your help. Thank you to Dr. Helen Ma for teaching me about EWOD based microfluidic systems; Dr. Shiliin Cheung for her advice on analytical chemistry techniques and her input on the overall direction of positron emission tomography; Jeffery Collins for his help with getting me started in radiochemistry and for all of his help and input on my experiments; and Noel Ha for his friendship and all of his help with tracer production and microfluidic fabrication. I also want to thank the newer members of the van Dam lab. Thank you to Ksenia Lisova for all of her help with microchip radiochemistry and analytical techniques; thank you to Alejandra Rios for her help with experiments and chemistry; thank you to Travis Holloway for his advice in organic chemistry techniques; and thank you to Jason Jones for his input on electrical circuit design. Lastly, I wanted to also thank all of the

volunteers and undergraduate researchers that have made a huge impact on the lab as well as on my research. Thank you to Sebastian Hanet, Max Putintsev, Louie Putterman, and Alec Barajas.

I would also like to thank all of our close collaborators: Dr. Arion Chatziioannou for his knowledge on radiation and radiation safety; Dr. Alex Dooraghi for his advice on LabVIEW and radiation detection; Dr. Maruthi Narayanam for his help with radiochemistry and analytical techniques; Dr. Christopher Waldmann for his help with radiochemistry; Dr. Raymond Gamache for his warm friendship and help with radiochemistry; Dr. Gaoyuan Ma for her friendship and radiochemistry advice; Dr. Joseph Argus for his assistance with GC-MS; James McDaniel for his advice on proper organic chemistry techniques; Dr. Mehrdad Balandeh for his knowledge and expertise in electrochemistry, and Adrian Gomez for all of his help on analytical chemistry techniques. Thank you to Dr. Michael E. Phelps for welcoming me into the Pharmacology department and for all of his support. I would also like to thank our collaborators from Sofie Biosciences: Alex Hsiao, Melissa Moore, Brandon Maraglia, Nam Lai, Aaron Funk, Natasha Reeves. Thank you all for giving me an opportunity to gain insight into product design in an industrial setting and also for teaching me skills in mechanical and electrical engineering.

I would like to also thank everyone at the Crump Preclinical Imaging Technology Center. Thank you to Waldemar Ladno, Olga Sergeeva and Theresa Falls for your help with preclinical imaging. Thank you to Dr. Jason Lee for his help with preclinical imaging and lessons on image and data processing. His passion for the field and attention to detail is something I strive to possess. I also greatly appreciate all of the members of the UCLA Biomedical Cyclotron Facility, both past and present. I want to thank Dr. Sam Sadeghi, Dr. Umesh Gangadharmath, and Dr. Roger Slavik for their generous supply of [ $^{18}\text{F}$ ]fluoride as well as [ $^{68}\text{Ga}$ ] $\text{Ga}^{3+}$ . In particular I want to thank Dr. Roger Slavik for all of his input on [ $^{68}\text{Ga}$ ] $\text{Ga}^{3+}$  concentration, purification, and labeling. Furthermore, I also want to thank Chris Bobinski, Daniel Yeh, Phillip Marchis, Andrew

Grice and Hemantha Kumara for all of their assistance in accommodating my [ $^{18}\text{F}$ ]fluoride and [ $^{68}\text{Ga}$ ] $\text{Ga}^{3+}$  needs.

I want to thank the administrative teams from the pharmacology department, bioengineering department, and the California Nano Systems Institute (CNSI). From the pharmacology department I want to thank Emily Fitch, Elizabeth Arce, Sandy Ma, Stacey Chiong, Erika Corrin, Caroline Cortez, Cecilia Canadas, and Jessica Kim. I want to especially thank Emily for always making me feel welcome at pharmacology events, and for helping me with my graduate funding; Sandy, Karen, Caroline, and Cecilia for helping with purchasing, and reimbursements; Jessica and Stacey for help with student parking and graduate funding; Elizabeth for help with travel reimbursements and general administrative things; and lastly Erika Corrin for going above and beyond whenever I needed any administrative help from access cards, to meeting room scheduling, to reimbursements. From the Bioengineering department, I would like to thank Anne-Marie Dieters, Stacey Fong, Apryll Chin, and Melissa Tran for helping me reach all of my graduation requirements. From CSNI, I would like to thank Frank Alcala, Pierre Decastro, Kerry Harris, Nikki Lin. Thank you for all of your help in delivering packages, scheduling meeting rooms, and ensuring that I have a comfortable environment to work in.

I want to also thank my family and friends whom have supported me through not only my PhD career by also through my entire life. I want to thank my parents, James and Vivian Chao for their loving support, guidance, and words of wisdom. I would not be where I am today without their love and support. I want to also thank my undergraduate roommate, Brandon Wong for helping me become the researcher I am today. It's always been a pleasure to talk to you about both life and science. To my girlfriend Natalie Vu, I am especially thankful to have had your love and support throughout my PhD career. Thank you for helping me in all aspects of my life. Finally, a big thank you to all of my childhood and undergraduate friends. Your support and friendship is really appreciated and has kept me happy throughout my PhD career.

Lastly, I want to thank my doctoral committee for working with me to advance my research and for developing me into the researcher I am today. Thank you to Dr. Eric Chiou for all of your input on microfluidic design and microfabrication. Thank you for your perspective on the field of microfluidics beyond applications for radiochemistry. Thank you to Dr. Sam Sadeghi for all of your insightful advice on my projects, and your detailed questions (that really inspired critical thinking) during my presentations throughout my PhD career. Thank you Dr. Jennifer Murphy for all of your assistance and advice in my projects during my PhD career. Your expert input on the field of radiochemistry has helped me focus my research on new and novel topics. Thank you also for your detailed edits on my manuscripts, resume, and curriculum vitae. Finally, I would like to thank Dr. Michael van Dam for everything he has done to help me during my PhD career. Mike is an incredible professor who dedicates all of his time and effort to his students to help them grow not only as researchers but also into better individuals that are well prepared to take on anything life may throw their way. Mike is selfless – he puts the needs and desires of his students before all else. During my PhD career in Mike’s lab, I’ve been given the opportunity to propose new research ideas, design meaningful experiments, develop a diverse set of technical skills, write grants, manuscripts, and patent applications, attend conferences to present my research and network with fellow peers, mentor undergraduate students and volunteers, and collaborate with companies in industry. The skills I have learned from these experiences are priceless, and I am sure that I will be able to rely on these skills to improve the fields of medicine and bioengineering. Mike not only provided me the means to fully immerse myself in all of these opportunities, but also provided me with guidance, and encouragement. Most importantly, he has instilled in me the ideals of performing research with integrity, efficiency, and thoroughness. In addition to being a great mentor and boss, Mike has also been a great friend and colleague. Thank you for everything.

**Chapter 2: Microfluidic membrane concentration of purified tracers is a modified version of:**

Chao, P. H., Collins, J., Argus, J. P., Tseng, W. Y., Lee, J. T., & van Dam, R. M. (2017). Automatic concentration and reformulation of PET tracers via microfluidic membrane distillation. *Lab on a Chip*, 17(10), 1802-1816.

**Chapter 3: Concentration of [<sup>18</sup>F]fluoride is a modified version of:**

Chao, P. H., Lazari, M., Hanet, S., Narayanam, M. K., Murphy, J. M., & van Dam, R. M. (2018). Automated concentration of [<sup>18</sup>F] fluoride into microliter volumes. *Applied Radiation and Isotopes*, 141, 138-148.

**Chapter 4: Concentration of radiometals is a modified version of a manuscript in preparation.**

**Chapter 5: Design of a simple and reliable microfluidic radiosynthesizer is a modified version of:**

Wang, J., Chao, P. H., Hanet, S., & van Dam, R. M. (2017). Performing multi-step chemical reactions in microliter-sized droplets by leveraging a simple passive transport mechanism. *Lab on a Chip*, 17(24), 4342-4355.

**Chapter 6: Combined radionuclide concentration and PET tracer synthesis is a modified version of a manuscript in preparation.**

## VITA

### EDUCATION

---

Doctor of Philosophy in Bioengineering Expected June 2019  
University of California, Los Angeles, Los Angeles, CA

Masters of Science in Bioengineering 2015  
University of California, Los Angeles, Los Angeles, CA

Bachelor of Science in Biomedical Engineering 2012  
University of California, Irvine, Irvine, CA

### ACADEMIC RESEARCH EXPERIENCE

---

Graduate Research Assistant 2013 – 2019  
Crump Institute for Molecular Imaging,  
Department of Molecular and Medical Pharmacology  
University of California, Los Angeles

Undergraduate Research Assistant 2008 – 2012  
Department of Bioengineering  
University Of California, Irvine

### INDUSTRIAL RESEARCH EXPERIENCE

---

Associate Scientist 2012 – 2013  
Triple Ring Technologies – Newark, Ca

### SELECTED JOURNAL PUBLICATIONS

---

**Chao, P. H.**, Wang, J., Slavik, R. & van Dam, R. M. Concentration of gallium-68 to microliter volumes for microfluidic radiolabelling. *Manuscript in preparation*.

**Chao, P. H.\***, Wang, J.\* & van Dam, R. M. Curie Level Radiochemical Reactions in Microliter-sized droplets. *Manuscript in preparation*. \*Authors contributed equally to this work

**Chao, P. H.**, Lazari, M., Hanet, S., Narayanam, M. K., Murphy, J. M., & van Dam, R. M. (2018). Automated concentration of [<sup>18</sup>F] fluoride into microliter volumes. *Applied Radiation and Isotopes*, 141, 138-148.

Wang, J., **Chao, P. H.**, Hanet, S., & van Dam, R. M. (2017). Performing multi-step chemical reactions in microliter-sized droplets by leveraging a simple passive transport mechanism. *Lab on a Chip*, 17(24), 4342-4355.

**Chao, P. H.**, Collins, J., Argus, J. P., Tseng, W. Y., Lee, J. T., & van Dam, R. M. (2017). Automatic concentration and reformulation of PET tracers via microfluidic membrane distillation. *Lab on a Chip*, 17(10), 1802-1816.

## PATENT APPLICATIONS

---

**Chao, P.H.**, van Dam, R. M. Method for concentration and formulation of radiopharmaceuticals. PCT/US17/50236, filed Sept 6, 2017. [Priority data: 62/384,084, filed Sept 6, 2016]

## SELECTED CONFERENCE PRESENTATIONS

---

**Chao, P.H.**, Wang, J. & van Dam, R.M. A fully automated radiosynthesis platform for scalable production and purification of PET tracers. The Twenty Second International Conference on Miniaturized Systems for Chemistry and Life Sciences ( $\mu$ TAS 2018); Kaohsiung, Taiwan. (poster presentation)

Wang, J., **Chao, P.H.** & van Dam, R.M. GBq-level radiochemical reactions in microliter-sized droplets. 2018 World Molecular Imaging Congress; September 2018; Seattle, WA, USA. (oral presentation)

Rios, A., Wang, J., **Chao, P.H.** & van Dam, R.M. Optimization of [ $^{18}$ F]fallypride radiosynthesis using a high-throughput microdroplet reaction platform. 2018 World Molecular Imaging Congress; September 2018; Seattle, WA, USA. (poster presentation)

**Chao, P.H.**, Lazari, M., Hanet, H., & van Dam, R.M. A fully-automated system for Concentration of [ $^{18}$ F]Fluoride into Microliter Volumes. 2018 World Molecular Imaging Congress; September 2018; Seattle, WA, USA. (poster presentation)

**Chao, P. H.**, Collins, J., Argus, J. P., Tseng, W. Y., Lee, J. T., & van Dam, R. M. An automated microfluidic system for reformulation and concentration of PET tracers for preclinical imaging. 2017 UC Systemwide Bioengineering Symposium, Los Angeles, Ca, USA (oral presentation)

**Chao, P. H.**, Collins, J., Argus, J. P., & van Dam, R. M. Automated Microfluidic Device for Reformulation and Concentration of PET tracers. 2016 World Molecular Imaging Congress; September 2016; New York, NY, USA. (poster presentation)

**Chao, P. H.**, & van Dam, R. M. The use of microfluidics in the concentration and formulation of PET tracers. The International Chemical Congress of Pacific Basin Societies 2015; Honolulu, Hi, USA (oral presentation)

## HONORS

---

NIBIB DEBUT Challenge Competition – 1st place Honorable Mention	2012
Henry Samueli School of Engineering – Cum Laude Honors	2012
Tau Beta Pi – Engineering Honor Society	2011

# 1 Chapter 1: Introduction

## 1.1 Positron emission tomography

Positron emission tomography (PET) is an imaging modality that relies on the use of radiolabeled tracers for monitoring the metabolism of biomolecules *in vivo*. PET imaging can provide tremendous amounts of data for both clinical and research applications. Imaging with PET can provide *in vivo* measurements of the reaction rates of different biological processes such as glucose metabolism, DNA replication, or gene expression based on interaction events between the specific PET tracer and cellular enzymes, or can provide information about the distribution and density of specific receptors or other binding targets. [1–3] In the clinical setting, biological information obtained from PET imaging is widely used in diagnosing disease, monitoring response to therapy, and aiding in personalized medicine. [4–6] By providing the ability to monitor specific cellular processes / response (e.g. apoptosis), or microenvironment (e.g. hypoxia) PET can be a crucial tool for drug screening and development in preclinical animal models, and can be critical for measuring pharmacokinetic properties of drugs in research patients. [7–9] Lastly, in the field of novel drug development, radiolabeled drugs can provide *in vivo* analysis of various drug properties such as metabolic stability, pharmacokinetics, biodistribution, and targeting. [10–13]

PET tracers are typically in the form of a biomolecule labeled with a positron emitting radionuclide (e.g. fluorine-18, carbon-11, nitrogen-13, and oxygen-15). For example, the most commonly used PET tracer currently is 2-[<sup>18</sup>F]fluoro-2-deoxy-D-glucose ([<sup>18</sup>F]FDG), a glucose analog labeled with fluorine-18. Once the PET tracer is injected into a subject, the tracer circulates throughout the body and becomes localized due to binding interactions (i.e. for tracers that interact with receptors), or due to trapping within cells (i.e. for tracers that interact with enzymes). From here, positrons emitted as the radionuclide decays travel a short distance and

combine with electrons in the neighboring tissue. Upon combining, an annihilation event occurs where the mass of the positron and electron are converted into their energy equivalent (through the equation  $E= mc^2$ ) releasing two 511 keV photons (gamma rays) 180° apart. [1] The photons can then be detected as a coincidence event when they strike opposing detectors at the same time. During a PET scan, millions of photon pairs in all orientations are detected. [1] These detected events are then used to reconstruct a 3-dimensional tomographic image of the distribution of the PET tracer within the body. A schematic of an annihilation event during PET imaging can be seen in Figure 1-1.

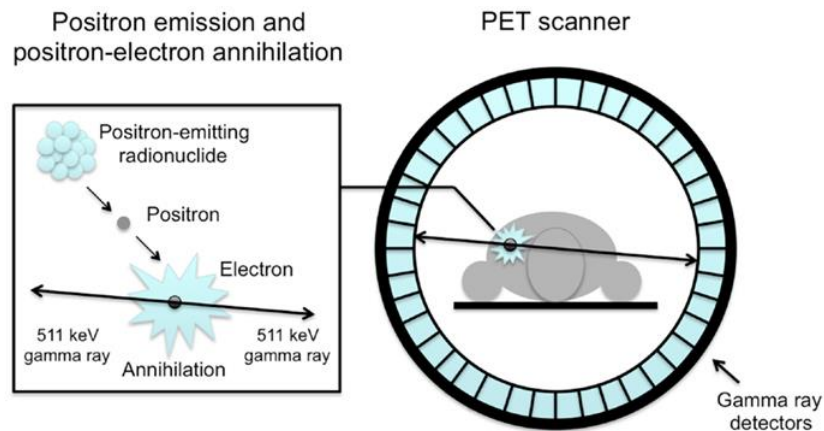


**Figure 1-1: Mechanism of action during PET**

Positron released from a radionuclide meets with a nearby electron causing an annihilation event releasing two co-linear 511keV gamma rays which can be detected by surrounding gamma ray detectors

Of the various types of positron emitting radionuclides, fluorine-18 is most commonly used due to its availability from cyclotrons and its favorable physical properties, i.e. half-life (109.7 minutes), high positron yield (97%) and low positron energy (0.635MeV). [14] Compared to carbon-11 and nitrogen-13 which have 20.4 minute and 9.96 minute half-lives respectively, fluorine-18 provides adequate working time during synthesis of the tracer, and provides the opportunity to produce tracers centrally and then ship them to an imaging facility. [14] The lower

positron energy of fluorine-18 compared to 0.96MeV of carbon -11 allows for increased resolution during PET scans as positrons annihilate closer to their emission source. [14]

Despite substantial development efforts on labeling small molecules with the radionuclides mentioned above, there are associated limitations. One limitation is the specificity of these small molecule tracers for particular biological targets. [<sup>18</sup>F]FDG monitors increased glucose transport and elevated glycolysis allowing for differentiation between cancer cells and benign cells due to difference in metabolism. [15] This tracer, however, is not target specific and cannot differentiate between cells that have an increased metabolic rate due to cancer or other stimuli such as infection or inflammation. [15] Another limitation of small molecule based PET tracers are their short biological half-lives making imaging of longer lasting biological processes difficult to visualize. [16] Several groups have explored labeling other small molecules with fluorine-18 and demonstrated more target specificity (than [<sup>18</sup>F]FDG) to different biological targets. [17,18] Concurrently, researchers are also exploring the use of peptides and antibodies as PET imaging agents. [15,19]

For peptides and antibodies, labeling with fluorine-18 through direct fluorination of the biomolecule may prove to be difficult due to incompatibility of the biomolecule and the fluorinating conditions (e.g. high temperatures, organic solvents, acidic conditions). [15,20,21] To facilitate peptide and antibody labeling, constructs called “prosthetic groups” containing fluorine-18 have been developed. [15,19–21] The prosthetic groups themselves are prepared under harsh conditions, but can then be used for rapid radiolabeling of biomolecules under mild reaction conditions (e.g. room temperature, physiological pH) and have been used for <sup>18</sup>F-fluoroalkylation, <sup>18</sup>F-fluoroacylation, and <sup>18</sup>F-fluoroamidation. [15] N-succinimidyl-4-[<sup>18</sup>F]fluorobenzoate ([<sup>18</sup>F]SFB), one of the most common prosthetic groups, can be used for acylation with amine groups at the N-terminus and on lysine residues of peptides or proteins.

[22,23] This is generally considered a “random” labeling approach due to the many possible locations where [<sup>18</sup>F]SFB may react. Alternatively, prosthetic groups have also been designed to target thiol moieties as these groups are less abundant than amines within peptides, proteins and antibodies and may allow for more chemoselectivity within the biomolecule. [15] One example of a thiol targeting prosthetic group is 4-[<sup>18</sup>F]fluorobenzamido-ethylmaleimide ([<sup>18</sup>F]FBEM). To further increase chemoselectivity and regiospecificity in labeling of biomolecules, researchers have also used “biorthogonal” reactions such as alkyne and azide reactions (also referred to as click-chemistry). [24] These functional groups do not naturally exist in biology. Introduction of these functional groups to biomolecules and prosthetic groups, therefore, can be used to ensure the prosthetic group is attached at one single specific location in the biomolecule. This approach, however, does require the modification of the biomolecule in advance with an appropriate complementary moiety (e.g. azide or alkyne).

Certain biomolecules such as antibodies can have varying biological half-lives ranging from hours to days. [19] In order to track these biomolecules throughout their biological half-lives, longer-lived positron-emitting radiometals (e.g. Zirconium-89, Copper-64) must be used. Zirconium-89 has a half-life of 78.5 hours, a positron yield of 23% and a positron energy of 396 keV. [19] Copper-64 has a half-life of 12.7 hours, a positron yield of 18% and a positron energy of 278 keV. [19] On a separate note, some radiometals (e.g. gallium-68) can be conveniently produced from a benchtop “generator” not requiring an expensive cyclotron. [25] While the half-life of gallium-68 is only 68 min, the convenient supply of the isotope may have advantages over fluorine-18 for labeling biomolecules with short biological half-lives.

Labeling of peptides, proteins, and antibodies with radiometals requires an intermediate to link the radiometal to the biomolecule of interest. The intermediate used is typically a bi-functional metal chelator which has affinity for certain metals based on the coordination

chemistry of that specific metal ion. [16] This chelator can be linked directly to the biomolecule of interest or through a short chemical linker. Work done by Zettlitz et al. demonstrated the labeling of an anti-CD20 cys-diabody (GAcDb) with various radionuclides (e.g. fluorine-18, zirconium-89, and iodine-124) through different prosthetic groups and chelators showing the flexibility of labeling with different radionuclides. [26,27] Zirconium-89 labeling of GAcDb was implemented through the use of the chelator and linker complex, deferoxamine-maleimide (mal-DFO). [26] The maleimide moiety allows for specific labeling to thiol groups [19], while the deferoxamine group designed to be an iron chelator is commonly also used for binding Zr(IV). [16] Iodine-124 labeling of GAcDb was performed through direct radioiodination. [26] GAcDb was labeled with fluoride-18 through the use of [<sup>18</sup>F]SFB (random labeling of amine groups throughout the diabody) and [<sup>18</sup>F]FBEM (site-specific labeling of single thiol group). [27] Comparing [<sup>89</sup>Zr]Zr-DFO-GAcDb to <sup>124</sup>I-GAcDB, [<sup>89</sup>Zr]Zr-DFO-GAcDb produced greater target specific uptake and retention in mice. [26] [<sup>18</sup>F]FBEM-GAcDb and [<sup>18</sup>F]SFB-GAcDb showed different blood clearance rates and biodistribution when injected in mice for imaging. Despite a slower blood clearance, [<sup>18</sup>F]SFB-GAcDb showed more favorable *in vivo* pharmacokinetics compared to [<sup>18</sup>F]FBEM-GAcDb. [27] Due to the biological half-life of GAcDb being 4-5 hours, the fluorine-18 labeled versions of GAcDb ([<sup>18</sup>F]FBEM-GAcDb or [<sup>18</sup>F]SFB-GAcDb) with a shorter radioactive half-life compared to the radiometal labeled analogs (<sup>124</sup>I-GAcDB, and [<sup>89</sup>Zr]Zr-DFO-GAcDb), resulted in less radiation exposure to subjects. [27] One caveat to using different radionuclides however, is that differences in the molecular structure (due to differences in radionuclides, chelators, and prosthetic groups) play a significant role in the pharmacokinetics of the biomolecule as well as the *in vivo* stability of the tracer. Researchers are just beginning to accumulate data to better understand the impact of different labeling strategies.

One added benefit of working with biomolecules labeled with radiometals through chelator chemistry is the direct translation from PET tracers for imaging to tracers for targeted radiotherapy (RTT) by switching the chelated radiometal from a positron-emitting isotope to a beta- or alpha-emitting isotope. Song *et al.* labeled an anti-EGFR antibody with both  $^{64}\text{Cu}$  and  $^{177}\text{Lu}$  via the same chelator (PCTA) for immuno-PET imaging and RTT. [28] RTT relies on a biomolecule to deliver a therapeutic radionuclide to the site of interest. As opposed to primarily positron emission from PET imaging tracers, RTT agents emit beta, alpha, or Auger electrons which can cause localized cell death through irreversible DNA damage. [29] As highlighted by Tsai and Wu (2018), there are wide variety of suitable radiometals for RTT - choice of radionuclide depends on the type of cancer being targeted, target density, and heterogeneity as radiometals differ in particle emission ranges and linear energy transfer. [19]

PET is an extremely powerful tool commonly used for disease diagnosis, treatment progression monitoring, drug discovery, and can also be used to provide insight on developing agents for RTT. PET imaging agents can be based on small molecules, peptides, proteins, nanoparticles, and intact or modified antibodies. Different radionuclides can be used depending on desired half-life and decay characteristics (ie. positron yield, positron energy). In order to label these small molecules and biomolecules, there exists many different labeling strategies including: direct labeling, prosthetic groups, and bifunctional chelators.

## 1.2 Production of PET tracers

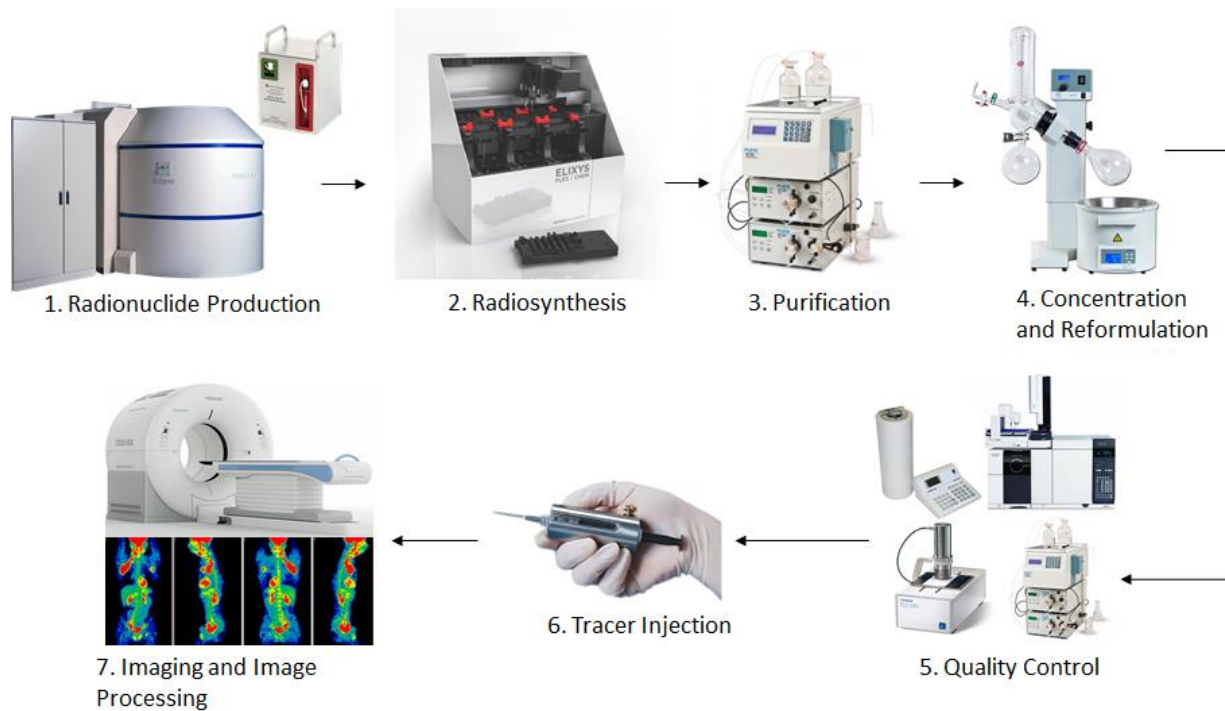


**Figure 1-2: The typical process flow for production of PET tracers for patient imaging**  
Production starts with creation of radionuclides (e.g. fluorine-18 and gallium-68) followed by radiosynthesis, purification, concentration and reformulation, quality control testing of produced tracer, injection, imaging and image processing.

### 1.2.1 General production scheme of PET tracers

Due to the short half-life of the radionuclides mentioned above, PET tracer production must typically be performed immediately prior to an imaging event. Production of a PET tracer can be broken down into three major parts: production of the radionuclide, radiochemical synthesis of the tracer, and lastly purification, formulation and quality control of the tracer. Immediately after production, the tracer is injected into the patient for a scan. A detailed flow chart of the PET tracer production process can be seen in Figure 1-2. Production of radionuclides is most commonly performed by the use of a cyclotron. Within a cyclotron, a proton or deuteron beam is generated by the combination of a magnetic field (to direct particle

trajectory) and an electrical potential coupled with radiofrequency (to accelerate particles in a periodic fashion). [30] These high energy particles are then directed at a target material for high energy bombardment, creating an atom with excess nuclear energy (i.e. radionuclide). In the case of fluorine-18, production can be performed within a cyclotron through two different nuclear reactions. The first reaction,  $^{20}\text{Ne}(d,\alpha)^{18}\text{F}$ , requires bombardment of a neon gas target and produces  $[^{18}\text{F}]\text{F}_2$  in electrophilic form. Recovery of  $[^{18}\text{F}]\text{F}_2$  is performed by passing through  $\text{F}_2$  as a carrier gas to desorb the activated  $[^{18}\text{F}]\text{F}_2$  from the target surfaces. The recovered  $[^{18}\text{F}]\text{F}_2$  contains large portions of non-radioactive  $\text{F}_2$ , reducing the specific activity of the  $[^{18}\text{F}]\text{F}_2$ . [30] The second reaction,  $^{18}\text{O}(p,n)^{18}\text{F}$ , relies on the bombardment of oxygen-18 enriched water. The reaction provides high specific activity nucleophilic  $[^{18}\text{F}]\text{F}^-$  in enriched water. The  $^{18}\text{O}(p,n)^{18}\text{F}$  reaction can also be performed on an oxygen-18 gas target, but the addition of fluorine-19 carrier gas is required to recover  $[^{18}\text{F}]\text{F}_2$  from the target, lowering the specific activity as was the case for the  $^{20}\text{Ne}(d,\alpha)^{18}\text{F}$  reaction. [30]

In addition to cyclotron production of radionuclides, several radiometals (e.g. gallium-68, and copper-62) can be produced by a generator. [16] A generator is a self-contained standalone system typically the size of a small coffee machine containing a mixture of parent and daughter radionuclides in equilibrium. In the case of gallium-68, the parent radionuclide is germanium-68 which has a half-life of 270 days. [25] Inside a gallium-68 generator, germanium-68 is immobilized on a matrix where it naturally decays to gallium-68 and further to zinc-68. [25] Depending on the immobilization matrix within the generator, a specific elution solution (e.g. 0.1M HCl) can be tailored to elute the gallium-68 from within the generator. Generator production requires significantly less resources and infrastructure making radionuclide production cost effective and simple to do.

Following production of the radionuclide, the radionuclide needs to be chemically linked to the small molecule or biomolecule of interest. This labeling reaction is typically performed in an automated radiochemistry system – a semi or fully automated system comprised of reaction vial(s), heater(s), tubing, reagent reservoirs, and electronic valving. [31] Many groups have recently focused on commercializing single-use cassette-based synthesizers to simplify reagent preparation, reduce cleaning time, and reduce overall system and operating complexity. Some of these systems include: ABT Molecular Imaging Inc. “Biomarker Generator”, Bioscan, Inc. “F18-Plus”, Eckert & Ziegler “Modular-Lab PharmTracer”, IBA “Synthera”, and Sofie Biosciences “Elixys”. The majority of the systems presented above, with the exception of PharmTracer, and Elixys, are designed for “one-pot” syntheses. However, some tracers require multiple reaction steps with intermediate purification processes in between. Increasing synthesis steps to accommodate other tracers therefore requires either user modification of the system or purchasing additional modules which further expands the cost for tracer synthesis. The Elixys system relies on a cartridge-based design, however, still maintains the flexibility to accommodate different radiosynthesis requirements (e.g. high temperatures, high pressures, multi-pot reactions) thus allowing for synthesis of a diverse range of imaging probes. [32]

As mentioned above, many PET tracers rely on the use of fluorine-18 as the labeling radionuclide. Labeling of fluorine-18 to a biomolecule can be performed through either electrophilic fluorination (using  $[^{18}\text{F}]\text{F}_2$ ) or nucleophilic fluorination (using  $[^{18}\text{F}]\text{F}^-$ ). In electrophilic fluorination,  $[^{18}\text{F}]\text{F}_2$  is directly used to react or can be transformed to acetyl $[^{18}\text{F}]$ hypofluorite ( $\text{CH}_3\text{COO}[^{18}\text{F}]\text{F}$ ) which is less reactive. [30] Electrophilic fluorination also typically requires labeling of electronically enriched structures limiting the compatibility of this method with all types of biomolecules. [30] Due to the low starting specific activity of  $[^{18}\text{F}]\text{F}_2$ , the molar activity ( $A_m$ ) of the product is limited as well. The maximum theoretical yield from reacting with  $[^{18}\text{F}]\text{F}_2$  is

50% as only one of the  $F^-$  is incorporated into the molecule of interest. [30] In nucleophilic fluorination, fluorine-18 is in anionic form typically dissolved within an aqueous solution ( $[^{18}O]H_2O$ ). Due to the high electronegativity of the fluoride ion, while in water  $[^{18}F]$ fluoride ions form hydrogen bonds which decreases their nucleophilicity. [33] As such, it is often necessary to isolate  $[^{18}F]$ fluoride from an aqueous environment in order to increase its reactivity.

There have been many different methods to isolate  $[^{18}F]$ fluoride including evaporation of  $[^{18}O]H_2O$ , the use of a strong anion exchange cartridge (SAX) to trap  $[^{18}F]$ fluoride and elute in smaller volumes, electrochemical separation to trap  $[^{18}F]$ fluoride from solution based on charge, or a combination of these individual strategies. [33] The most common method for obtaining isolated  $[^{18}F]$ fluoride is the use of a strong anion exchange (SAX) cartridge followed by azeotropic evaporation. In this method,  $[^{18}F]$ fluoride in  $[^{18}O]H_2O$  produced from a cyclotron (typically 1-5mL in volume) is passed through the SAX trapping the  $[^{18}F]$ fluoride on the cartridge while the  $[^{18}O]H_2O$  is allowed to pass through the cartridge into another receptacle for disposal or recycling. The trapped  $[^{18}F]$ fluoride is then eluted from the SAX cartridge (typically in a volume  $< 1$ mL) with a mixture containing acetonitrile, water, potassium carbonate ( $K_2CO_3$ ) and a phase transfer catalyst such as Kryptofix-222. The acetonitrile serves to decrease water content, while the carbonate ion displaces the trapped  $[^{18}F]F^-$  from the cartridge. The phase transfer catalyst aids in increasing the solubility of  $[^{18}F]$ fluoride in an organic solvent and also increases the reactivity of  $[^{18}F]F^-$  (i.e. by separating fluoride from counter cations like  $K^+$ ). [34] After elution, the product undergoes azeotropic drying which entails initial drying of the eluent, loading of 100% acetonitrile and repeated drying. The process can be repeated several times to ensure thorough removal of water to increase reactivity of the  $[^{18}F]$ fluoride. Isolated  $[^{18}F]$ fluoride can then be redissolved into polar aprotic solvents such as acetonitrile, DMF, or DMSO for downstream reaction with the desired precursor molecule.

Radiolabeling of small molecules (usually aliphatic or aromatic) with activated [ $^{18}\text{F}$ ]fluoride is typically done through direct nucleophilic substitution ( $\text{S}_{\text{N}}2$  reaction). A model reaction synthesizing [ $^{18}\text{F}$ ]fallypride from its precursor, tosyl-fallypride can be seen in Figure 1-3. In this example, [ $^{18}\text{F}$ ]F $^-$  is substituted for the tosylate group which serves as a leaving group. For biomolecules which are sensitive to the conditions typically used for nucleophilic substitution (e.g. high temperature, organic solvents), prosthetic groups are used.

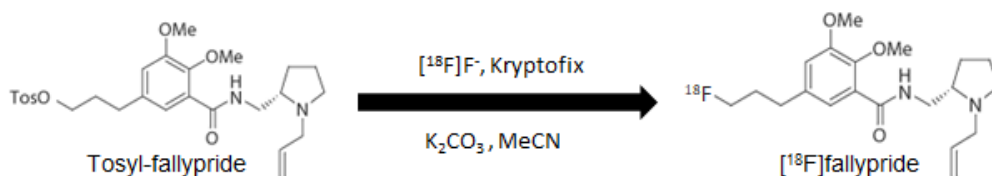


**Figure 1-3: Chemical scheme for the synthesis of [ $^{18}\text{F}$ ]fallypride [35].**

After synthesis of the PET tracer, the tracer is typically purified through high performance liquid chromatography (HPLC) and/or solid phase extraction (SPE). Generally HPLC purification consists of injecting a sample of interest into a liquid mobile phase and then flowing the sample through a porous stationary phase (typically housed inside of a column). HPLC can be broken down into two main types - normal-phase (NP-HPLC) and reversed phase (RP-HPLC) depending on the polarity of the stationary phase. In RP-HPLC, the stationary phase is non-polar, thus interactions of analytes with the stationary phase depends on how well the analyte interacts with a non-polar species. Non-polar analytes that have stronger interactions with the non-polar stationary phase will elute from the column at a later time. The polarity of the mobile phase used also affects analytes and their interaction with the stationary phase. In RP-HPLC, the use of more polar solvents in the mobile phase will increase the interaction of non-polar analytes with the stationary phase resulting in longer retention times. The use of less polar solvents will decrease analyte interaction with the stationary phase and

result in shorter retention times. Analytes, therefore, can be separated by their polarities. In NP-HPLC the stationary and mobile phase polarities are reversed (ie. stationary phase is polar and the mobile phase is non-polar). Non-polar analytes therefore interact less with the stationary phase and elute at an earlier time.

Downstream of the stationary phase (column) is a detector (e.g. UV-vis absorbance, gamma-radiation) or a series of detectors to detect the separated analytes. The detector outputs are typically plotted versus time as a chromatogram. The time at which the analyte reaches the detector is denoted as the retention time of that analyte. Proper separation results in analytes with distinguishably different retention times. Mobile phase composition in the HPLC modes described above are assumed to be kept constant during purification (isocratic). Another mode of operation relies on the use of changing mobile phase polarity (gradient). Gradient operation allows for exploration of a wide range of solvent polarities within one separation run, which could improve separation of analytes that have similar retention times (i.e. when analyte peaks are sharp but overlap) during isocratic operation. The analyte (along with the mobile phase that the analyte is in) after being separated and detected, can then be collected for downstream use. Depending on the flow rates used during separation, the analyte is often collected in 10-50 mL of mobile phase despite the initial injected crude sample being only 1 mL.

Oftentimes the mobile phase used for separation, which is also collected with the purified product, contains toxic solvents (e.g. acetonitrile) requiring reformulation prior to injection into patients or subjects. One approach for reformulation is evaporation of mobile phase at elevated temperature until dryness (commonly performed with a rotary evaporator), followed by reconstitution of the dried residue with saline. Occasionally other additives are used in small amounts to stabilize the tracer against radiolysis (e.g. radical scavengers such as ethanol or citrate), to stabilize the tracer against chemical decomposition (e.g. pH modifiers), or

to increase solubility (e.g., polyethylene glycol, DMSO, etc.). The major downside of this method is the amount of time required to evaporate the mobile phase, especially if starting with large volumes (~50mL). Alternatively, an SPE method can be used for reformulation. In reversed-phase SPE (e.g. with a C18 cartridge), the collected HPLC fraction is first diluted with water to ensure the organic solvent content is sufficiently low (typically <5-10%), and then passed through the SPE cartridge to trap the PET tracer. The mobile phase is diverted to waste during the trapping process. The trapped tracer is released with EtOH which can then be diluted to injectable concentrations (<10% by volume) or evaporated completely and reconstituted in saline. While effective, the SPE process can be time consuming due to the large diluted sample volume and the evaporating and reconstitution process. Following reconstitution, the sample is passed through a filter for sterilization. An aliquot is taken for quality control (QC) testing to assure the identity and purity of the PET tracer, and if the tests pass, the tracer can then be injection to the patient or subject.

For tracers injected into humans, there are strict regulatory requirements requiring QC testing of each batch of tracer that is produced. The specific criteria for these QC tests are outlined by regulatory agencies worldwide. [36] QC tests, generally, can be broken up into two categories. The first category, pharmaceutical tests, involve testing of pH, color and clarity, chemical purity, residual solvents, pyrogenicity, and sterility. [36] These tests ensure that the tracer matches physiological conditions with absence of biological, chemical, and pyrogenic contamination. Secondly, QC tests on the radioactive characteristics of tracers are also performed. These tests include analyzing radiochemical identity, radiochemical purity, radionuclide identity, radionuclide purity, and radioactivity concentration. [36] The majority of these tests are typically performed manually and require an extensive amount of expensive analytical chemistry equipment (e.g. HPLC, gas chromatography – mass spectrometry)

There are many challenges that are associated with the production scheme of PET tracers presented above (Figure 1-2). First, due to the short half-lives of the radionuclides used, the entire production process (ie. synthesis, purification, reformulation, QC) must be performed in a rapid manner to ensure that enough of the radionuclide remains after production. Further improvements on the speed of any of these production steps would have a substantial impact on the overall yield of the tracer after factoring in radioactive decay. Secondly, with existing technology, production of PET tracers requires a large capital investment in equipment, infrastructure, and trained personnel. The majority of the infrastructure cost is associated with adding in safety precautions to either minimize or prevent radiation exposure to workers. Heavy, lead shielded chemical hoods (also known as “hot-cells”) and automated radiosynthesizers are required to facilitate in safe synthesis of PET tracers. These infrastructure requirements pose a large barrier of entry for researchers or clinicians. In order to combat these limitations, PET tracers are currently produced and supplied in a “centralized” manner. [31] In this centralized approach, tracers are produced at centralized facilities (e.g. radiopharmacies) and then are shipped to local imaging centers for use. In this way, the high infrastructure, personnel, and maintenance costs to produce these tracers are split amongst all parties which use the synthesized tracers, reducing the cost of each patient dose to an affordable level. This centralized model has proven to be cost effective and an efficient method for producing [<sup>18</sup>F]FDG for clinicians and researchers. There are, however, several limitations associated with this production scheme. This strategy is only a benefit for tracers in high demand, where many doses are needed at the same time. Therefore, the cost of less widely used tracers, or the cost

of developing new tracers, remains extremely high, and unaffordable for many applications.

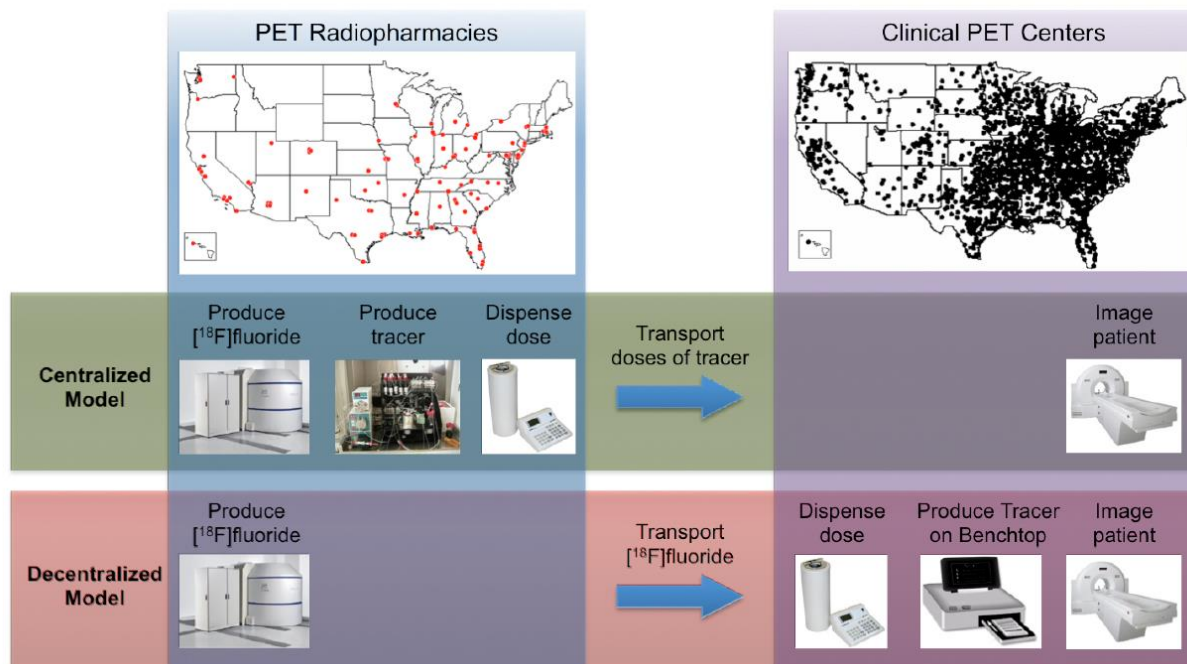


**Figure 1-4: Different production schemes of PET tracers**

Centralized production relies on production of a few different tracers at a central facility and then shipment of these tracers to imaging sites across the US. Decentralized production relies on synthesis of tracers at the imaging site. Figure courtesy of R. Michael van Dam

An alternative to the centralized approach is a decentralized approach where any desired tracer is synthesized at the imaging site just prior to an imaging event. [31] In this approach, users would rely on a low-cost supply of the radionuclide (delivered from a centralized production facility), but would synthesize the desired tracers on demand. A schematic of both production schemes can be seen in Figure 1-4. Currently, the barrier to entry for the decentralized approach lies in high start-up and operation costs. For start-up, proper infrastructure must be established which includes purchasing expensive equipment (e.g. automated radiosynthesizers, plus hot-cells to reduce radiation exposure). The use of traditional radiosynthesizers and analytical equipment requires significant user training, increasing

operation costs. Furthermore, reaction in traditional radiosynthesizers typically are optimized to produce large quantities of tracers. For studies that only require a small amount of tracer, production by traditional radiosynthesizers may not provide the tracer in the needed concentration or molar activity.

Thus decentralized production does not currently provide a way for researchers to obtain diverse PET tracers at low cost. To make the decentralized model viable, the fundamental technologies for production of PET tracers must change to lower the overall cost of production of each batch. The needed changes include: i. Self-shielded radiosynthesizers and analytical equipment allowing for benchtop operation, removing the need for hot-cells ii. Automated, reliable, easy to use radiosynthesizers and analytical equipment, removing the need for intensive operation training and iii. Reconfigurable radiosynthesizers to allow for the synthesis of many different tracers, in both small and large quantities, using one set of hardware (or to enable the development of new tracers). Production of radionuclides can be performed on-site through the use of generators or radionuclides can be purchased at low cost from radiopharmacies as described above.

Although groups have moved towards designing automated, self-contained, radiosynthesizers suitable for decentralized tracer production, there still remains a need to automate other equipment used for tracer production (e.g. HPLC, evaporators). Furthermore, synthesis and analytical systems can be made to be faster and more efficient reducing losses due to radioactive decay.

### **1.3 Microfluidic production of PET tracers**

Due to the desire towards making decentralized PET tracer production more accessible and affordable, there has been strong interest to explore alternative methods for faster, automated, cheaper, and more reliable production of PET tracers while reducing the need for

hot-cells and other infrastructure. One promising field that may aid in achieving these goals is the field of microfluidics. Microfluidics, generally speaking, is the science and technology of systems that process or manipulate small ( $\mu\text{L}$  –  $\text{aL}$ ) amounts of fluids using channels in micrometer dimensions. [37] Microfluidics exploits both its small size and also changes in fluidic behavior such as laminar flow to improve upon standard laboratory processes. [37] Reduction in volumes can enable more accurate control of reaction parameters (e.g. heating, cooling, mixing). In regards to radiosynthesis, microfluidics has been demonstrated to have geometric advantages compared to large scale traditional systems. [38–40] The miniaturized size of the microfluidic platforms allow for faster heating, cooling, and mixing during reaction and the compact size of microfluidic systems enables reduction in the amount of radiation shielding required.

Microfluidic platforms for PET tracer production can be categorized into two main approaches – “flow-through” and “batch”. Flow-through microreactors rely on reactions occurring as reagent streams flow-through mixers and preheated channels or capillaries. The synthesis of [ $^{18}\text{F}$ ]FDG has been successfully demonstrated in several flow-through systems with varying channel materials (e.g. polymer chips, glass chips, capillary tubes). [41–43] Despite reduced overall size, flow-through systems typically require the entire length of the reaction channel to be filled for proper fluid handling resulting in total volumes comparable to those of macroscale systems ( $> 1\text{mL}$ ). Batch microfluidic devices rely on smaller reaction volumes ( $< 50\ \mu\text{L}$ ) and are typically designed with a centralized reactor and reagent channels. Batch based microfluidic synthesis of [ $^{18}\text{F}$ ]FDG was first demonstrated in a polydimethylsiloxane (PDMS) chip with a  $40\text{nL}$  reaction volume. [44] A chip with a larger reactor volume ( $5\ \mu\text{L}$ ) was designed to allow for increased starting activity and thus amount of final product. [45] The total amount of product desired could easily be adjusted by changing starting activity levels and precursor

amounts, enabling small batch production for smaller studies. Following further experimentation, PDMS was determined to be a poor material due to high [ $^{18}\text{F}$ ]fluoride interaction (ie. reducing tracer yield) and chemical incompatibilities with certain reagents leading to chip failure. [45] More recently, groups have focused on a new type of batch microfluidic radiosynthesizer that relies on digital droplet manipulation between two parallel plates, known as electrowetting-on-dielectric (EWOD). [46,47] As opposed to relying on valving and fluidic channels to redirect reagents to the central reactor, EWOD based systems control droplet movement through on-chip electrodes reducing the need for bulky valve actuators and pumps. Because EWOD chips are fabricated using inert and thermally stable materials, a wide range of reagents and reaction conditions can be explored without fear of system failure. [48] The versatility of EWOD based batch radiosynthesizers was demonstrated through production of a series of different fluorine-18 labeled radiotracers and prosthetic groups (e.g. [ $^{18}\text{F}$ ]FLT, [ $^{18}\text{F}$ ]SFB, [ $^{18}\text{F}$ ]FDG, [ $^{18}\text{F}$ ]Fallypride) resulting in yields comparable to conventional methods. [47,49,50]

### **1.3.1 Benefits of microfluidics for PET tracer production**

There exist several unique advantages for performing radiosynthesis in microliter volumes. First, the small dimensions of microfluidic chips enable improved control of reaction conditions by rapid reagent mixing, and efficient heat transfer. [51] These improved conditions allow for faster and higher yielding reactions. Miniaturization of the system allows for the potential to integrate all apparatus need for production (radiosynthesizer, purification unit, formulation unit) into one compact system. Reduction in size is critical for reducing radiation shielding. For example, systems with ~ 20 inch dimensions shrunken down to ~2 inch dimensions would be able to provide the same degree of radiation protection with 100 times less mass of radiation shielding. [51] This reduction could enable bench top operation removing the need for expensive hot-cells.

By using microfluidic platforms for radiosynthesis, radiolysis can be reduced. Radiolysis is a process characterized by chemical bond cleavage caused by radiation. Molecules used in tracer production (e.g. precursor, synthesized probe) can undergo irradiation from the surrounding radioactive species (autoradiolysis). [52, 53] Irradiation can lead to reduced tracer yield as well as formation of side products. The mechanism of action for causing damage is the formation of radical species in the solvent due to interactions of high energy particles (e.g. positrons). [52] While the final formulated product can be stabilized against autoradiolysis by addition of radical scavengers (e.g. ethanol) [53], introduction of radical scavengers during earlier steps of tracer production may prove to be challenging. Since formation of radical species is typically caused by interactions of high energy particles and reaction solvents, radical formation can be reduced by reducing the amount of time these particles have to interact with the reaction solvent. Radiolysis within a system is therefore geometrically dependent. [54] In reactors where at least one dimension is significantly smaller than the range of the charged particle (e.g. positron), radiolysis is reduced since the charged particle can escape the solvent before depositing all of its energy to form radical species. [51] Microfluidic reactors, with reduced solvent volumes can therefore minimize formation of radical species and reduce radiolysis compared to large scale radiosynthesizers.

Microfluidics can also aid in reagent reduction which can both save on tracer production costs and can also simplify the purification process. Batch microfluidic chips handle volumes that are 2-3 orders of magnitude less than conventional systems. [51] Typically, precursor is the most expensive reagent during tracer synthesis. If precursor costs hundreds of dollars for one macroscale production (e.g. 10 mg of precursor), microscale synthesis (e.g. 10-100  $\mu\text{g}$  of precursor) of the same tracer could drop production costs down to dollars per run enabling production of small batches on demand for a single user. In fluorine-18 chemistry, the amount of

precursor used is typically orders of magnitude higher than the amount of [ $^{18}\text{F}$ ]fluoride used in order to increase reaction kinetics. [51] As a result, at the end of synthesis, there remains a large amount of unreacted precursor that must be separated from a small amount of desired product. Because the precursor and product are often chemically quite similar, a long semi-preparative HPLC purification may be required to isolate the desired product (resulting in the purified product being diluted by large solvent volumes). In humans where injection volumes are large (e.g. 10mL) this dilute tracer may not be a problem, however, in small animal imaging where injection volumes are small (e.g., <100  $\mu\text{L}$  for mice), injecting enough tracer for high quality images may become an issue. By using smaller amounts of reagents in microfluidic synthesizers, several groups have demonstrated successful purification on analytical-scale HPLC [47,55], resulting in a much more concentrated purified product and faster purification times (due to shorter analyte retention time), compared to semi-prep purification.

Lastly, microfluidic radiosynthesis has the ability to increase  $A_m$  of a synthesized PET tracer. Molar activity of a PET tracer (e.g. labeled with fluorine-18) is defined as the ratio of the radioactivity (i.e. amount of  $^{18}\text{F}$ -labeled molecules) to the sum of both fluorine-18 and fluorine-19 labeled molecules. PET tracers with high  $A_m$  are more desirable for several reasons. In order to minimize pharmacological effects it is desirable to inject only a small amount of tracer. The importance of high  $A_m$  is amplified when imaging biological targets in low-abundance (e.g. neurological imaging). In such cases, it is therefore especially important to inject a tracer with high  $A_m$  to avoid saturation of receptors with  $^{19}\text{F}$ -labeled biomolecules (which are not detectable by PET scanners). High  $A_m$  tracers are also highly advantageous in small animal imaging where much higher concentrations of tracer must be injected per mass of the animal (compared to human imaging) to ensure sufficient signal-to-noise ratio. [56–58] Finally, by increasing  $A_m$  of the synthesized product, any losses in  $A_m$  due to radioactive decay (i.e. 50% loss in  $A_m$  for each

half-life) can also be compensated allowing for high signal-to-noise images even after several radioactive half-lives.

Molar activity of tracers largely depends on the number of fluorine-19 atoms present (as contamination) during tracer synthesis. Some of the fluorine-19 contamination originates from the production of fluorine-18 (e.g. [ $^{18}\text{O}$ ]H $_2\text{O}$ , cyclotron target materials, tubing materials) and is more difficult to remove. [59,60] Other sources of contamination originate from the synthesis process (e.g. QMA cartridges, reagents, fluorinated materials such as tubing and stir bars). [61] Several groups have observed that microfluidic synthesis resulted in significantly higher  $A_m$  compared to macroscale synthesis given the same starting activity [47,62,63], suggesting the ability of microfluidics to significantly reduce fluorine-19 contamination during the synthesis process. In work published by Sergeev *et al.*,  $A_m$  decreased dramatically for macroscale synthesis when reaction volumes were increased. [63]  $A_m$  for microscale synthesis, however, stayed constant despite changing reaction volume. When comparing starting activity and  $A_m$  for macro and microscale syntheses, microscale syntheses resulted in a higher and constant  $A_m$  for all starting radioactivities while macroscale syntheses demonstrated a linear increase in  $A_m$  as starting activity was increased. [63] The highest  $A_m$  seen in macroscale syntheses, was only ~40% of that seen in microscale syntheses and required high starting activity (~13GBq). This study confirms that microscale production compared to macroscale production results in higher tracer  $A_m$ . More importantly, this study shows that microscale synthesis results in higher  $A_m$  (than macroscale synthesis) and that this high  $A_m$  can be achieved even with starting activities as low as 0.9GBq. [63] Microscale synthesis, therefore, can enable low activity (<1GBq) production of small tracer batches (e.g. single patient dose or batch for small animal imaging) with high  $A_m$ ; something that simply cannot be achieved in macroscale synthesizers (with the

consequence that large batches must be produced, even when only small amounts of tracer are needed).

### **1.3.2 Limitations of current microfluidic technologies**

Despite all of the advantages highlighted above of microfluidic radiosynthesizers, there are several disadvantages associated with the technology. First, because of the limited reaction volumes (10s of  $\mu\text{L}$ ), one must also consider how to load sufficient radionuclide to ensure PET tracers are produced with enough radioactivity. Cyclotron produced  $[^{18}\text{F}]$ fluoride is typically produced at Ci levels dissolved within 1-5mL of  $[^{18}\text{O}]\text{H}_2\text{O}$ . Similarly, gallium-68 is typically eluted from a generator in 5mL of a dilute HCl solution. [25] In order to load this entire volume into a 20  $\mu\text{L}$  microfluidic reactor, the volume would need to be concentrated  $\sim 50$ -250 fold. There exists a need for fast and reliable concentration of radionuclide down to  $\mu\text{L}$  volumes to bridge the volume discrepancy between radionuclide and reactor.

Although EWOD based radiosynthesizers have been proven to be useful for radiosynthesis of PET tracers, their design and fabrication is complicated oftentimes resulting in reliability or cost issues. [64] Furthermore, these EWOD based radiosynthesizers could also benefit from full automation. Currently, synthesis steps like loading of reagents into the chip, or extraction of product still require manual user intervention. The ability to automate the synthesis process, would reduce radiation exposure to users and also reduce user training requirements. There remains interest in exploring other designs outside of EWOD that would allow for automated radiosynthesis while also increasing system reliability and decreasing fabrication costs.

While large efforts have been spent on designing microfluidic radiosynthesizers, there exists a need to also design miniaturized approaches to other steps within the tracer production scheme. Purification (performed with HPLC), formulation (performed with rotary evaporators),

and QC (performed with gas chromatography, thin layer chromatography, and other analytical equipment) could benefit from miniaturization through microfluidic technologies.

## 1.4 Focus of this dissertation

Microfluidics as explained above, can play an important role in the production of PET tracers. In addition to microfluidics for PET tracer synthesis, several groups have also explored using microfluidic technologies for PET tracer QC to leverage some of the benefits from microfluidic technology (e.g. reduced reagent volume, faster reaction times, and better control of reaction parameters) for QC analysis. A very thorough review of these techniques has been presented recently by Ha *et al.* [36] Referring back to Figure 1-2, there remains several steps in the overall PET tracer production scheme that could benefit from translation into the microscale. For example, evaporation of solvent during the concentration and reformulation steps after purification is currently performed on slow (e.g. evaporation rates of 1mL/min) and bulky rotary evaporators. Microfluidic technology could aid in size reduction while also leveraging characteristics like faster heat transfer to aid in increasing evaporation rates.

In chapter 2 of this dissertation, I explore addressing the limitations associated with current rotary evaporators used for concentration and reformulation of PET tracers. More specifically, I present the development and optimization of a fully-automated microfluidic system based on sweeping gas membrane distillation to rapidly perform the concentration and formulation of PET tracers after HPLC purification. After detailed characterization of the system I focused on thorough optimization of operation parameters to increase system performance and reliability. Next, I demonstrated fast and efficient concentration and formulation of several different PET tracers resulting in high tracer recovery. Lastly, I evaluated residual solvent content of several different solvents in a tracer that was concentrated and formulated with the system to establish the safety of formulated tracers for injection, and also showed that the

formulated tracer can be used for *in vivo* imaging of [ $^{18}\text{F}$ ]D-FAC. The newly designed system resulted in evaporation rates up to 3 times faster than commercially available rotary evaporators and a physical size that was substantially smaller than bulky rotary evaporators. Automation of the system minimizes user intervention and reduces radiation exposure to the operator compared to traditional techniques for concentration and reformulation.

The next two chapters revolve around enabling increased synthesis scale of microfluidic PET tracer synthesizers, specifically bridging the volume gap between radionuclides and microfluidic reactors. Concentration of [ $^{18}\text{F}$ ]fluoride has been mentioned in literature both through the use of miniaturized SAX cartridges or on-chip evaporation [45,50,65], however, reports have lacked details about system designs, operation, and performance. In addition, for SAX cartridge based approaches, the concentration systems are directly connected to the reactor reducing system customizability. In chapter 3 I describe in detail a standalone, compact, fast, fully-automated radionuclide concentration system based on a micro-sized SAX cartridge for the concentration of [ $^{18}\text{F}$ ]fluoride. The platform enables automated concentration of [ $^{18}\text{F}$ ]fluoride (in mL starting volumes) down to volumes as low as 12.4 $\mu\text{L}$  in under 5 minutes. This concentrated [ $^{18}\text{F}$ ]fluoride can be transferred to a downstream radiosynthesis platform for tracer production with high starting activity.

By eluting trapped [ $^{18}\text{F}$ ]fluoride from the SAX cartridge with a solution containing high organic solvent content, our system can also be used to provide highly concentrated [ $^{18}\text{F}$ ]fluoride with minimal water content. For macroscale syntheses this concentrated [ $^{18}\text{F}$ ]fluoride can be diluted with organic solvent to macroscale reaction volumes (mL), further decreasing water content. This approach enables macroscale radiosynthesis without the need for azeotropic drying, reducing processing time and complexity during syntheses. In chapter 3, I

also demonstrate how the concentrator can produce varying starting activities of [ $^{18}\text{F}$ ]fluoride for the macroscale synthesis of N-boc-5- $^{18}\text{F}$ fluoroindole without the need for azeotropic drying.

As mentioned above, in addition to [ $^{18}\text{F}$ ]fluoride labeled tracers, groups have also explored radiolabeling of tracers with radiometals such as gallium-68. By appropriate choice of solid-phase resin, flow conditions, and eluent solution, we believe the cartridge-based concentration approach (presented in chapter 3) can be extended beyond [ $^{18}\text{F}$ ]fluoride to other radionuclides such as gallium-68. In chapter 4, I present work focused on repurposing the radionuclide concentrator for concentration of gallium-68. I designed and fabricated new cartridges using various strong cation exchange (SCX) resins for trapping of gallium-68. Next, I performed detailed characterization and optimization of trapping and elution behavior of gallium-68 by exploring different cartridge geometries, resin types, different resin masses, and different eluent solutions. I present an optimized trap and elution protocol enabling concentration from 10mL starting volume of gallium-68 down to 60 $\mu\text{L}$  in an acidic acetone solution. This volume can be further reduced on a microfluidic radiosynthesizer through the rapid evaporation of acetone, enabling arbitrarily small volumes in the subsequent labeling reactions. The automated concentration of gallium-68 can be reliably performed in under 15 minutes. Future work will be performed to demonstrate successful microfluidic gallium-68 labeling of biomolecules with reduced precursor amounts (compared to macroscale techniques) while maintaining high yield and high  $A_m$ .

In chapter 5, I aim to address the issues associated with EWOD based microfluidic radiosynthesizers, which include the poor reliability and high cost of prototype chips and system operating complexity. To address these issues, my colleague and I developed a novel microfluidic device based on patterned wettability that carries out spontaneous droplet manipulations to perform multi-step radiochemical reactions in microliter droplets, and

implemented automated systems for reagent loading and collection of the crude product after synthesis. In this chapter, I describe a simple and inexpensive method for fabricating the chips based on patterned wettability, and demonstrate the feasibility of prototype chips for performing multi-step radiochemical reactions to produce [ $^{18}\text{F}$ ]fallypride in an automated and reliable fashion with yields comparable to EWOD based approaches. The reaction chips used in this platform can be up to 100 times less expensive than EWOD based reactors. Furthermore, the reaction chips rely entirely on passive actuation (i.e. patterned wettability), and therefore do not require complex control hardware (e.g. actuators to control on chip electrodes) normally found in EWOD based systems.

Lastly, in chapter 6, I first demonstrate successful integration of the radionuclide concentrator (described in chapter 3) and the microfluidic radiosynthesizer (described in chapter 5) through the automated synthesis of [ $^{18}\text{F}$ ]fallypride. Following successful integration, I demonstrate scaled up production of [ $^{18}\text{F}$ ]fallypride by using highly concentrated high starting activities of [ $^{18}\text{F}$ ]fallypride. In this chapter, I provide detailed analysis on concentrator performance with newly designed miniaturized SAX cartridges, transfer efficiency between the two systems, and synthesis performance of [ $^{18}\text{F}$ ]fallypride. By performing concentration and synthesis with varying starting activities up to 1 Ci, I then explored the effects of fluorination efficiency and overall radiochemical yield of [ $^{18}\text{F}$ ]fallypride as a function of starting activity. Most importantly, in this chapter I demonstrated the ability of our new radiosynthesis platform to successfully and reliably synthesize PET tracers with high starting activities. In chapter 6 I conclude by presenting my views on the future direction of the microfluidic technologies presented in this dissertation.

## 2 Chapter 2: Microfluidic Membrane Concentration of Purified Tracers

### 2.1 Introduction

The preparation of PET tracers is usually carried out inside radiation-shielded “hot cells” by automated radiosynthesizers that perform the needed chemical reactions, purify the crude product via high performance liquid chromatography (HPLC), and formulate the tracer for injection. Because most synthesizers are designed for clinical use, the output volume is often in the 10s of mL range. As a result these synthesizers are not suitable for preparing small amounts of research tracers in high enough concentration for small animal imaging or *in vitro* assays without the use of very high starting activities (1-5Ci). *In vivo* imaging in mouse tumor models typically requires 100-200  $\mu\text{Ci}$  in a volume of 100  $\mu\text{L}$  or less (limited by low blood volume of the mouse) [66] which is a concentration of  $\sim 37\text{-}74 \text{ MBq/mL}$  [1-2 mCi/mL]. Similarly, existing and emerging platforms for *in vitro* cancer studies such as binding or uptake assays, drug response assays, enzyme activity assays, or kinetic modeling have reported the need for concentrations up to  $\sim 37\text{MBq/mL}$  [1 mCi/mL]. [67] Though these concentrations can be achieved by using large amounts of radioactivity in the synthesis and just discarding what is not needed, this approach increases radiation exposure and cost of the radionuclide and may not be practical for novel tracers where the yield is often very low. For example, if the uncorrected yield is  $\sim 1\%$ , then 100 mCi of the radionuclide would be needed to produce 37 MBq [1 mCi] of the tracer. This is sufficient for a preclinical study of 10 mice if it can be concentrated down to  $\sim 1 \text{ mL}$ . On the other hand, if the final volume is 10 mL, then 370 MBq [10 mCi] would need to be produced, initially requiring 37GBq [1 Ci] of the radionuclide. In this case, 37 MBq [1 mCi] would be used and 333 MBq [9 mCi] would be discarded: the extra activity is simply to increase the concentration. These numbers are even higher if the radiochemical yield is lower, if the probe

must be transported a long distance, or if the probe must be used for imaging throughout the work day.

Instead, to avoid this issue, tracers can be concentrated after production as part of the reformulation process. After the radiosynthesis, the crude product volume is typically on the order of ~1 mL, but the HPLC purification process results in volumes of 10-50 mL of mobile phase due to the high flow rates that are used. Mobile phases typically consist of mixtures of ethanol (EtOH) or acetonitrile (MeCN) in water, often with additives to control pH. EtOH-based mobile phases may be directly injected after sterile filtration if the EtOH content is sufficiently low (10% v/v for EtOH [68]). However if the mobile phase contains too much EtOH, or contains MeCN or other toxic solvents, these must be nearly completely removed (e.g. allowed injection limit of MeCN is 410 ppm [69]). In one approach, a rotary evaporator is used to evaporate off the mobile phase at elevated temperature, and then the dried residue is replaced with saline. However, rotovap systems are bulky and consume significant space in the hot cell, and due to the significant amount of water to be removed, this process can be rather slow especially in more compact systems. [70,71] Alternatively, a solid-phase extraction (SPE) method can be used. In reversed-phase SPE, the collected HPLC fraction is first diluted with water to ensure the organic solvent content is sufficiently low (typically <5-10%), and then passed through the SPE cartridge to trap the PET tracer. The mobile phase is diverted to waste. After rinsing the cartridge, 1-2 mL of EtOH can then be used to release the tracer from the cartridge. For use in humans, this sample would be diluted with saline to reduce the EtOH content below the allowed limit; however, to avoid the volume increase an alternative is to directly evaporate the EtOH and then suspend the tracer in saline. While effective, the SPE process can be time consuming due to the large diluted sample volume, and the evaporation and resuspension in small volumes cannot be performed in most radiosynthesizers.

We developed a compact microfluidic device based on membrane distillation for rapid solvent removal to address this problem. [72] Compared to other microfluidic techniques such as using trapped air pockets to capture vapor from a liquid stream [73], or using droplet traps [74], atomization [75], or a sheath flow [44] to expose a large liquid surface area to a gas flow, implementations of membrane distillation have significantly faster evaporation speed and greater sample capacity. [72,76] In this chapter, we present a second-generation chip with a 5-fold improved evaporation rate (3.4 versus 0.65 mL/min for water at 100°C), increased scope of mobile phases (now compatible with practically any PET tracer), and an improved modular construction that enables the chip material to be matched with the PET tracer for optimal performance. In addition, though we previously focused only on concentration, here the system performs simultaneous concentration and formulation for injection, and is now fully automated. The dramatic performance improvements, increased diversity of compatible tracers, simultaneous concentration and reformulation, and automation has translated our previous proof of concept system into mature technology suitable for routine use in the preparation of PET tracers. We present in this chapter a detailed characterization of the system, demonstration of concentration and formulation of several PET tracers, evaluation of residual solvent content to establish the safety of the formulated tracers for injection, and demonstration of *in vivo* imaging.

## **2.2 Materials and Methods**

### **2.2.1 Microfluidic concentrator design and fabrication**

The microfluidic device is designed to perform sweeping-gas membrane distillation, in which a fluid sample and a sweeping gas are separated by a hydrophobic porous membrane. [76,77] The porous membrane prevents passage of the liquid as long as the contact angle is > 90°, but vapor generated as the aqueous sample is heated can pass through the membrane

and into the sweeping gas stream. In distillation, the vapor carried away is condensed and collected for downstream use; however, in the case of sample concentration, the vapor is discarded, and the reduced volume of sample (containing the desired solute in more concentrated form) is collected.

The design is based on preliminary work we previously reported [72] but with numerous improvements.

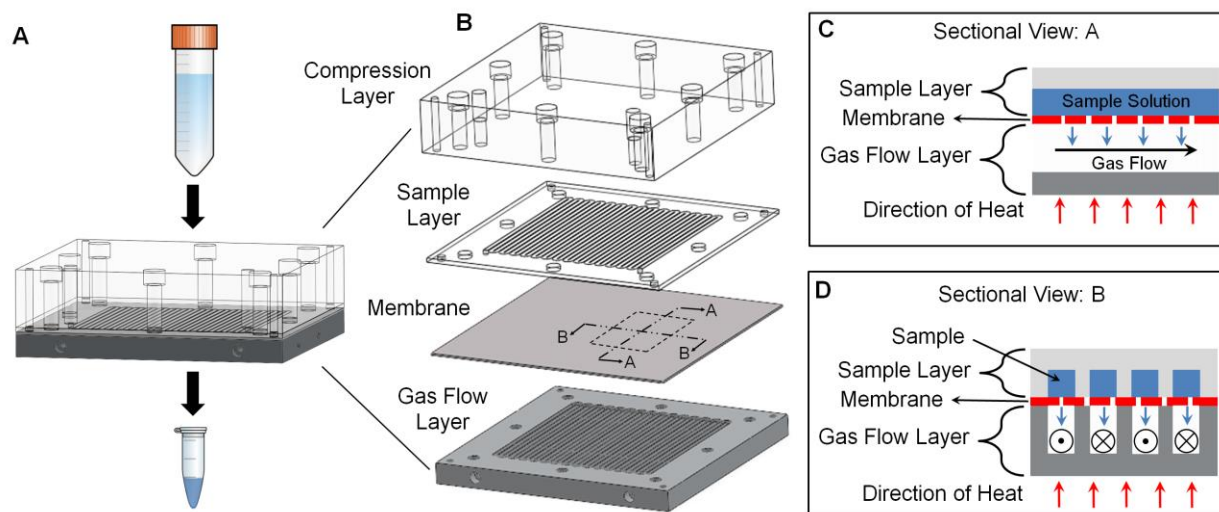


**Figure 2-1: Schematic of the microfluidic concentrator chip**

(A) Assembled chip with the ability to concentrate large volumes into ~1 mL volume. (B) Exploded view of the chip showing acrylic compression layer, sample layer made of different plastics, a Teflon membrane with 0.2 $\mu$ m pore size and aluminum gas flow layer. (C) Sectional view A shows a cross-section along a channel during operation. (D) Sectional view B shows a cross-section through a channel during operation.

The new device (Figure 2-1) measures 120 mm x 120 mm in lateral dimensions. The top layer (25.4 mm thick acrylic) provides optical transparency for visual monitoring of the concentration process and rigidity for clamping all layers together. The sample layer is made out of 2 mm thick plastic with a patterned serpentine channel (2.25mm wide x 0.05mm deep channels with 0.5mm spacing). The channel has rounded corners to avoid dead volumes that interfere with efficient sample recovery, and was designed with smaller channel width than previously used (4.5 mm) to avoid “sagging” of the membrane while still maintaining nearly identical evaporation surface

area (~57 cm<sup>2</sup>). The open side of the sample channel is in contact with a porous membrane (PTFE, 0.2 μm pore size; Sterlitech, Kent, WA, USA). The pore size was substantially smaller than our previous device (1.0 μm) and thus the device was expected to tolerate a wider range of operating pressures. The final layer is a 10 mm thick 6061 aluminum alloy block with a 3.5 mm deep serpentine channel matching the sample layer (CNC machined by Proto Labs, Inc., Maple Plain, MN, USA). This layer served to provide heat, and the channel carried the sweeping gas. The layers are clamped together using bolts; small deformation of the membrane layer ensures good sealing along channel walls to both the sample and gas flow layers.

Prior work suggested that some PET tracers had adverse reactions (adsorption or absorption) with the chip [72]. Suspecting a material-dependence, we fabricated sample layers from a variety of materials, including: poly(methyl methacrylate) (PMMA), polytetrafluoroethylene (PTFE), glass-filled PTFE (glass-PTFE), polyetherimide (Ultem), cyclic olefin copolymer (COC) and polyether ether ketone (PEEK). These plastics were chosen for their chemical inertness, high temperature stability, and/or transparency. An initial proof-of-concept PMMA sample layer was fabricated by Aline Inc. (Rancho Dominguez, CA, USA) via laser ablation, and then sample layers of all materials were fabricated via CNC machining by Delmar Company (Lakeville, MN, USA). Holes through the acrylic top layer and sample layer provide fluid access to the inlet and outlet of the sample channel. Similarly, holes through the gas flow layer provide access to the inlet and outlet of the sweeping gas channel. To distinguish the two methods of fabricating PMMA layers, we refer to them as PMMA-machined and PMMA-ablated.

## 2.2.2 Automated concentrator system

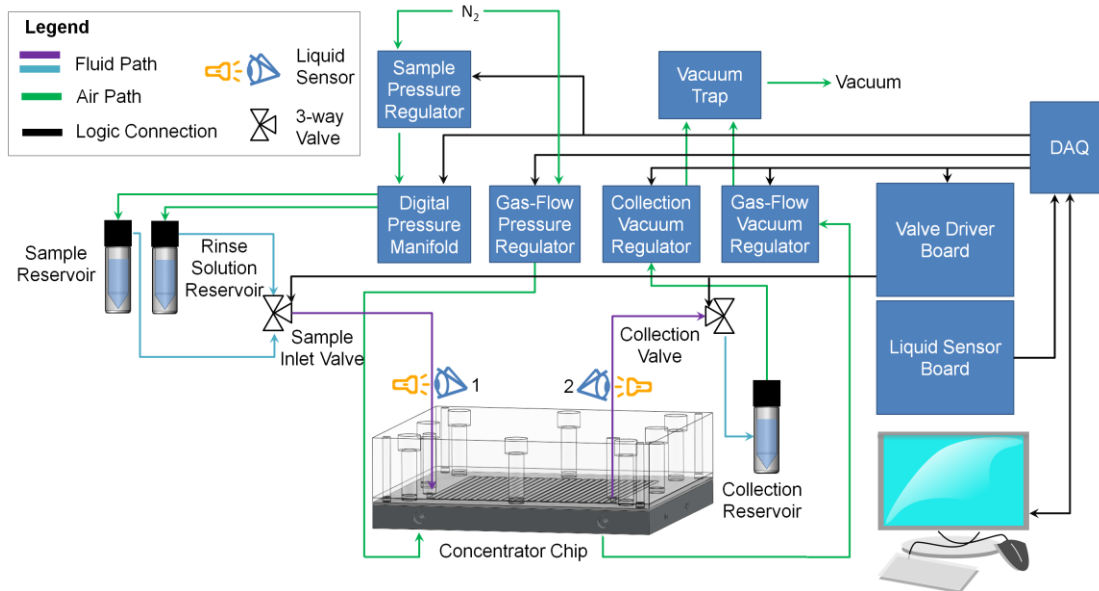


**Figure 2-2: Fluidic and electronic wiring diagram of the automated microfluidic concentration system**

To automate its operation, the chip is integrated into the system shown in Figure 2-2. Reservoirs for the sample as well as the rinsing solution (e.g. saline, to help collect the sample after concentration) comprise 15mL conical tubes (352096, BD Biosciences, San Jose, CA, USA). Two holes were drilled in the cap of each tube, one for 1/8" polyurethane tubing to pressurize the reservoir, and one for 1/16" OD ETFE tubing (1517L, IDEX Health & Science, Oak Harbor, WA, USA) to deliver the reservoir contents. Tubing was sealed in place with a hot glue gun. The fluid delivery lines from the reservoirs are connected to the two inlet ports of an electronic 3-way valve (LVM105R, SMC Corporation, Japan). The output of this "sample inlet valve" is connected via 1/16" OD ETFE tubing to the sample inlet of the concentrator chip. An electronic pressure regulator (ITV0010-2BL, SMC) connected to a nitrogen source supplies pressure to the reservoirs through independently controlled solenoid valves (S070B-5DG, SMC).

The sample outlet from the chip is connected via 1/16" OD ETFE tubing to another 3-way valve to choose whether the outlet is blocked (during evaporation) or connected to the sample collection reservoir. The collection vial is connected via a vacuum trap to a digitally controlled vacuum regulator (ITV2090, SMC) which in turn was connected to a central "house" vacuum. This vacuum source was capable of pressure as low as -90 kPa with a vacuum capacity of 1.9 L/min. The gas flow layer was connected via 1/4" polyurethane tubing through an electronic pressure regulator (ITV2010, SMC) to the nitrogen source, and through a vacuum regulator (ITV2090, SMC) to the vacuum pump.

The regulators and valves were digitally controlled using a data acquisition module (NI USB-6009, National Instruments, Austin, TX, USA). A custom-built Darlington transistor array board was used to step up the voltage and current needed to drive the 3-way valves. Two tubing fluid sensors (OPB350W062Z, Optek Technologies, Carrollton, Texas, USA) are positioned on the 1/16" tubing between the sample inlet valve and the concentration chip inlet (sensor 1) and on the 1/16" tubing between the concentrator chip outlet and the sample collection valve (sensor 2). Analog voltage readings from the sensors are connected to the data acquisition module (NI USB-6009, National Instruments) for computer analysis. Comparison to a threshold value is used to determine if the tubing under the sensor is filled with air or liquid.

Heat was provided to the chip by 100W cartridge heaters (8376T27, McMaster Carr, Santa Fe Springs, CA, USA) inserted into holes drilled in the metal gas-flow layer. Thermal paste (OT-201-2, OMEGA Engineering, Inc., Stamford, CT, USA) was used to provide good thermal contact. For each cartridge heater, a K-type thermocouple (5TC-GG-(K)-30-(72), OMEGA Engineering, Inc., Stamford, CT, USA) was also inserted into the heating block near the heater. Feedback control of each heater-thermocouple pair was performed with an

independent PID temperature controller (CN7500, OMEGA Engineering, Inc., Stamford, CT, USA). Control parameters were set by the “auto-tune” feature.

The heating power was selected based on the following considerations. To heat water from room temperature to 100°C and convert it to vapor form at a rate of ~3 mL/min (maximum we have observed so far) requires ~130W of power. Empirical testing showed that the theoretical minimum power was not sufficient to maintain the temperature of the heating block, presumably due to other thermal losses and the finite time needed for transport of heat from the cartridge heaters to the sample channel. Using two 100W heaters during a 100°C evaporation, we observed the measured temperature to be ~6°C below the setpoint. On the other hand, with four 100 W heaters, the measured temperature matched the setpoint within  $\pm 1.5^\circ\text{C}$ , and this configuration was used for all experiments. Further increased heating power (e.g., four 300W heaters) could heat the chip more quickly but gave similar temperature stability and was not used because the chip could be pre-heated prior to use.

## 2.2.3 Concentrator operation



**Figure 2-3: Photographs showing system operation during the concentration process for a sample of diluted food dye**

After initialization and pre-heating of the chip (1), the sample reservoir is pressurized to begin loading the sample (2). Once the chip is filled (3)

The concentration process (described in Figure 2-3) was automated using a custom-written LabVIEW (National Instruments) program based on a finite state machine architecture. Prior to the concentration process, the chip is first heated to the desired temperature (~5 min to reach steady state), the sample collection valve is closed, and the sample inlet valve is switched to the “sample” position. Sample is loaded into the chip by pressurizing the sample vial, to a pressure ( $P_{sample}$ ) that is constantly applied for the duration of the concentration process. Air initially in the system ahead of the sample readily escapes by passing through the membrane into the gas flow layer, allowing the sample to reach the chip. The sample advances until the sample channel is filled and sample begins to emerge from the outlet of the chip (due to compression of the remaining trapped air), triggering sensor 2. At this point, the sweeping gas flow is initiated (by applying  $P_{gas\_in}$  and  $P_{gas\_out}$  at the gas flow inlet and outlet, respectively). As solvent evaporates, additional space is created within the sample channel, allowing new sample to enter the chip. The solute becomes progressively more concentrated within the chip.

When the sample reservoir is exhausted, the trailing end of the sample passes through sensor 1 (i.e. liquid to air transition), and the concentrated sample volume matches the chip volume. The sample volume can be further reduced by continuing the heating process for an additional delay time to achieve a final volume smaller than the chip volume. This delay is needed because even though the designed chip volume is ~0.29 mL, the collected volume without further evaporation is ~2.75 mL. This discrepancy is presumably due to significant deflection of the membrane under the operating conditions. (Note, we explored the possibility of using a “laminated membrane”, i.e. thin 0.2  $\mu\text{m}$  pore PTFE membrane bonded to a more rigid membrane with larger pores, and found the recovered volume to be ~0.80 mL. However, evaporation speed and sample recovery were quite poor in initial tests and so this direction was not pursued further.) The actual delay time was varied, depending on the mode of operation.

The delay time needed to achieve a desired collected volume was measured empirically. We measured the recovered volume to determine the additional evaporation delay needed to reduce the volume <0.5 mL. The chip was preheated to 100°C, and other parameters were set to values described within this chapter. For each measurement, 4 mL of water was loaded into the sample reservoir. The extra delay time was set in the automated concentration program, and the number of rinses was set to zero. After completion of the automated concentration process, the volume of the collected product was measured using a 1mL pipette (P1000 Pipetman, Gilson Inc., Middleton, WI, USA). Samples with volumes larger than 1mL were measured by first removing and counting 1.0 mL portions. The remaining volume was measured by aspirating into the pipette and adjusting the volume setting until it matched the sample volume (i.e. with no additional air aspirated into the tip). 50 sec was sufficient to achieve a collected volume <0.5 mL.

When performing partial solvent evaporation, a delay time of 50 s was used, resulting in a recovered volume from the chip of 0.4-0.5 mL. On the other hand, when performing complete solvent evaporation, the delay time was typically set to 270 s (corresponding to ~220 s for water to completely evaporate at 100°C plus a safety margin.)

When operating in partial evaporation mode, the concentrated sample is first collected, and then the chip is rinsed multiple times. In complete evaporation mode, there is no initial collection step and rinsing (described below) is performed directly after complete dryness is achieved.

To collect the concentrated sample, the sample collection valve opens after the delay time, and the sample is driven to the collection reservoir by the sample inlet pressure. During the collection process, the vacuum connected to the collection reservoir ( $P_{\text{vacuum}}$ ) is turned on at -1.0 psi. The sample is collected for a set period of time that is empirically determined; for the concentrated sample volume resulting from 50s delay time, ~4s was sufficient for collection, but we chose 14s to incorporate a safety margin. Next, the vacuum is ramped to - 8.8 psi ( $P_{\text{vacuum\_ramp}}$ ) to recover any residual fluid trapped within the fluidic path. Residual fluid recovery is typically complete within ~3s, but 9s was chosen to include a safety margin. We found it necessary to gradually ramp the vacuum pressure to prevent the fluid from breaking up in the tubing.

To perform a rinse, the sample collection valve is closed, and the sample inlet valve is switched to the rinsing solution reservoir. The rinse solution reservoir is pressurized to  $P_{\text{sample}}$ , and rinse solution is loaded just as initially performed for the sample. However, when it reaches sensor 2, the sample inlet valve is switched back to the empty sample reservoir (which is still pressurized at  $P_{\text{sample}}$ ). At this point, the total volume of rinse solution (including that in the chip, tubing, etc.) is ~3 mL. The rinse solution is concentrated just like the initial sample, and when

the trailing end of the rinse solution passes sensor 1, a timer is started for additional delay time. Finally, the concentrated rinse plug is ejected in the same fashion as the original sample. Multiple rinse steps can be performed to improve sample recovery.

#### **2.2.4 Measuring evaporation rate**

Evaporation rate was measured by placing a 5 mL Fisherbrand graduated serological pipet (13-678-11D, Fisher Scientific, Pittsburgh, PA, USA) inline between the sample reservoir and the chip. Connections were made via 1/4" OD polyurethane tubing (TIUB07, SMC Pneumatics, Yorba Linda, CA). Evaporation rates were measured by observing the sample fluid meniscus as it passed through the graduated pipette. The amount of time it took for the fluid meniscus to move by 1 mL was recorded and used to calculate the evaporation rate. Evaporation rates were determined for five successive 1 mL increments and averaged.

For some experiments, we aimed to study the evaporation rate over a longer period of time (larger volume evaporated). For these cases, the sample reservoir was replaced with a larger conical tube (50mL Falcon conical tube; Corning Inc., Corning, NY, USA), and a larger graduated pipette (50 mL Fisherbrand serological pipet, Fisher Scientific, Pittsburg, PA, USA) was used to monitor liquid movement. Though vertical orientation of the pipette adds a hydrostatic pressure to the sample pressure (~0.4 psi in the worst case) this pressure was found to have negligible effect on evaporation rate.

#### **2.2.5 Reagents**

Ethanol (EtOH; 200 proof) was purchased from the UCLA Chemistry Department (Los Angeles, CA, USA). Anhydrous acetonitrile (MeCN), ammonium dihydrogen phosphate ( $\text{NH}_4\text{H}_2\text{PO}_4$ ), potassium carbonate ( $\text{K}_2\text{CO}_3$ ), dimethyl sulfoxide (DMSO), and trifluoroacetic acid (TFA) were purchased from Sigma-Aldrich (Milwaukee, WI USA). Deionized water was obtained from a Milli-Q water purification system (EMD Millipore Corporation, Berlin, Germany). Food dye

used in the experiments was purchased from Kroger (Cincinnati, OH, USA). Food dye was diluted with 18M $\Omega$  dionized water in the ratio of 1:50 v/v. Saline (0.9% w/v) was purchased from Hospira (Lake Forest, IL, USA). [ $^{18}\text{F}$ ]fluoride in [ $^{18}\text{O}$ ]H $_2\text{O}$  was obtained from the UCLA Biomedical Cyclotron (Los Angeles, CA, USA). 4,7,13,16,21,24-hexaoxa-1,10-diazabicyclo[8.8.8]hexacosane (Kryptofix 222; K222) was purchased from ABX (Radeberg, Germany). Unless otherwise noted, all materials were used as received.

1-(2'-deoxy-2'-[ $^{18}\text{F}$ ]- $\beta$ -D-fluoroarabinofuranosyl) cytosine ([ $^{18}\text{F}$ ]D-FAC), 2-deoxy-2-[ $^{18}\text{F}$ ]fluoro-5-ethyl- $\beta$ -D-arabinofuranosyluracil ([ $^{18}\text{F}$ ]D-FEAU), (S)-N-((1-allyl-2-pyrrolidinyl)methyl)-5-(3-[ $^{18}\text{F}$ ]fluoropropyl)-2,3-dimethoxybenzamide ([ $^{18}\text{F}$ ]fallypride), and 9-(4-[ $^{18}\text{F}$ ]fluoro-3-hydroxymethylbutyl)-guanine ([ $^{18}\text{F}$ ]FHBG) were synthesized using the ELIXYS radiosynthesizer (Sofie Biosciences, Culver City, CA, USA) as described previously. [55,78] Synthesis of N-[2-(4-[ $^{18}\text{F}$ ]fluorobenzamido)ethyl]maleimide ([ $^{18}\text{F}$ ]FBEM) was synthesized on the ELIXYS radiosynthesizer by straightforward adaptation of literature methods. [79] All tracers and prosthetic groups were purified using semi-preparative HPLC, and the collected fraction of each (suspended in its respective mobile phase; see Table 2-1) was used directly without further formulation. [ $^{18}\text{F}$ ]D-FAC was formulated for use in imaging as described below.

### 2.2.6 Determining Operating Conditions

In our previous work, we showed several constraints in operating parameters. [72] Briefly,  $P_{\text{sample}}$  should be high enough that the chip remains full of sample during evaporation. In addition, the highest pressure in the gas flow layer must be less than the sample pressure, i.e.  $P_{\text{gas\_in}} < P_{\text{sample}}$ . Finally, the largest pressure difference across the membrane must not exceed the breakthrough pressure (BTP), i.e.  $P_{\text{sample}} - P_{\text{gas\_out}} < \text{BTP}$ . BTP is defined as the applied pressure at which sample (in liquid form) can directly leak through the pores of the membrane into the gas flow layer. It is closely related to the concept of capillary pressure,  $P_C$ , which is the

pressure needed to cause fluid to enter a pore with radius  $r$ ,  $BTP \approx P_C = 2\gamma\cos(\pi-\theta)/r$ , where  $\gamma$  is the surface tension of the sample (at an air interface) and  $\theta$  is the contact angle of the liquid sample with respect to the membrane surface. The implications of realistic pore geometries and size distribution is described in [80,81]. Since  $\gamma$  and  $\theta$  depend on the composition of the mobile phase and temperature, the BTP is a function of these variables as well. Spontaneous permeation of the membrane (i.e. 'breakthrough') always occurs when  $\theta < 90^\circ$ . For  $\theta > 90^\circ$ , permeation of the membrane only occurs when the fluid sample is pressurized against the membrane with a pressure exceeding the BTP.

First, measurements of contact angle for various solvent compositions and temperatures were made to determine the conditions under which  $\theta > 90^\circ$ , indicating the extent of the operating range in terms of solvent composition and temperature. Contact angle of droplets of various solvent compositions were measured at different temperatures. For each condition, a 1 cm x 1 cm square piece of 0.2  $\mu\text{m}$  PTFE membrane (Sterlitech, Kent, WA, USA) was placed on top of a heated aluminum block with an embedded cartridge heater (8376T27, McMaster Carr, Santa Fe Springs, CA, USA) and K-type thermocouple (5TC-GG-(K)-30-(72), OMEGA Engineering, Inc., Stamford, CT, USA). Temperature was controlled via a PID controller (CN7500, OMEGA Engineering, Inc, Stamford, CT, USA). After preheating the membrane for 1 min, a 5  $\mu\text{L}$  sample was pipetted onto the membrane surface and a side-view image was taken with a digital camera (Canon Rebel XT, Canon, Irvine, CA USA) with a Canon MP-E 65mm 1-5x macro lens. Contact angle was determined from each photograph with ImageJ software (U.S. National Institute of Health, Bethesda, MD, USA) using a plugin called Low-Bond Axisymmetric Drop Shape Analysis (LBADSA). Three replicates (load new membrane, preheat, pipette droplet, image and analyze) were performed for each sample condition and averaged to produce a representative value. Results are shown in Figure 2-4.

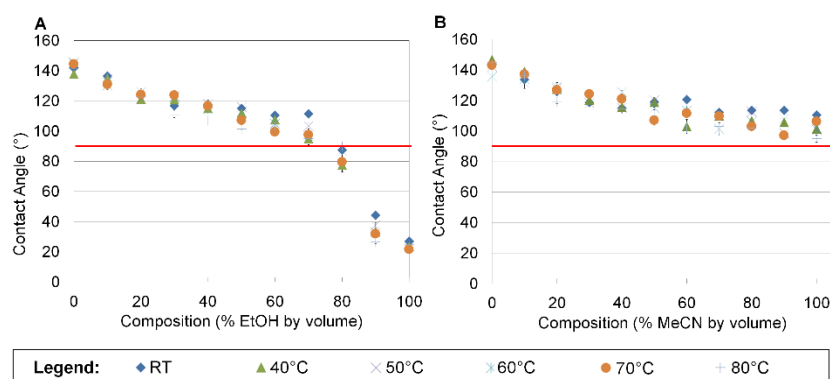


**Figure 2-4: Contact angle measurements for (A) EtOH and (B) MeCN mixtures with water at different temperatures**

Each data point represents the average of n=3 replicates; error bars represent the standard deviation. The red line represents a contact angle of 90°, the barrier between wetting and nonwetting.

Since it is important to operate under an adequate safety margin, more direct measurements of BTP were also determined for various solvent compositions and temperatures. Once BTP was known, other operating parameters were selected to meet the above constraints. To directly measure BTP, a custom temperature-controlled test fixture (described below) was built to hold small pieces of the membrane material. One side of each membrane was exposed to the desired sample at a controlled pressure; the other side was vented to atmospheric pressure. On the input side, a tubing connection is made from a sample reservoir (Falcon 15 mL conical tube, BD Biosciences, San Jose, CA, USA) to the testing fixture. The sample was manually primed up to the membrane via syringe and then the sample pressure was controlled with a pressure regulator (ITV0010, SMC Corporation, Japan) and monitored with a pressure gauge (MLH-050PGB01E, Honeywell International Inc. Golden Valley, MN, USA). These two components were connected to a laptop via a data acquisition module (NI USB-6212, National Instruments, Austin, TX, USA) and were controlled using a custom LabVIEW program. A fluidic flow sensor (SLI-2000, Sensirion Westlake Village, CA, USA) was positioned along the input tubing.

Flow rate was monitored as pressure was increased automatically from 0.0 to 13.5 psi in 0.3 psi increments. (The maximum tested pressure was 13.5 psi, because when higher pressures are used in the chip, severe membrane deformation that causes blocking of the gas flow layer is observed.) After each change in pressure, there was an 8s delay to allow for equilibration, and then the pressure and flow rate were recorded. In general, fluid flow rate stayed close to ~0.0 mL/min below breakthrough, but increased dramatically upon reaching the breakthrough pressure, ultimately reaching the maximum reading limit of the sensor (5 mL/min).

BTP was identified as the point on a plot of flow rate versus pressure where the flow measurement exceeded a threshold value, 25 $\mu$ L/min, corresponding to the worst-case measurement error specified for the sensor. The pressure corresponding to the threshold flow rate was interpolated by performing a fit of flow rate versus pressure between the closest points on either side of the threshold. The BTP identification process can be seen in Figure 2-5.

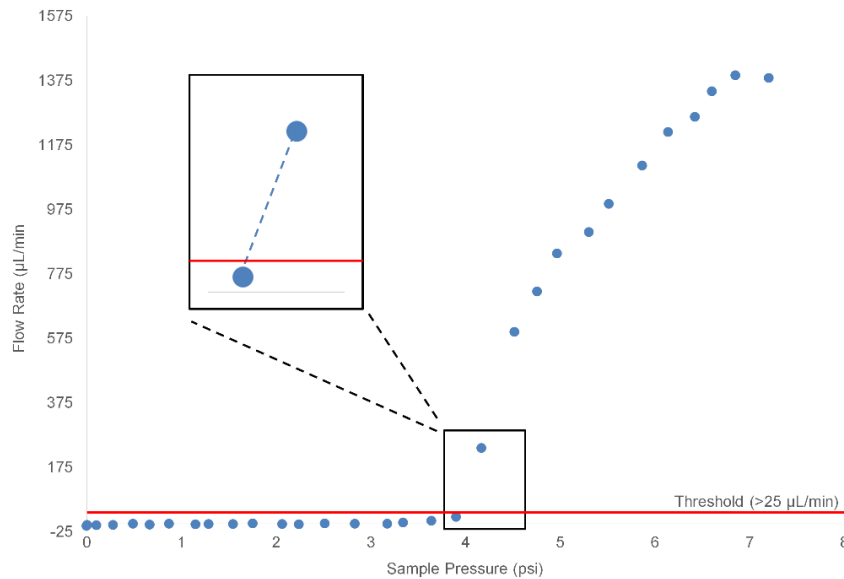


**Figure 2-5: Determination of BTP**

Fluid flow rate is plotted as a function of pressure. BTP is defined as the point where the flow rate exceeds the threshold value (25 $\mu$ L/min; red line). BTP was interpolated from adjacent data points after first performing a linear fit (blue dotted line).

The testing fixture was built out of 6061 aluminum alloy and could split apart into two halves. One half contained four individual wells. Membrane samples (cut slightly larger than the wells) were inserted into each well, followed by a square profile rubber o-ring (4061T115, McMaster-Carr, Santa Fe Springs, CA, USA). The second half of the fixture was then secured via nine bolts to secure the membranes in place. The fixture and experimental setup are shown in Figure 2-6.

Initially, heating was performed by placing the fixture inside a convective oven (Isotemp Oven Model# 825F, Fisher Scientific, Pittsburgh, PA, USA). Heat transfer from the air within the oven to the chip, however, was not sufficient to maintain the internal temperature of the aluminum fixture during operation. Thus, two heater blocks were mounted on the top and bottom of the fixture, each containing one 100W cartridge heater (8376T27, McMaster Carr) as well as one K-type thermocouple (5TC-GG-(K)-30-(72), OMEGA Engineering, Inc., Stamford, CT). Heaters and thermocouples were coated with thermal paste (OT-201-2, OMEGA Engineering, Inc., Stamford, CT) before insertion into the block. Temperature of each heater block was independently maintained via a PID temperature controller (CN7500, OMEGA Engineering, Inc., Stamford, CT). The combination of heating blocks and oven heating resulted in stable temperatures.

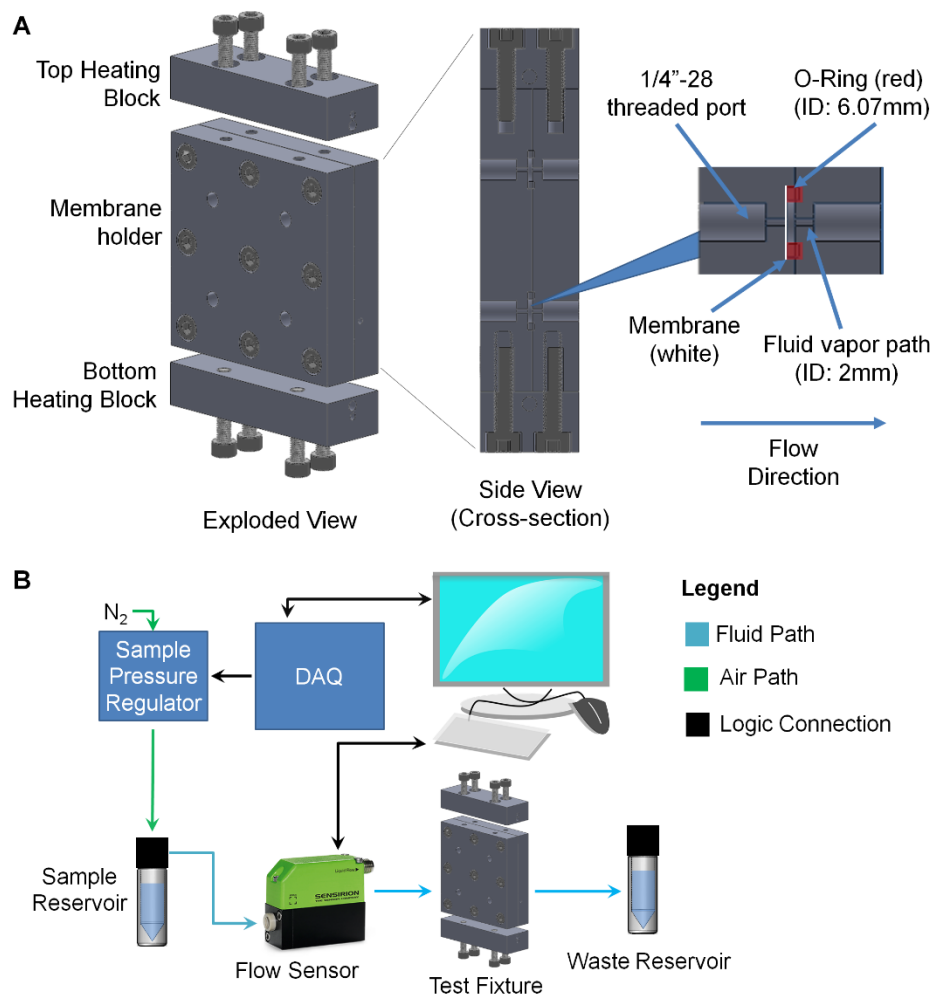


**Figure 2-6: Breakthrough pressure testing rig and testing setup**

(A) Schematic of custom-built fixture for testing the breakthrough pressure of membrane samples at different temperatures. (B) Experimental setup for measuring breakthrough pressure with the test fixture.

### 2.2.7 Determining Sample Recovery Efficiency

The efficiency of sample recovery (i.e. amount of solute recovered compared to amount in initial sample) was quantitatively evaluated using radioactive solutions. Experiments used either a [<sup>18</sup>F]fluoride solution or a solution of an <sup>18</sup>F-labeled PET tracer. [<sup>18</sup>F]fluoride solutions consisted of 11.1 – 46.3 MBq [0.3–1.25 mCi] of [<sup>18</sup>F]fluoride, 2.25 mg K222 (0.6 mM final concentration) and 0.41 mg of K<sub>2</sub>CO<sub>3</sub> (0.3 mM final concentration) in 10 mL ddH<sub>2</sub>O. The amount of solute directly corresponds to the amount of radioactivity, which was measured using a

calibrated dose calibrator (CRC-25 PET, Capintec Inc., Ramsey, NJ). Labeled PET tracers were suspended in their respective HPLC mobile phase (Table 2-1) and had activity levels ranging from 7.4 – 37 MBq [0.2–1.0 mCi]. Radioactivity measurements were made of the original sample, the collected concentrated sample and of each five subsequent rinse steps. In the case of complete solvent evaporation method, the collected sample is obtained from an initial rinse step. Measurements were corrected for radioactive decay, and the fraction of initial radioactivity was calculated for each portion of the output volume.

**Table 2-1: Semi-preparative HPLC conditions used for the purification of example PET tracers** [<sup>18</sup>F]D-FAC and [<sup>18</sup>F]FHBG were purified using Phenomenex Gemini-NX column (10mm x 250mm); others used a Phenomenex Luna column (10mm x 250mm).

Tracer	HPLC Mobile Phase (all ratios are v:v)	Flow Rate (mL/min)	Purification Method
[ <sup>18</sup> F]D-FAC	1:99 EtOH/10mM NH <sub>4</sub> H <sub>2</sub> PO <sub>4</sub>	5.0	Isocratic
[ <sup>18</sup> F]FHBG	5:95 MeCN/50mM NH <sub>4</sub> OAc	5.0	Isocratic
[ <sup>18</sup> F]D-FEAU	8:92 MeCN/water	5.0	Isocratic
[ <sup>18</sup> F]FBEM	20:80 MeCN/water	5.0	Isocratic
[ <sup>18</sup> F]Fallypride	60:40 MeCN/25mM NH <sub>4</sub> HCO <sub>2</sub> with 1%TEA	5.0	Isocratic

### 2.2.8 Assessing thermal stability of tracers

Radiochemical stability of tracers under microfluidic concentration conditions was determined via analytical radio-HPLC comparison of samples before and after concentration. Analytical HPLC was performed on a Smartline HPLC system (Knauer, Berlin, Germany) with an inline ultraviolet (254 nm) detector (Knauer, Berlin, Germany) and a gamma-radiation coincidence detector and counter (B-FC-4100 and BFC-1000; Bioscan, Inc., Poway, CA, USA). Separations were performed using a Luna C18 column (5 µm particle size, 4.6 x 250 mm; 00G-

4252-E0, Phenomenex, Torrance, CA, USA) according to the conditions in Table 2-2.

Chromatograms were collected by a GinaStar analog-to-digital converter (Raytest Inc., Straubenhardt, Germany) and GinaStar software. The purified product peak was verified by co-injection of non-radioactive standard, and purity was quantified by calculating the area in the product peak divided by the area of all peaks in the chromatogram.

**Table 2-2: Analytical HPLC conditions for PET tracers and prosthetic groups**

Tracer	Analytical HPLC mobile phase composition (all ratios are v:v)	Flow Rate (mL/min)	Purification Method
[ <sup>18</sup> F]D-FAC	10:90 EtOH / 50 mM NH <sub>4</sub> OAc	1.0	Isocratic
[ <sup>18</sup> F]FHBG	10:90 MeCN / 50mM NH <sub>4</sub> OAc	1.0	Isocratic
[ <sup>18</sup> F]D-FEAU	15:85 MeCN / water	1.0	Isocratic
[ <sup>18</sup> F]FBEM	5:95 MeCN / water at 0 min 35:65 MeCN / water at 35 min	1.0	Gradient
[ <sup>18</sup> F]Fallypride	60:40 MeCN / 25mM NH <sub>4</sub> HCO <sub>2</sub> with 1%TEA	1.0	Isocratic

Chromatograms for the various tracers are shown in Figure 2-7. No differences in radiochemical purity were observed for [<sup>18</sup>F]FHBG, [<sup>18</sup>F]D-FAC, and [<sup>18</sup>F]FBEM, indicating stability at 100°C. These were all concentrated via the partial evaporation method. Note the [<sup>18</sup>F]FBEM chromatogram shows a small impurity corresponding to hydrolyzed [<sup>18</sup>F]FBEM. This may suggest a very slight amount of degradation during the concentration process. [<sup>18</sup>F]D-FEAU and [<sup>18</sup>F]Fallypride were concentrated via the complete evaporation method and recovered in saline. No differences in chromatograms were observed before and after concentration, indicating these molecules are stable under the concentration conditions. The chromatogram for [<sup>18</sup>F]D-FEAU showed a slight shift in retention times for samples before and after concentration,

but follow up co-injection studies confirmed that the peak corresponds to the same molecule.

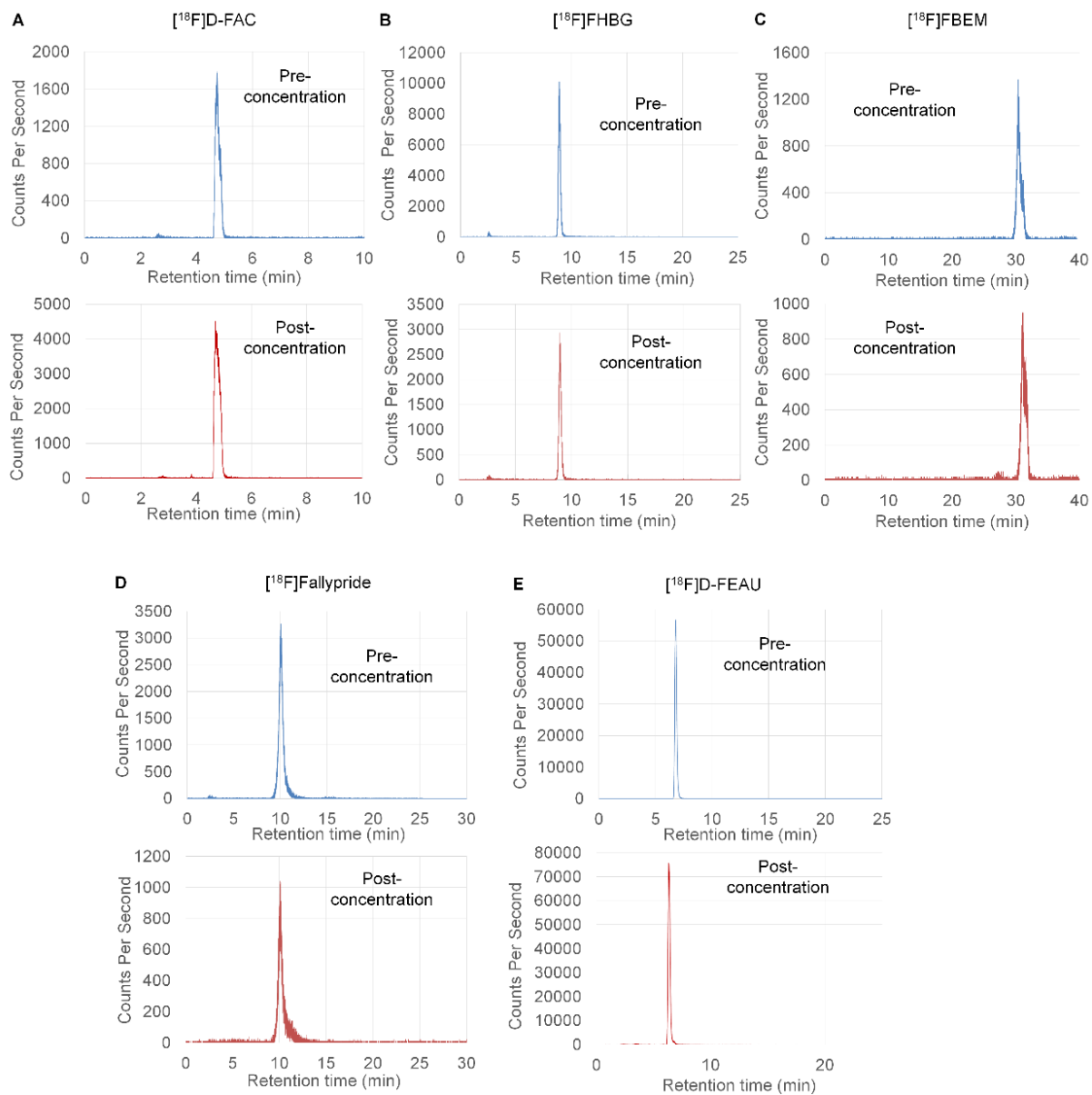


**Figure 2-7: Radio-chromatograms to assess radiochemical purity of PET tracers before and after microfluidic concentration**

(A) [<sup>18</sup>F]D-FAC. (B) [<sup>18</sup>F]FHBG. (C) [<sup>18</sup>F]FBEM. (D) [<sup>18</sup>F]Fallypride. (E) [<sup>18</sup>F]D-FEAU.

### 2.2.9 Determining residual organic solvent content

After partial or complete evaporation methods, the organic solvent content of several samples was assessed via gas chromatography mass spectrometry (GC-MS). Samples and standards were analyzed using an Agilent 7890A GC system equipped with an Agilent DB-Wax column (122-7033) connected to an Agilent 5975C MSD run in electron ionization (EI) mode at 70 eV. 0.5  $\mu$ L of the sample (or standard) was injected at a 1:200 split ratio. The carrier gas was helium and the column flow rate was maintained at 1 mL/min. The transfer line, MS source, and quadrupole temperatures were 250°C, 230°C, and 150°C, respectively, and the detector was run in SIM mode. For acetonitrile (MeCN) and ethanol (EtOH) the inlet temperature was set to 250°C. The GC oven temperature started at 70°C for 6.5 min, then was increased to 240°C at 85°C/min and held for 1.5 min. Analysis of DMSO was done at a later time and was performed with a modified method. Samples containing DMSO were injected in 0.5  $\mu$ L volume at a 1:200 split ratio. The inlet temperature used for injection of DMSO was 200°C. For the analysis of DMSO, the GC oven temperature started at 50°C for 1 min, then was increased to 220°C at 25°C/min and held for 5 min. MeCN, EtOH, and DMSO were monitored at 41, 31 and 63 m/z peaks, respectively. Area under the curve (AUC) quantitation was conducted on ChemStation software (Agilent).

Residual solvent concentration was calculated by fitting sample AUCs to the appropriate standard curve. Piecewise standard curves (Figure 2-8) of AUC versus sample composition were produced for each type of solvent. The standards of EtOH and MeCN with solvent composition ranging from 0.0-0.3% (v/v) show high linearity resulting in the use of a linear fit for AUCs that fall within this region. A second piece of the standard curve was generated for interpolating compositions above 0.3% (up to 10%) and was based on a higher order parabolic fit. The parabolic fit, however, still includes the low end composition values (0 – 0.3%). AUCs

that fall above the 0.3% AUC value are fitted with this second piece of the standard curve. For DMSO, high linearity was seen in solvent compositions ranging from 0.0-1.0% (v/v), and a higher order fit was used for interpolating compositions above 1% (up to 10%).

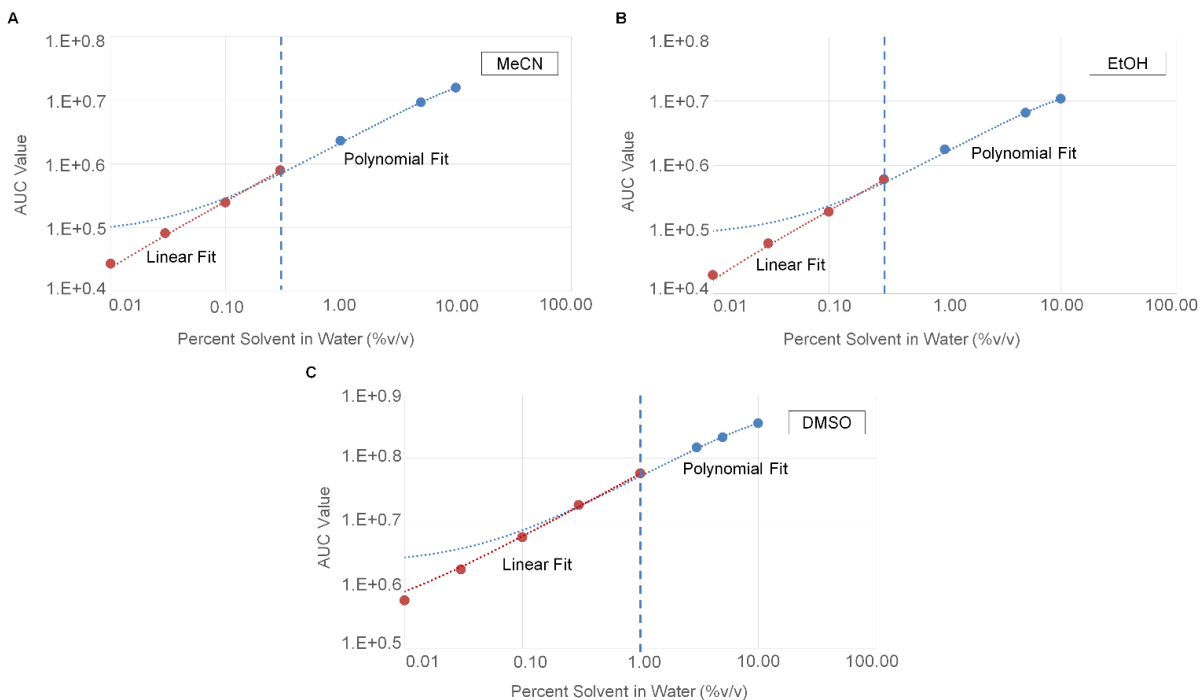


**Figure 2-8: Standard curve comparing AUC and organic solvent composition**

(A) MeCN, (B) EtOH and (C) DMSO. The dotted line represents the transition between linear fit for low solvent concentrations and the higher order fit used for higher solvent concentrations.

### 2.2.10 Theoretical vapor pressures that may affect BTP measurements

Theoretical vapor pressures of solvent mixtures (Table 2-6) were calculated using Raoult's Law. Raoult's Law states that the vapor pressure of a mixture is the sum of the partial vapor pressures of the solute (e.g. MeCN and EtOH) and solvent (e.g. water). [82] Each partial vapor pressure is the vapor pressure of the pure compound [83] multiplied by the mole fraction in the mixture.

### 2.2.11 Evaporation rate of rotary evaporator

Concentration rates of water was also determined via a commercial rotary evaporator to serve as a comparison to our system. A schematic of the experimental setup is shown in Figure 2-9 . A vacuum pump (2010 SD Pascal, Adixen Vacuum Products, Annecy Cedex, France), is connected via a vacuum trap (CG-4516-01, Chemglass Inc., Vineland, NJ) to a remote-controlled rotary evaporator customized for radiochemistry use. Inline between the pump and the trap are a manual vacuum regulator (VR1000-N01, Poweraire, Anaheim, CA) and digital pressure gauge (ISE30A-N01-C, SMC Corporation). Water bath temperatures were selected to match temperatures tested in the microfluidic concentrator. Operation at 100°C was omitted as maintaining the rotary evaporator water bath at this temperature was not possible. Vacuum pressures during operation were chosen based on the 20/40/60 rule set by Buchi Inc. [84,85] The 20/40/60 rule states that enough vacuum should be applied to the sample such that the effective boiling point of the sample is 20°C lower than that of the set point temperature. Vacuum pressures used for this experiment based off of the vapor pressure of water (used as the sample) can be seen in Table 2-3. In the case of 40-60°C set point temperatures our vacuum pump was unable to reach the desired vacuum levels; instead, the vacuum pump was set to the maximum vacuum level (-920 mBar) for each temperature, corresponding to an effective boiling point of 34°C.

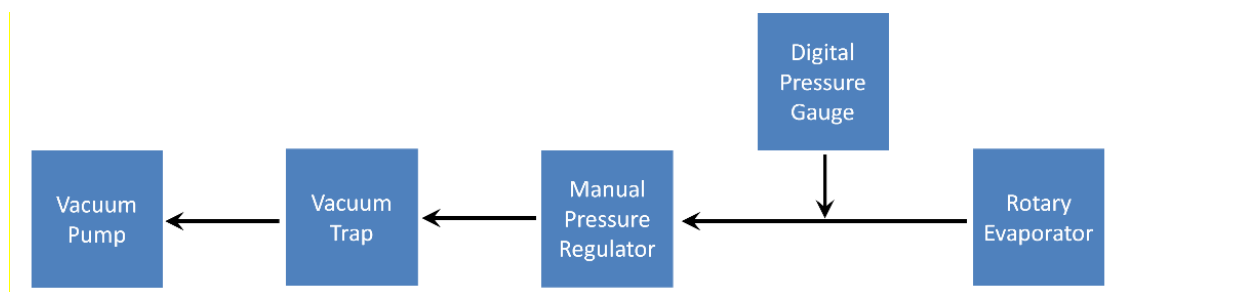


**Figure 2-9: Schematic of setup to measure speed of rotary evaporation**

Black arrows show pneumatic and vapor path

**Table 2-3: Desired and actual operating parameters for the rotary evaporator**

Water bath setpoint (°C)	Vapor pressure of sample (mBar)	Desired effective boiling point of sample (°C)	Desired gauge pressure (mBar)	Applied gauge pressure (mBar)	Actual effective boiling point of sample (°C)
40	23.4	20	-990	-920	34
50	42.5	30	-950	-920	34
60	73.8	40	-941	-920	34
70	123	50	-870	-870	50
80	199	60	-819	-819	60
90	312	70	-680	-680	70

### 2.2.12 Additional designs considered for optimization of heating

Several additional chip architectures were explored that have different heat flow characteristics (Figure 2-10). Though not characterized in detail, evaporation rates were measured for each.

1. Gas-flow layer heating. This architecture is the focus of the chapter (Figure 2-1), with a 2.54 cm thick transparent acrylic support layer, 2 mm thick plastic sample layer, and a 1 cm thick 6061 aluminum alloy gas flow layer. Heating is supplied from the gas flow layer.
2. Sample layer heating. In this design, heat is applied on the sample side of the membrane by a 0.735 cm thick heating block (6061 aluminum alloy) containing four 100W cartridge heaters and K-type thermocouples. The heating block was placed in direct thermal contact with the sample layer (thickness: 2 mm; channel depth: 50  $\mu\text{m}$ ). The gas flow layer was a 2.4 cm thick piece of Ultem, a plastic with good temperature stability, solvent resistance, and transparency.
3. Metal chip
  - 3.1. Metal chip with sample layer heating. This design was the same as that described in #2, except with a 1.0 cm thick 6061 aluminum alloy gas-flow layer. Heating was supplied via the metal block on the sample side of the membrane.
  - 3.2. Metal chip with gas-flow layer heating. This design used the same chip architecture as #3.1, except that heating was supplied via the metal gas-flow layer instead of the layer adjacent the sample layer.
  - 3.3. Metal chip with dual heating. This design used the same chip architecture as #3.1 and #3.2, except that heating was supplied both from the sample-side metal block as well as the metal gas-flow layer. Four 100W heaters were used, two positioned in each of the heated layers.
4. All-metal chip. This architecture was the same as #3.3, but the 2 mm thick plastic sample layer was replaced with a 3.2 mm thick 6061 aluminum alloy block. The block did not contain any channel patterns: the sample channel in this case is formed due to deflection of

the permeable membrane into the channels of the gas flow layer, making room for the sample fluid.

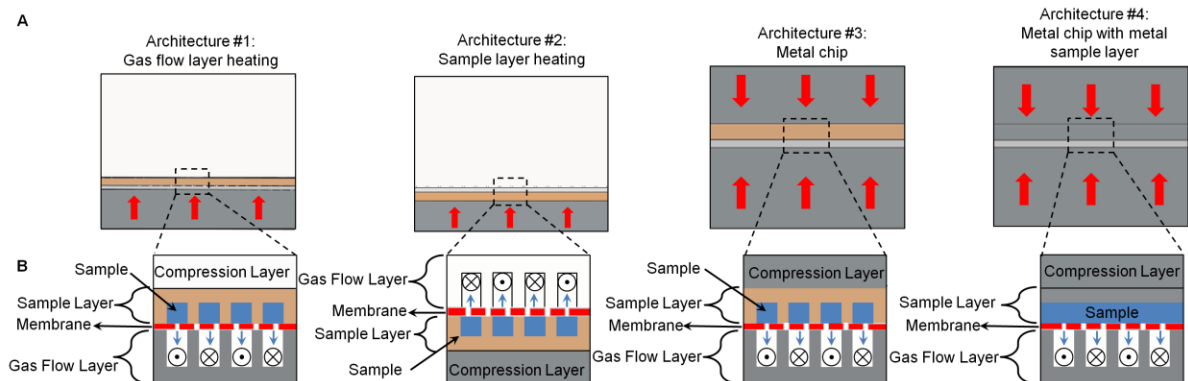


**Figure 2-10: Alternative heating designs**

(A) Chip layer configuration for different designs (to scale), with red arrows representing the direction that heat is applied. (B) Cross-section schematics of each design, with blue arrows showing the direction of vapor transport.

### 2.2.13 Comparison of surface temperatures

To help understand the differences in performance, we used infrared (IR) thermal imaging to measure steady-state temperatures close to the location of the sample fluid for different chip architectures. Imaging was performed with a T420 IR camera (FLIR, Boston, MA, USA). Transparent materials and reflective surfaces were coated with flat black spray paint (#51602 Krylon Industrial, Cleveland, OH, USA) in order to increase the thermal emissivity (~0.95) for imaging.

For gas flow layer heating, the gas flow layer surface that is in direct contact with the membrane was imaged. From this surface, only the thin membrane must be traversed before heat reaches the sample fluid. For sample layer heating, the membrane-contacting surface of the sample layer (i.e. where the sample channel is located) was imaged. After activating the temperature control, time was given for the temperature at the surface of interest to equilibrate. (The time to reach equilibrium was not thoroughly characterized as it is possible to pre-heat the

microfluidic concentrator.) Surface temperatures were quantified by using the averaging capabilities built into the FLIR camera software. A square ROI was drawn around the channel portion of the surface being imaged, and the average temperature within this ROI was recorded (Figure 2-11). Temperature uniformity was assessed qualitatively through the generated “heat maps” as well as looking at maximum and minimum values within the ROI.

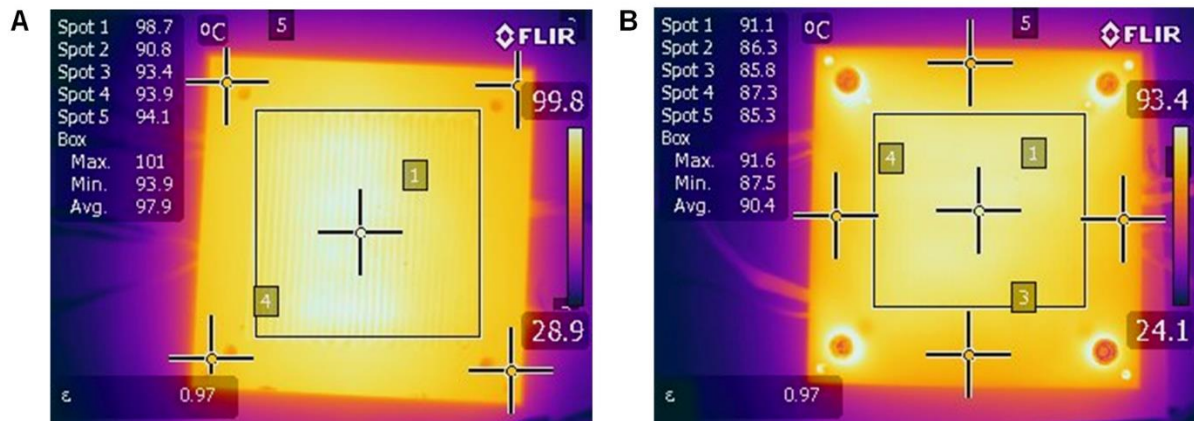


**Figure 2-11: Sample IR thermal images of a (A) gas flow layer, and a (B) sample layer**  
 Temperature measurements at individual points as well as the ROI are shown. It can be seen that for the same 100°C setpoint, temperatures in the sample layer heating architecture are significantly lower on average than temperatures in the gas flow layer heating architecture.

### 2.2.14 Surface roughness characterization

To better understand the surface roughness differences between sample layers produced with laser ablation vs. traditional milling, sample layers with identical patterns were fabricated using the two techniques. Surface topography was measured using a Dektak 150 Surface Profiler (Veeco Inc, Plainview, NY, USA). The stylus radius used was 12.5 μm, force was set to 3 mg, and the measurement profile was set to measuring hills and valleys. Scanning was performed across the width of the channel. The scan length was set to 6 mm and resulted in a resolution of 0.17 μm per scanned sample.

For each sample, an average height value was obtained for a region of the scan that represents the bottom of the channel. The standard deviation in height was then calculated to quantify the roughness of the channel bottom. For the PMMA layer made by laser ablation, the roughness was 9  $\mu\text{m}$ . For the PEEK sample layer fabricated with traditional milling, the surface was much smoother, with a roughness of 0.6  $\mu\text{m}$ .

### 2.2.15 Total operating time

Total operating time for concentration / formulation for the partial evaporation and complete evaporation methods is given by the following equations:

$$T_{\text{partial}} = T_{\text{load}} + R_{\text{evap}} \times (V_{\text{sample}} - V_{\text{chip}}) + T_{\text{delay}(\text{partial})} + T_{\text{collect}} + N_{\text{rinse}} \times T_{\text{rinse}}$$

$$T_{\text{complete}} = T_{\text{load}} + R_{\text{evap}} \times (V_{\text{sample}} - V_{\text{chip}}) + T_{\text{delay}(\text{complete})} + T_{\text{collect}} + T_{\text{load}} + T_{\text{delay}(\text{partial})} \\ + N_{\text{rinse}} \times T_{\text{rinse}}$$

where:

- $T_{\text{load}}$  is the sample loading time (25 s)
- $R_{\text{evap}}$  is the evaporation rate
- $V_{\text{sample}}$  is the initial sample volume
- $V_{\text{chip}}$  is the volume of the chip (~2.75 mL)
- $T_{\text{delay}(\text{partial})}$  is the delay time used for partial solvent evaporation (50 s)
- $T_{\text{delay}(\text{complete})}$  is the delay time used for complete solvent evaporation (270 s)
- $T_{\text{collect}}$  is the time to collect the sample (23 s)
- $N_{\text{rinse}}$  is the number of rinse steps
- $T_{\text{rinse}} = T_{\text{load}} + T_{\text{delay}(\text{partial})} + T_{\text{collect}}$  is the time required per rinse step

In the case of concentrating a 10 mL sample at a temperature of 100°C with an evaporation rate of 2.0 mL/min, and 2 rinse steps,  $T_{\text{partial}} \sim 8.5$  min and  $T_{\text{complete}} \sim 13.5$  min. The difference

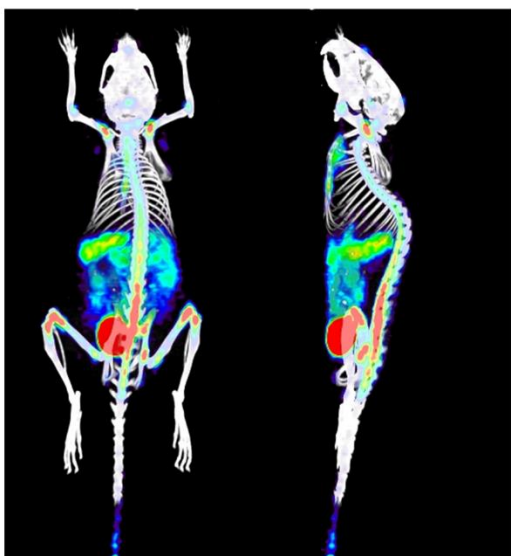
between the two methods arises mainly from the difference in delay time for complete vs partial evaporation (220 s longer for complete evaporation), plus the extra step of loading and concentrating saline prior to collection (25 s + 50 s).

### **2.2.16 In vivo mouse imaging of [<sup>18</sup>F]D-FAC**

[<sup>18</sup>F]D-FAC was concentrated via conventional rotary evaporation and using the microfluidic concentrator. Rotary evaporation was performed at 80°C with pressure of ~ -10 psi (adjusted to prevent sample bumping during evaporation) before re-suspension in saline. Concentration of [<sup>18</sup>F]D-FAC in the microfluidic concentrator was carried out at 100°C using the partial evaporation method. A longer than usual final delay time of 110 s was used in the initial concentration and rinse steps to reduce collected sample volume. Two additional rinse plugs were performed with 0.9% sterile saline resulting in a total collected volume of ~1.2mL.

Static scans of the two animals per condition were performed with a microPET scanner (Inveon, Siemens, Washington, D.C., USA). Mice were injected with the formulated tracers (~100 µCi) via the tail vein. After 60 min uptake time, mice were anesthetized with 2% isoflurane and placed in a dedicated imaging chamber with heating. PET images were acquired for 600 s, followed by microCT imaging. PET data was processed by 3D histogramming and reconstruction with a zoom factor of 2.1 using 3D-OSEM with 2 iterations followed by MAP with 18 iterations (beta=0.1). Images were analyzed using AMIDE version 1.0.52. (Figure 2-12). Uptake at 60 min in the bone and bone marrow, thymus, gastrointestinal tract, spleen, and bladder was compared via ROI analysis of the mean injected dose per gram (ID/g) (Table 2-4). All animal studies presented in this chapter were approved by the UCLA IACUC's Animal Research Committee and were carried out following guidelines set by the Department of Laboratory Medicine at UCLA.

**A** [<sup>18</sup>F]D-FAC concentrated and formulated using rotary evaporator



**B** [<sup>18</sup>F]D-FAC concentrated and formulated using microfluidic system

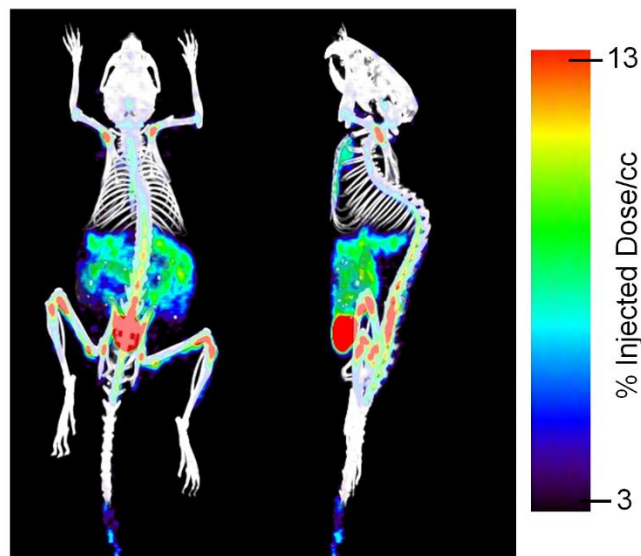


**Figure 2-12: PET/CT maximum intensity projection (MIP) image of mouse one hour after injection with [<sup>18</sup>F]D-FAC**

[<sup>18</sup>F]D-FAC was concentrated and formulated with (A) a conventional rotary evaporator, and (B) the microfluidic chip in complete evaporation mode.

**Table 2-4: Comparison of biodistribution showing similar uptake in key organs**

Values represent average uptake from n=2 animals.

Organ	Organ uptake (%ID/cc ± stdev)	
	Rotary evaporator	Microfluidic evaporator
Thymus	6.4 ± 0.3	6.8 ± 0.5
Bone and bone marrow	13.0 ± 0.5	11.0 ± 2.6
Spleen	7.8 ± 0.9	7.1 ± 0.6
Gastrointestinal tract	7.3 ± 0.9	7.0 ± 0.4
Bladder	18.2 ± 1.8	21.1 ± 5.6

## 2.3 Results and Discussion

### 2.3.1 Scope of HPLC mobile phases

In the synthesis of PET tracers and radiolabeled prosthetic groups (for labeling biological molecules), HPLC purification methods nearly always use mixtures of EtOH in water or MeCN in water, sometimes with additives to buffer the pH to improve separation or stability. Examples of mobile phases for purification of several radiolabeled molecules are listed in Table 2-1.

We first examined contact angles (Figure 2-4) in order to determine the range of solvent compositions and temperatures for which  $\theta > 90^\circ$  (i.e. for which no spontaneous breakthrough would be expected). For mobile phases consisting of MeCN and water mixtures, we observed that  $\theta > 90^\circ$  for all compositions (from 0 to 100% MeCN in water, v/v) and all temperatures (RT to 80°C). For EtOH, concentrations up to 70% EtOH in water (v/v) can be sustained ( $\theta > 90^\circ$ ) at all temperatures (RT to 80°C) without breakthrough, but compositions  $\geq 80\%$  EtOH (v/v) would not be suitable at any temperature. Unfortunately, for temperatures above 80 °C, droplets rapidly evaporated, preventing accurate contact angle measurement, and thus this method does not provide a good way to estimate the behavior under the most aggressive temperatures. For both solvents, the effect of composition on wetting property appears to be more significant than the effect of temperature. This is expected because Eötvös rule describes a linear decrease in surface tension with increasing temperature [86], but surface tension has been observed to decrease superlinearly with increasing mole fraction of organic solvent. [87]

**Table 2-5: Breakthrough pressures measured with the membrane test rig**

Vapor pressure for (A) MeCN and (B) EtOH were measured. Pressures are in units of psi, and represent the average  $\pm$  standard deviation of n=3 repeats.

A % MeCN in H <sub>2</sub> O (v/v)	Temperature (°C)				
	RT	40	60	80	100
0	>13.5	>13.5	>13.5	>13.5	N.M.
10	>13.5	>13.5	>13.5	>13.5	N.M.
20	>13.5	>13.5	>13.5	>13.5	N.M.
30	>13.5	>13.5	>13.5	>13.5	N.M.
40	>13.5	>13.5	>13.5	>13.5	N.M.
50	>13.5	>13.5	>13.5	>13.5	N.M.
60	>13.5	>13.5	>13.5	>13.5	N.M.
70	>13.5	>13.5	>13.5	>13.5	N.M.
80	>13.5	12.2 $\pm$ 0.5	11.6 $\pm$ 1.4	>13.5	N.M.
90	12.0 $\pm$ 0.2	10.6 $\pm$ 0.8	8.6 $\pm$ 0.5	8.1 $\pm$ 0.3	N.M.
100	7.3 $\pm$ 0.3	5.6 $\pm$ 0.2	3.3 $\pm$ 0.4	2.0 $\pm$ 0.4	N.M.
B % EtOH in H <sub>2</sub> O (v/v)	Temperature (°C)				
	RT	40	60	80	100
0	>13.5	>13.5	>13.5	>13.5	N.M.
10	>13.5	>13.5	>13.5	>13.5	N.M.
20	>13.5	>13.5	>13.5	>13.5	N.M.
30	>13.5	>13.5	>13.5	>13.5	N.M.
40	>13.5	>13.5	>13.5	>13.5	N.M.
50	11.5 $\pm$ 1.2	11.3 $\pm$ 0.7	12.0 $\pm$ 0.2	>13.5	N.M.
60	7.9 $\pm$ 0.3	7.6 $\pm$ 0.3	7.6 $\pm$ 0.2	12.7 $\pm$ 0.5	N.M.
70	4.4 $\pm$ 0.2	4.1 $\pm$ 0.2	4.2 $\pm$ 0.3	5.4 $\pm$ 0.6	N.M.
80	1.8 $\pm$ 1.0	0.4 $\pm$ 0.4	< 0.5	2.2 $\pm$ 0.8	N.M.
90	< 0.5	< 0.5	< 0.5	3.9 $\pm$ 0.3	N.M.
100	< 0.5	< 0.5	< 0.5	5.5 $\pm$ 0.2	N.M.

While the contact angle gives an idea about spontaneous wetting, it does not indicate whether the BTP is sufficiently large for proper operation of the chip without breakthrough in practice. Using a specially designed test rig measurements of BTP for various solvent compositions and temperatures (up to 80°C) were made (Table 2-5).

As expected, for samples containing either solvent (MeCN and EtOH), an increase in temperature or organic solvent composition results in decreased breakthrough pressure. For MeCN/water mixtures, BTP was very high (>13.5 psi) for all compositions up to 70% MeCN v/v (at all temperatures), and was moderately high (> 7.5 psi) for all compositions up to 90% MeCN v/v (at all temperatures). Moderate BTP values still allow considerable freedom in choice of operating conditions ( $P_{sample}$ ,  $P_{gas\_in}$ , and  $P_{gas\_out}$ ). Only at 100% MeCN at elevated temperatures is the BTP low enough that reliable operation may be difficult. For EtOH/water mixtures, on the other hand, BTP was very high (>13.5 psi) for compositions up to 40% EtOH v/v at all temperatures tested, and was moderately high (>7.5 psi) for compositions up to 60% EtOH v/v at all temperatures. For all compositions  $\geq 70\%$  EtOH v/v, the BTP is low enough that reliable and efficient operation may be difficult. These results correspond well to the contact angle data.

Note that we observed some evidence that BTP could not be reliably measured in the test rig for temperatures  $\geq 80^\circ\text{C}$ . For example, starting with 80% MeCN at 80°C or 80% EtOH at 80°C, increased solvent composition would be expected to decrease the BTP, but the measurement actually increases. We hypothesize that the small surface area of the testing membranes ( $\sim 29\text{ mm}^2$ ) cannot transport the high vapor flux at high temperatures, leading to a buildup of pressure within the vicinity of the membrane. The vapor pressures of H<sub>2</sub>O, EtOH, and MeCN at 80°C are 6.9, 15.8, and 14.2 psi [83] respectively (estimated by Raoult's Law), and thus the vapor pressure of the tested mixtures will thus be >6.9 psi at 80°C (Table 2-6).

**Table 2-6: Vapor pressure as a function of temperature for various mobile phase compositions based on (A) MeCN and (B) EtOH**

Reported values are in psi.

A % MeCN in H <sub>2</sub> O (v/v)	Temperature (°C)					B % EtOH in H <sub>2</sub> O (v/v)	Temperature (°C)				
	RT	40	60	80	100		RT	40	60	80	100
0	0.46	1.07	2.89	6.88	14.71	0	0.46	1.07	2.89	6.88	14.71
10	0.53	1.24	3.15	7.15	15.06	10	0.48	1.12	3.02	7.17	15.30
20	0.60	1.42	3.45	7.46	15.46	20	0.51	1.18	3.18	7.51	15.99
30	0.69	1.64	3.79	7.83	15.93	30	0.54	1.25	3.35	7.91	16.81
40	0.79	1.90	4.20	8.25	16.48	40	0.58	1.33	3.57	8.39	17.77
50	0.92	2.21	4.68	8.77	17.14	50	0.62	1.44	3.82	8.97	18.94
60	1.07	2.58	5.27	9.39	17.94	60	0.68	1.56	4.14	9.68	20.39
70	1.25	3.05	6.01	10.16	18.93	70	0.75	1.72	4.54	10.59	22.23
80	1.49	3.64	6.94	11.15	20.20	80	0.84	1.92	5.07	11.78	24.63
90	1.80	4.43	8.17	12.45	21.87	90	0.97	2.21	5.79	13.40	27.92
100	2.24	5.51	9.88	14.24	24.18	100	1.15	2.62	6.84	15.75	32.68

The build-up of vapor pressure counteracts the sample pressure, leading to an apparent increase in applied pressure needed to cause breakthrough. If sufficiently high, it can even push the sample away from the membrane, as was seen for samples at 100°C, making measurement of BTP impossible. Overall, these results suggest that the accuracy of this method of BTP measurement may be limited, especially when the vapor pressure is significant compared to the actual BTP (i.e. high organic solvent fractions and high temperatures).

### 2.3.2 Operating conditions

We chose a lower limit of BTP of ~7.5 psi as a good compromise of compatibility with a wide range of solvent mixtures and temperatures as well as ensuring some room for optimizing the operating conditions. As a starting point, we selected  $P_{sample} = 5.3$  psi,  $P_{gas\_in} = 4.5$  psi, and  $P_{gas\_out} = -0.25$  psi. This ensures all the constraints described in Section 2.2.6 are met.  $P_{sample}$  was sufficient to ensure the chip was always filled with sample under all conditions explored in this chapter. The maximum pressure across the membrane is 5.6 psi, which is below 7.5 psi by a 35% safety margin.  $P_{gas\_in}$  is below  $P_{sample}$  by a ~20% safety margin.

A limited exploration of gas-flow pressure differential and sample pressure was performed to determine the effect on evaporation rate performance. The effect of gas-flow pressure differential ( $P_{gas\_out} - P_{gas\_in}$ ) and sample pressure ( $P_{sample}$ ) on the evaporation rate can be seen in Figure 2-13. Increased gas-flow pressure differential will proportionately increase the volumetric flow rate of gas in the gas-flow channel. It is expected that increased gas flow helps to remove vapor and thus reduce the partial pressure of solvent vapor on the gas-flow side of the membrane, and thereby promote increased evaporation and movement of vapor across the membrane. Indeed, this was observed experimentally suggesting that the maximum allowable gas flow (that satisfies operating constraints) should be used.

In contrast, the sample pressure was found to have negligible effect on evaporation rate. This indicates that even the lowest sample pressure is sufficient to ensure that the sample channel within the chip remains full of sample during the concentration process.

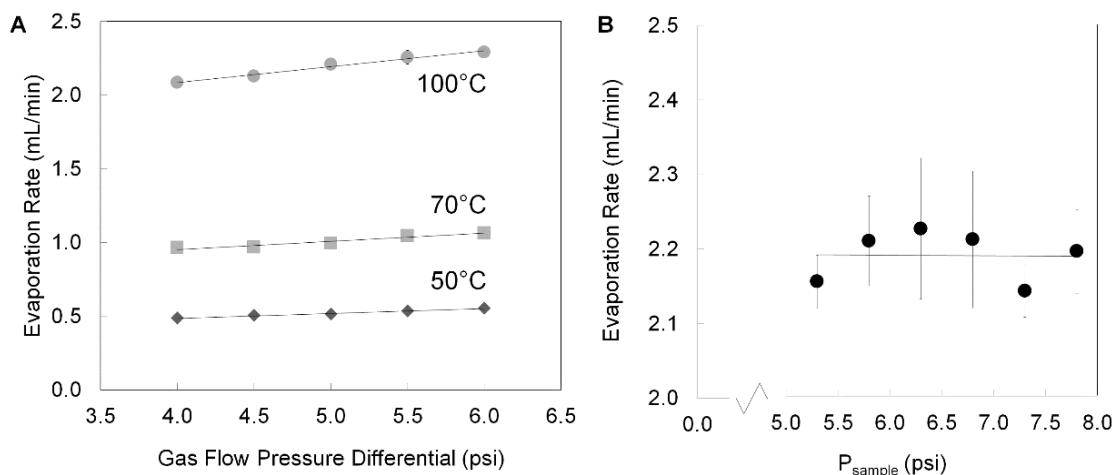


**Figure 2-13: Evaporation rates as a function of different operating parameters**  
 (A) Evaporation rates as a function of gas flow differential in the gas flow layer with the system operated at different temperature set points. (B) Evaporation rates as a function of sample inlet pressure (performed at 100°C).

Over the range tested,  $P_{sample}$  was found to have negligible effect on the evaporation rate. The gas-flow pressure differential did have a small effect, as was also observed in our

previous work. Changing to a differential of 6.0 psi instead of 4.75 psi would increase evaporation rate by ~ 5%, but if similar safety margins were used, the minimum BTP that could be tolerated would be ~10 psi, which would exclude several solvent compositions; thus this change was not implemented.

Parameters related to sample collection were set to maximize sample recovery.  $P_{vacuum} \leq -2.0$  psi resulted in break-up of the sample in tubing during recovery, so  $P_{vacuum}$  was set to -1.0 psi. This was ramped up to  $P_{vacuum\_ramp} = -8.8$  psi, near the best vacuum that could be achieved with the pump used.

### 2.3.3 Evaporation rate

Using the above operating conditions, evaporation rates were extensively characterized. Maximum evaporation rates of water at 100°C exceeded 2 mL/min, compared to ~0.6mL/min observed in our previous system. [72] We also performed concentration using a rotary evaporator according to parameters recommended by the manufacturer.

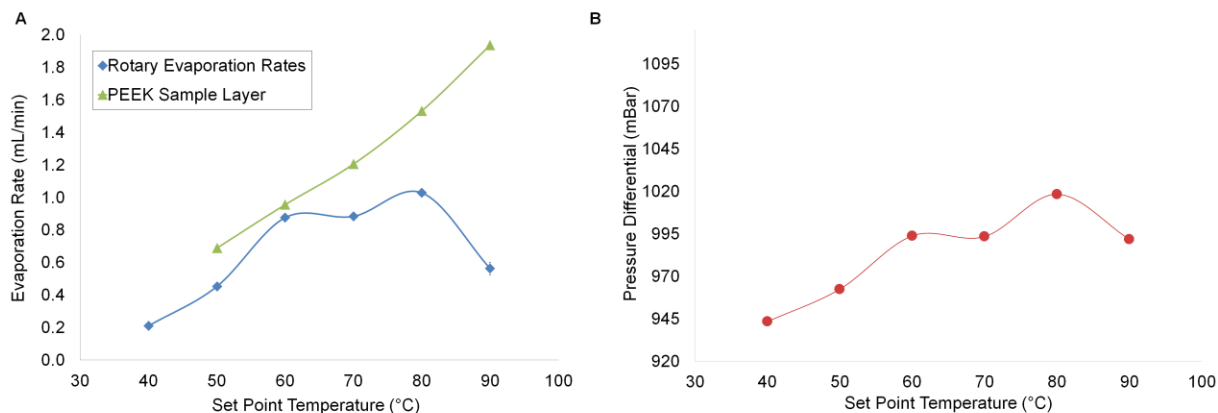


**Figure 2-14: Evaporation rate comparison between microfluidic and rotary evaporator** (A) Evaporation rate of water as a function of temperature in the rotary evaporator and the microfluidic concentrator with PEEK sample layer. (B) Pressure difference between vapor pressure and vacuum pressure in the rotary evaporator system during operation at each temperature.

The results (Figure 2-14) show that the evaporation rate of the microfluidic system exceeds that of the rotary evaporator at all operating temperatures. The rotary evaporator

reached a maximum evaporation rate of  $1.03 \pm 0.04$  mL/min at  $80^{\circ}\text{C}$ . The microfluidic concentrator (with PEEK sample layer) achieved  $1.53 \pm 0.02$  mL/min at the same temperature.

A complex relationship was observed between evaporation rate and temperature for the rotary evaporator. This behavior appears closely correlated to the resulting pressure difference between the sample vapor pressure and the vacuum pressure, suggesting that the effective driving pressure of vapor out of the rotary evaporator is the dominant factor affecting performance. It may be possible to further optimize the rotary evaporator performance by tuning operating parameters or changing the hardware configuration but this was not pursued.

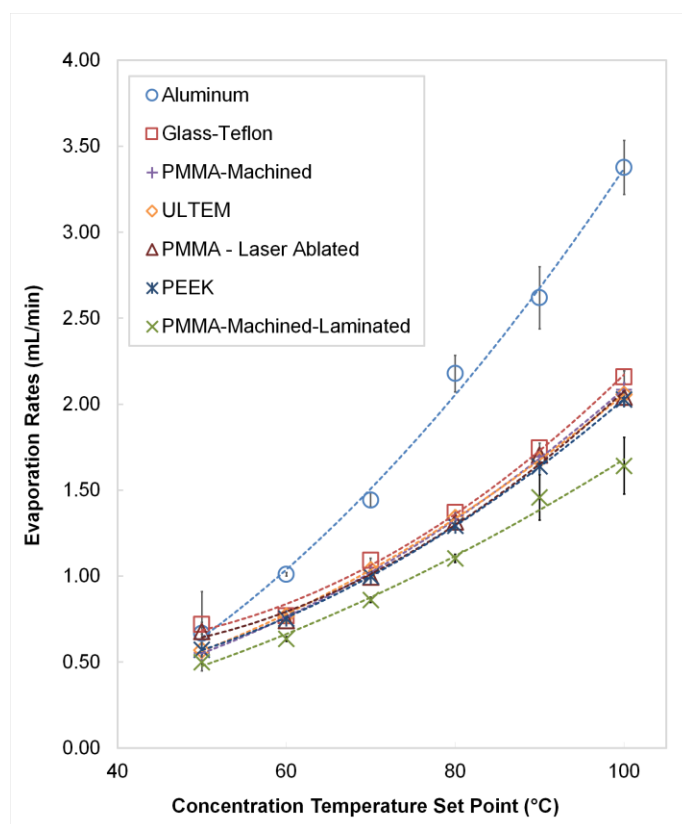


**Figure 2-15: Evaporation rates of deionized water as a function of temperature for different chip materials**

Data points show an average of 5 repeats and error bars represent standard deviation.

We found the evaporation rate at  $80^{\circ}\text{C}$  to be  $1.03 \pm 0.04$  mL/min compared with  $1.53 \pm 0.02$  mL/min achieved in the microfluidic chip at the same temperature. The observed

evaporation rate of the chip depended somewhat on the material that was used for the sample layer (Figure 2-15).

Evaporation rates using PMMA-machined, PMMA-ablated, Ultem, and PEEK, were very similar across the temperature setpoints. The evaporation rate for glass-Teflon is significantly higher than the other materials. The differences may be related to the thermal conductivity of the sample layer materials. Thermal conductivities of PMMA, Ultem, and PEEK are all similar (0.19, 0.22, 0.25 W/mK, respectively), whereas the thermal conductivity of glass-PTFE is significantly higher (0.42 W/mK). [88] Note that PTFE and COC turned out not to be suitable materials. For PTFE, significant deformation occurred at the inlet and outlet locations, most likely due to compressive forces from fluidic connections, interfering with sample loading and ejection. The COC material exhibited cracking and leaks, perhaps as a result of the elevated operating temperatures in combination with the compressive forces to hold the layers of the chip together.

In addition to comparing sample layer materials, different chip architectures were explored to compare the effect of heater placement. PEEK sample layer material was chosen as the main testing material for comparing alternative heating configurations. Evaporation rates of deionized water at 100°C using the various designs are shown in Figure 2-16. The evaporation rate of architecture #1 was  $2.02 \pm 0.04$  mL/min (n=5).

In architecture #2, with sample layer heating instead of gas-flow layer heating, the evaporation rate was significantly lower, i.e.  $1.03 \pm 0.01$  mL/min (n=5). In gas flow heating, heat must travel from the metal gas-flow layer through only the ~50 µm thick PTFE membrane to reach the contents of the sample channel. In contrast, with sample layer heating, heat must travel through the whole thickness of the sample layer minus the channel depth (i.e.  $2000 - 50 \approx 2000$  µm of PEEK) to reach the sample. Despite the superior thermal contact area of sample

layer heating (i.e. whole surface of heater is in contact with whole surface of sample layer) compared to the small contact area of gas flow heating (i.e., only at the walls between channels in the gas-flow layer), the performance of the latter is still superior, suggesting that the detrimental effect of the thick plastic layer in the heat transfer path is dominant. It is also possible that large deflection of the membrane allows it to contact the walls of the gas-flow layer during operation, providing additional thermal contact area for gas-flow layer heating. Presumably, performance of sample layer heating could be improved if the thickness of the sample layer could be significantly reduced.

In the metal chip configuration, the plastic gas-flow layer is replaced with a metal one. With heating from the sample side (architecture #3.1), the evaporation rate was  $1.38 \pm 0.06$  mL/min ( $n=5$ ). Using the same layers but heating from the gas-flow side instead of sample side (architecture #3.2) increased the evaporation rate to  $1.99 \pm 0.03$  mL/min ( $n=5$ ). Overall, providing heat to the sample via the membrane (from gas-flow layer heater) is more effective than heating through the sample layer to reach the sample. By providing heating from both sides, evaporation rate was  $2.22 \pm 0.06$  mL/min ( $n=5$ ), only slightly higher than if only the gas-flow layer was heated, despite the significant extra complexity of fabrication and operation of heating from both sides.

In architecture #4, the plastic sample layer of the metal chip was replaced with a 3.2 mm thick 6061 aluminum alloy block. In this case, significant further increase in evaporation rate was observed, i.e.  $3.38 \pm 0.16$  mL/min ( $n=5$ ). The high thermal conductivity of the 6061 aluminum alloy sample layer (167 W/mK) is likely important here, consistent with the observed trend that evaporation rate in architecture #1 seems to correlate with thermal conductivity of the sample layer material (Figure 2-15).

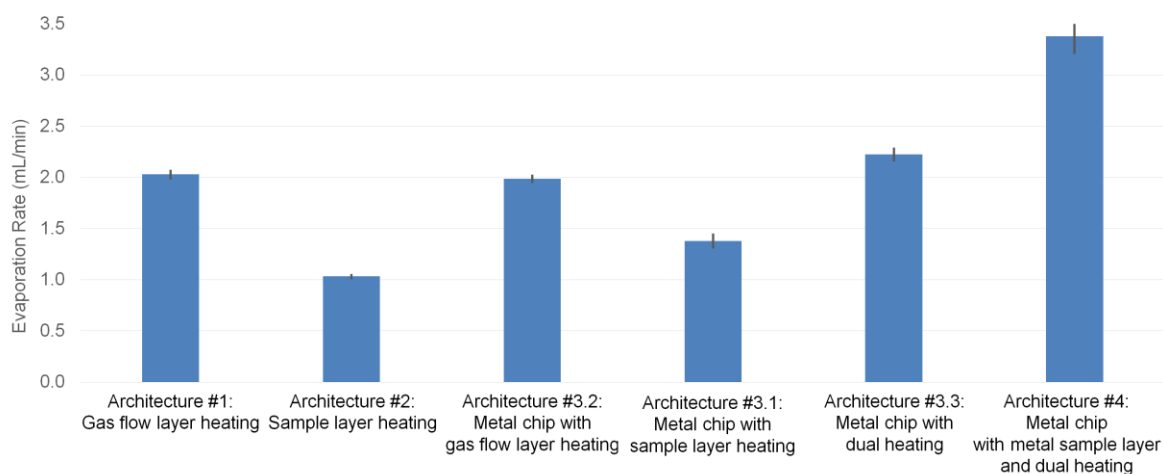


**Figure 2-16: Evaporation rates of deionized water for different designs**

Temperature set point was at 100°C. Each bar represents the average of n=5 replicates. Error bars represent standard error of the mean.

For imaging of the surface temperatures of the gas-flow layer, deviations between the measured surface temperature and the setpoint were: +0.4 °C for  $T_{set}=50^{\circ}\text{C}$ , -0.1°C for  $T_{set}=60^{\circ}\text{C}$ , -0.9 °C for  $T_{set}=70^{\circ}\text{C}$ , -1.5°C for  $T_{set}=80^{\circ}\text{C}$ , -1.7°C for  $T_{set}=90^{\circ}\text{C}$ , and -2.1°C for  $T_{set}=100^{\circ}\text{C}$ . On the other hand, imaging of the sample layer resulted in much larger deviations of -1.3 °C for  $T_{set}=50^{\circ}\text{C}$ , -2.8°C for  $T_{set}=60^{\circ}\text{C}$ , -4.8 °C for  $T_{set}=70^{\circ}\text{C}$ , -6.2°C for  $T_{set}=80^{\circ}\text{C}$ , -8.2 °C for  $T_{set}=90^{\circ}\text{C}$ , and -9.6°C for  $T_{set}=100^{\circ}\text{C}$ . Although these are surface measurements and may not reflect the actual temperatures inside an assembled device, the data suggest that when heating a plastic sample layer, the temperature of the sample fluid may be substantially lower than what can be achieved by heating through the gas-flow layer. Due to the strong dependence of evaporation rate on temperature, this temperature difference could explain why the geometries exhibit such a large difference in evaporation performance.

Most designs had similar or inferior performance with the exception of one design having a 3.2 mm thick 6061 aluminum alloy sample layer (thermal conductivity 167 W/m<sup>2</sup>K [89]) instead of a plastic sample layer. At 100°C, evaporation rate was 3.38±0.16 (n=5) mL/min compared to

2.02 ± 0.04 mL/min (n=5) for the PEEK sample layer, though the results are not directly comparable due to different arrangement of heaters. Because the opaqueness of the metal prevents convenient visualization, the plastic sample layers were used for all remaining experiments, but this result shows the potential improvement that may be possible by considering materials with high thermal conductivity.

#### **2.3.4 Effect of solutes and solvents on evaporation rate**

Radiolabeled molecules may be in HPLC mobile phase volumes as large as ~50 mL prior to concentration and formulation using the microfluidic chip, leading to large increases (~50x) in concentration of salts and additives that may be present in the mobile phase. Investigations of dynamic evaporation rate during concentration of 50 mL samples at 100°C were performed to determine if buildup of solutes or depletion of volatile organic solvent components would lead to changes in evaporation rates over time.

First, evaporation of 50 mL of deionized water was monitored as a negative control (Figure 2-17A). Despite some fluctuations that likely represent experimental error, evaporation rate appears constant during the whole process. Indeed, no significant difference was found in statistical comparison of the average evaporation rate of the first 5 mL and the last 5 mL. Next, concentration of NH<sub>4</sub>OAc solutions up to 750 mM in water was performed (Figure 2-17B). Only at very high concentrations, i.e. ≥ 500mM, was a significant decrease in evaporation rate observed during the concentration process. These concentrations are ~10x higher than normally used in HPLC purification of PET tracers.

The effect of organic solvents was also considered. For large sample volumes, we expected the evaporation rates to be initially higher and then decrease as the lower boiling point organic solvent was evaporated off leaving mostly water within the chip. The effect of solvents were explored by concentrating samples of EtOH in water (up to 20% v/v) and MeCN in water

(up to 40% v/v) (Figure 2-17C,D). Evaporation rates were found to be consistent throughout the concentration process. Not surprisingly, increasing concentration of organic solvent in the mobile phase led to increase in evaporation rate.

Finally, as a relevant example containing both high solute content and organic solvents, we used the mobile phase for [<sup>18</sup>F]FHBG (5% v/v MeCN in 50 mM NH<sub>4</sub>OAc) (Figure 2-17A). The evaporation rate was constant throughout the concentration process. Statistical analyses of all evaporation runs are summarized in Table 2-7. Though an increase in solute concentration can lower the vapor pressure [90] (which would be expected to reduce the evaporation rate), we found that evaporation rates of 50 mL samples were remarkably constant throughout the entire evaporation process. Solutes became a factor during concentration only when the starting concentration of salts was 10x higher than normally used in HPLC mobile phases.

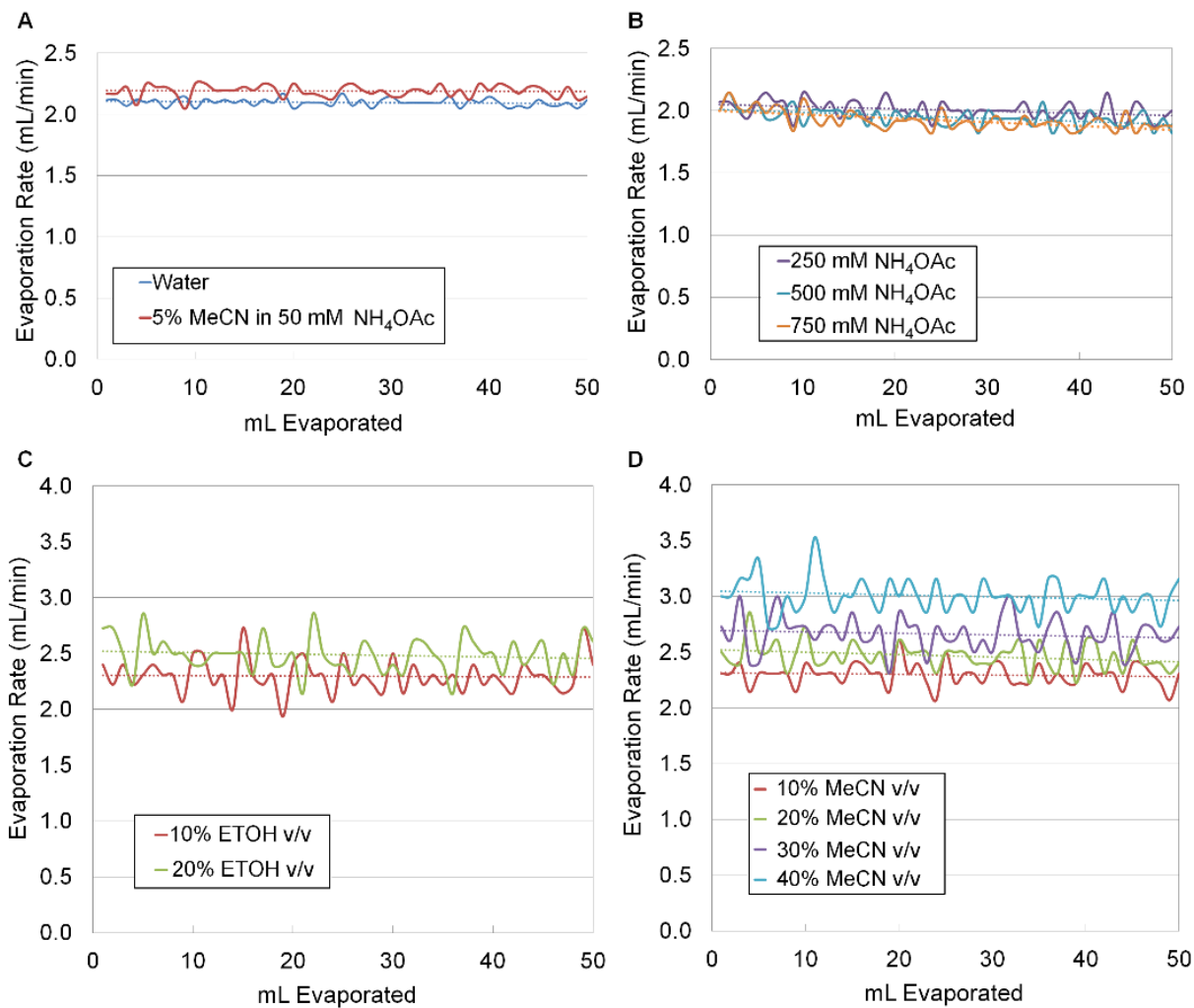


**Figure 2-17: Dynamic evaporation rates of different solvents**

Evaporation rates are plotted as a function of the volume that has already evaporated in large volume (50 mL) samples. (A) Deionized water and [<sup>18</sup>F]FHBG mobile phase. (B) NH<sub>4</sub>OAc in water solutions. (C) ETOH/water solutions. (D) MeCN/water solutions.

**Table 2-7: Unpaired t-test of evaporation rates**

T-tests compare evaporation rates at the start (first 5 mL) and at the end (last 5 mL) when evaporating large volume (50 mL) samples.

Sample	Average evaporation rate for first 5 mL	Average evaporation rate for last 5 mL	P-Value	Significant?
Deionized water	2.13 ± 0.06	2.07 ± 0.08	0.13	No
[ <sup>18</sup> F]FHBG mobile phase	2.18 ± 0.07	2.16 ± 0.04	0.29	No
50mM NH <sub>4</sub> OAc	2.07 ± 0.08	2.03 ± 0.06	0.19	No
100mM NH <sub>4</sub> OAc	2.06 ± 0.08	2.00 ± 0.00	0.06	No
250mM NH <sub>4</sub> OAc	2.03 ± 0.06	1.98 ± 0.07	0.13	No
500mM NH <sub>4</sub> OAc	2.04 ± 0.06	1.90 ± 0.08	0.01	Yes
750mM NH <sub>4</sub> OAc	2.05 ± 0.06	1.86 ± 0.03	0.00	Yes
10% EtOH v/v	2.31 ± 0.09	2.32 ± 0.23	0.45	No
20% EtOH v/v	2.61 ± 0.25	2.47 ± 0.21	0.19	No
10% MeCN v/v	2.29 ± 0.09	2.26 ± 0.12	0.48	No
20% MeCN v/v	2.53 ± 0.19	2.38 ± 0.04	0.38	No
30% MeCN v/v	2.63 ± 0.25	2.68 ± 0.06	0.49	No
40% MeCN v/v	3.13 ± 0.14	2.98 ± 0.16	0.42	No

### 2.3.5 Sample recovery

After recovery of the concentrated sample, additional rinse steps are used to recover residual amounts of the sample. However, because rinse steps have the undesirable effect of increasing the final collected volume, we experimentally studied the effect of rinsing so the number of rinse steps could be optimized. Using samples containing [<sup>18</sup>F]fluoride, the amount of radioactivity recovered in the initially ejected plug and five subsequent rinse plugs is plotted in Figure 2-18.

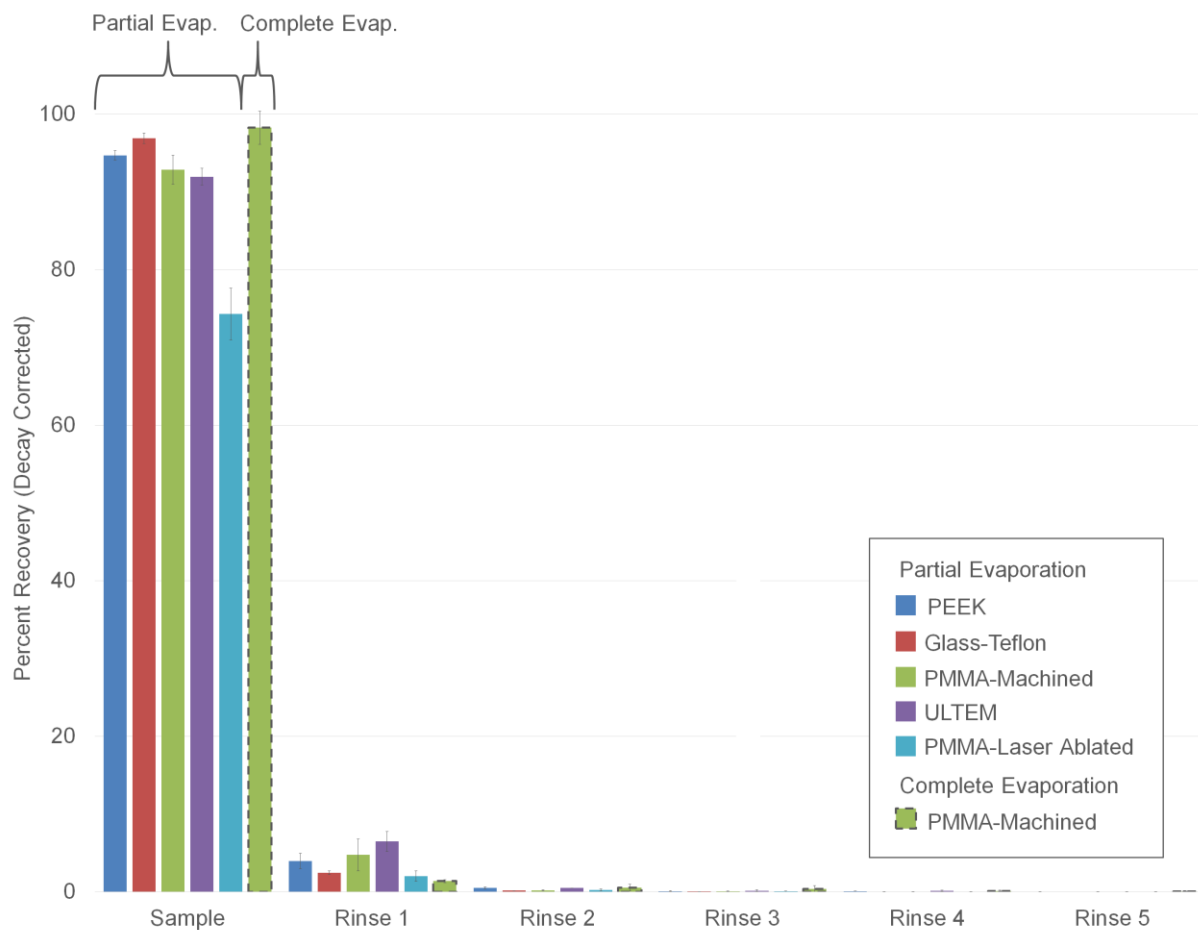


**Figure 2-18: Sample recovery measurements using [18F]fluoride solutions**  
 Results are shown for different sample layer materials. All data is for the partial evaporation method of operation, except PMMA-machined, for which both partial and complete evaporation modes were tested. Each data point represents n=3 repeats with error bars denoting standard deviation.

For the majority of materials used as sample layers (glass-PTFE, Ultem, PEEK, PMMA-machined), 92-97% of [<sup>18</sup>F]fluoride is recovered from the initial ejection. Following the initial ejection with two sample rinses increases [<sup>18</sup>F]fluoride recovery for all materials (>97%). Subsequent rinses recover negligible amounts of activity.

On the other hand, using PMMA-ablated, recovery following two rinses was poor ( $74 \pm 3\%$ ,  $n=3$ ). Since PMMA fabricated by CNC machining exhibited excellent recovery, this result is most likely explained by either higher surface roughness of the laser ablated surface (Section 2.2.14), or chemical modifications during laser ablation. Laser ablated PMMA was therefore not used in further experiments. In practice, it is likely that sample layers would be manufactured via injection molding and should be immune to this issue.

Sample recovery performance was also tested for cases where the system was operated in complete evaporation mode (Figure 2-18). A proof-of-concept experiment using PMMA-machined sample layer showed  $98 \pm 2\%$  ( $n=3$ ) recovery with the initial ejection and  $100 \pm 2\%$  ( $n=3$ ) recovery with two additional rinses.

### **2.3.6 In-chip measurements of breakthrough**

Sample recovery experiments also provided a way to measure BTP *in situ*. As described above, measurements of contact angle or BTP using the test rig had limitations at high temperatures and could not make measurements at all  $>80^\circ\text{C}$ . Loss due to breakthrough was monitored using 10 mL samples of different solvent compositions containing 0.6mM  $\text{K}_{2.2.2}$  and 0.3mM  $\text{K}_2\text{HCO}_3$  spiked with  $\sim 5\text{-}10 \mu\text{L}$  of a solution containing [<sup>18</sup>F]fluoride ( $\sim 18 \text{ MBq}$  [ $0.5 \text{ mCi}$ ]). Results are summarized in Figure 2-19.

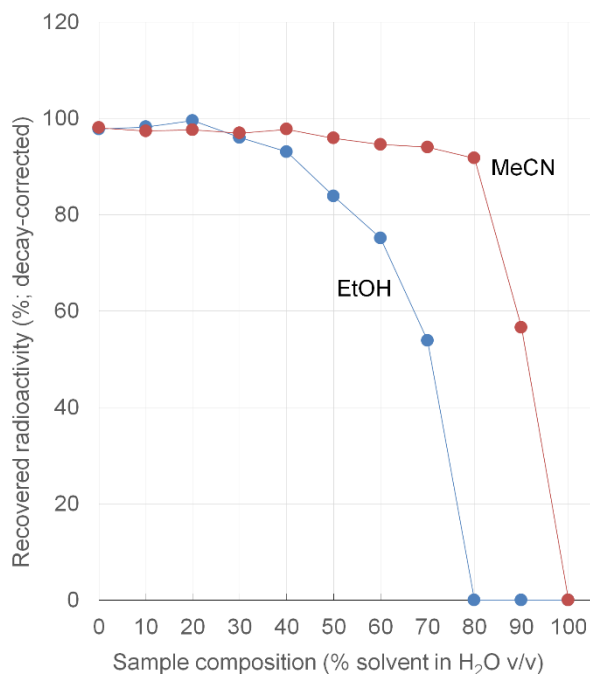


**Figure 2-19: In-chip measurement of the effects of sample breakthrough**

Sample recovery measurements using [<sup>18</sup>F]fluoride solutions were performed in-chip. The data indicate minimal loss of solute for mobile phases containing up to 80% MeCN v/v, or up to 40% EtOH v/v.

We found that concentrations of MeCN up to 40% can be concentrated at 100°C with almost no sample loss, and only minor loss (<6%) when MeCN content is 40-80%. EtOH compositions up to 20% showed no apparent activity loss, and solutions with 30-40% EtOH showed minor (<7%) loss. Interestingly, the loss is not a binary effect, i.e. zero loss below breakthrough and 100% loss above breakthrough. This may be explained by slight non-uniformity in the membrane (e.g. where some regions have slightly larger pore size, with lower BTP), or by the pressure gradients in the system (i.e. such that BTP is exceeded only near the sample outlet, where the pressure across the membrane is greatest). In either case, breakthrough may only occur over a small fraction of the membrane area, limiting its effect. Since losses of 6-7% would be considered acceptable, we can conclude that mobile phases with up to 80% MeCN in water (v/v), or up to 40% EtOH in water (v/v) can be concentrated with

the chip at all temperatures up to 100°C. This range is sufficient to cover *all* HPLC mobile phases used in the purification of PET tracers.

## **2.3.7 Concentration of PET tracers**

### **2.3.7.1 Partial Evaporation Method**

As a demonstration, batches of four PET tracers ( $[^{18}\text{F}]\text{D-FAC}$ ,  $[^{18}\text{F}]\text{FHBG}$ ,  $[^{18}\text{F}]\text{Fallypride}$  and  $[^{18}\text{F}]\text{FEAU}$ ) as well as a prosthetic group for peptide and protein labeling ( $[^{18}\text{F}]\text{FBEM}$ ) were concentrated with the system. Initially, the partial evaporation method (100°C, plus 2 rinse steps) was explored (Figure 2-20).  $[^{18}\text{F}]\text{D-FAC}$  was concentrated with recovery >96% for all chip materials. Concentration of  $[^{18}\text{F}]\text{FHBG}$  using PEEK, Ultem and glass-Teflon exhibited >97% recovery, but recovery was significantly lower for PMMA-machined, i.e.  $86.2 \pm 0.4\%$  (n=3). Recovery of concentrated  $[^{18}\text{F}]\text{Fallypride}$  was  $94.2 \pm 4.6\%$  (n=4) with the Ultem chip, slightly lower ( $91.7 \pm 2.2\%$ , n=4) for the PMMA-machined chip, and only 83.1% (n=1) for the glass-Teflon chip. (PEEK was not tested.) For  $[^{18}\text{F}]\text{FEAU}$ , recovery in the Ultem chip was  $97.1 \pm 1.9\%$  (n=2). Slightly lower recovery was seen in the PMMA-machined chip ( $91.1 \pm 0.2\%$ , n=3) and glass-Teflon chips ( $91.8 \pm 1.7\%$ , n =2), and significantly worse performance was observed for PEEK ( $87.8 \pm 4.0\%$ , n=2). After concentration, the prosthetic group  $[^{18}\text{F}]\text{FBEM}$  was recovered with  $91.2 \pm 1.2\%$  (n=3) recovery in the glass-PTFE chip. The PEEK and Ultem materials produced slightly lower recovery rates of  $84.5 \pm 5.3\%$  and  $88.4 \pm 2.0\%$ , respectively, and PMMA-machined performed the worst (recovery of  $79.0 \pm 2.9\%$ , n=3). Partial evaporation could be completed at a rate of ~2 mL/min (depending on conditions) plus a 4.0 min “overhead” for sample loading and final rinse steps.

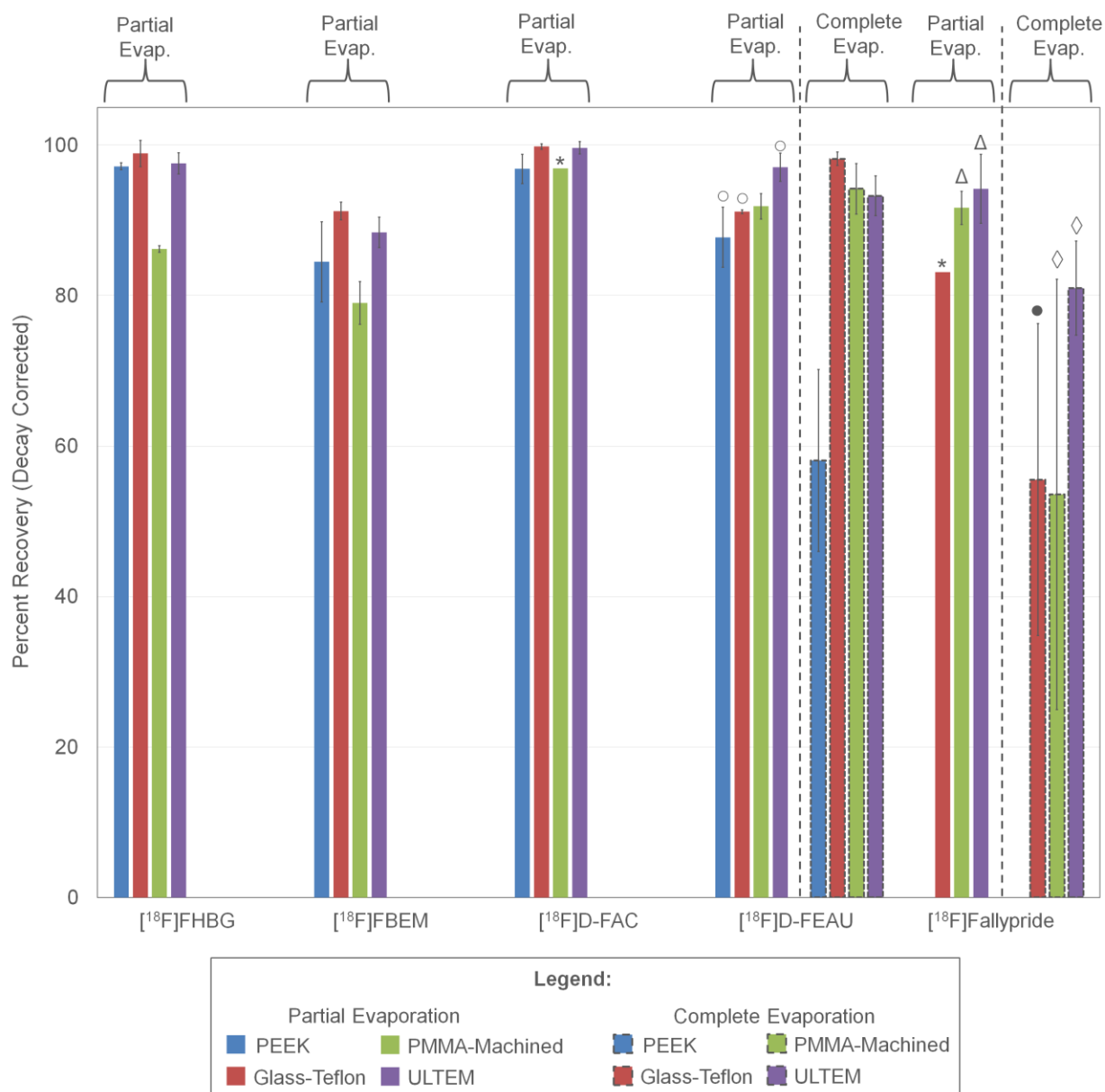


**Figure 2-20: Percent recovery of different tracers on different sample layer materials concentrated with both partial and complete evaporation modes**

Unless otherwise stated, each bar represents three repeats. (\*) represents one repeat, (o) represents two repeats, (Δ) represents four repeats, (●) represents six repeats and (◇) represents nine repeats. Error bars represent standard deviation.

In post-experiment analysis, residual radioactivity was found to be localized on the sample layer (rather than on the Teflon membrane) suggesting adverse tracer interaction is with the sample layer surface. Considering that the layers were fabricated using the same milling method resulting in similar surface finish, we hypothesize that loss of the tracer is due to chemical interaction with the surface rather than due to mechanical trapping on rough surfaces.

Even at the 100°C operating temperature, radio-HPLC analysis of tracers showed no significant difference in purity before and after concentration (see Section 2.2.8) suggesting that tracers are stable under these conditions. Since high sample recovery was observed in all cases for one or more chip materials, we can also assume the tracers do not have significant volatility at 100°C.

We next examined the degree of organic solvent removal during the concentration process. Since MeCN and EtOH are significantly more volatile than water (MeCN bp=82°C; EtOH bp= 78.37°C), we suspected that these solvents would be preferentially lost compared to water. Figure 2-21 summarizes GC-MS measurements of the remaining organic solvent content after the concentration process as a function of starting solvent composition, evaporation temperature, and starting volume. Surprisingly, the starting sample volume (and hence total time to perform concentration process) has very minor effect on the final composition. We suspect the system rapidly reaches an “equilibrium” where the majority of the chip is filled with water (due to preferential removal of solvent), a small portion at the inlet is filled with the incoming sample solution, and a concentration gradient exists in between.

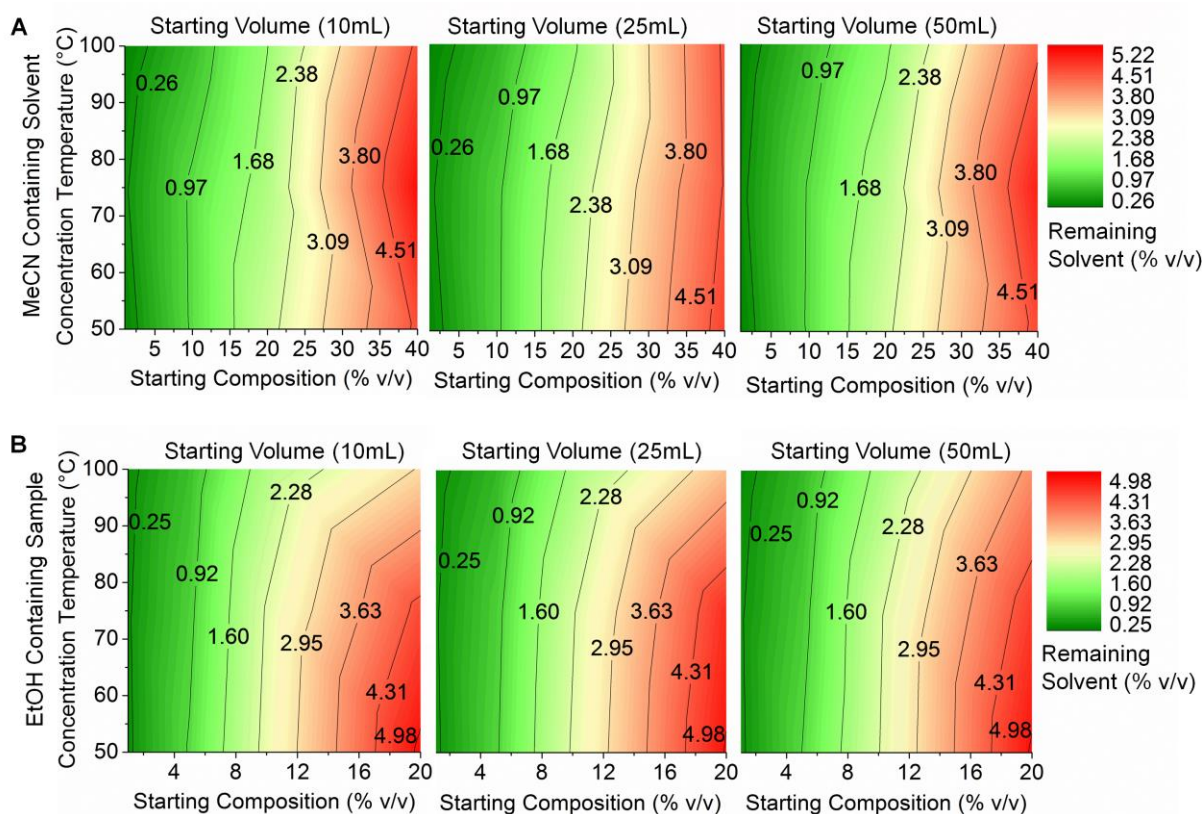


**Figure 2-21: Contour plots of % residual solvent after concentration by partial evaporation** Concentration was performed with MeCN/water mixtures (A) and EtOH/water mixtures (B).

Attainment of such a steady-state concentration gradient in the chip is consistent with the results of the 50 mL evaporation experiments described above that showed no change in evaporation rate throughout the concentration process. Temperature had a small effect on final solvent composition, with higher temperature resulting in lower final solvent amount. The starting composition had the dominant effect on the final composition after concentration. The concentration procedure seems to reduce the initial organic solvent fraction roughly 10x for MeCN mixtures and roughly 5x for EtOH mixtures. Since the allowable injection limit for EtOH is 10% v/v [68], adequate EtOH removal will occur after concentration of samples with mobile phase composition up to 50% v/v EtOH; thus the chip effectively performs formulation in addition to concentration. This encompasses the full range of EtOH-based mobile phases

compatible with the chip. On the other hand, the allowed injection limit of MeCN is much lower (410 ppm or 0.041% v/v [69]). Since typical HPLC mobile phases contain > 0.41% MeCN, the amount of residual MeCN will be too high for injection and an additional formulation process will be needed.

### **2.3.7.2 Complete evaporation method**

One way that the composition of MeCN could be reduced more than 10x would be to extend the “delay time”, i.e. the additional evaporation time after the volume has already shrunk to the chip volume. Though we did not investigate the relationship between delay time and residual solvent amount, we studied the extreme case where the mobile phase is completely evaporated, leaving only a dry residue of the PET tracer.

To assess the ability to recover the tracer residue in an injectable solution such as saline, complete evaporation and recovery was characterized for two tracers (Figure 2-20). In the case of [<sup>18</sup>F]Fallypride, the best recovery was achieved with the Ultem chip ( $81.0 \pm 6.3\%$ , n=9). Recoveries in PMMA-machined and glass-PTFE were only  $53.6 \pm 28.6\%$  (n=9) and  $55.5 \pm 20.7\%$  (n=6), respectively.

The low recovery and large variation suggests an adverse reaction of the tracer with the sample layer for these materials. For [<sup>18</sup>F]D-FEAU, PMMA-machined, glass-PTFE, and Ultem all yielded high recovery (>93%) with glass-PTFE being the best ( $98.2 \pm 0.9\%$ , n=3). Recovery with PEEK was significantly worse and exhibited high variability ( $58.1 \pm 12.1\%$ , n=3), suggesting an adverse interaction. Since the performance appears to be tracer-specific, the ability to easily switch the sample layer material to suit the tracer is a major advantage of the chip design. Complete evaporation could be completed at a rate of ~2 mL/min (depending on conditions) plus a 9.0 min “overhead” for sample loading, drying of solvent, collection of solute, and final rinse steps.

For 3 samples of [<sup>18</sup>F]D-FEAU concentrated via the complete evaporation method, the residual MeCN concentrations in the first rinse measured via GC-MS were 700, 185, 87 ppm. Since, during operation, the initial rinse will be followed by two subsequent rinses, the final MeCN composition is therefore well below the allowed injection limit. As further assessment of tracer safety and stability, a [<sup>18</sup>F]D-FAC sample was injected into mice immediately after concentration via the partial evaporation method.

No adverse reactions were observed in mice and the biodistribution was very similar to that from [<sup>18</sup>F]D-FAC injection obtained via conventional concentration and formulation with rotary evaporation (see Section 2.2.16). Furthermore, the biodistribution is similar to literature reports, showing the expected high uptake in immune-related organs such as the thymus, bone/bone marrow, and spleen. [91]

In addition to solvents in the mobile phase itself, the purified HPLC fraction can also contain small amounts of the reaction solvent and it is important to consider whether these can be adequately removed, especially high-boiling (bp = 189°C) solvents such as DMSO. To answer this question, we first measured the evaporation rate of pure DMSO in the device at 100°C with the PEEK sample layer and found it to be  $0.87 \pm 0.03$  mL/min (n = 5). This relatively fast rate suggested that adequate DMSO removal should be possible in a reasonable time. Next, we measured residual DMSO content after performing microfluidic concentration. A 10 mL solution of DMSO (10,000 PPM in water) was concentrated using the complete evaporation method at 100°C using different delay times (270, 600, 870s) and then recovered with a water rinse. The normal delay time for complete evaporation (270s) resulted in a DMSO content of 1,400 PPM. Increased delay times of 600 and 870s resulted in remaining DMSO content of 800 PPM and 700 PPM, respectively. Operation at all delay times resulted in final compositions less than the injectable limit of 5000 PPM. Of course, the amount of solvent present in the purified

fraction will depend on details of the purification protocol so measurements of residual solvents during synthesis optimization are recommended.

## 2.4 Conclusion

We have developed, optimized, and automated a compact microfluidic device to concentrate and formulate various types of radiolabeled molecules such as PET tracers as well as prosthetic groups used to convert fragile biological molecules into PET tracers. It is especially useful for tracers intended for preclinical or *in vitro* applications where the needed radioactivity concentration is high [92] but the total amount of radioactivity needed is low. The system, however, could also be used to perform formulation in clinical applications.

The system can readily be integrated with upstream (e.g. purification) and downstream (e.g. sterile filtration) processes via tubing connections, and operation is fully automated, ensuring straightforward operation and minimal operator exposure to radiation. The entire concentration and collection of a 10mL starting sample at 100°C can be completed in under 9 min for partial evaporation and under 14 min for complete evaporation. The small physical footprint of the complete system allows for relatively compact and lightweight shielding, or frees up valuable space inside existing radiation-shielded hot cells that would otherwise be needed for concentration and formulation systems. This microfluidic approach is ideally suited for integration with either conventional radiosynthesizers lacking integrated or automated formulation systems, or for use in conjunction with emerging compact microscale radiosynthesizers. [48,93] Since the vast majority of conventional synthesizers are focused on clinical production and do not include a means to concentrate the final tracer, this microfluidic concentration system could be used to extend their functionality to the production of tracers for preclinical imaging.

Improvements in design resulted in significant performance increase compared to our previous proof-of-concept. [72] Depending on the architecture of the chip, evaporation rates of up to 3.4 mL/min for water were observed at 100°C operating temperature. By using a serpentine channel with rounded corners, the system is able to achieve high tracer recovery (>97%) with the use of two rinse plugs, resulting in a total sample volume after concentration of ~1.0-1.5 mL. The range of compatible solvents was also greatly expanded. At 100°C operating temperature, the system can handle samples with up to 80% (v/v) MeCN in H<sub>2</sub>O, and up to 40% (v/v) EtOH in H<sub>2</sub>O without significant loss of the sample. While these limits include the majority of mobile phases used in the production of PET tracers [14,55,94–97], these limits of organic solvent content could likely be further extended if needed, by decreasing operating temperatures (at the expense of evaporation rate) or by seeking membrane with even smaller pore dimensions.

In partial evaporation mode, the amount of EtOH can be adequately reduced to safely allow direct injection after concentration (for mobile phases containing up to 50% EtOH v/v). To directly use samples containing MeCN, the complete evaporation method must be used to ensure the residual MeCN is below the allowed limit. Concentration to dryness could also be used if the mobile phase contained other toxic solvents that needed to be removed, such as DMSO. This ability to perform formulation at the same time as concentration significantly streamlines the overall PET tracer production process.

The ability to customize sample layer material was valuable for ensuring the highest possible performance. Several tracers exhibited significant (20-50%) losses when partnered with an unsuitable chip material, presumably due to adsorption or other adverse interactions. Future investigation of materials with high thermal conductivity that are inert (or with protective

inert coating) may provide a way to achieve the highest possible evaporation speed combined with high sample recovery.

## 3 Chapter 3: Concentration of [ $^{18}\text{F}$ ]fluoride

### 3.1 Introduction

As mentioned in Chapter 1, there has recently been considerable interest in the development of microscale technologies for the synthesis of the short-lived radiolabeled tracers that must be injected prior to a PET scan. [93] Some microscale approaches can reduce required radiation shielding and reagent costs, compared to macroscale approaches, and could make it practical and affordable to produce small batches of diverse PET tracers on demand. Although there has been significant progress in “flow-through” type microreactors for microscale radiosynthesis, including demonstration of a wide range of tracers [98] and clinical use of tracers produced by this approach [99], there are considerable advantages of using microscale “batch” reactors. [48] For example, reaction volume can be significantly smaller (e.g.  $\leq 50 \mu\text{L}$ ), reducing reagent related expenses. In addition, for microfluidic chips that do not require large supporting pumps and valves, the overall system size can be much more compact, and potentially the system can be shielded and operated on a benchtop without the need for a conventional radiochemistry hot cell. An added advantage of low reaction volume is an improvement in molar activity of the synthesized PET tracer compared to macroscale methods [47,63]; high molar activity is critical for imaging of scarce biological targets (e.g. neuroreceptors).

However, a challenge is that the radionuclide is typically produced/supplied in a volume much greater than these microreactors. For example, [ $^{18}\text{F}$ ]fluoride is typically produced in amounts of 10s of GBq or higher as a dilute solution in  $\sim 1\text{-}5 \text{ mL}$  of [ $^{18}\text{O}$ ]H<sub>2</sub>O. At a typical concentration of about 37 GBq/mL [1.0 Ci/mL], it would be necessary to load 40-80  $\mu\text{L}$  of the radionuclide solution at the start of synthesis to produce a single patient dose ( $\sim 370\text{-}740 \text{ MBq}$  [10-20 mCi] [100]), assuming an overall decay-corrected yield of  $\sim 50\%$  and synthesis time of 1

half-life. To produce enough tracer for multiple human doses, or to produce enough for long-distance transport to the imaging site, especially when working with low-yield reactions, would require even more activity (and volume) to be loaded. To ensure sufficient activity can be loaded into the microreactor, the radionuclide therefore needs to be concentrated before use. If a sufficient degree of concentration can be achieved, the entire batch of radionuclide could be used for the microscale synthesis, rather than the highly undesirable situation of using e.g. 10  $\mu\text{L}$  and discarding the remaining 99% of a 1 mL target bombardment.

Concentration of [ $^{18}\text{F}$ ]fluoride can also be useful to reduce water content in conventional macroscale radiosynthesizers. For nucleophilic fluorination reactions, the presence of water severely reduces the reactivity of [ $^{18}\text{F}$ ]fluoride [101,102], and thus water must be removed prior to fluorination, typically through a multi-step azeotropic drying process. Concentration of [ $^{18}\text{F}$ ]fluoride to a few microliters can substantially reduce water content and facilitate a reactive [ $^{18}\text{F}$ ]fluoride without the need for azeotropic drying. For example, concentration down to 5  $\mu\text{L}$  would result in <0.5% (v/v) water content if added to a reactor containing 1 mL of precursor solution in organic solvent. The base content can also be reduced. This approach has been used to increase the yield and simplify the preparation of human doses of [ $^{18}\text{F}$ ]5-Fluorouracil ([ $^{18}\text{F}$ ]5-FU). [100] This method can be considered an alternative to other approaches that have previously been reported for reducing water and/or base content for macroscale reactions. For example, Lemaire *et al.* [101] demonstrated nearly quantitative elution of [ $^{18}\text{F}$ ]fluoride from a conventional QMA cartridge with a solution containing organic base in MeCN with either a small amount of alcohol or water (0.2-2.5%). The eluate was directly used in fluorination reactions and resulted in high yields without the need for azeotropic drying. Iwata *et al.* [103,104] demonstrated efficient elution of [ $^{18}\text{F}$ ]fluoride from a conventional QMA cartridge with anhydrous MeOH containing a minimal amount of phase transfer catalyst and base. The amounts could be

even further reduced by the flowing through a downstream cation exchange cartridge. This reduction of phase transfer catalyst and base combined with removing the need for azeotropic drying allowed for improved fluorination yields across various model PET tracers. Finally, Richarz *et al.* [105] presented a method wherein water, base, and phase transfer catalyst could be eliminated altogether by eluting the  $[^{18}\text{F}]$ fluoride directly from a conventional QMA cartridge using a charged precursor in anhydrous MeOH. The MeOH could then be evaporated and replaced with a more suitable solvent (e.g. DMSO, DMF) for efficient fluorination.

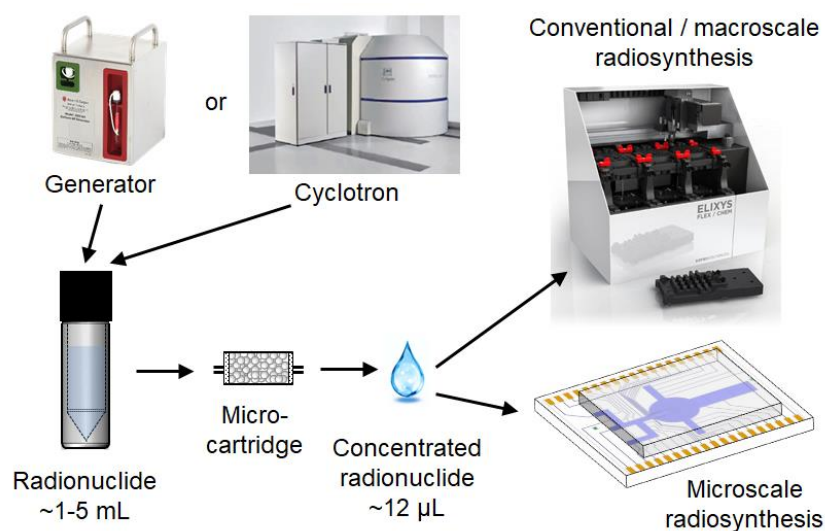


**Figure 3-1: Concept image illustrating the role of radionuclide concentration**

A batch of radionuclide produced either by a generator or a cyclotron is rapidly concentrated from 1-5mL to ~12  $\mu\text{L}$  and can be used in either microscale or macroscale synthesis.

Due to the importance of concentrating  $[^{18}\text{F}]$ fluoride (Figure 3-1), several groups, including ours, have reported methods to perform the concentration step. In one approach, water was removed by evaporation: a 200  $\mu\text{L}$  open droplet of  $[^{18}\text{F}]$ fluoride in  $[^{18}\text{O}]\text{H}_2\text{O}$  on an electrowetting-on-dielectric (EWOD) microfluidic chip was concentrated down to 5  $\mu\text{L}$  in 10 min by heating the substrate. [50] Once the droplet volume had been reduced, electrodes were activated to draw the droplet under the cover plate onto the EWOD transport pathways.

Radioactivity loss during the concentration process, qualitatively visualized through Cerenkov imaging, proved to be negligible. This straightforward approach is suitable for modest starting volumes, but may require impractically large chip real estate, or take too much time for sequential 200  $\mu\text{L}$  evaporations to handle volumes in the 1-5 mL range that are expected from most cyclotrons. Another approach is to use miniature anion exchange cartridges to trap  $[^{18}\text{F}]\text{fluoride}$  from the large volume of  $[^{18}\text{O}]\text{H}_2\text{O}$  and to then recover this  $[^{18}\text{F}]\text{fluoride}$  in smaller volumes ranging from 5 - 500  $\mu\text{L}$ . [45,65,106,107] Elizarov *et al.* demonstrated concentration of 32.4 GBq [876 mCi] of  $[^{18}\text{F}]\text{fluoride}$  with a starting volume of 2 mL to a final volume of 5  $\mu\text{L}$  within a custom-built micro cartridge with 2  $\mu\text{L}$  bed volume filled with AG-1-X8 QMA resin (Bio-Rad Laboratories, Inc., USA). [45] During the concentration process, 99.5% of the starting  $[^{18}\text{F}]\text{fluoride}$  was trapped, and 92.7% of the trapped activity was recovered during elution of the  $[^{18}\text{F}]\text{fluoride}$  off of the cartridge (n=1). Flow rates used during concentration were 2 mL/min allowing for complete concentration in  $\sim 3$  min. Lebedev *et al.* demonstrated concentration of  $[^{18}\text{F}]\text{fluoride}$  (up to 110GBq [3 Ci]) in 2 mL of  $[^{18}\text{O}]\text{H}_2\text{O}$  to a final volume of 45  $\mu\text{L}$  within a commercial micro-cartridge (OptiLynx, Optimize Technologies, Inc., USA; 5  $\mu\text{L}$  bed volume) packed with the same resin. [65] Trapping and release of various  $[^{18}\text{F}]\text{fluoride}$  amounts resulted in  $\sim 95\%$  recovery of the starting amount. Concentration was performed in  $\sim 3$  min. De Leonardi *et al.* loaded anion exchange resin (Chromabond PS-HCO<sub>3</sub>, ABX, Germany) into a microfluidic channel and demonstrated concentration of 5-7 GBq [140-190 mCi] samples of  $[^{18}\text{F}]\text{fluoride}$  in 4 mL  $[^{18}\text{O}]\text{H}_2\text{O}$ . [106] Trapping efficiency was  $>90\%$  and  $\geq 95\%$  of the trapped activity could be eluted in 250  $\mu\text{L}$  with a total processing time of 6 min. Ismail *et al.* demonstrated the use of a functionalized porous polymer monolith (polystyrene imidazolium chloride) instead of packed resin beads. [108] Trapping of  $[^{18}\text{F}]\text{fluoride}$  solutions (1.5-7.4 MBq [40-200  $\mu\text{Ci}$ ]) at a flow rate up to 250  $\mu\text{L}/\text{min}$  had an efficiency of  $97 \pm 4\%$  (n=39) and it was shown theoretically that higher

activities could be trapped by extending the length of the monolith. Of various eluents tested,  $\text{CaCO}_3$  performed the best, recovering  $94 \pm 6\%$  ( $n=2$ ) of the activity in a volume of 100  $\mu\text{L}$ . Recently, Salvador *et al.* demonstrated concentration of [ $^{18}\text{F}$ ]fluoride within a manually-operated custom built PDMS microfluidic system with 10-15 mg embedded QMA resin (from Sep-Pak Accell Plus cartridge, Waters, Inc., USA). [107] For activities of 19 GBq [0.5 Ci], trapping of 2 mL of [ $^{18}\text{F}$ ]fluoride in [ $^{18}\text{O}$ ]H $_2$ O was achieved with 98% efficiency; trapped activity could then be eluted into a volume of 20  $\mu\text{L}$  with >87% recovery. Trapping was performed with a flow rate of 180  $\mu\text{L}/\text{min}$ .

Concentration has also been performed using an electrochemical cell instead of anion exchange resin. Saiki *et al.* reported a microfluidic cell with 16  $\mu\text{L}$  internal volume that could trap [ $^{18}\text{F}$ ]fluoride from 1-2 mL of [ $^{18}\text{O}$ ]H $_2$ O at up to 700  $\mu\text{L}/\text{min}$  flow rate by applying a 10V potential, and then release the activity into a smaller volume of an eluent solution with an overall efficiency (deposition and release) of ~60%. [109] The release process used a total volume of 275  $\mu\text{L}$  of eluent solution, but a radiation detector showed that the majority of activity was released into the first ~60  $\mu\text{L}$  and concentration could thus be achieved using a switching valve. [110] In this chapter, we focus on the micro-cartridge approach due to its fast operation, high efficiency, commercial availability of components, and ability to realize very small output volumes by minimizing the bed volume of the cartridge. We have developed a standalone, fully-automated system for rapid concentration of [ $^{18}\text{F}$ ]fluoride into microliter-scale volumes for a variety of applications. Though a previous version of this system has been used to avoid azeotropic drying in the preparation of clinical doses of [ $^{18}\text{F}$ ]5-FU [100], this is the first report of the detailed design, operation, and performance of this system. As an additional demonstration we also report new data on the use of the concentrator to reduce water content (while potentially

increasing starting activity) to perform Ni-mediated radiosynthesis of a model compound (*N*-*boc*-5-<sup>18</sup>F]fluoroindole) without azeotropic drying.

## 3.2 Materials and Methods

### 3.2.1 Reagents

Anhydrous acetonitrile (MeCN), potassium bicarbonate (KHCO<sub>3</sub>), tetrabutylammonium bromide (TBAB), 1,4,7,10,13,16-hexaoxacyclooctadecane (18-crown-6), ethyl acetate (C<sub>4</sub>H<sub>8</sub>O<sub>2</sub>), hexane (C<sub>6</sub>H<sub>14</sub>), and monobasic potassium phosphate (KH<sub>2</sub>PO<sub>4</sub>) were purchased from Sigma-Aldrich (Milwaukee, WI USA). Deionized water was obtained from a Milli-Q water purification system (EMD Millipore Corporation, Berlin, Germany). Saline (0.9% w/v) was purchased from Hospira (Lake Forest, IL, USA). 4,7,13,16,21,24-hexaoxa-1,10-diazabicyclo[8.8.8]hexacosane (Kryptofix 222; K222) was purchased from ABX (Radeberg, Germany). Sodium chloride (NaCl) was purchased from Fisher Scientific (Pittsburgh, PA, USA). [<sup>18</sup>F]fluoride in [<sup>18</sup>O]H<sub>2</sub>O was produced in a cyclotron (RDS-112, Siemens, Knoxville, TN, USA) through (p,n) reaction of [<sup>18</sup>O]H<sub>2</sub>O (98% isotopic purity, 18-98-050, Rotem Medical, Israel) at 11 MeV using a 1 mL internal volume tantalum target with Havar foil. Unless otherwise noted, all materials were used as received. A variety of different preconditioning solutions (based on KHCO<sub>3</sub>, NaCl, or KH<sub>2</sub>PO<sub>4</sub> in water) and eluent solutions (based on K<sub>2</sub>CO<sub>3</sub>/K222, TBAB, NaCl, or K<sub>3</sub>PO<sub>4</sub>/18-crown-6 in water/MeCN) were prepared for different experiments (see Table 3-4, Table 3-6, Table 3-7, and Table 3-8). The nickel aryl precursor complex and the hypervalent iodine oxidant used for the synthesis of *N*-*boc*-5-<sup>18</sup>F]fluoroindole were synthesized following the methods of Lee *et al.* [111]

### 3.2.2 Miniature anion exchange cartridge

Strong anion exchange (SAX) resin (AG-MP1; 200-400 mesh size) was sourced from Bio-Rad (Hercules, CA, USA). Quaternary ammonium (QMA)-based resin was chosen for its

lower affinity to the fluoride ion compared to other anions (e.g.  $\text{Cl}^-$ ,  $\text{HCO}_3^-$ ) allowing for easier elution of fluoride with these other anions. Resin was packed by Optimize Technologies (Oregon, OR, USA) into OPTI-LYNX micro trap cartridges (11-04755-ES, Optimize Technologies). The cartridges have a bed volume of  $\sim 4 \mu\text{L}$  and hold  $\sim 2 \text{ mg}$  of resin. The cartridge was placed in an OPTI-LYNX micro holder (Optimize Technologies) to facilitate connection to fluidic paths via standard fittings and tubing. This resin/cartridge combination was selected to due to the small bed volume, commercial availability, compatibility with standard fittings, and previous reports that high amounts of activity ( $110 \text{ GBq}$  [ $3 \text{ Ci}$ ]) could be efficiently trapped [65].

### **3.2.3 System design**

#### **3.2.3.1 Overview**

The overall concentration system has several components. One portion controls the flows for trapping the [ $^{18}\text{F}$ ]fluoride onto the micro-cartridge and later releasing it. Another part generates the low volumes of eluent solution for the release step. Finally, the third part is responsible for controlling which reagents are passing through the cartridge. Each of these components is described in detail below.

Reagents were driven either by inert gas pressure or vacuum. The inert gas was provided from an electronic pressure regulator (ITV0010-2BL, SMC Corporation, Japan) connected to a nitrogen source. Vacuum was supplied from an electronic vacuum regulator (ITV2090, SMC) connected to a central “house” vacuum ( $1.9 \text{ L/min}$ ,  $-90 \text{ kPa}$ ). A small vacuum pump could be used instead. Unless otherwise specified, liquid pathways were implemented with  $0.02''$  ID,  $1/16''$  OD ETFE tubing (1516L, IDEX).

### 3.2.3.2 Trapping and elution

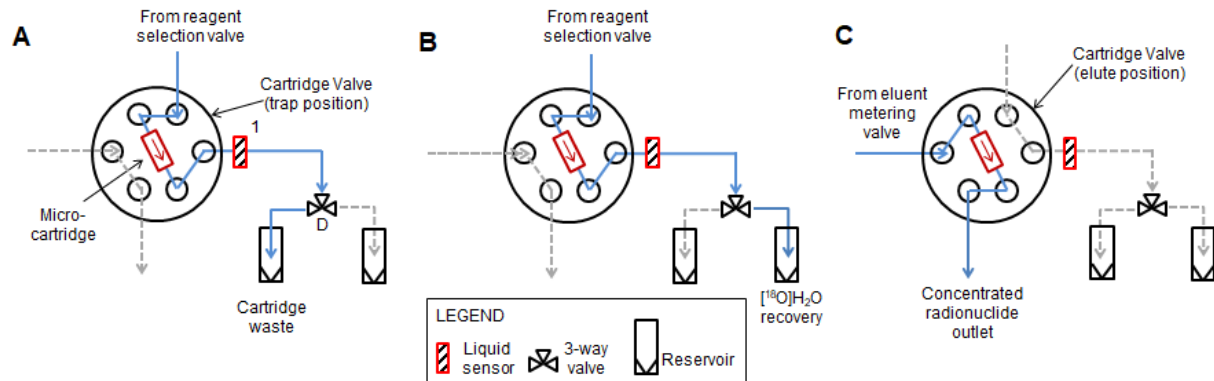


**Figure 3-2: Fluidic and pneumatic diagram for micro-cartridge and associated valve**

Configuration for (A) preconditioning the micro-cartridge, (B) trapping of [ $^{18}\text{F}$ ]fluoride on the cartridge, and (C) elution of [ $^{18}\text{F}$ ]fluoride from the cartridge.

At the core of the system, the micro-cartridge is connected to a low dead volume HPLC injection valve (“cartridge valve”, Titan HT 715-000, IDEX Health & Science) via 0.01” ID 1/16” OD PEEK tubing (Figure 3-2). In one state, the valve allows large volumes (up to several mL) of solution (i.e., preconditioning solution, [ $^{18}\text{F}$ ]fluoride/[ $^{18}\text{O}$ ]H $_2$ O, or wash solutions) from the reagent selection system (described in Section 3.2.3.4) to flow through the cartridge, and then to one of two waste outputs (“cartridge waste” or “[ $^{18}\text{O}$ ]H $_2$ O recovery”), selected by a downstream 3-way valve (D; “cartridge waste valve”; LVM105R, SMC Corporation, Japan). A liquid sensor (#1, OCB350L062Z, OPTEK Technologies, Carrollton, TX, USA) was positioned at this output to enable automatic determination of when a reagent had entirely passed through the cartridge.

After trapping [ $^{18}\text{F}$ ]fluoride and drying the micro-cartridge, the cartridge valve is switched to its other state, allowing a small volume of eluent solution to efficiently flow through the cartridge to an output where the concentrated radionuclide is collected for downstream use (e.g. in a microfluidic radiosynthesis chip or macroscale reaction vessel).

### 3.2.3.3 Metering eluent solution

To measure the desired small volumes of the eluent solution, another identical rotary injection valve (“eluent metering valve”) was used in conjunction with a 6.2  $\mu\text{L}$  “loop”, consisting of a 12.25 cm length of 0.01” ID 1/16” OD PEEK tubing (1531, IDEX). Note that this loop size was the minimum length of tubing that could reliably be connected into the eluent metering valve. The position of the eluent loop is shown in Figure 3-3.

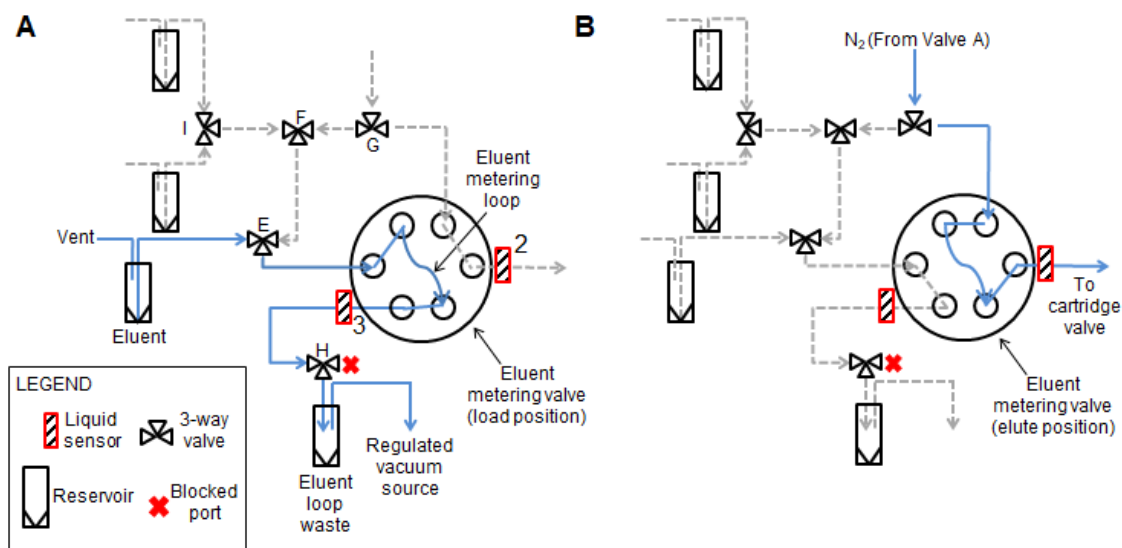


**Figure 3-3: Fluidic and pneumatic diagram for the eluent metering subsystem**

Configuration for (A) metering of eluent solution, and (B) elution of [ $^{18}\text{F}$ ]fluoride to the micro-cartridge.

The eluent solution was pre-loaded in a septum-capped glass V-vial (3 mL, W986277NG, Wheaton, Millville, NJ, USA) with a hole punched through the septum for a dip tube, and a #23 needle (BD 305145, BD Scientific, Sparks, MD, USA) inserted to provide a vent to atmosphere. Eluent washing solutions (MeCN and DI water) were each pre-loaded in plastic centrifuge tubes (50 mL Falcon conical tube; Corning Inc., Corning, NY, USA) with two holes drilled in each cap (one for a dip tube and one acting as a vent). Reagents were connected to the eluent metering valves as shown in Figure 3-3.

In one state of the valve, fluids (i.e. either eluent solution to fill the loop, or wash solution to clean the loop) flow through the loop and out to an “eluent waste vial” (60942A40, Kimble Chase, Vineland, NJ, USA) via a 3-way “eluent waste valve” (H; LVM105R, SMC Corporation, Japan). Reagents were driven with vacuum by connecting the headspace of the eluent waste vial to a regulated vacuum source. Additional 3-way valves (I, E, F, G; LVM105R, SMC Corporation, Japan) are used to select which input reagent flows through the loop (i.e. eluent solution or eluent washing solutions: MeCN or DI water). A liquid sensor (#3; OCB350L062Z, OPTEK Technologies, Carrollton, TX, USA) was positioned at the eluent waste output of the eluent metering valve to determine when the loop had been completely filled.

In the other position of the rotary valve, the metered plug of eluent solution in the loop is driven by inert gas toward the cartridge valve via a ~3 cm segment of 0.02” ID 1/16” OD PFA HP plus tubing (1902L, IDEX). A liquid sensor (#2; OCB350L062Z, OPTEK Technologies, Carrollton, TX, USA) was positioned half way along this tubing segment to monitor the passage of the metered eluent plug toward the cartridge valve.

#### **3.2.3.4 Reagent delivery**

During operation, several different reagents (e.g. cartridge preconditioning solution, preconditioning wash solution (DI water), [ $^{18}\text{F}$ ]fluoride/[ $^{18}\text{O}$ ]H<sub>2</sub>O, and rinse solution (MeCN)) must be flowed through the micro-cartridge connected to the cartridge valve. Selection of the reagent is controlled via a 7-port, 6-position rotary stream selection valve (“reagent selection valve”; Titan HT 715-105, IDEX). This type of valve connects any one of its 6 inlets to a common outlet.

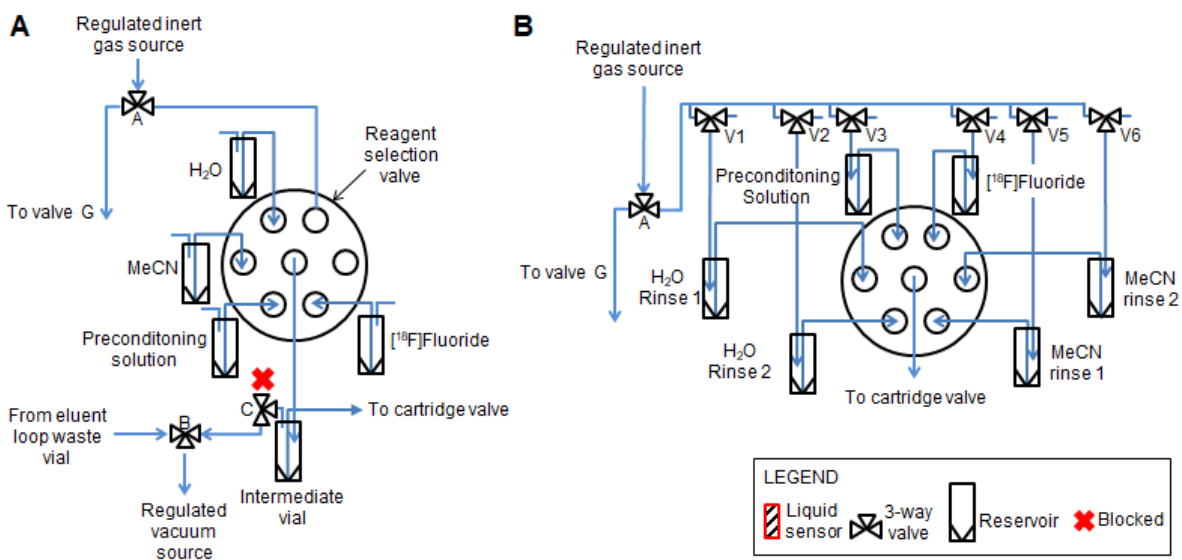


**Figure 3-4: Fluidic and pneumatic diagram for the reagent delivery subsystem**

The diagrams for the intermediate vial system are shown in (A) and for the direct loading system in (B).

Two generations of prototype systems were built during this study with slightly different methods of measuring and delivering the solutions. In the “intermediate” vial system (Figure 3-4A), each reagent was delivered by first filling the desired amount of the reagent from a larger reservoir into an intermediate vial using vacuum, and then pushing this volume out of the vial to the inlet of the cartridge valve (and through the micro-cartridge). In this system, the output of the reagent selection valve was connected via 1/16” OD PEEK tubing to the headspace of a septum-capped 3 mL glass V-vial (03-410-036, Wheaton). The headspace of this intermediate vial was connected to a regulated vacuum source via the “intermediate vial vent valve” (C; LVM105R, SMC Corporation, Japan). Opening this valve for a specified time (at specified vacuum pressure) controlled the amount of the currently selected reagent that was loaded into the intermediate vial. (Calibrations are described below.) This valve was then closed to allow inert gas (from the reagent selection valve) to push the contents via a dip tube toward the inlet of the cartridge valve.

[<sup>18</sup>F]fluoride solution was stored in a septum-capped glass V-vial (3mL, W986277NG, Wheaton, Millville, NJ, USA) and connected to an input of the reagent selection valve via a dip tube made of 0.01" ID 1/16" OD PEEK tubing (1532, IDEX). A #23 needle was inserted as a vent port. Other reagents were stored in capped plastic centrifuge tubes (50 mL; Falcon conical tube; Corning Inc., Corning, NY, USA) and connected via dip tubes made of 0.04" ID 1/16" OD ETFE tubing (1517L, IDEX). An additional small hole was drilled into each cap to serve as a vent. Another input of the reagent selection valve was connected to a regulated inert gas source via valve A (LVM105R, SMC Corporation, Japan) for driving the contents of the intermediate vial towards the cartridge valve.

The volume of reagents delivered to the intermediate vial was determined as a function of vacuum pressure and time. The volume of MeCN and DI water delivered are plotted in Figures Figure 3-5A and Figure 3-5B, respectively, as a function of vacuum pressure and flow time. Data was measured at different pressures (-1, -2, -4, -6, and -7 psig) and different flow times (5, 10, 15, and 20 s). Volumes were determined by weight measurements of the intermediate vial before and after loading, and then converting weight to volume using the known density of each fluid. Each measurement was repeated n=5 times. The transfer conditions ultimately used for each reagent during the concentration process are listed in Table 3-1.

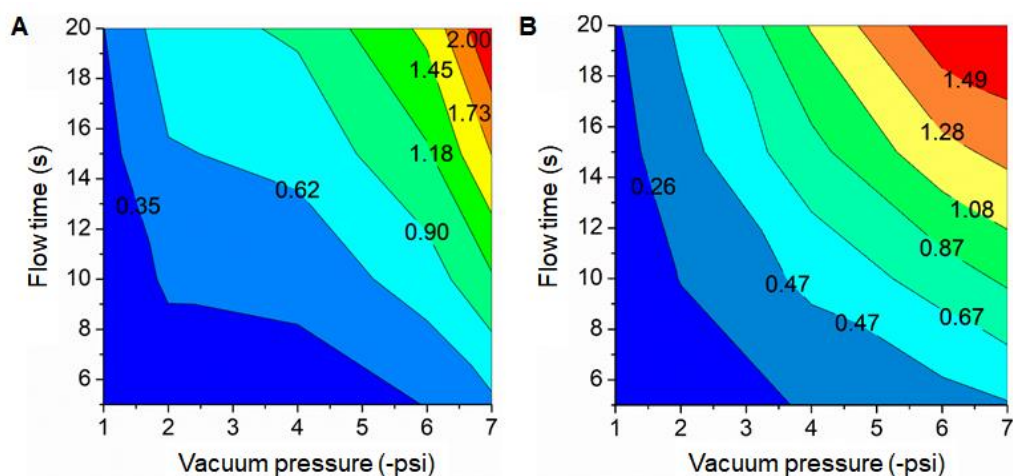


**Figure 3-5: Contour plots of volume loaded into the intermediate vial as a function of vacuum pressure and flow time for (A) MeCN and (B) DI water**

**Table 3-1: Parameters used to load the specified volumes from reagent reservoirs into the intermediate vial**

Solution	Vacuum pressure (psig)	Duration (s)	Volume loaded into intermediate vial (mL)
Pre-conditioning	-7.0	7.0	0.60
DI water	-7.0	90.0	3.0
DI water	-7.0	9.0	0.8
MeCN	-7.0	9.0	1.0
[ <sup>18</sup> F]fluoride	-7.0	11.0	0.5

In the direct loading system the output of the reagent selection valve is connected directly to the inlet of the cartridge valve via 1/16"OD PEEK tubing. We chose to operate the system such that each reagent vial contained a pre-measured amount of the reagent, but it would be possible to meter reagent volumes by performing time- or pressured-based calibrations as was done for the intermediate vial system. For reagents that are needed twice during the concentration process (i.e. DI water and MeCN), we filled two vials with the same reagent.

Reagents were stored in septum-capped glass V-vials (1 mL, W986284NG, Wheaton).  $[^{18}\text{F}]$ fluoride solution was stored in a septum-capped glass V-vial (3mL, W986277NG, Wheaton, Millville, NJ, USA) and connected to an input of the reagent selection valve via a dip tube made of 0.01" ID 1/16" OD PEEK tubing (1532, IDEX). PEEK tubing was used rather than ETFE to avoid the introduction of  $[^{19}\text{F}]$ fluoride into the system that can occur due to radiolysis of fluorine-containing materials in contact with the  $[^{18}\text{F}]$ fluoride solution. Another input of the reagent selection valve was connected to a regulated inert gas source via valve A (LVM105R, SMC Corporation, Japan).

To drive reagents, vials were each connected to an inert gas source (20 psig) via a 3-way valve (V1-V6) (S070B-5DG, SMC). The third port of each valve was vented to atmosphere. A schematic and photograph of the full system using direct loading are given in Table 3-6.

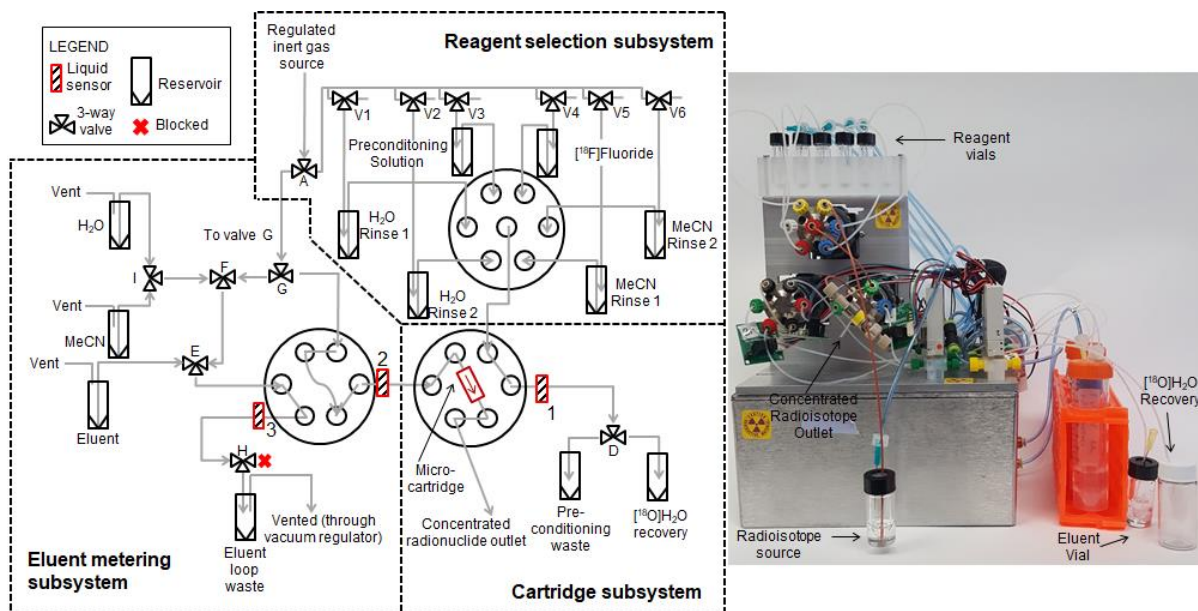


**Figure 3-6: Fluidic and pneumatic diagram for the complete direct loading system (left), and a photograph of the direct loading system (right)**

### 3.2.3.5 Control system

All electronic components were connected to a computer to enable automated operation.

The rotary injector valves and stream selection valve were controlled via valve driver boards

(8382-108 and 8382-103, respectively, IDEX). Electronic 3-way valves (A-I) were driven via a custom-built Darlington transistor array board. All of the valve drivers and pressure and vacuum regulators were controlled via a data acquisition (DAQ) module (Minilab 1008, Measurement Computing, Norton, MA, USA). A second DAQ (NI DAQ-6501, National Instruments, Austin, TX, USA) was used in the direct loading system to control (via a Darlington transistor array) the set of valves that control the reagent driving pressure. 24V and 5V power for valves, liquid sensors, and regulators were provided by a DC power supply (RD-125, Meanwell, Fremont, CA, USA).

The liquid sensors required calibration when the system was initialized (i.e. when the tubing was filled with air). The calibration pin of each sensor was thus connected to a digital output on the DAQ module (Minilab 1008) to allow the momentary grounding needed to programmatically trigger the calibration process. The analog outputs of each liquid sensor were connected to the DAQ for computer analysis. Since the reading for an empty tube was ~2.5V, and that for a liquid-filled tube was ~5.0V, the threshold of dry to wet was set at 3.3V.

All hardware was controlled by a custom written LabVIEW program (National Instruments). The complete wiring schematic for the intermediate vial and direct loading systems are shown in Figures Figure 3-7 and Figure 3-8, respectively.

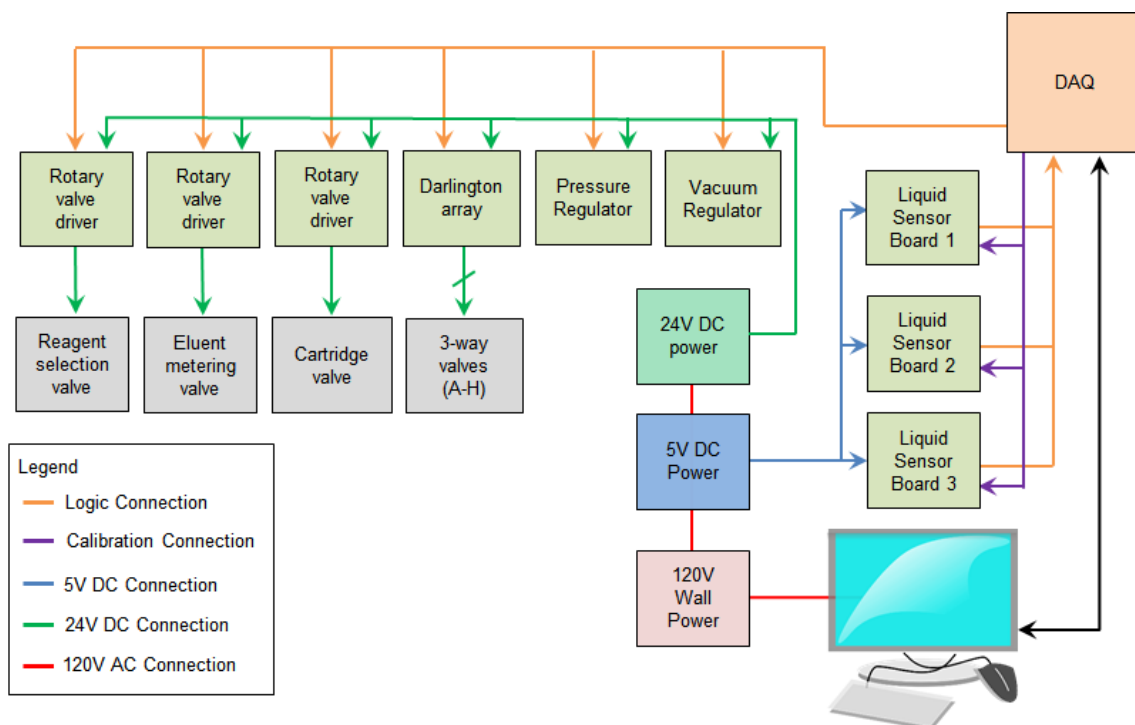


Figure 3-7: Electronic wiring diagram of the intermediate vial system of the concentrator

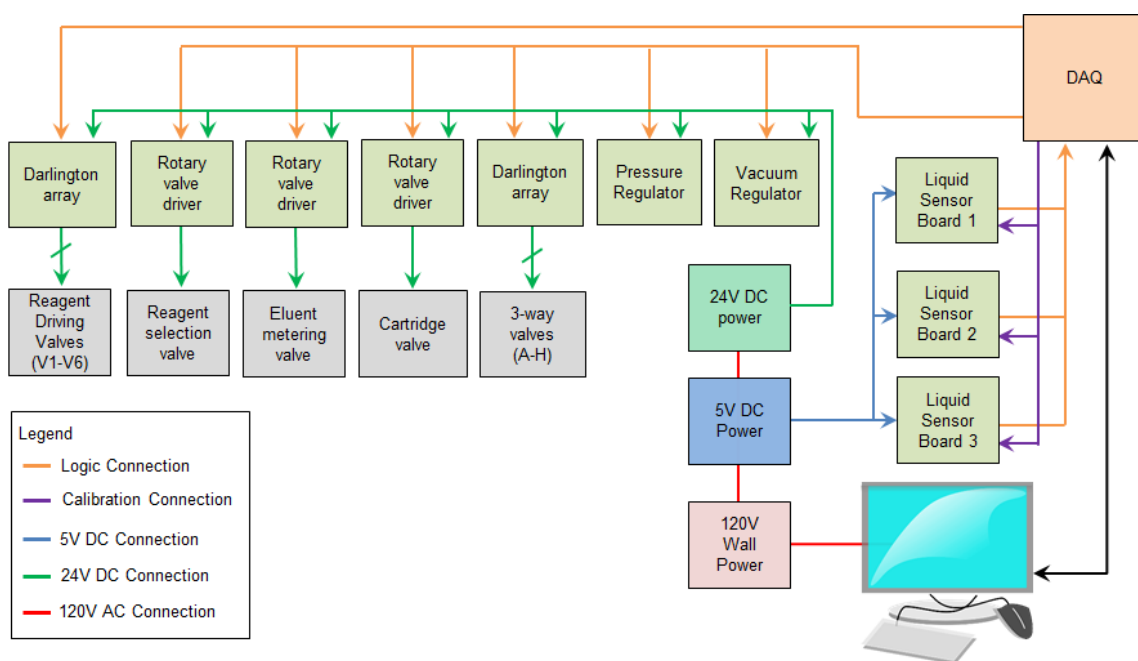
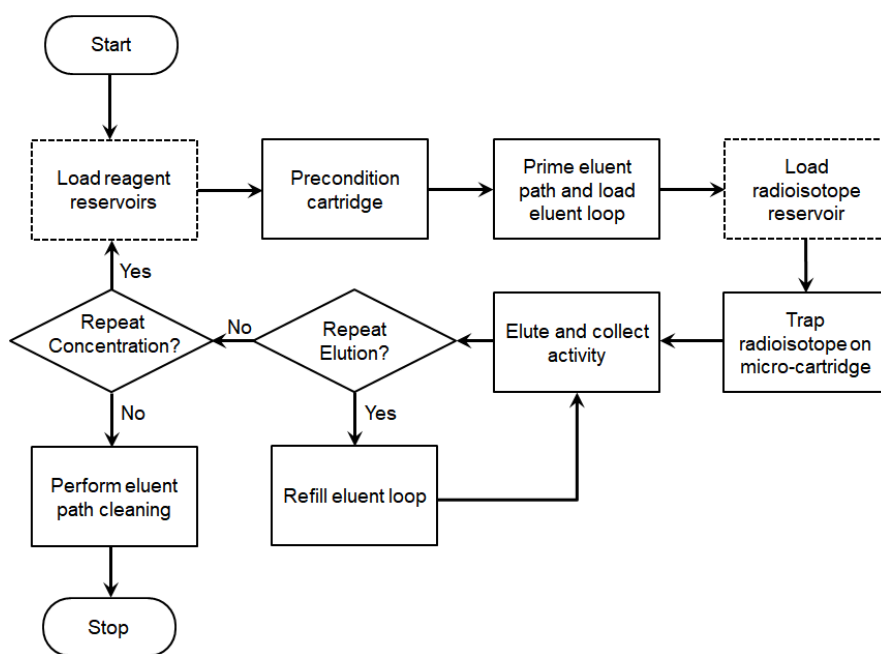


Figure 3-8: Electronic wiring diagram of the direct loading system of the concentrator

### 3.2.4 Concentration process

#### 3.2.4.1 Overview

To carry out the concentration process, first, all reagent vials are filled except for the radionuclide. The cartridge is then preconditioned and rinsed, and the eluent metering loop is filled with eluent solution. Next, the radionuclide is introduced into the system, and is trapped on the micro-cartridge. Finally, the radionuclide is recovered by flowing the contents of the eluent loop through the cartridge. Additional elution steps can be performed if desired. A flowchart representation of these steps is shown in Figure 3-9.



**Figure 3-9: Process flow for concentration of a radionuclide**

Boxes outlined with a dotted line represent steps that require manual intervention. All other steps within the process flow are automated.

#### 3.2.4.2 Setup

Before operation, all waste vials (cartridge waste, [ $^{18}\text{O}$ ]H $_2\text{O}$  recovery, and eluent loop waste) were emptied. In the intermediate vial system, reagent vials were loaded with the following volumes of reagents: DI water for precondition rinsing (40 mL), MeCN (40 mL),

preconditioning solution (10 mL), eluent solution (2 mL), MeCN for eluent metering valve (40 mL), DI water for eluent metering valve (40 mL).

In the direct loading system, the following volumes were used: preconditioning solution (1 mL), DI water for precondition rinsing (0.5 mL x 2 vials), eluent solution (2 mL), MeCN (0.5 mL x 2 vials), MeCN for eluent metering valve (40 mL), and DI water for eluent metering valve (40 mL)

#### **3.2.4.3 Preconditioning**

Before trapping [ $^{18}\text{F}$ ]fluoride, the micro-cartridge must be pre-conditioned (Figure 3-2A). First, the cartridge valve is set into the “trap” position and the cartridge waste valve is set to cartridge waste (Figure 3-2A). Pre-conditioning solution (0.6 mL for intermediate vial system, 1.0 mL for direct loading system) was passed through the micro-cartridge to the waste vial. In the intermediate vial system, 3.0 mL of DI water was then loaded to rinse the intermediate vial and discarded to waste by temporarily switching the cartridge valve to the “elute” position to bypass the cartridge. Next, the cartridge was rinsed twice with DI water (0.8 mL each time for the intermediate vial system, 0.5 mL each time for the direct loading system). Finally, DI water was eliminated from the cartridge by flowing MeCN (1.0 mL for the intermediate vial system and 0.5 mL for the direct loading system) through the cartridge, followed by a flush with inert gas (40 s). Note that the volumes were slightly higher for the intermediate vial system to improve reliability by accounting for losses that could occur within the intermediate vial.

#### **3.2.4.4 [ $^{18}\text{F}$ ]Fluoride trapping**

In typical experiments, the [ $^{18}\text{F}$ ]fluoride vial was loaded with ~0.5 mL (~ 9-1220 MBq [0.25-33 mCi]) [ $^{18}\text{F}$ ]fluoride/[ $^{18}\text{O}$ ]H<sub>2</sub>O prior to trapping. In practice, this vial could be filled via tubing directly from the cyclotron or other [ $^{18}\text{F}$ ]fluoride sources. In the case of the intermediate vial system, a vacuum pull time of 11 s was used to ensure complete transfer of the [ $^{18}\text{F}$ ]fluoride

into the intermediate vial, even though calibration indicated that only 5 s was needed to transfer 0.5 mL.

With the cartridge valve in “trap” position, the [ $^{18}\text{F}$ ]fluoride solution was then driven by inert gas (20 psig) through the micro-cartridge and to the [ $^{18}\text{O}$ ]H $_2$ O recovery vial (Figure 3-2B). The micro-cartridge traps the fluoride ions while the [ $^{18}\text{O}$ ]H $_2$ O passes through. After trapping, a portion of MeCN (1.0 mL for the intermediate vial system and 0.5 mL for the direct loading system) is passed through the cartridge (to remove residual water) to the cartridge waste vial. Finally, the cartridge is dried by flowing inert gas at 20 psig for 40 s through the same fluid pathway.

#### **3.2.4.5 [ $^{18}\text{F}$ ]Fluoride elution**

For each elution step, a 6.2  $\mu\text{L}$  plug of eluent solution is prepared. With the eluent metering valve in the “load” position (Figure 3-3A), the eluent path is primed by applying vacuum (-10 psig) to the eluent waste reservoir. Once the loop is filled (detected by an air-to-liquid transition at the eluent waste liquid sensor (#3)), valve H is closed, and the eluent metering valve is switched to the “elute” position (Figure 3-3B). At the same time, the cartridge valve is switched to the “elute” position (Figure 3-2C). Inert gas pressure is then applied to push the eluent plug toward the cartridge valve, through the micro-cartridge, and to the concentrated radionuclide outlet for downstream radiosynthesis. To ensure the small plug of eluent solution remains intact, the inert gas pressure is gradually ramped up (0.5 psi every 5 s). Once liquid sensor #2 detects that the whole eluent plug has passed (via air-to-liquid then liquid-to-air transitions), pressure is increased by 5 psig for an additional 10 s. The majority of the eluent volume is ejected from the cartridge within 4 s following the pressure ramp, but an additional 10 s was chosen to provide a safety margin as well as to recover any residual droplets formed on the concentrated radionuclide outlet tubing during ejection.

The eluent loop can be refilled to perform additional elution steps. Note that upon switching the eluent metering valve back to the load position, the eluent loading system is still full of eluent except for a gap of air in the loop. Thus the system can be re-primed by applying vacuum to the eluent waste vial until the liquid sensor (#3) detects a liquid-to-gas followed by a gas-to-liquid transition. The elution process can then be repeated exactly as above. The eluent loop can also be filled with water or MeCN to perform rinsing steps or to perform cleaning of the system.

To clean the system after use, the cartridge is first rinsed with DI water followed by MeCN. The volumes and pressures are identical to those used during the preconditioning step. In the case of the direct loading system, reagent vials for DI water (0.5 mL) and MeCN (0.5 mL) were refilled before rinsing. For the intermediate vial system, DI water and MeCN were pulled from the previously loaded reservoirs. After the cartridge has been cleaned, it is removed and stored by submerging in a solution of 50:50 v/v MeCN/H<sub>2</sub>O. In cases where there is significant residual radioactivity (> 37 MBq [1 mCi]) on the cartridge (which can be estimated from amount collected during elution), the majority of the activity can be removed by performing a preconditioning process prior to cartridge removal and storage.

To clean the eluent lines and loop, the MeCN rinse vial is first loaded with 40 mL of MeCN. The eluent vial is emptied, rinsed three times with DI water and is then filled with DI water (1 mL) and placed back into the system. The eluent line, from the eluent vial to the eluent valve, to the eluent loop and to eluent waste is rinsed with the 1 mL of DI water from the eluent vial by pulling vacuum on the eluent waste vial (Figure 3-3A). Following rinsing of the system with water, the eluent path is rinsed with 1 mL MeCN from the MeCN vial and is then purged with nitrogen at 20 PSIG for 3 minutes to dry out the lines. The rinsing configuration of the

eluent valve for MeCN can be seen in Figure 3-10A and the eluent valve configuration for purging can be seen in Figure 3-10B.

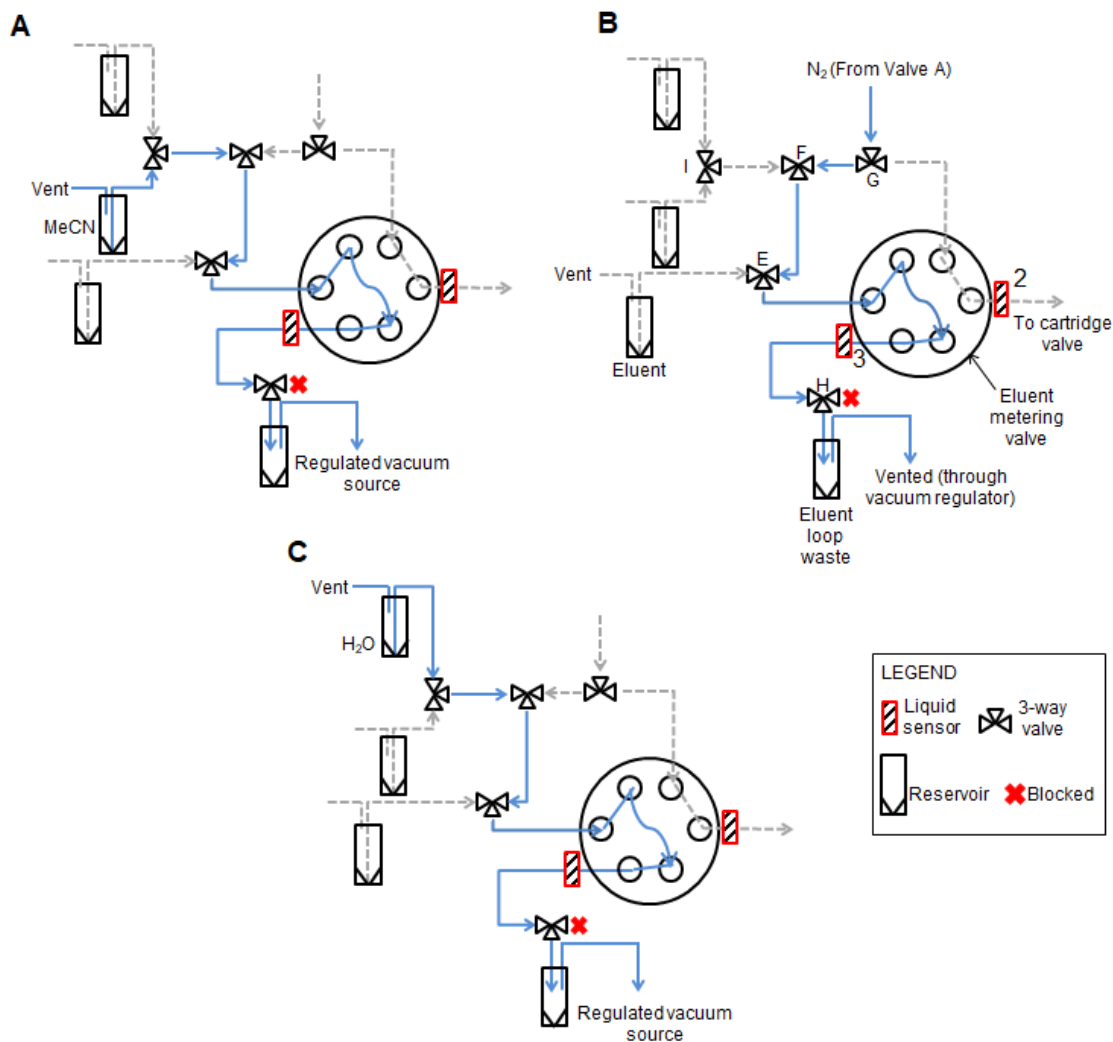


**Figure 3-10: Fluidic and pneumatic diagram of the eluent valve during MeCN rinse of the eluent line (A), eluent line purge (B), and DI water rinse of the eluent line (C)**

Next, the reagent loading system is cleaned. For the intermediate vial system, 50 mL reagent vials are emptied and disposed of after a completed run. 50 mL reagent vials, each containing 10 mL of DI water, are temporarily connected to each reagent inlet. DI water (3 mL) is pulled into the intermediate vial and then transferred through the cartridge valve to cartridge

waste for each reagent input allowing for cleaning of the fluid path from reagent reservoir to the intermediate vial. During cleaning, the cartridge valve is in the “elute” position allowing for the rinse solution to bypass the cartridge as it passes through the valve (Figure 3-11) to waste. Next, for each reagent, air is pulled into the intermediate vial for 30 s to dry the corresponding reagent line. After drying, the lines are now clean. In the case of the direct loading system, all reagent vials are first emptied. Reagent vials containing 1 mL of DI water are connected to each reagent input, water is then transferred through the cartridge valve (in “elute” position) to cartridge waste. This process is repeated three times for each input. Following the water rinse, each reagent input is dried by flowing nitrogen through the input and system for 30 s.

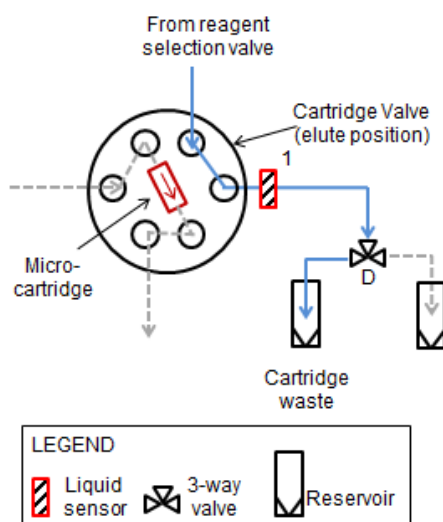


**Figure 3-11: Fluidic and pneumatic diagram of the cartridge valve during DI water rinse of the reagent loading system.**

### 3.2.5 Characterization of trapping and elution efficiency

Characterization of trapping and elution efficiency was performed by taking radioactivity measurements with a calibrated dose calibrator (CRC-25 PET, Capintec, Inc., Ramsey, NJ) during the trapping and elution processes. For the purposes of calculations, all radioactivity measurements were decay-corrected to a common timepoint. Measurements were made of the

starting activity in the [<sup>18</sup>F]fluoride (“source”) vial before trapping ( $A_{0\text{source}}$ ), activity in the source vial after trapping ( $A_{\text{source}}$ ), activity on the cartridge after trapping ( $A_{\text{cartridge}}$ ), activity in the [<sup>18</sup>O]H<sub>2</sub>O recovery vial after trapping ( $A_{\text{waste}}$ ), and the collected activity after elution ( $A_{\text{collect}}$ ). Trapping efficiency (%) was computed as  $A_{\text{cartridge}} / (A_{0\text{source}} - A_{\text{source}}) \times 100\%$ . Elution efficiency (%) was calculated as  $A_{\text{collect}} / (A_{\text{cartridge}} - A_{\text{source}}) \times 100\%$ . In early experiments,  $A_{\text{cartridge}}$  was measured directly, however in later experiments  $A_{\text{cartridge}}$  was measured indirectly (i.e. calculated as  $A_{0\text{source}} - (A_{\text{waste}} + A_{\text{source}})$ ) to prevent unnecessary radiation exposure to the operator. Measurements via the two approaches were found to agree within ~0.5% of the starting activity.

### 3.2.6 Synthesis of N-boc-5-[<sup>18</sup>F]Fluoroindole

Using concentrated [<sup>18</sup>F]fluoride to limit water content, we performed the synthesis of N-boc-5-[<sup>18</sup>F]fluoroindole via nickel-mediated oxidative fluorination (Figure 3-12A) as reported by Lee *et al.* [111]

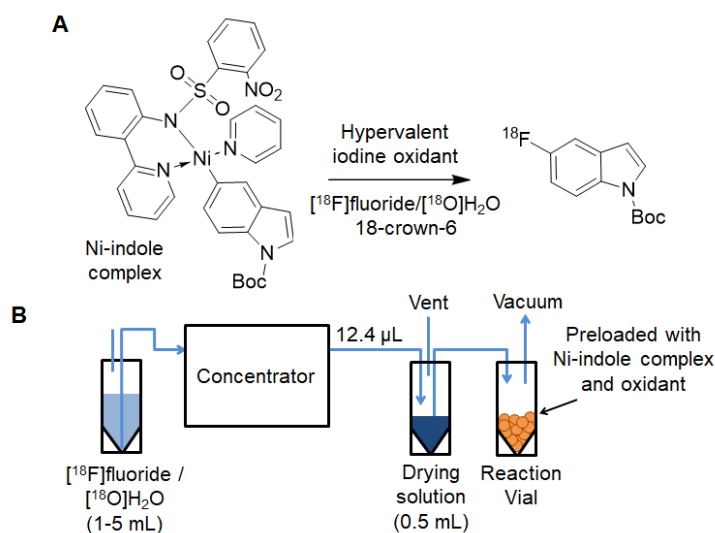


**Figure 3-12: (A) Reaction scheme for synthesis of N-boc-5-[<sup>18</sup>F]fluoroindole from Ni-indole complex. (B) System configuration for production of N-boc-5-[<sup>18</sup>F]fluoroindole.**

The setup of the experiment is shown in Figure 3-12B. Concentration of [<sup>18</sup>F]fluoride was performed using 1 M KH<sub>2</sub>PO<sub>4</sub> for preconditioning the micro-cartridge, and 24 mM K<sub>3</sub>PO<sub>4</sub> + 136

mM 18-crown-6 in a 20:80 v/v mixture of DI water and MeCN for elution. The eluted solution had a volume of 12.4  $\mu$ L (two elution plugs). The concentrator output was connected into a 3 mL vial (Wheaton) containing 500  $\mu$ L of a “drying” solution (salt in MeCN). The concentrated [ $^{18}$ F]fluoride was thus “dried” by dilution, resulting in a [ $^{18}$ F]fluoride solution with a low and well-controlled amount of water. A #23 needle in this vial provided a vent during the transfer of the concentrated [ $^{18}$ F]fluoride. Two drying solutions were tested – one containing 38 mM 18-crown-6 in MeCN (drying solution #1), and the other containing 38 mM 18-crown-6 + 10 mM  $K_3PO_4$  in 1:400 v/v  $H_2O$ :MeCN (drying solution #2).

The drying/dilution vial was connected via a dip-tube to a second “reaction” vial. This vial was pre-filled with a 2:3 mixture of the Ni-indole complex (1.0 - 1.3 mg) and hypervalent iodine oxidant (1.3 - 1.6 mg) prepared under argon prior to each experiment. The dried [ $^{18}$ F]fluoride was transferred by applying vacuum to the headspace of the second vial, and the resulting mixture was then allowed to react for 1 min. Determination of water content in the reaction mixture for synthesis of N-boc-5- $[^{18}F]$ fluoroindole was performed using Karl Fischer titration.

The Karl Fischer titration was carried out with a coulometric Karl Fischer titrator (C20; Mettler Toledo, Columbus, OH, USA). A polarized double pin platinum electrode (DM143-SC; Mettler Toledo) was used. Mixing power was set to 45% and mixing time was set to 15 seconds. The polarizing current for bipotentiometric end-point determination was 5 $\mu$ A and the end point voltage was 100mV. Maximum starting drift was set to 25  $\mu$ g/min. The end-point criterion was drift stabilization (3.0 $\mu$ g/min) or maximum titration time (60 min). CombiCoulomat fritless (Millipore Sigma, Burlington, MA, USA) was the titrant used within the Karl Fischer system. Through Karl Fischer titration, the amount of water present in each sample was determined in milligrams. The mass of water in each sample was then converted to a volume and the volume fraction of the sample that is water was determined.

Water content was determined for mock (i.e. non-radioactive) samples as follows. First 0.5mL DI water was passed through the cartridge to simulate trapping of [ $^{18}\text{F}$ ]fluoride. Next the eluent solution was passed through the cartridge and the eluate dissolved in the drying solution (Table 3-8). The mock concentration was performed using the direct loading system as described above. The reaction solution was then analyzed for water content via Karl Fischer titration. This entire process was repeated twice for each drying solution. As a control, water content of anhydrous MeCN used in these experiments was measured and determined to be negligible (0.01% v/v; n = 1).

The crude product was then analyzed by radio thin layer chromatography (radio-TLC) for determination of radiochemical conversion (RCC). A 1  $\mu\text{L}$  droplet of the crude product was spotted on a silica TLC plate (JT4449-2, J.T. Baker, Center Valley, PA, USA) with a micropipette. The TLC plate was developed in 10% v/v ethyl acetate in hexane and then analyzed with a radio-TLC reader (MiniGITA Star, Raytest, Germany). The chromatograms contained two peaks (Figure 3-13): [ $^{18}\text{F}$ ] fluoride ( $R_f = 0.0$ ) and N-boc-5-[ $^{18}\text{F}$ ]fluoroindole ( $R_f = 0.58$ ). The RCC of N-boc-5-[ $^{18}\text{F}$ ]fluoroindole was calculated as the area under the N-boc-5-[ $^{18}\text{F}$ ]fluoroindole peak divided by the area under both peaks.

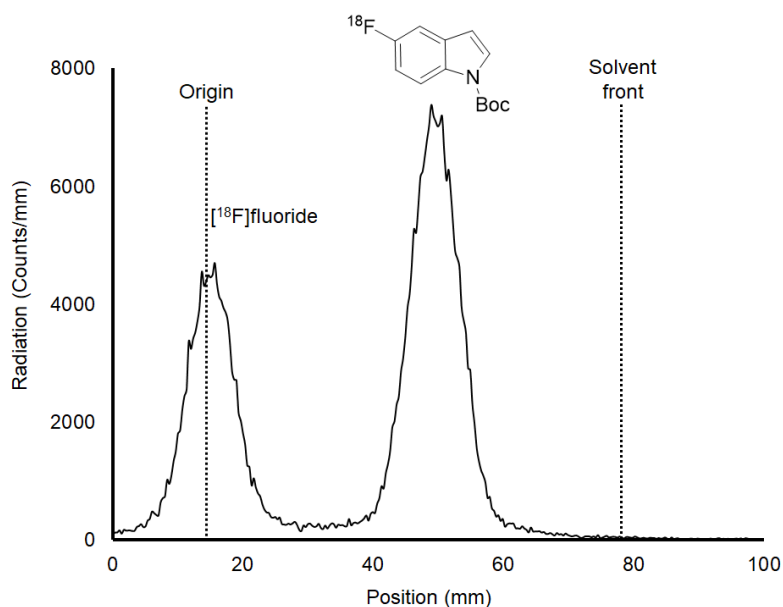


**Figure 3-13: A model radio-TLC chromatogram of the crude N-boc-5-[<sup>18</sup>F]fluoroindole synthesized using concentrated [<sup>18</sup>F]fluoride**

### 3.2.7 Duration of concentration process

Time required to complete each low-level step of the three main unit operations (preconditioning, trapping, and elution) in the concentration process were recorded for the intermediate vial system and the direct loading system. The duration of each process was measured n=3 times. Timing is based on operation with real reagents, except that DI water was substituted for [<sup>18</sup>F]fluoride. The preconditioning solution was 1 M NaCl.

### 3.3 Results and Discussion

#### 3.3.1 Duration of concentration process

**Table 3-2: Duration for each low-level step of the concentration process (intermediate vial system)**

Each data point represents the average of n=3 repeats and the standard deviation (SD).

	Concentration Unit Operations	Time $\pm$ SD (s)
Preconditioning steps	Meter preconditioning solution (0.6 mL)	7 $\pm$ 0
	Load preconditioning solution through cartridge	39 $\pm$ 2
	Flood common vial with water	93 $\pm$ 2
	Dump common vial to waste	26 $\pm$ 3
	Meter water into common vial (0.8 mL)	9 $\pm$ 0
	Pass through cartridge into waste	39 $\pm$ 3
	Meter water into common vial (0.8 mL)	9 $\pm$ 1
	Pass through cartridge into waste	51 $\pm$ 5
	Meter MeCN (1 mL)	9 $\pm$ 0
	Pass through cartridge to waste	28 $\pm$ 2
	Air dry cartridge	22 $\pm$ 1
	Air dry cartridge	22 $\pm$ 1
	<b>Total Preconditioning Time</b>	<b>355 <math>\pm</math> 3</b>
Trapping Fluoride	Load $^{18}\text{F}$ into common vial (0.5 mL)	11 $\pm$ 1
	Transfer $^{18}\text{F}$ through cartridge to O-18 Waste	40 $\pm$ 6
	Meter MeCN into common vial (1 mL)	9 $\pm$ 0
	Load MeCN through cartridge	29 $\pm$ 0
	Air dry cartridge	22 $\pm$ 0
	Air dry cartridge	22 $\pm$ 0
	<b>Total Trapping Time</b>	<b>134 <math>\pm</math> 6</b>
Elution	Purge & fill loop with eluent	25 $\pm$ 1
	One elution (6.2 $\mu\text{L}$ total)	62 $\pm$ 2
	Two elutions (12.4 $\mu\text{L}$ total)	112 $\pm$ 1
	<b>Total Elution Time (two elutions)</b>	<b>137 <math>\pm</math> 1</b>
	<b>Total Process Time (two elutions)</b>	<b>625 <math>\pm</math> 9</b>

**Table 3-3: Duration for each low-level step of the concentration process (direct loading system)**

Each data point represents the average of n=3 repeats and the standard deviation (SD).

	Concentration Unit Operations	Time $\pm$ SD (s)
Preconditioning	Push preconditioning solution (0.6 mL) through cartridge to waste	39 $\pm$ 2
	Push water (0.8 mL) through cartridge to waste	39 $\pm$ 3
	Push water (0.8 mL) through cartridge to waste	51 $\pm$ 5
	Push MeCN (1.0 mL) through cartridge to waste	28 $\pm$ 2
	Air dry cartridge	22 $\pm$ 1
	Air dry cartridge	22 $\pm$ 1
	<b>Total Preconditioning Time</b>	<b>202 <math>\pm</math> 5</b>
Trapping	Push [ <sup>18</sup> F]fluoride (0.5 mL) through cartridge to [ <sup>18</sup> O]H <sub>2</sub> O recovery	40 $\pm$ 6
	Push MeCN (1.0 mL) through cartridge to waste	29 $\pm$ 0
	Air dry cartridge	22 $\pm$ 0
	Air dry cartridge	22 $\pm$ 0
	<b>Total Trapping Time</b>	<b>113 <math>\pm</math> 6</b>
Elution	Purge & fill loop with eluent	25 $\pm$ 1
	One elution (6.2 $\mu$ L total)	62 $\pm$ 2
	Two elutions (12.4 $\mu$ L total)	112 $\pm$ 1
	<b>Total Elution Time (two elutions)</b>	<b>137 <math>\pm</math> 1</b>
	<b>Total Process Time (two elutions)</b>	<b>452 <math>\pm</math> 4</b>

The times required to complete each of the main operations (i.e. preconditioning, trapping, and elution) for the intermediate vial and direct loading systems and shown in Table 3-2 and Table 3-3, respectively. For the intermediate vial system, the preconditioning process took 355  $\pm$  3 s (n= 3), trapping took 134  $\pm$  6 s (n=3), and elution took 137  $\pm$  1 s (n=3) for two elution plugs. In total, the entire concentration process for the intermediate vial system took 625  $\pm$  9 s (n=3). Of the preconditioning time, 119  $\pm$  4 s (n=3) was spent rinsing the intermediate vial to eliminate residue of the preconditioning solution.

The direct loading system reduces the overall concentration time as certain steps, including rinsing of the intermediate vial and transferring from reagent reservoirs to intermediate vial, are not needed. The total time in this case was ~3 min shorter, i.e. 452  $\pm$  4 s (n=3).

Likely, one would eventually use micro-cartridges that are pre-conditioned at the manufacturer, or one would perform the preconditioning ahead of time (i.e. before addition of [ $^{18}\text{F}$ ]fluoride solution). In such a case, the total time for concentration after adding the [ $^{18}\text{F}$ ]fluoride solution would be  $271 \pm 7$  s (n=3) and  $250 \pm 7$  s (n=3) for the intermediate vial and direct loading systems, respectively.

### 3.3.2 Trapping efficiency

The efficiency of trapping [ $^{18}\text{F}$ ]fluoride was assessed for several pre-conditioning solutions ( $\text{KHCO}_3$ ,  $\text{KH}_2\text{PO}_4$ , and  $\text{NaCl}$ ) using the intermediate vial system.  $\text{KHCO}_3$  is commonly used in conjunction with  $\text{K}_2\text{CO}_3$  / Kryptofix 2.2.2 or  $\text{KHCO}_3$  / Kryptofix 2.2.2 as an eluent.  $\text{KH}_2\text{PO}_4$ , in conjunction with  $\text{K}_3\text{PO}_4$  / 18-crown-6 has been shown to be useful for metal-mediated fluorination reactions where certain precursors unfavorably react with the amine functionality found in Kryptofix 2.2.2. [112] Use of  $\text{NaCl}$  as both preconditioning solution and eluent has been demonstrated in isotopic exchange reactions [113], where it helps to simplify the purification and quality control processes since  $\text{NaCl}$  is injectable, though introduction of chloride ion can interfere with nucleophilic fluorination reactions.

Since flow rates of reagents through the cartridge determine how long the solutes have to interact with the resin within the cartridge, flow rates were set to 1 mL/min, which is slower than the report of Lebedev *et al.* [65] (in which the same cartridges were used) by a safety factor of 2.

Under all conditions tested, at least 94% trapping efficiency was observed (Table 3-4). Of the three preconditioning solutions tested,  $\text{KHCO}_3$  and  $\text{KH}_2\text{PO}_4$  resulted in the highest trapping efficiencies of  $99 \pm 1\%$  (n=13) and  $96 \pm 4\%$  (n=16), respectively. Of the anions used for preconditioning,  $\text{Cl}^-$  has the highest affinity for the resin, while  $\text{HCO}_3^-$  and  $\text{H}_2\text{PO}_4^-$  are lower

[114], explaining the higher displacement by [<sup>18</sup>F]fluoride (and thus higher trapping efficiency) for these latter anions.

**Table 3-4: Efficiencies of [<sup>18</sup>F]fluoride trapping after preconditioning with various solutions measured in the intermediate vial system**

The cartridge was preconditioned with 0.6 mL of preconditioning solution, rinsed twice with 0.8 mL DI water, rinsed with 1.0 mL MeCN, and air dried for 40 s.

Preconditioning Solution	Trapping efficiency (%)
1 M KHCO <sub>3</sub>	99 ± 1 (n=13)
1 M NaCl	94 ± 8 (n=10)
1 M KH <sub>2</sub> PO <sub>4</sub>	96 ± 4 (n=16)

### 3.3.3 Effect of initial volume of radionuclide solution

We anticipated that the starting volumes of radioactivity for a downstream radiosynthesis may vary (e.g. preparing multiple tracers from a single master batch of [<sup>18</sup>F]fluoride), therefore we explored the effect of the volume of [<sup>18</sup>F]fluoride solution in the source vial on trapping efficiency. We hypothesized that there are some dead volumes associated with the tubing interface into the source vial, and that losses would become more significant as starting volume was reduced, resulting in lower apparent trapping efficiencies. For example, the liquid could become distributed on the vial surface, on tubing, and inside valves before reaching the cartridge valve.

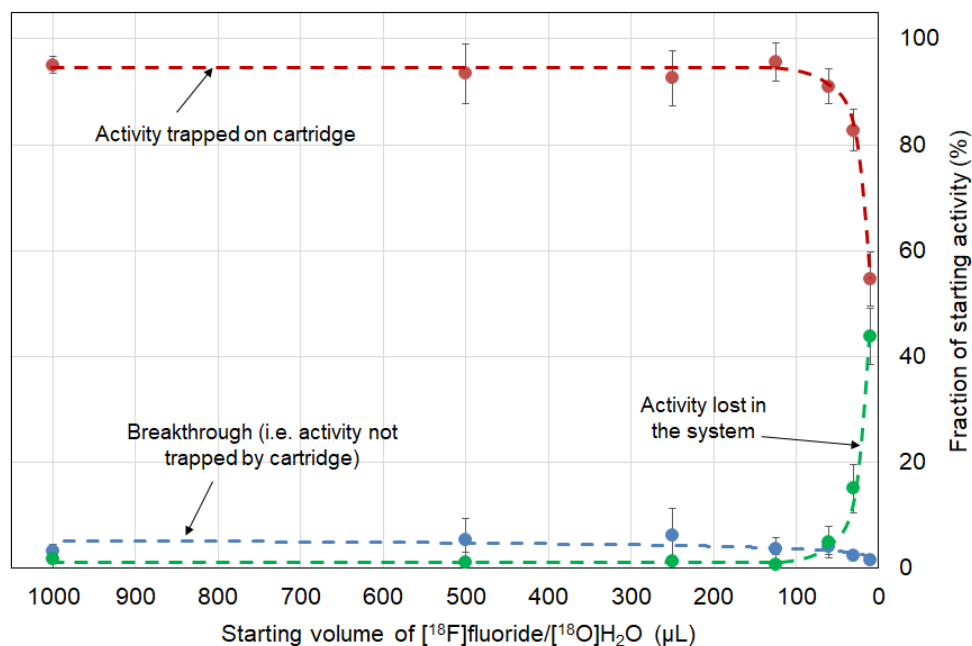


**Figure 3-14: Trapping efficiency on the cartridge as a function of the starting volume of  $[^{18}\text{F}]\text{fluoride}$**

Also shown is the “breakthrough”, i.e. the fraction of initial  $[^{18}\text{F}]\text{fluoride}$  found in the cartridge waste as well as fraction of activity lost within the system (i.e. not in radionuclide vial, trapped in cartridge, or in cartridge waste). Data points represent an average of 3 repeats and error bars represent the standard deviation. Dashed lines are guides for the eye.

Trapping efficiencies for various starting volumes, using the direct loading system, are summarized in Figure 3-14. Pre-conditioning was performed with 1 M NaCl. The volume can be scaled down quite far without adverse effect on the trapping efficiency. For volumes ranging from 1.0 down to 0.125 mL, activity lost within the system (i.e. activity not in  $[^{18}\text{F}]\text{fluoride}$  vial, trapped on cartridge, or in cartridge waste vial) is low (< 2%). For starting volumes of 0.06, 0.03, and 0.01 mL, losses increase dramatically to  $5.0 \pm 2.9\%$  ( $n = 3$ ),  $15.0 \pm 4.6\%$  ( $n=3$ ) and  $44.0 \pm 5.3\%$  ( $n=3$ ), respectively.

These results suggest at least 0.06 mL should be used in the source vial to ensure efficient overall operation of the concentrator. To accommodate smaller volumes, one could always dilute the  $[^{18}\text{F}]\text{fluoride}$  source with DI water to increase the volume into this range (at the

expense of requiring more time for trapping), or potentially could rinse the full fluid path with DI water (through the cartridge) after trapping with little effect on overall duration or system complexity.

### 3.3.4 Effect of number of eluent plugs

Recovery of trapped [<sup>18</sup>F]fluoride from strong anion exchange cartridges has been shown to be more efficient when eluted with multiple smaller elution plugs rather than one larger single plug. [65] With the intermediate vial system, we explored the influence of the number of eluent plugs on elution efficiency in a set of experiments using 1 M NaCl for preconditioning and 0.15 M NaCl for elution. In Table 3-5, we observe that only a small fraction of the activity ( $21.9 \pm 2.6\%$ ,  $n=3$ ) is recovered with one elution rinse. The cumulative amount recovered by two rinses was  $88.4 \pm 1.3\%$  ( $n=3$ ). An additional 2 rinses recovered an additional  $10.1 \pm 2.9\%$  ( $n=3$ ) of the initial amount, and further rinses recovered negligible amounts of additional activity. To ensure the highest concentration and lowest water content, we used 2 elution steps for most experiments.

**Table 3-5: Performance as a function of number of eluent and rinse plugs**

Each plug is 6.2 $\mu$ L in volume. The eluent solution and rinse solution were 0.15 M NaCl and MeCN, respectively. Trapping data represents decay-corrected fraction of starting activity trapped on cartridge  $\pm$  standard deviation ( $n=3$ ). Elution data represents decay-corrected fraction of trapped activity  $\pm$  standard deviation ( $n=3$ ).

Step in concentration process	Radioactivity measurement (% of trapped activity, decay-corrected)		
	Protocol 1: 6x eluent plugs	Protocol 2: 2x eluent plugs, 4x MeCN plugs	Protocol 3: 1x eluent plug, 5x MeCN plugs
After trapping	$95.6 \pm 3.5$	$91.8 \pm 1.0$	$92.6 \pm 1.3$
Elution #1	Not measured	Not measured	$21.9 \pm 2.6$
Elution #2	Not measured	Not measured	$51.6 \pm 8.1$
Elutions #1, #2 (combined)	$88.4 \pm 1.3$	$87.6 \pm 3.3$	$73.6 \pm 5.6$
Elutions #3, #4 (combined)	$10.1 \pm 2.9$	$6.1 \pm 1.4$	$5.5 \pm 1.9$
Elutions #5, #6 (combined)	$1.0 \pm 0.4$	$0.3 \pm 0.1$	$0.8 \pm 0.2$
Total eluate collected	$99.5 \pm 2.1$	$94.0 \pm 1.9$	$79.9 \pm 3.7$

We were curious as to why the recovery was so low for a single elution plug. Since other reports had shown highly efficient recovery in 5  $\mu\text{L}$  [45] (lower than the volume of one elution plug in our setup), we hypothesized that the majority of activity may successfully be released from the cartridge with a single elution plug but is lost between the cartridge and the system output. In order to explore this hypothesis, we trapped [ $^{18}\text{F}$ ]fluoride, then performed one rinse with eluent solution, followed by multiple rinses with MeCN and measured the activity recovered at each step. To minimize carryover of eluent solution, paths in the eluent metering subsystem, with the exception of the tubing connecting the eluent valve to the cartridge valve were rinsed with MeCN three times prior to filling the eluent loop with MeCN. It was not possible to rinse the tubing between the eluent metering valve and cartridge valve, but residual eluent solution was expected to be negligible in this region. Results are summarized in Table 3-5. Indeed, by following the elution rinse with just one MeCN rinse improved the recovery from  $21.9 \pm 2.6\%$  ( $n=3$ ), to  $73.6 \pm 5.6\%$  ( $n=3$ ). Though this is still less than the amount recovered with 2 eluent rinses (i.e.  $88.4 \pm 1.3\%$  ( $n=3$ )), this result strongly supports the hypothesis.

Next, we compared the amount recovered using 1 eluent plug followed by 5 MeCN rinses, 2 eluent plugs followed by 4 MeCN rinses, and 6 eluent plugs and found recoveries of  $79.9 \pm 3.7\%$  ( $n=3$ ),  $94.0 \pm 1.9\%$  ( $n=3$ ), and  $99.5 \pm 2.1\%$  ( $n=3$ ), respectively. It can be seen in the second and third cases that additional eluent plugs help to further release residual fluoride from the cartridge, and thus that the overall efficiency is related to both release of fluoride from the resin as well as flushing this fluoride through the fluid pathway to the output tubing.

### **3.3.5 Elution efficiency**

Elution efficiency was explored for several different eluent solutions using the intermediate vial system and two elution plugs (12.4  $\mu\text{L}$  total volume). Results are summarized in Table 3-6. Recovery was found to be  $>88\%$  under all conditions tested.

**Table 3-6: Efficiencies of [<sup>18</sup>F]fluoride elution using different eluent solutions measured in the intermediate vial system**

Elutions were performed with two plugs of eluent solution (12.4  $\mu$ L total volume).

Eluent (in DI water)	Elution efficiency based on trapped activity (%)
0.01 M K <sub>2</sub> CO <sub>3</sub> and 0.05 M K222	89 $\pm$ 7 (n=8)
0.08 M TBAB	92 $\pm$ 8 (n=2)
0.15 M NaCl (Saline)	96 $\pm$ 5(n=10)
0.01 M K <sub>3</sub> PO <sub>4</sub> and 0.07 M 18-Crown-6	88 (n=1)
0.18 M K <sub>3</sub> PO <sub>4</sub>	90 (n=1)
1.19 M K <sub>3</sub> PO <sub>4</sub>	100 (n=1)

With other conditions constant, we expected that elution efficiency would depend on the anion strength and concentration of the eluent solution as well as the amount of the anion present. Indeed, affinity of Br<sup>-</sup> and Cl<sup>-</sup> anions to the cartridge are high, and elution efficiencies with the corresponding eluents (TBAB and NaCl, respectively) were very high, i.e. 92  $\pm$  8% (n=2) and 96  $\pm$  5% (n=10), respectively. Relative strengths of CO<sub>3</sub><sup>2-</sup> and PO<sub>4</sub><sup>3-</sup> to the cartridge were not provided by the manufacturer. In addition, we observed that increasing amount of K<sub>3</sub>PO<sub>4</sub> in the eluent leads to increasing recovery of [<sup>18</sup>F]fluoride. For eluent containing 0.01 M, 0.18 M and 1.19 M K<sub>3</sub>PO<sub>4</sub>, the elution efficiencies were 88, 90, and 100%, respectively.

### 3.3.6 Elution with organic solvent containing eluent

We showed above that one could elute with a single eluent plug (6.2  $\mu$ L water) followed by organic solvent (6.2  $\mu$ L MeCN) rinse instead of two eluent plugs, as long as one is willing to tolerate the ~20% loss in recovered activity (i.e. 73.6  $\pm$  5.6% (n=3) versus 88.4  $\pm$  1.3 % (n=3)). To further reduce water content, e.g. to avoid the need for azeotropic drying, we explored the possibility of introducing portions of organic solvents into the eluent solution itself to further reduce water content. (Another approach would be to reduce the volume of each eluent plug, but for practical reasons, it was difficult to reduce the volume of the eluent loop.) Since it is

known that decreasing water content decreases elution efficiency [101], we explored the impact in our system to determine the lower limit of water content. Experiments were performed with two eluent plugs (12.4  $\mu\text{L}$  total) containing 0.02 M  $\text{K}_3\text{PO}_4$  and 0.14-0.15 M 18-crown-6 in various mixtures of DI water and MeCN. (The same eluent is used later in a fluorination reaction.) Preconditioning solution used was 1 M  $\text{KH}_2\text{PO}_4$ .

Results of these experiments are shown in Table 3-7. Even with 50% (v/v) MeCN content, elution efficiency was high, i.e. 96% (n=1), but as MeCN content further increased, recovery diminished further. At 80% MeCN, recovery using 2 eluent plugs was  $84 \pm 6\%$  (n=6), suggesting that a further ~60% reduction in water content is possible if one is willing to tolerate a ~12% loss in elution efficiency.

**Table 3-7: Recovery of [ $^{18}\text{F}$ ]fluoride (with respect to trapped activity) with the intermediate vial system as a function of eluent with varying compositions of MeCN**

Recovery values are average of n repeats  $\pm$  standard deviation.

Solvent composition (% MeCN in DI water v/v)	$\text{K}_3\text{PO}_4$ (mM)	18-crown-6 (mM)	Recovery (% of trapped activity, decay-corrected)
50	24	152	96 (n=1)
80	24	136	$84 \pm 6$ (n= 6)
90	24	136	66 (n=1)
93	24	152	43 (n=1)

### 3.3.7 Synthesis of N-boc-5- $^{18}\text{F}$ fluoroindole

As a proof of concept of using the concentrator to reduce water content for radiofluorination, we explored the synthesis of a model compound, N-boc-5- $^{18}\text{F}$ fluoroindole. This reaction has previously been performed without azeotropic drying, but because the amount of water was limited to  $\leq 1\%$  v/v, this greatly limited the amount of starting activity of [ $^{18}\text{F}$ ]fluoride/ $^{18}\text{O}$ ]H $_2\text{O}$  that could be used in the reaction. [111]

**Table 3-8: Reaction conditions and radiochemical yield (RCY; decay-corrected) for synthesis of N-boc-5-[<sup>18</sup>F]fluoroindole using concentrated [<sup>18</sup>F]fluoride**

In each experiment, the concentrated [<sup>18</sup>F]fluoride was recovered with two plugs (total 12.4  $\mu$ L) of eluent solution (24 mM K<sub>3</sub>PO<sub>4</sub> + 136 mM 18-crown-6 in 1:4 v/v H<sub>2</sub>O:MeCN). Drying solution 1 is 38 mM 18-crown-6 in MeCN (500  $\mu$ L). Drying solution 2 is 38 mM 18-crown-6 + 10 mM K<sub>3</sub>PO<sub>4</sub> in 1:400 H<sub>2</sub>O:MeCN (500  $\mu$ L).

Starting activity (mCi)	Ni-indole complex amount (mg)	Oxidant amount (mg)	Drying solution	H <sub>2</sub> O content in reaction (calculated) (%v/v)	H <sub>2</sub> O content (Karl-Fischer) (%v/v)	RCY (%)
3.28	1.12	1.31	1	0.48	0.32±0.02 (n=2)	49
1.06	1.02	1.30	1	0.48		52
Average ± SD						51 ± 2
1.49	1.31	1.55	2	0.73	0.57±0.01 (n=2)	53
1.17	1.2	1.4	2	0.73		47
Average ± SD						50 ± 4

Results are summarized in Table 3-8. Starting activities ranged from 41 – 122 MBq [1.1 – 3.3 mCi]. Two pairs of reactions were carried out, each pair using a different solution for “drying” the concentrated [<sup>18</sup>F]fluoride by dilution. The final water content of the reaction mixtures for drying solution 1 and drying solution 2 are estimated to be 0.48% v/v and 0.73% v/v, respectively. Interestingly, the water contents as measured via Karl Fischer titration were found to be slightly lower, i.e. 0.32 ± 0.02% v/v (n = 2) and 0.57 ± 0.01% v/v (n = 2), respectively, suggesting that transfer of the eluent solution through the cartridge may pick up some residual MeCN remaining after the cartridge is rinsed following the [<sup>18</sup>F]fluoride trapping step. Radiochemical conversions for the two pairs of experiments were found to be 51% ± 2% (n=2) and 50% ± 4% (n=2), respectively. The results were nearly identical despite the higher amount of K<sub>3</sub>PO<sub>4</sub> and water in the second pair of experiments. Notably, the yields were comparable to those reported by Lee *et al.* (53 ± 7%, n = 6) using 18-crown-6 in 100% MeCN (no salts) as the drying solution. [111]

This proof of concept experiment suggests that [<sup>18</sup>F]fluoride concentrated within our platform can be used to increase the activity scale of nickel-mediated oxidative fluorination reactions. The activity levels used in experiments by Lee *et al.* were low, i.e. 3.7 – 18.5 MBq [100-500 µCi] per reaction, due to the ≤1% v/v limit in the amount of water (2-5 µL) that could be added to the reaction volume (0.2 - 0.5 mL). [111] Even by using more concentrated [<sup>18</sup>F]fluoride (e.g. 37 GBq/mL [1.0 Ci/mL] is routinely available from cyclotrons), the maximum starting activity would have been 185 MBq [5.0 mCi], making it impractical to produce a clinically-relevant dose (~370 MBq [~10 mCi]), especially after accounting for losses during reaction (~50% conversion) and purification/formulation. Notably, by using these small volumes of [<sup>18</sup>F]fluoride out of 99.5% of the initial radioactivity would have been wasted. By using the [<sup>18</sup>F]fluoride concentrator, we were able to boost activity levels by 10x compared to the report of Lee *et al.*, and further increase in output could be achieved by concentrating a larger amount of initial activity. In fact, we have previously demonstrated the ability to concentrate ~63 GBq [1.7 Ci] of activity down to ~12.4 µL with 94.3% (n=1) efficiency. [100] If using 5 µL of this solution (identical to the volume used by Lee *et al.*) the volume would contain ~24 GBq [650 mCi], sufficient for a larger number of human doses, even after accounting for losses during the fluorination reaction and subsequent processing.

### **3.3.8 Comparison of operational differences between concentration system architectures**

Overall, the intermediate vial and direct loading systems functioned similarly, but the direct loading system was slightly simpler and faster (since it was not necessary to perform the rinsing of the intermediate vial. It should be appreciated, however, that the reagent loading method is independent of the system setup: pre-metering could be used in conjunction with the

intermediate vial system, or a time or pressure-based calibration could be used in the direct loading system, if desired.

### 3.3.9 Concentration of other radionuclides

In addition to concentrating [ $^{18}\text{F}$ ]fluoride, this system would likely be useful for concentrating other radionuclides. For example, researchers often use radiometals, such as Cu-64, Ga-68, and Zr-89, for labeling of peptides and antibodies. Ga-68 is recovered from a generator in volumes of several mL and the output of the generator decreases over time requiring larger volumes of eluent (HCl) to collect the desired amount of activity. These concentrations are not only too dilute for microscale synthesis but may also present a challenge for macroscale synthesis of clinical doses. Several groups have developed techniques to minimize the volume (e.g. using only the initial fraction), or to concentrate the Ga-68 after recovery. Gebhardt *et al.* described a QMA-cartridge-based method that reduces volumes from 3.5 mL to 0.2 mL in 15 min with ~67% overall recovery. [92] Potentially, using our setup with a micro-QMA cartridge, this final volume could be reduced to ~12.4  $\mu\text{L}$  and the time reduced to ~3 min. Zr-89 is produced in a cyclotron and is typically recovered in oxalic acid after a process to separate Zr-89 from the Y-89 target material. [115,116] Due to the toxicity of oxalic acid, several groups have presented a method to convert [ $^{89}\text{Zr}$ ]Zr-oxalate to [ $^{89}\text{Zr}$ ]ZrCl<sub>2</sub> prior to chelation through the use of a QMA cartridge followed by elution with 300-500  $\mu\text{L}$  of saline or HCl. [115,116] Using the micro-QMA cartridge in our system offers the potential to further shrink this volume and time required. Similar to microfluidic advancements for [ $^{18}\text{F}$ ]fluoride chemistry, several groups have also turned to leveraging microfluidic technologies for labeling radiometals. [117–119] Zeng *et al.* has demonstrated that increasing starting radiometal amounts (e.g.  $^{64}\text{Cu}^{2+}$ ,  $^{68}\text{Ga}^{3+}$ ) in microfluidic radiosynthesizers results in increased radiolabeling yields. [117] The ability to concentrate radiometals, therefore, not only enables the loading of more

radioactivity into an experiment but could also enable higher synthesis yields. In the near future we hope to explore concentration of these other radionuclides within our platform.

### 3.4 Conclusion

In this chapter, we have developed, optimized and automated a compact microfluidic platform to concentrate radionuclides such as [ $^{18}\text{F}$ ]fluoride into microliter-scale volumes. The standalone system can easily fit into a hot cell or mini-cell along with other equipment. It can be easily integrated with various types of radiosynthesis platforms (e.g. microfluidic droplet based systems, microfluidic flow-through systems, and macroscale systems). The system has applications in microfluidic radiochemistry, enabling the delivery of high amounts of activity into small-volume microreaction devices, e.g. based on droplet radiochemistry [48,64], an area of active investigation in our laboratory.

It also has valuable applications in macroscale radiochemistry, such as enabling quick “drying” of [ $^{18}\text{F}$ ]fluoride simply by the reduction of water volume followed by dilution in an anhydrous reaction solvent. An application of the latter was demonstrated: using  $\leq 1\%$  v/v water content in the reaction mixture. Radiochemical conversion of N-boc-5- $^{18}\text{F}$ fluoroindole was similar to that reported in literature, but with the advantage of being able to introduce orders of magnitude higher quantities of [ $^{18}\text{F}$ ]fluoride into a single reaction. For chemistries relying on such an approach to reduce water content, the concentrator will facilitate the production of clinically relevant amounts of tracers. Furthermore, low eluent volumes used in the system can enable significant reduction in eluent salts/base that are carried into the downstream reaction, potentially providing a way to improve the performance of base-sensitive reactions.

Reliable concentration of [ $^{18}\text{F}$ ]fluoride was performed starting with 60 – 1000  $\mu\text{L}$  volumes, but even larger volumes (e.g. a full cyclotron target volume, i.e. 1-5 mL) could readily be used if a longer trapping time could be tolerated. Indeed, concentration of  $\sim 63 \text{ GBq}$  [1.7 Ci]

with a prototype version of the system described here has been reported. [100] The entire concentration process can be completed in  $452 \pm 4$  s ( $n=3$ ) using the direct loading system. If certain steps (e.g. preconditioning) are performed in advance, then the trap and release process only requires  $250 \pm 7$  s ( $n=3$ ).

Different preconditioning solutions were tested resulting in 94-99% trapping efficiencies, and different aqueous eluent solutions resulted in 85-99% elution efficiencies. We also explored the relationship of recovered activity and number of eluent plugs and identified that two elution plugs (12.4  $\mu$ L total volume) provides an excellent tradeoff between overall efficiency and final output volume. Water content could be reduced by replacing the second eluent plug with MeCN or by diluting the eluent solution in a solvent / DI water mixture (e.g. up to 80% v/v MeCN in DI water).

This standalone automated concentrator enables fast, reliable concentration of [ $^{18}$ F]fluoride enabling high starting activities, low water and salt content, leading to efficient fluorination of PET tracers. With the possibility of concentrating radiometals, the benefits of this system can be further extended for peptide- and antibody- based PET imaging.

## 4 Chapter 4: Concentration of Radiometals

### 4.1 Introduction

Due to the convenience of production, as well as their theranostic applications, there has been great interest in the exploration and use of positron-emitting radiometals that can be produced via a compact generator. Generator produced radionuclides include gallium-68, rubidium-82, and copper-62. [120] Of these three radionuclides, gallium-68 is of great interest as an alternative to fluorine-18 due to similar physical properties. Gallium-68 has a moderate half-life of 68 minutes, a high positron yield of 89%. Many  $^{68}\text{Ga}$ -labeled imaging agents based on small molecules, peptides, antibodies, and particles have been developed for imaging of various physiological diseases. [121] In the field of oncology, gallium-68-labeled tracers have been developed for targeting specific receptor and receptor families (e.g. G-protein coupled receptor family, human epidermal growth factor receptor, prostate-specific membrane antigen) for diagnosis and treatment monitoring of certain cancers. [120–124] In addition, gallium-68 based tracers have also been created for imaging of biological processes such as angiogenesis, hypoxia, proliferation, apoptosis, glycolysis, inflammation, and infection [121,125] to aid in monitoring and quantifying other biological diseases.

Expanding beyond disease diagnosis and treatment monitoring, there is intense interest in radiometals due to their potential in theranostic applications where the same or similar targeting molecule is labeled with a positron-emitting radionuclide for diagnostics or other radionuclides for targeted radionuclide therapy applications. A gallium-68 based diagnostic agent can be used in therapy development by providing information about biodistribution and dosimetry, and in patient management can be used for staging the disease, computing patient-specific dosimetry to optimize the therapeutic dose, and lastly monitoring the response to the treatment. [124] Compared to diagnostic tracers, therapeutic tracers use radionuclides that emit

very short-range beta, alpha, or Auger electrons instead of positrons in order to cause localized irreversible DNA damage leading to cell death. [29] Due to gallium-68 having the same coordination chemistry as some radionuclides used for therapy (e.g.  $^{90}\text{Y}$ ,  $^{177}\text{Lu}$ ), there exists a possibility wherein diagnostic imaging and radiotherapy are performed using the same targeting biomolecule but imaging radionuclides are exchanged for therapeutic radionuclides. An example of this can be seen in imaging agents targeting somatostatin receptors (e.g. [ $^{68}\text{Ga}$ ]Ga-DOTA-TATE) and therapeutic agents for treatment of patients with neuroendocrine tumors (e.g. [ $^{177}\text{Lu}$ ]Lu-DOTA-TATE). [126]

Recently, groups have been exploring the use of microfluidics to perform radiosynthesis in microliter volumes resulting in improved reaction performance through more efficient heat transfer, and rapid reagent mixing. [38–40,51] Using microfluidic reactors (typically sized to 10s of microliters) also aids in reagent reduction (i.e. up to 2-3 orders of magnitude less than conventional approaches) [51], which can reduce production costs (especially for expensive precursors) and simplify downstream purification processes. Furthermore, molar activity of the synthesized tracer can also be increased through radiosynthesis in microliter volumes [47,62,63] which can aid in increased image quality during a PET scan. [63] In our lab, we have recently developed a microfluidic radiosynthesizer with a reactor volume of 2  $\mu\text{L}$  (presented in Chapter 5). [64] We believe that with this system, we can further push the limits of reducing precursor amount while maintaining high yields and molar activity.

Though most work in microfluidic radiochemistry has focused on fluorine-18, several groups have also successfully demonstrated radiometal labeling with copper-64, gallium-68, and zirconium-89 within microfluidic reactors. [117,118,127] For example, Zeng *et al.* reported successful labeling of NOTA-cyclo(RDGfK) and DOTA-cyclo(RGDfK) with both  $^{64}\text{Cu}$  and  $^{68}\text{Ga}$ , resulting in yields and molar activities higher than conventional techniques. [117] An experiment

was also performed exploring the effects of radiometal and ligand concentrations on labeling yields, in which concentrations were varied from 1-200  $\mu\text{M}$ , while maintaining a constant radiometal to ligand ratio of 1:1. In order to achieve the high radiometal concentrations required, the authors added in non-radioactive  $\text{Cu}^{2+}$  and  $\text{Ga}^{3+}$  to copper-64 and gallium-68 (i.e. carrier-added conditions). Results showed a dramatic increase in labeling yields from 10% with 1  $\mu\text{M}$  of radiometal to 90% with 90 $\mu\text{M}$  of radiometal, a trend that held true for all radiometal and ligand combinations. [117] In conventional radiosynthesis with a 1:1 ligand to metal ratio, the final concentrations of radiometal are typically less than 1  $\mu\text{M}$  which would lead to poor labeling yields based on the results shown above [117]. As a result, conventional radiosynthesis is typically performed with excess ligand to ensure higher labeling yield. Labeling with excess ligand, however, increases synthesis costs, can lower molar activity which can decrease signal to noise ratio of PET images, and can complicate purification following labeling. Labeling with excess ligand is generally also performed in microfluidic radiosynthesizers; however, since the reaction volume is orders of magnitude smaller than conventional methods, the total molar quantity of ligand used in microfluidic labeling can still be orders of magnitude less. If radiometal solutions from the generator can be concentrated down to a small volume to ensure microfluidic labeling with radiometal concentrations  $\geq 90 \mu\text{M}$  and a radiometal to ligand ratio of 1:1, precursor amounts can be even further reduced. The work presented by Zeng *et al.* clearly suggests that technologies for concentration of radiometals could be very useful in this field, i.e. concentrated radiometals could enable reduced precursor consumption while maintaining high labeling yields, and should therefore be further investigated.

Inside of a gallium-68 generator, radioactive germanium-68 is housed and immobilized on a column filled with a matrix (i.e. inorganic, organic, or a mixture). [25] Gallium-68 is formed

as a daughter product from germanium-68 decay. Gallium-68 is typically eluted (“milked”) from the generator in a weak acidic solution (0.1N HCL) in volumes ranging from 4-10mL. During the elution process, metal contaminants (e.g. Ti(IV), Zn(II), Fe(III)) are also eluted along with very small amounts of the long lived germanium-68 parent species. [25] Ti(IV) contamination originates from the column matrix material, Zn(II) is present as it is the decayed product of Gallium-68, and Fe(III) is a contaminant present in acidic eluate used in the milking of the generator. [25,128] These contaminants can compete with gallium-68 during downstream labeling reactions and therefore need to be removed. Furthermore, due to the long half-life of  $^{68}\text{Ge}$  (270 days), injecting  $^{68}\text{Ge}$ -labeled ligand poses a significant safety concern. Several groups have explored concentration and purification (i.e. to eliminate these contaminants) of generator-produced gallium-68 via solid-phase extraction using strong cation exchange cartridges. Zhernosekov *et al.* demonstrated concentration and purification by first trapping gallium-68 on a strong cation exchange cartridge and then eluting purified  $^{68}\text{Ga}$  in a 400 $\mu\text{L}$  acidic acetone solution. [128] Eppard *et al.* and Mueller *et al.* presented similar approaches for concentration and purification of  $^{68}\text{Ga}$  but relied on ethanol and saline-based eluents for recovering the purified  $^{68}\text{Ga}$  in volumes ranging from 0.5-1mL. [129,130] Ethanol and saline are commonly used additives in formulated pharmaceuticals and can be safely injected. [129] Using such eluents instead of acetone simplifies the purification and formulation process for the final labeled tracer (often rendering it unnecessary) and avoids the need for a “residual solvent” quality control test to determine residual acetone.

In chapter 3, we presented work on a standalone [ $^{18}\text{F}$ ]fluoride concentrator relying on a miniaturized strong anion exchange cartridge to trap the [ $^{18}\text{F}$ ]fluoride and allow it to be later eluted into a small volume. [131] We also combined this system with a microfluidic radiosynthesizer developed in our lab [64] (chapter 5) and demonstrated synthesis of

[<sup>18</sup>F]fallypride with high starting activity (chapter 6). In this chapter, we present a modified version of our [<sup>18</sup>F]fluoride concentrator for concentration of gallium-68 to microliter volumes to enable further exploration of microfluidic radiometal labeling (e.g. at high metal concentrations, 1:1 metal:ligand ratios, and low total amounts of ligand).

## 4.2 Methods

### 4.2.1 Materials

Anhydrous methanol (MeOH, 99.8%), Hydrochloric acid (HCL, 37%), ethanol (EtOH, 99.5%), Acetone (HPLC Plus ≥ 99.9%) were purchased from Sigma-Aldrich (St. Louis, MO, USA). Sodium acetate (99%) was purchased from Cambridge isotope laboratories Inc. (Tewksbury, MA, USA). DI water was obtained from a Milli-Q water purification system (EMD Millipore Corporation, Berlin, Germany). Gallium-68 was obtained in 10mL of 0.1N HCl from a generator (IGG100, 3131-0900, 50mCi rating, Eckert & Ziegler, Valencia, CA, USA) located at the UCLA Ahmanson Biomedical Cyclotron Facility.

### 4.2.2 Radionuclide concentrator

A detailed report of the design and operation of the [<sup>18</sup>F]fluoride concentrator was presented in chapter 3. Briefly, our concentration system relies on three subcomponents. One portion of the system controls flows for trapping of [<sup>18</sup>F]fluoride onto a miniaturized strong anion exchange cartridge and later releasing the trapped [<sup>18</sup>F]fluoride. Another part of the system generates the low volumes of eluent solution for [<sup>18</sup>F]fluoride release. The third part is responsible for controlling which reagents are passing through the cartridge. A few minor changes were made to the system to enable concentration of gallium-68. In order to load larger starting volumes (~10mL) typical of gallium generator eluate (compared to cyclotron target volumes in which [<sup>18</sup>F]fluoride is produced), the source vial was changed to a 15mL conical (352096, BD Biosciences, San Jose, CA, USA). Two holes were drilled in the cap of the tube,

one for 1/8" polyurethane tubing to pressurize the reservoir, and one for 1/16" OD 0.04" ID ETFE tubing (1517L, IDEX Health & Science, Oak Harbor, WA, USA) to deliver the reservoir contents to the system. The eluent loop was changed to 19.7cm of 0.01" ID 1/16" OD ETFE (1529L, IDEX Health & Science, Oak Harbor, WA, USA) tubing to increase eluent volume from 6.2µL to 10.0µL since larger resin masses (and larger corresponding eluent volumes) were used compared to our previous work. [131] The micro-cartridge was changed from a strong anion exchange to a strong cation exchange to enable trapping of positively charged [<sup>68</sup>Ga]Ga<sup>3+</sup>. Lastly, the "[<sup>18</sup>O]H<sub>2</sub>O recovery vial" used for [<sup>18</sup>F]fluoride concentration will here be referred to as "trapping waste vial" as the collected contents will not be recycled or reused.

#### **4.2.3 Cartridge fabrication**

Cartridges were made in house in similar fashion to those used for concentration of [<sup>18</sup>F]fluoride as presented in more detail in chapter 6.

##### **4.2.3.1 Resin types**

Due to the cationic nature of gallium-68, a strong cation exchange resin was used for trapping. We explored two different resin types that we removed from two commercially available cartridges. The first resin was Chromafix PS-H<sup>+</sup> (from Chromafix PS cartridge, 220mg sorbent weight, 100 µm particle size, 731861, Macherey-Nagel, Bethlehem, PA, USA). The second resin was Oasis MCX plus (from Oasis MCX Plus Short cartridge, 225 sorbent weight, 60 µm particle size, 186003516, Waters Corporation, Milford, MA, USA).

##### **4.2.3.2 Cartridge design**

Cartridges were fabricated using tubing of different inner and outer diameters. Short segments of 1/16" OD ETFE tubing (IDEX Health and Sciences, Wallingford, CT, USA) with 0.03" (1528L, IDEX) and 0.04" (1517L, IDEX) inner diameters were used. Larger PFA tubing with 1/8" OD 0.063" ID (AP-231SH, Zeus Industrial Product, Inc. Orangeburg, SC, USA) was

also explored. Different inner diameters were used to compare the impact on performance. Resins and frits were directly inserted into the 1/16" OD ETFE tubing. For the larger ID tubing, two segments of 0.03" ID 1/16" OD (1528L, IDEX) tubing were connected to a short piece of larger ID tubing into which the resin and frits were loaded. This design allowed significantly more resin to be loaded without increasing the fluidic resistance (i.e. compared to packing more resin into a longer section of small ID tubing).

#### **4.2.3.3 Cartridge fabrication**

For the smaller cartridges using 1/16" OD tubing, tubing with desired inner diameter was cut into 11cm segments. A small polyethylene frit (1/8" thick, 20 micron porosity) was punched out of a larger disk (FT20751P, UCT, Inc., Bristol, PA USA) and was inserted into the tubing segment. Depending on inner diameter of the tubing used for cartridge fabrication, a punch with matching diameter was used to create the frit. For 0.03" and 0.04" ID tubing, 0.70mm (504529, World Precision Instruments, and 1mm (504646, World Precision Instruments) biopsy punches were used, respectively. Once the frit was inserted into the tubing, it was pushed down 4cm using the needle clearing rod from a spinal needle (Quincke Spinal Needle, BD Biosciences, San Jose, CA, USA) and secured within the tubing by pinching the tube to plastically deforming the tube near the frit. The deformation was performed on the side of the frit closest to the opening in which the frit was loaded (i.e. to block movement of the frit when pressure/flow is applied from the other end of the tubing).

For the cartridges using the larger 1/8" OD tubing, two segments of 1/16" OD 0.03" ID tubing were cut to 4cm length. The 1/8" OD tubing was stretched until point of plastic deformation and then cut to 3cm length. The tubing was stretched to reduce the ID to the point where it snugly fit with the outside of the 1/16" OD tubing. One segment of 1/16" OD tubing was inserted a distance of 0.5cm into the larger OD tubing. A small polyethylene frit (1/8" thick, 20

micron porosity) was punched out of a larger disk (FT20751P, UCT, Inc., Bristol, PA USA) and was inserted into the larger tubing segment and pushed until it contacted the 1/16" OD tubing. The frit was punched using a 1mm punch (504646, World Precision Instruments, Sarasota, FL, USA). The second piece of 1/16"OD 0.03" ID tubing was also temporarily inserted (for the resin loading step) into the other end of the larger diameter.

Next, one end of the partial cartridge is connected to vacuum (-12 PSI), i.e. with the frit side positioned closest to the vacuum source. To prepare a cartridge, loose resin was weighed on a balance (Excellence Plus, Mettler Toledo, Columbus, OH, USA) and placed within a 0.2 mL PCR tube (Fisherbrand, Fisher Scientific, Pittsburg, PA, USA). A slurry was then prepared by adding 0.2mL of DI water into the PCR tube. After slurry formation, the other end of the partial cartridge is inserted into the bottom of the PCR tube to aspirate the slurry into the tubing. The PCR tube is refilled with 0.2mL DI water and aspiration is repeated. Rinsing of the PCR tubing is performed two times after the initial slurry loading. For the cartridges with 1/16" OD tubing, after completion of resin loading, a second frit is punched and placed into the tubing. The frit is pushed until it rests against the resin bed. The tubing near this second frit is pinched to secure the frit and resin bed in place. For the cartridges using 1/8" OD tubing, the second piece of 1/16"OD 0.03" ID tubing is removed, a punched frit is inserted into the large diameter tubing, and is pushed to contact the resin bed. The second piece of 1/16"OD 0.03" ID tubing is then reinserted and is pushed until it is against the frit. The smaller pieces of 1/16" OD 0.03" ID tubing that are inserted into the larger ID tubing keep the frit in position, no tubing pinching is required.

#### **4.2.3.4 Cartridge testing**

After cartridge fabrication, the cartridges undergo a flow rate test to ensure that cartridge flow performance does not deviate significantly from cartridge to cartridge and to also quantify

whether each cartridge design has sufficient flow rate to performing trapping of Ga-68 from the whole generator eluate in a reasonable amount of time. A sample reservoir (Falcon 15 mL conical tube, BD Biosciences, San Jose, CA, USA) was connected to the input of a fluidic flow sensor (SLI-2000, Sensirion Westlake Village, CA, USA) through 25 cm of 0.03"ID 1/16" OD (1528L, IDEX) tubing. The input end of a cartridge was connected directly to the output of the flow sensor. the output end of the cartridge was directly inserted into is a waste reservoir (Falcon 15 mL conical tube, BD Biosciences, San Jose, CA, USA) through a 1/16" OD hole made in the lid of the waste reservoir. The waste reservoir was vented through a second 1/16" OD hole also located in the lid of the reservoir. 3mL of DI water was loaded into the sample reservoir. The sample reservoir was pressurized to 20 psi via a manual pressure regulator (ARX21-N01, SMC Corporation, Japan). Flow rate of DI water through the cartridge was recorded until the 3mL in the sample reservoir was depleted. Flow rates were sampled every 74ms. An average flow rate and standard deviation was determined by averaging the last 500 samples recorded before the sample reservoir was depleted.

#### **4.2.3.5 Cartridge preconditioning**

All cartridges were preconditioned before use with 1mL MeOH followed by a 1mL rinse of DI water based on manufacturer suggesting preconditioning methods.

#### **4.2.4 Trapping and elution testing**

A 1-10mL stock solution of gallium-68 was prepared by either taking the volume directly from the generator or by diluting up a portion of the eluate with 0.1N HCL solution. These solutions contained activities ranging from 13MBq – 970Bq. Different eluent solution compositions were selected based on the work described by Eppard *et al.*, Zhernosekov *et al.*, and Mueller *et al.* [128–130] The eluents chosen were 0.9N HCL in 90% (v/v) EtOH/H<sub>2</sub>O, 0.05N HCL in 98% (v/v) acetone/H<sub>2</sub>O, and 0.13N HCL in 5M NaCl.

Trapping and elution experiments were performed as follows. First, gallium-68 stock solutions were pushed through the cartridge with positive pressure into the trapping waste vial. Following trapping of gallium-68, a 0.5mL rinse of DI water was pushed through the cartridge (via positive pressure) to rinse out residual gallium-68 within the fluidic path. The rinse was also collected in the trapping waste vial. The trapping waste vial was then measured to determine trapping efficiency. Next, a series of 10 $\mu$ L elution operations were performed. Measurements of radioactivity were made after each pair of elutions. Up to a total of 8 elutions were performed. Measurements of elution efficiency were made after each elution operation to optimize the number of elution operations needed.

Characterization of trapping and elution efficiency was performed by taking series of radioactivity measurements with a calibrated dose calibrator (CRC-25 PET, Capintec, Inc., Ramsey, NJ) during the trapping and elution processes. For the purposes of calculations, all radioactivity measurements were decay-corrected to a common time point.

For gallium-68 trap and elute experiments, measurements were made of the starting activity of gallium-68 (“source”) before trapping ( $A_{0\text{source}}$ ), activity remaining in the source container (e.g. vial or syringe) after trapping ( $A_{\text{source}}$ ), activity in the trapping waste vial after trapping ( $A_{\text{waste}}$ ), and the collected activity after elution ( $A_{\text{collect}}$ ). In some cases,  $A_{\text{collect}}$  was measured between individual elution steps to help determine the number of elution steps needed. Activity trapped on the cartridge,  $A_{\text{cartridge}}$ , was measured indirectly (i.e. calculated as  $A_{0\text{source}} - (A_{\text{waste}} + A_{\text{source}})$ ) to prevent unnecessary radiation exposure. Measuring of  $A_{\text{cartridge}}$  directly also gave very inconsistent results, most likely due to variation of cartridge position within the dose calibrator from measurement to measurement. Trapping efficiency (%) was computed as  $A_{\text{cartridge}} / (A_{0\text{source}} - A_{\text{source}})$ . Elution efficiency (%) was calculated as  $A_{\text{collect}} / A_{\text{cartridge}}$ . Recovery efficiency (%) was calculated as trapping efficiency x elution efficiency ( $A_{\text{cartridge}} /$

$(A_{0\text{source}} - A_{\text{source}}) \times (A_{\text{collect}}/A_{\text{cartridge}})$  and describes how much activity is recovered after concentration (i.e. factoring both trapping and elution efficiency).

### 4.3 Results and discussion

#### 4.3.1 Radiometal concentrator cartridge optimization

##### 4.3.1.1 Cartridge fabrication and flow rates

Cartridges were made with varying resin types, resin mass, and tubing inner diameter and flow rates measured for each (Table 4-1). Note that cartridges with 0.06" ID were packed within the larger (1/8" OD) tubing.

**Table 4-1: Flow rates of cartridges fabricated with different resin, resin mass, and tubing inner diameter (ID)**

Each data point represents average  $\pm$  standard (n = 500)

Resin mass	3	3	5	5	7	9	7	9	9	11	15
Resin type	Oasis MCX	Oasis MCX	Oasis MCX	Oasis MCX	Oasis MCX	Oasis MCX	Chroma-fix PS-H+	Chroma-fix PS-H+	Oasis MCX	Oasis MCX	Oasis MCX
Tubing ID (inch)	0.03	0.04	0.03	0.04	0.04	0.04	0.04	0.04	0.06	0.06	0.06
Flow rate ( $\mu\text{L}/\text{min}$ )	1020 $\pm$ 10	3060 $\pm$ 20	630 $\pm$ 0	2000 $\pm$ 10	1580 $\pm$ 20	820 $\pm$ 10	2630 $\pm$ 30	1470 $\pm$ 20	4330 $\pm$ 40	3800 $\pm$ 20	3080 $\pm$ 20

Since starting volumes of gallium-68 can be up to 10mL, we wanted cartridges to have flow rates high enough to ensure trapping can be completed in a reasonable time while also enabling reliable elution (i.e. slow flowing cartridges may impede eluent flow through the resin bed). Acceptable flow rates were chosen to be  $\geq 0.75\text{mL}/\text{min}$ . For all cartridges, with the exception of 5mg Oasis MCX resin in 0.03" ID straight tubing, flow rates were above  $0.75\text{mL}/\text{min}$  (Table 4-1), suggesting that any of these cartridges may be suitable from a flow perspective. Not surprisingly when comparing cartridges with the same resin mass and resin type but varying tubing inner diameter, the cartridges with the largest tubing inner diameter

resulted in the highest flow rates. When comparing cartridges made with the same resin mass and tubing inner diameter but different resin (Chromafix PS-H<sup>+</sup> or Oasis MCX), Chromafix PS-H<sup>+</sup> resin resulted in higher flow rates suggesting that Chromafix PS-H<sup>+</sup> resin should be used when trying to increase cartridge resin mass while minimizing flow rate drop.

## **4.3.2 Trapping and elution optimization**

### **4.3.2.1 Initial cartridge comparison**

An initial series of experiments were performed to compare the trapping and elution efficiencies of different cartridges to help identify which cartridge characteristics (e.g. resin mass, tubing inner diameter) should be prioritized in order to achieve high trapping efficiency, high elution efficiency, and low eluent volume. The total eluted volume from the generator (10 mL) was divided into 1 mL aliquots to use as the source solutions. Elution was performed with a single 200  $\mu$ L volume of 0.9N HCL in 90% (v/v) EtOH/H<sub>2</sub>O. Cartridges were fabricated with Oasis MCX resin with masses ranging from 3 – 15mg and various tubing inner diameters. In these experiments, solutions were manually pushed through the cartridge with a syringe (at ~1 mL/min). Trapping and elution data are shown in Table 4-2.

With only 3mg of resin, we found similar trapping efficiencies of 81% and 83%. Overall, we can see that higher resin masses improve trapping, and lower tubing diameters seem to improve elution, suggesting that maybe the ideal cartridge would be packed with larger resin mass (i.e.,  $\geq$ 7mg) in 0.03" ID tubing. However, this is not possible as flow rates become too low (Table 4-1). Instead, we elected to focus on cartridges with 0.04" ID packed with resin masses  $\geq$ 7 mg, acknowledging that development of improved elution protocols is a key area that needs optimization.

**Table 4-2: Trapping and elution data for various sized cartridges packed with Oasis MCX resin**

Trapping was performed from a 1 mL solution of generator eluate. Elution of the cartridge was performed with 200 $\mu$ L of 0.9N HCL in 90% (v/v) EtOH/H<sub>2</sub>O. Each condition was measured once (n=1).

Tubing ID (inch)	0.03	0.04	0.04	0.04	0.06	0.06	0.06
Resin mass (mg)	3	3	5	7	9	11	15
Trapping Efficiency (%)	83	81	90.	94	99	98	99
Elution Efficiency (%)	94	71	63	70.	29	35	20.

#### 4.3.2.2 Optimization of trapping and elution

Cartridges were prepared with different resin masses and different resin types packed into 0.04" ID tubing. Starting activities ranged from 20MBq – 40MBq in 1mL of 0.1N HCL. (Though initial experiments used only 1 mL of solution from the generator, we scale this up in later experiments to confirm the cartridge capacity.) Trapping and elution were performed with the automated concentrator. Experiments examined different numbers of elution steps and all three eluent solutions.

Trapping efficiency across all resin types and resin masses was nearly quantitative (Table 4-3). Trapping efficiency was slightly lower (~2% less) for 7 mg cartridges versus 9 mg ones. In all cases (resin masses, eluent solutions), the cumulative elution efficiency was significantly higher for the Chromafix PS-H+ resin compared to the Oasis MCX resin.

Focusing on this resin, the acetone-based eluent resulted in 96%  $\pm$  0% (n = 2) and 96%  $\pm$  1% (n = 2) efficiency after 3 elutions for 7mg and 9 mg cartridges, respectively (Table 4-3). With fewer elutions (2 or 1), the elution efficiency dropped significantly, i.e. 68-74% (for 2 elutions) or 5-12% (for 1 elution). With 0.13N HCL in 5M NaCl, the elution efficiency was only 87%  $\pm$  10% (n = 2) after 3 elutions for the same cartridge size (9 mg). For the 0.9N HCL in 90% (v/v) EtOH/H<sub>2</sub>O eluent, elution efficiency was only 10%  $\pm$  9% (n = 2) for the 9mg cartridge.

For subsequent experiments, we chose to use cartridges with 9 mg of Chromafix PS-H<sup>+</sup> resin paired with acetone-based eluent, as this combination best met the goals of maximal trapping and elution efficiencies with minimal eluent volume.

**Table 4-3: Performance of automated trapping and elution with different cartridges (resin type and resin mass) and different eluent solutions**

Each data point represents average  $\pm$  standard deviation (n=2).

Eluent Type	0.05N HCL in 98% (v/v) acetone/H <sub>2</sub> O				0.13N HCL in 5M NaCl		0.9N HCL in 90% (v/v) EtOH/H <sub>2</sub> O	
	Chromafix PS-H <sup>+</sup>	Oasis MCX	Chromafix PS-H <sup>+</sup>	Oasis MCX	Chromafix PS-H <sup>+</sup>	Oasis MCX	Chromafix PS-H <sup>+</sup>	Oasis MCX
Resin Mass	7	7	9	9	9	9	9	9
Activity Trapped	97 $\pm$ 1	99 $\pm$ 0	99 $\pm$ 0	99 $\pm$ 0	99 $\pm$ 1	99 $\pm$ 0	99 $\pm$ 0	99 $\pm$ 0
Elution 1 + 2 Efficiency (%)	5 $\pm$ 6	6 $\pm$ 2	12 $\pm$ 20	1 $\pm$ 0	28 $\pm$ 27	10 $\pm$ 3	2 $\pm$ 1	1 $\pm$ 1
Elution 3 + 4 Efficiency (%)	69 $\pm$ 10	53 $\pm$ 5	55 $\pm$ 3	24 $\pm$ 2	40 $\pm$ 0	3 $\pm$ 3	2 $\pm$ 3	0 $\pm$ 0
Elution 5 + 6 Efficiency (%)	22 $\pm$ 8	31 $\pm$ 7	28 $\pm$ 15	42 $\pm$ 1	19 $\pm$ 10	4 $\pm$ 5	6 $\pm$ 7	0 $\pm$ 0
Elution 1-4 Efficiency (%)	74 $\pm$ 8	59 $\pm$ 7	68 $\pm$ 14	25 $\pm$ 2	68 $\pm$ 30	12 $\pm$ 6	4 $\pm$ 2	1 $\pm$ 1
Elution 1-6 Efficiency (%)	96 $\pm$ 0	90 $\pm$ 0	96 $\pm$ 1	67 $\pm$ 1	87 $\pm$ 10	16 $\pm$ 10	10 $\pm$ 9	1 $\pm$ 1

#### 4.3.2.3 Scale-up of source activity and volume

We wanted to confirm whether the above optimal results would be effective in concentrating a maximal amount of Ga-68 solution from the generator, i.e. volume ~10 mL and high activity of Ga-68 (up to 970MBq for our generator). We first verified that large starting volumes do not negatively impact trapping and elution behavior. We diluted the 1 mL gallium-68 stock solutions (37-74 MBq) used previously up to 10 mL by adding 0.1N HCl solution and repeated the trapping and elution experiments (results seen in Table 4-4). Trapping was high (99%  $\pm$  0%; n = 2) and elution efficiency following 3 elutions was also high (96%  $\pm$  0%; n = 2), confirming that scaling up volume alone (and amount of HCl passing through the cartridge) did not adversely affect performance.

Next, higher starting activity in 10mL starting volume was tested (Table 4-4). For a starting activity of 440 MBq, 5mL of generator eluent was taken and diluted to 10mL with 0.1N HCl solution. Trapping efficiency in this case was 99% (n = 1) and elution efficiency was 93% (n = 1). Trapping and elution experiments were performed with even higher starting activities (760-970MBq) in 10mL starting volume. For these experiments, 10mL of eluent from the generator was used directly without modification. Trapping efficiency was still quantitative ( $100 \pm 0$ ; n = 2) and elution efficiency remained high ( $93 \pm 0$ ; n = 2). These results confirmed that the previously optimized cartridge design and automated concentration protocol is suitable for processing the entire generate eluate.

Concentration of 10mL of gallium-68 to 60  $\mu$ L took a total of ~ 12 min (ie. ~ 7 min for the trapping process and 5 min for the 3 elution operations combined). Since the first elution operation recovered at most ~10% of the trapped activity (amount recovered drops to ~2% with 760-970 MBq starting activity), the output volume could potentially be reduced (with a small sacrifice in amount recovered) by discarding the liquid from the first elution operation. Despite having established an efficient and reliable trapping and elution protocol, it may still prove to be interesting to explore how eluent conditions (e.g. HCL concentration, organic solvent content, varying organic solvents) play a role in elution efficiency.

**Table 4-4: Trap and elution performance of gallium-68 for straight tubing cartridges with 9 grams of Chromafix PS-H<sup>+</sup> resin and 0.05N HCL in 98% (v/v) acetone/H<sub>2</sub>O as an eluent solution**

Each data point represents average  $\pm$  standard deviation (n=2), except for columns marked with \* where n=1.

<b>Starting Activity (MBq)</b>	37-74	440*	760-970
<b>Trapping Efficiency (%)</b>	99 $\pm$ 0	99	100. $\pm$ 0
<b>Elution 1+2 Efficiency (%)</b>	9 $\pm$ 1	5	2 $\pm$ 1
<b>Elution 3+4 Efficiency (%)</b>	71 $\pm$ 4	75	72 $\pm$ 20
<b>Elution 5+6 Efficiency (%)</b>	16 $\pm$ 5	12	20 $\pm$ 20
<b>Elution 1-4 Efficiency (%)</b>	80. $\pm$ 5	81	74 $\pm$ 20
<b>Elution 1-6 Efficiency (%)</b>	96 $\pm$ 0	93	93 $\pm$ 0

#### 4.3.3 Integration with synthesis platform to explore radiometal labeling

Now that we have developed a reliable concentration method for gallium-68 to 60  $\mu$ L, we envision that this activity can then be transferred to a downstream microfluidic radiosynthesizer for labeling. In chapter 6, we demonstrate high activity synthesis of [<sup>18</sup>F]fallypride through successful integration of our [<sup>18</sup>F]fluoride concentrator (chapter 3) with our microfluidic radiosynthesis platform (chapter 5). We plan on using the same integrated platform to explore radiometal labeling using microfluidics. Elution of concentrated gallium-68 in 60 $\mu$ L of 0.05N HCL in 98% (v/v) acetone/H<sub>2</sub>O can be further concentrated by evaporation on the reaction chips to completely remove the eluent solvent. The dried gallium-68 residue can then be dissolved with precursor solution in  $\mu$ L volumes. This will enable labeling with 1:1 metal to ligand ratios, potentially with extremely high metal concentrations. If we can replicate the results shown by Zeng *et al.* demonstrating increased labeling yields with increased radiometal concentration while maintaining a 1:1 metal to ligand ratio [117], we can make a dramatic impact to the radiometal labeling field. Labeling with a 1:1 metal to ligand ratio with high yields enables

reduction of precursor consumption (e.g. 100x less than current methods), and can also increase molar activity of the labeled product.

Though not discussed above, this further concentration process was also an important consideration in optimization of the elution methods. In addition to its higher elution efficiency (for a given volume), the acetone-based eluent is preferred over the saline-based eluent because the latter would result in a significant quantity of NaCl in the gallium-68 residue, resulting in extremely high salt concentrations that could impede downstream  $^{68}\text{Ga}$ -labeling. For example, starting with 60  $\mu\text{L}$  of 5M NaCl eluate, drying, and redissolving into a 6  $\mu\text{L}$  droplet of precursor solution would result in a 50M NaCl concentration.

#### **4.4 Conclusion and Future Work**

In this chapter, we have developed and optimized a new method for concentration of gallium-68 to microliter-scale volumes. Using an automated radionuclide concentration platform that features small physical size and reliable operation (highlighted in chapter 3), concentration of gallium-68 was achieved through the use of a miniaturized strong cation exchange cartridge. We evaluated several cartridge designs, resin types, resin masses, and eluent solutions and with optimal choices could achieve nearly quantitative trapping and elution of gallium-68. Concentration of gallium-68 (up to 970 MBq in 10mL of volume) down to 60 $\mu\text{L}$  was successfully performed in ~15 min with ~93% overall recovery efficiency. Compared to a 400 $\mu\text{L}$  final concentrated volume, currently the lowest volume that we could find in literature [128] for concentrated gallium-68, our system provides a substantial improvement (~7x).

For future work on the system, we will first perform a proof of concept labeling experiment of [ $^{68}\text{Ga}$ ]Ga-HBED-CC-PSMA-11 on our microfluidic reactor chip (described in chapter 5) to first verify the ability to translate macroscale labeling protocols onto our microfluidic radiosynthesizer, and to also verify gallium-68 quality for labeling post

concentration. Reagent loading and extraction for these initial experiments will be performed manually, using the reactor setup solely for heating. Following this proof of concept experiment, we will explore labeling of [<sup>68</sup>Ga]Ga-HBED-CC-PSMA-11 with reduced ligand amount to increase molar activity while maintaining high yield. Next, by using the radiometal concentrator integrated with our microfluidic radiosynthesizer (described in more detail in chapter 6), we will perform exploring automated labeling with 1:1 metal to ligand ratio and highly concentrated radiometal as highlighted by Zeng *et al.* [117] In order to achieve high metal concentrations, high starting activities will be used. These experiments, therefore will also verify that [<sup>68</sup>Ga]Ga-HBED-CC-PSMA-11 can be produced in large quantities. After successful demonstration with [<sup>68</sup>Ga]Ga-HBED-CC-PSMA-11, the same set of proof of concept, optimization and 1:1 metal to ligand labeling experiments will be performed on [<sup>68</sup>Ga]Ga-DOTATOC to explore the flexibility to label other ligands using the same apparatus and methods.

If low labeling yields are observed, we will perform analysis of trace metal contaminants (e.g. <sup>68</sup>Ge, Ti(IV), Zn(II), Fe(III)) as presence of these metals in the reaction can compete with gallium-68, lowering labeling yields. Using conventional cartridges, several groups have studied these metals and reported methods for reducing them that possibly could be adapted to our microscale approach. For example, Zhernosekov *et al.* demonstrated that during trapping, ~3% of <sup>68</sup>Ge is trapped to the cartridge with the majority passing to waste, and also demonstrated that ~93% Ti(IV) is trapped to the cartridge. [128] For both <sup>68</sup>Ge and Ti(IV) only trace amounts (<0.12% of starting) are released from the cartridge during gallium-68 elution with 0.4 mL of 0.05N HCL in 98% (v/v) acetone/H<sub>2</sub>O. [128] Both Zn(II) and Fe(III) are quantitatively trapped on the cartridge during the trapping step. Using a wash solution of 0.15N HCl in 80% (v/v) acetone/H<sub>2</sub>O (i.e. different HCl concentration than the eluent; discarded to waste instead of collected), Zn(II) was removed quantitatively regardless of rinse volume (0.6 mL or 5 mL), while

Fe(III) was partially retained on the cartridge (~38% removed with 0.6 mL; 87% removed with 5 mL). However, the wash solution partially released the gallium-68: 1.4% or 6.3% of the trapped amount was washed away with 0.6 mL or 5 mL of the wash solution, respectively. Using ICP-MS, we will study the contaminant profile in our generator eluate and concentrator output and compare to published levels of contamination. If high levels are found, we will perform an analysis of the system and method to ensure that metal-free components, reagents, and handling techniques are used throughout. For example, one metal component is the nozzle on the piezoelectric dispenser; if this is a significant contamination source, we will explore alternative nozzles and/or protective coatings to limit this issue. If necessary, we will also explore the addition of washing steps, using ICP-MS to quantify the effect on the levels of metal contaminants and labeling reactions to quantify the impact on yields. We believe removal of trace metals will help with improving molar activity and also result in high labeling yields when labeling with a 1:1 metal to ligand ratio. Demonstration of batch based microfluidic radiometal labeling as well as labeling with a 1:1 radiometal to ligand ratio with high radiometal concentration, to our knowledge has yet to be presented in the field. We believe that this concentration platform can play a key role in advancing the field of biomolecule labeling with radiometals.

## 5 Chapter 5: Design of a simple and reliable microfluidic radiosynthesizer

### 5.1 Introduction

To increase accessibility to diverse PET tracers, advances are needed in radiosynthesis technology that make it possible to produce smaller batches on demand at an affordable cost. In recent years there has been significant development of microfluidic devices to perform radiochemical synthesis of PET tracers. [93,132] Among the various approaches that have been explored, droplet-based systems have perhaps the most potential for cost reductions. [48,51] By performing reactions at the microliter scale, amounts of expensive reagents such as precursor can be reduced by 2-3 orders of magnitude compared to conventional approaches. In addition, miniaturization of the overall synthesizer can significantly reduce the cost of equipment and radiation-shielded facilities. Furthermore, the small volume scale reduces contamination, and  $^{18}\text{F}$ -labeled tracers can be produced in much higher molar radioactivity due to the reduction of fluorine-19 from reagents and other sources. Presented in chapter 1, we have shown automated droplet-based radiosynthesis of several PET tracers using electrowetting-on-dielectric (EWOD) systems. [46,47,49,50] In EWOD microfluidic chips, electrodes are used to transport reagents, as they are needed, from fixed reagent loading sites to a central, temperature-controlled zone where evaporation and reaction processes are carried out to perform multi-step radiosyntheses. Despite successful implementation, routine use of EWOD for radiochemical synthesis is limited by the complex fabrication of chemically-compatible chips (i.e. based on glass substrates). The large number of processing steps makes the chips expensive and the relatively large surface area (e.g., ~25 mm square) makes it challenging to produce the pinhole-free dielectric layers that are essential to avoid dielectric breakdown and electrolysis of droplets on the chip.

To address these issues, we investigated the use of microfluidic devices relying on passive droplet manipulation to provide the same function of moving reagent droplets from fixed loading sites to a central reaction region. Passive devices do not use electrodes or other active means of actuation, but rather rely on gradients in geometry or surface tension to transport droplets. [133] Xing et al. reported a capillary micropumping technique in which droplets could be pumped along superhydrophilic pathways toward a pre-existing larger droplet. [134] Yeh et al. reported a method to generate a gradient in the density of hydrophobic decyltrichlorosilane (DTS) molecules on a substrate and observed that droplets moved toward the more hydrophilic side. [135] Similarly, Liu et al. reported spontaneous droplet motion on a surface patterned with a gradient in the density of superhydrophilic pillars fabricated within a hydrophobic background. [136] Ng et al. reported a method to move droplets using the Marangoni force. An ethanol (EtOH) droplet was positioned next to the water droplet to be actuated. Evaporation of ethanol formed a vapor gradient that dissolved into the surface of the water droplet, and caused the water droplet to move away from the highest ethanol concentration. [137] Droplets can also be made to move spontaneously due to a height gradient between two non-parallel substrates. Whether the droplet is wetting or non-wetting determines whether it moves toward the side with narrowest or widest height, respectively. [138–140] In another geometric approach, a gradient in the width of a superhydrophilic path on a superhydrophobic surface was reported by Ghosh et al. to generate spontaneous motion of a droplet. [141] As seen in Figure 5-1B, a droplet on such a track experiences an imbalance in surface tension forces along the leading and trailing boundaries of the liquid footprint, leading to a net force on the droplet toward the wider end of the track. Not only is droplet transport possible, but multiple tracks can be merged, or droplets can be held in position until they accumulate enough volume to be further transported.

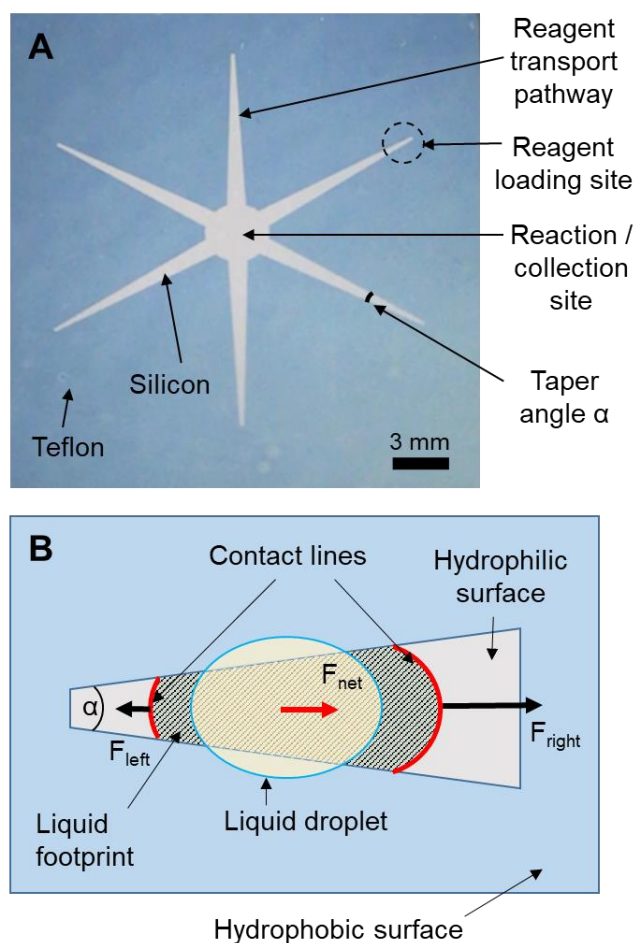


**Figure 5-1 Photograph and schematic of the passive microfluidic chip**

(A) Photograph of fabricated passive microfluidic chip (top view). The star pattern is a hydrophilic surface (silicon); the remainder is hydrophobic (Teflon). The diameter of the central circular reaction zone is 3.0 mm. The taper angle  $\alpha$  of each delivery channel is  $5^\circ$ , and length from the narrow end to center is 9.7 mm. The width of the narrow end of each delivery channel is 0.17 mm. (B) Illustration of passive transport mechanism of a droplet on a wedge-shaped pathway.  $F_{net}$  is the net force due to the larger contact line at the leading (right) edge of the liquid footprint compared to the trailing (left) edge, driving the liquid in the direction of the wider track.

While these techniques provide a wide range of possible transport mechanisms, not all would be suitable for loading reagents for performing multi-step chemical reactions. For example, capillary pumping relies on the presence of droplets at both the source and destination, but the reaction zone is often completely dried in one or more steps of the synthesis process. In approaches that rely on chemical gradients, the presence of solvents or surface-

bound molecules could potentially interfere with, or be affected by, the intended chemical reactions on the chip. Certain geometric gradients (e.g. variation in DTS density on surface or variation in height between two substrates) do not appear to lend themselves to the creation of sophisticated channel networks for multi-step reactions. We therefore elected to work with the approach of Ghosh et al., for which the “channels” can be routed in any direction via simple photolithographic fabrication processes.

We hypothesized that this latter passive transport mechanism could be used to develop a chip for multi-step chemical reactions based on the idea that reagents and solvents are sequentially delivered to a central reaction zone with intervening reaction (heating) and evaporation steps. To pattern the surface, Ghosh et al. used a mixture of TiO<sub>2</sub> powder and hydrophobic polymer, and then activated the TiO<sub>2</sub> with UV light in specific regions to catalyze destruction of the polymer. [141] However, TiO<sub>2</sub> has reactive properties [142] that may cause interference with the desired radiochemical reactions, and thus, in this report, we developed an alternative implementation that avoids the use of TiO<sub>2</sub> to generate similar patterned surfaces. In this chapter, we discuss the fabrication technique, characterize the movement of several important solvents on patterned surfaces, and design a chip for multi-step reactions. Finally, the multi-step radiosynthesis of (S)-N-((1-Allyl-2-pyrrolidinyl)methyl)-5-(3-[<sup>18</sup>F]fluoropropyl)-2,3-dimethoxybenzamide ([<sup>18</sup>F]fallypride) is demonstrated and then the syntheses is automated by implementation of reagent delivery and product collection mechanisms.

Compared to EWOD microsystems, it is expected that passive microfluidic devices will have advantages of significantly reduced chip cost and enhanced reliability (since the need for a dielectric layer, sensitive to defects, is eliminated entirely). In addition, the overall system should be simpler and less expensive since many droplet operations do not require actively-controlled actuators. Although the idea and mechanism of passive droplet manipulation has been studied

for several years, to the best of our knowledge, it has not yet been used as a means to deliver reagents for chemical reactions.

## 5.2 Materials and Methods

### 5.2.1 Materials

1% Teflon AF 2400 solution was purchased from Chemours. Positive photoresist (MEGAPOSIT SPR 220-7.0) and developer (MEGAPOSIT MF-26A) were purchased from MicroChem (Westborough, USA). Additional solvents and chemicals used for microfluidic chip fabrication, including methanol (MeOH, Cleanroom LP grade), acetone (Cleanroom LP grade), isopropanol (IPA, Cleanroom LP grade), sulfuric acid (96%, Cleanroom MB grade) and hydrogen peroxide (30%, Cleanroom LP grade), were purchased from KMG Chemicals (Fort Worth, USA).

Anhydrous dimethyl sulfoxide (DMSO, 99.9%), 2,3-dimethyl-2-butanol (hexyl alcohol, 98%), methanol (MeOH), anhydrous acetonitrile (MeCN, 99.8%), ammonium formate ( $\text{NH}_4\text{HCO}_2$ ; 97%), and trimethylamine (TEA, 99%) were purchased from Sigma-Aldrich. Tetrabutylammonium bicarbonate ( $\text{TBAHCO}_3$ , 75mM), tosyl fallypride (fallypride precursor, >90%), and fallypride (reference standard for [ $^{18}\text{F}$ ]fallypride, >95%) were purchased from ABX Advanced Biochemical Compounds (Radeberg, Germany). Dulbecco's phosphate-buffered saline (PBS, 1X) was purchased from Mediatech (Manassas, VA, USA). Food dye was purchased from Kroger (Cincinnati, OH, USA) and diluted with deionized (DI) water in the ratio of 1:100 (v/v). DI water was obtained from a Milli-Q water purification system (EMD Millipore Corporation, Berlin, Germany). No-carrier-added [ $^{18}\text{F}$ ]fluoride in [ $^{18}\text{O}$ ]H<sub>2</sub>O was obtained from the UCLA Ahmanson Biomedical Cyclotron Facility.

## 5.2.2 Design and fabrication of microfluidic droplet reactor

Batches of microfluidic chips were fabricated in the Integrated NanoSystems Cleanroom (California NanoSystems Institute, UCLA) from 4" silicon wafers using standard lithographic processes. A diagram of the process is shown below in Figure 5-2.

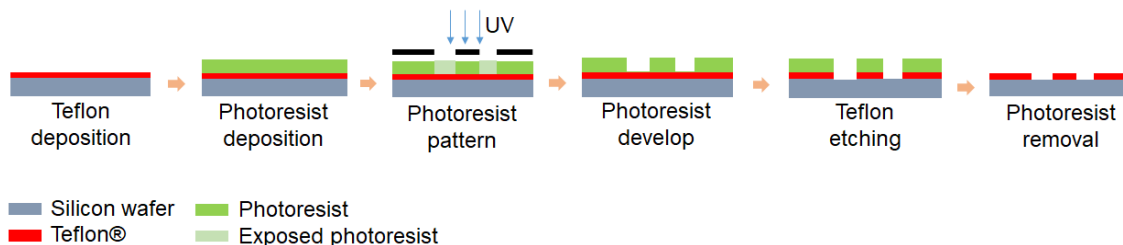


**Figure 5-2: Schematic of microfluidic chip fabrication process**

A silicon wafer is first spin-coated with Teflon® AF 2400. The Teflon is patterned by first spin-coating and patterning photoresist as an etch mask, and then removing exposed Teflon via dry-etching. Finally the wafer is diced into individual chips and each chip is subject to photoresist removal and treatment with Piranha solution to increase hydrophilicity of patterned pathways.

The wafer was spin-coated with Teflon AF 2400 solution at 1000 rpm for 30 s and then heated on a hotplate at 160°C for 10 min, 245°C for 10 min, and then annealed in an oven (HTCR 6 28, Carbolite, UK) at 340°C for 3.5 h under nitrogen atmosphere. The final thickness of the Teflon layer was ~150 nm as measured by surface profilometry (Dektak 150, Veeco, Plainview, NY, USA). The Teflon layer was patterned via dry etching. [143] A positive photoresist (SPR 220-7) layer was spin-coated at 3000 rpm for 30 s on top of the Teflon and then soft baked at 115°C for 3 min. After that, the photoresist layer was patterned by UV exposure (MA6 mask aligner, Karl Suss, Garching, Germany) and developed according to the manufacturer's recommended protocol. The exposed Teflon regions were then etched away via 30s exposure to oxygen plasma (PlasmaLab system 80 RIE plus, Oxford Instruments, UK) at 100 mTorr pressure, 200 W power and 50 sccm oxygen flow. The wafer was then diced into individual 25.0 x 27.5 mm microfluidic chips manually with a silicon wafer cutter. Afterwards,

chips were dipped into acetone for 1 min to remove photoresist, rinsed in IPA for 1 min, and dried with nitrogen. To further increase the hydrophilicity of the patterned surface, the microfluidic chips were cleaned with Piranha cleaning solution (96% sulfuric acid; 30% hydrogen peroxide, 3:1 v/v mixture) prior to use. Contact angles of the surface at different steps was measured with a contact-angle goniometer (VCA-3000S, AST, Billerica, MA, USA).

The microfluidic chip comprises a hydrophobic surface with a circular hydrophilic reaction zone in the center (3.0 mm diameter), and six inward-leading tapered hydrophilic pathways for reagent transport (Figure 5-1A). Liquid reagent droplets are transported passively from reagent loading sites to the central reaction region by the patterned wettability mechanism reported by Ghosh et al. [141] (Figure 5-1B). A simple chip design, consisting of a single delivery channel connected to a circular reaction zone, was fabricated to evaluate suitability of passive transport for various aqueous and organic solvents (Figure 5-3A). Taper angles  $\alpha$  were varied in  $1^\circ$  increments from  $1^\circ$  to  $10^\circ$  to investigate the droplet movement behavior. Video of droplet movement on the chip was recorded with an iPhone 7 camera at 60 fps (1080p HD). Transporting time was calculated by subtracting starting frame number (droplet just loaded on the pathway, Figure 5-3B) from ending frame number (droplet just reached the reaction zone, Figure 5-3C).

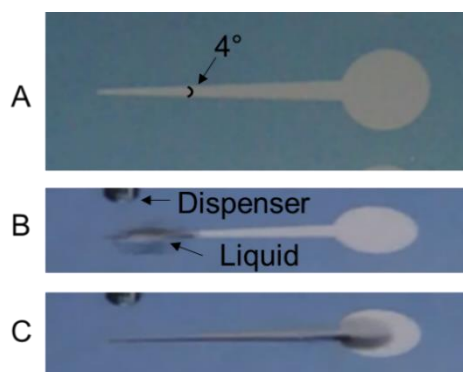


**Figure 5-3: Droplet dispensing and movement on simple passive microfluidic chips**

(A) Photograph of the simple passive microfluidic chip for characterizing droplet movement (top view). The taper angle of the pathway in this particular chip was  $4^\circ$ . (B) Video frame from video recording of  $1\ \mu\text{L}$  DI water on the pathway. Note that for practical reasons, the video was taken at a slightly oblique angle above the chip. The frame shows the droplet has just been deposited at the start of the pathway and was defined as starting frame. (C) Video frame showing the same droplet at the time it reached the reaction site (defined as the ending frame). The number of intervening frames could be used to compute the transport time.

Passive transport chips of six pathways and one reaction site were fabricated as described above. Droplets of various sizes ( $0.5\ \mu\text{L}$ ,  $1\ \mu\text{L}$ ,  $1.5\ \mu\text{L}$ ,  $2\ \mu\text{L}$ ,  $5\ \mu\text{L}$ ) were manually loaded on the narrow end of bottom pathway. Photos (Figure 5-4) were taken at the moment when solvents stopped moving. For DI water, the majority of the droplet maintained in the reaction site for droplet volumes smaller than  $2\ \mu\text{L}$ . MeOH and MeCN behaved similarly to DI water. The higher evaporation rate may help to prevent overflow of the reaction site. DMSO easily overflowed even with the lowest ( $0.5\ \mu\text{L}$ ) droplet volume.

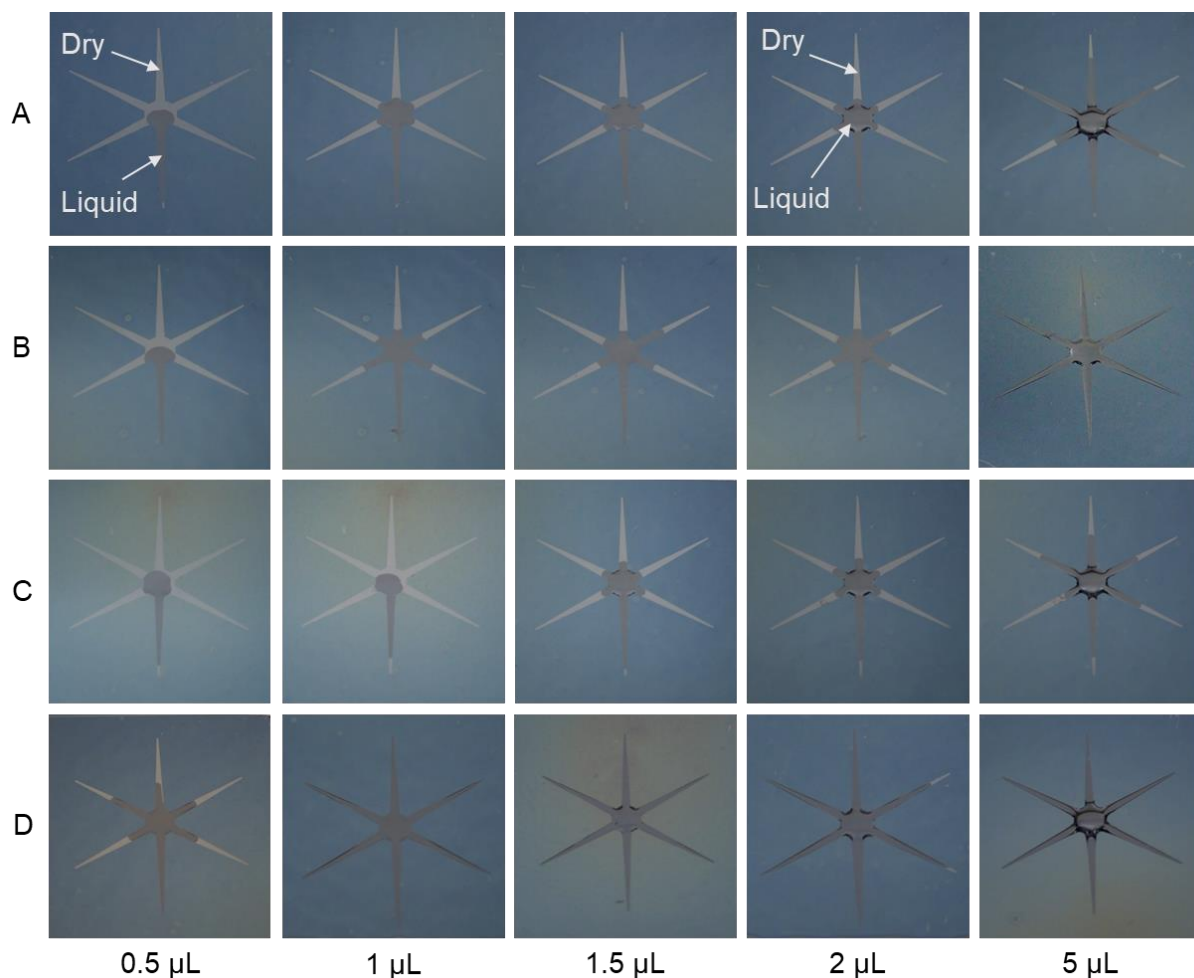


**Figure 5-4: Behavior of solvents droplets of different volumes after reaching the reaction site** (A) DI water; (B) MeOH; (C) MeCN; (D) DMSO.

### 5.2.3 Automation of microdroplet reactions

Operations on the microfluidic chip were automated by a custom-built temperature control platform, reagent dispensing subsystem and solution collection subsystem. Heating was provided by placing the chip in direct contact with a ceramic heater (Ultramic CER-1-01-00098, Watlow, St. Louis, MO, USA). The heater was affixed atop a 40 cm x 40 cm thermoelectric device (Peltier, VT-199-1.4-0.8, TE Technology, Traverse City, MI, USA) mounted to a heatsink and cooling fan (AFB0512VHD, Delta Electronics, Taipei, Taiwan). A custom plastic frame

above the Peltier (and bolted to the heatsink) helped keep the heater in place while also providing two flat vertical edges for rapidly positioning one corner of the microfluidic chip. The signal from a K-type thermocouple embedded in the heater was amplified through a K-type thermocouple amplifier (AD595CQ, Analog Devices, Norwood, MA, USA) and connected into a data acquisition device (DAQ; NI USB-6211, National Instruments, Austin, TX, USA). A digital output of the DAQ was used to drive a solid-state relay (SSR, Model 120D25, Opto 22, Temecula, CA, USA) to control the supply of 120 VAC to the heater. An on-off temperature controller was programmed in LabView (National Instruments). To cool the heater, the Peltier was driven by a 24V power supply (TDK-Lambda Americas, National City, CA, USA) operated through another SSR controlled by the LabView program. A power step down module (2596 SDC, Model 180057, DROK, Guangzhou, China) was connected to the 24V power supply to provide 12V for the cooling fan, which was switched on during cooling via an electromechanical relay (SRD-05VDC-SL-C, Songle Relay, Yuyao city, Zhejiang, China) controlled by the LabView program.

Droplets were loaded onto the microfluidic chip at reagent loading sites through miniature, solenoid-based, non-contact dispensers (INKX0514300A and INKX0514100A, Lee Company, Westbrook, CT, USA). A different dispenser (INKX0514100A) with seal material made of FFKM was used to dispense the fallypride precursor solution. Other solutions were loaded through dispensers (INKX0514300A) with seal material EPDM. Basically, each dispenser is connected to a pressurized source of a reagent, and the internal solenoid valve is opened momentarily to dispense liquid; the amount of liquid dispensed is related to the duration the valve is open. The inlet of each dispenser was connected to a 1 mL glass V-vial (03-410-024, V Vial™ with Open-Top Screw Cap, Wheaton, Millville, NJ, USA) sealed with a septum (224100-072, Wheaton) via ETFE tubing (1/16" OD, 0.010" ID, 1529L, IDEX Health & Science,

Oak Harbor, WA, USA). The septum was pre-punched with a 1 mm OD biopsy punch (Integra Miltex, York, PA, USA). A bevel was cut on the end of the tubing and positioned at the bottom of the vial. Nitrogen pressure was supplied to the headspace of the vial via a 25G needle (Beckton Dickinson, Franklin Lakes, NJ, USA) inserted directly through the septum. The needle was connected via 1/8" OD tubing to the output of an electronic pressure regulator (ITV0030-3UBL, SMC Corporation, Noblesville, IN, USA) controlled by the LabView program. The reagent stock solutions were pipetted directly into the vial. For precursor solution and [<sup>18</sup>F]fluoride solution, the smaller volume (30-50 μL) was loaded into a 250 μL vial insert (5181-1270, Agilent Technologies, Santa Clara, CA, USA) installed into the V-vial. The outlet of each dispenser was fitted with a nozzle (ID 0.005", INZA4650935K, Lee Company), which is recommended for generation of droplets with volume in the range of 100s of nL to several μL. Each dispenser was powered via a dedicated driver circuit (IECX0501350A, Lee Company) and controlled via the LabView program. Note that because the dispensing rate depends on the driving pressure, viscosity of solvent, tubing size, and nozzle site, a calibration was performed for each type of liquid to determine the valve opening time that should be used to dispense a particular volume.

Dispense volumes by the non-contact dispensers were measured by averaging the weight of dispensed solutions. The dispenser was opened for a certain duration at 5 psi and the dispensed solution was collected in an empty PCR tube. After n=10 such droplets were dispensed, the total mass of the dispensed liquid was determined on an analytical balance. Using the known density of the solution at room temperature, the total volume was determined. The average volume of an individual droplet was determined by dividing by n=10. Plots of dispensed volume versus valve opening time are shown in (Figure 5-5). The relationship was approximately linear for times > 10 ms. The curves could be used to determine the necessary

time to dispense a particular volume. Before use, each dispenser was manually primed (using 3 psi nitrogen) to ensure all air ahead of the liquid was eliminated.

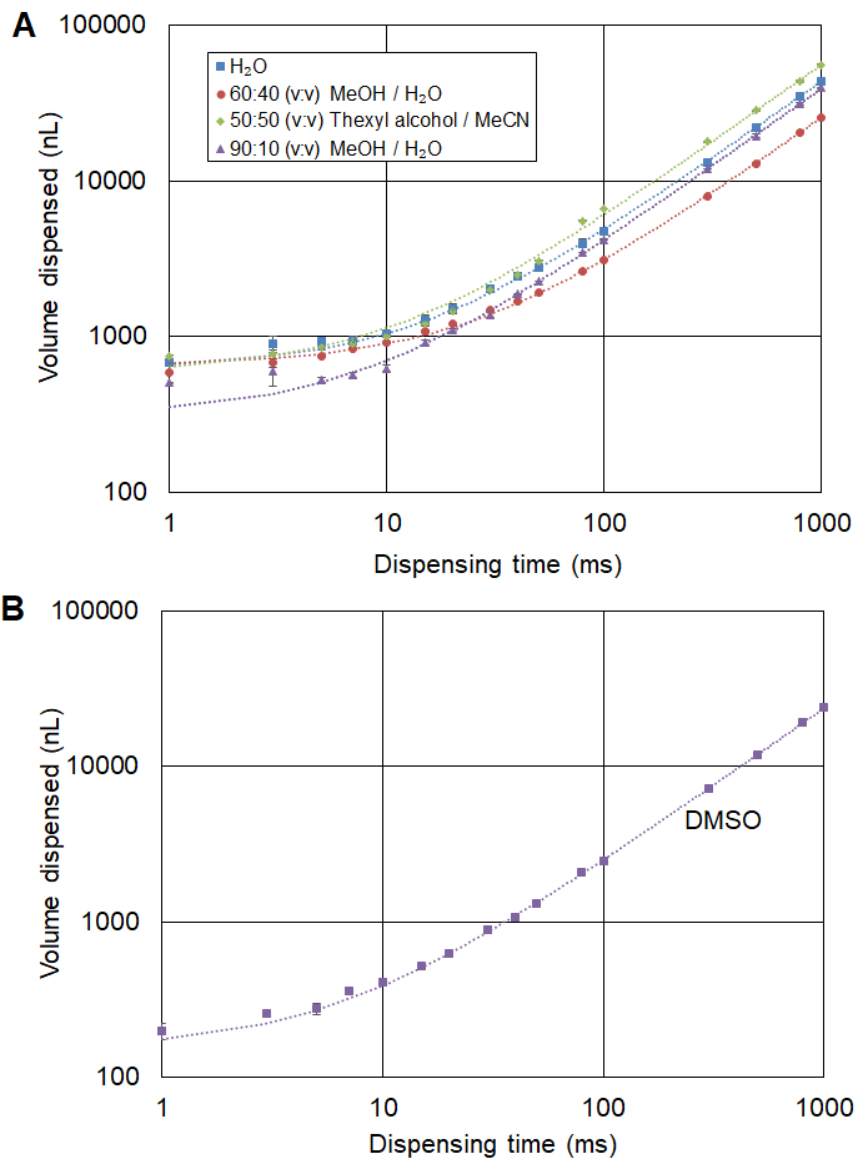


**Figure 5-5: Calibration curves for dispensed droplet volume**

(A) Various solvent mixtures using INKX0514300A dispensers with solvent reservoir pressurized to 5 psi. Trend lines are linear fits with  $R^2$  values of 0.9999 for DI water ( $H_2O$ ), 0.9999 for 60:40 v/v MeOH /  $H_2O$ , 0.9995 for 50:50 v/v thexyl alcohol / MeCN, and 0.9998 for 90:10 v/v MeOH /  $H_2O$ . (B) DMSO dispensed with INKX0514100A dispenser and reservoir pressurized to 7 psi.  $R^2$  for the linear fit was 1.0000.

A fixture (Figure 5-6C) was built to hold 6 dispensers with nozzles ~2 mm above the 6 loading sites of the microfluidic chip. Each dispenser was secured within a hole by an O-ring (ORBN005, Buna-N size 005, Sur-Seal Corporation, Cincinnati, OH, USA). After completing the multi-step reaction, each dispenser was flushed with 1 mL of DI water and MeOH sequentially at 69 kPa (~10 psi), and dried with nitrogen for 2 min.

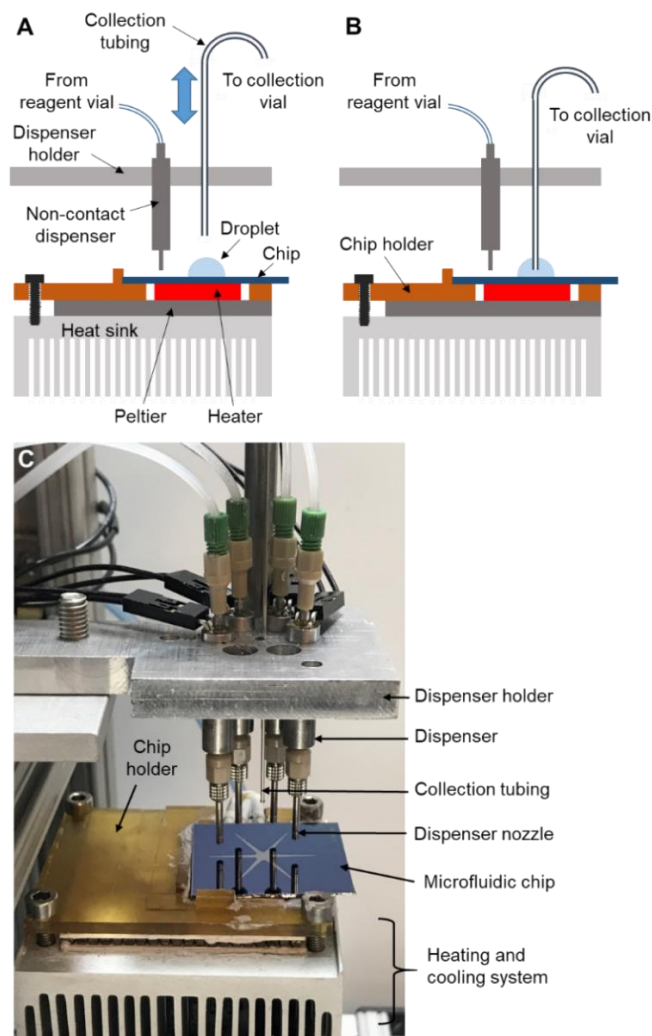


**Figure 5-6: Schematic and photograph of microreactor system**

(A) Schematic of droplet microreactor system, including reagent dispensing system, crude product collection system, and heating and cooling system. (B) Schematic showing configuration for product collection, i.e. with collection tubing lowered into the droplet. The pneumatic cylinder used to lower the tubing is omitted for clarity. (C) Photograph of the microfluidic platform.

A liquid collection subsystem was implemented to transfer the final crude reaction product droplet from the microfluidic chip to the collection vial. A 23G hypodermic metal tubing (304H23XX, MicroGroup, Medway, MA, USA) was inserted through a hole in the center of the dispenser fixture. The height of this tube was controlled by mounting it on a single-acting pneumatic cylinder (6498K511, McMaster-Carr, Santa Fe Springs, CA, USA). The pneumatic cylinder was activated by applying 138 kPa (~20 psi) pressure from an electronic pressure regulator (ITV0030-3UBL, SMC Corporation) controlled by the LabView program. In its non-active position, the end of the tubing was ~ 55.5 mm above the chip surface (Figure 5-6A). The droplet was collected by making close contact (~0.5 mm) to the chip (Figure 5-6B), and applying vacuum to the headspace of the collection vial using a compact vacuum pump (0-16" Hg vacuum range, D2028, Airpon, Ningbo, China) connected via a vacuum regulator (ITV0090-3UBL, SMC Corporation). Vacuum pressure was ramped from 0 to 21 kPa (~3 psi, 0.01 psi increment every 100 ms) over 30 s to collect the crude product droplet. After collecting the crude product, the collecting tubing was cleaned by flushing with a 1 mL mixture of MeOH and DI water (1:1, v/v).

#### **5.2.4 On-chip radiosynthesis of [<sup>18</sup>F]fallypride**

The synthesis conditions of [<sup>18</sup>F]fallypride (Figure 5-7) were adapted and further optimized from our previous work synthesizing this compound using EWOD chips. [49] A [<sup>18</sup>F]fluoride stock solution was prepared by mixing [<sup>18</sup>F]fluoride/[<sup>18</sup>O]H<sub>2</sub>O (100 μL, ~370 MBq; ~10 mCi) with 75 mM TBAHCO<sub>3</sub> solution (5 μL). Precursor stock solution was prepared by dissolving fallypride precursor (4 mg) in a mixture of MeCN and hexyl alcohol (1:1 v/v, 100 μL). A stock solution for dilution of the crude product prior to collection was prepared from a mixture of MeOH and DI water (9:1, v/v, 500 μL). These solutions were loaded into individual reagent vials connected to dispensers.

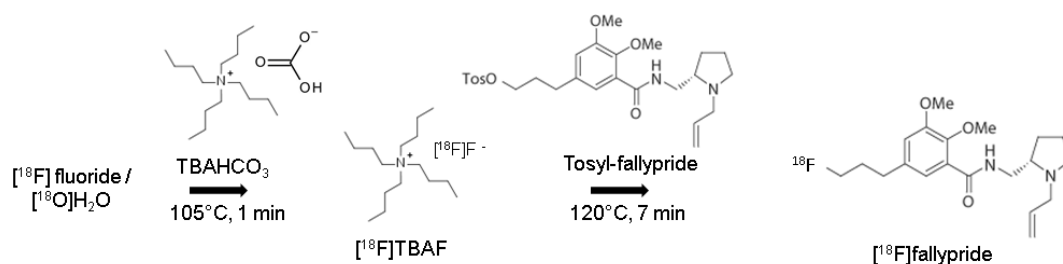


**Figure 5-7: Radiosynthesis scheme of  $[^{18}\text{F}]$ fallypride**

$[^{18}\text{F}]$ fluoride drying step is shown followed by radiofluorination of precursor.

To perform the on-chip synthesis, a 2  $\mu\text{L}$  droplet of  $[^{18}\text{F}]$ fluoride solution ( $\sim 7.4$  MBq;  $\sim 0.2$  mCi) was first loaded onto the chip and spontaneously transported to the reaction site. The microfluidic chip was heated to 105°C for 1 min to evaporate the solvent and leave a dried residue of the  $[^{18}\text{F}]$ tetrabutylammonium fluoride ( $[^{18}\text{F}]$ TBAF) complex at the reaction site. It was found that the typical azeotropic distillation process (i.e. addition and evaporation of MeCN) to remove residual moisture was not needed.

Next, a 1  $\mu\text{L}$  droplet of fallypride precursor solution was deposited at another loading site and was spontaneously transported to the reaction site, where it dissolved the dried residue. Then, another 1  $\mu\text{L}$  droplet of fallypride precursor solution was deposited and transported the same way. The chip was heated to 110°C and held for 7 min to accomplish the radiofluorination reaction. Then, ten 1  $\mu\text{L}$  droplets of collection solution were sequentially deposited at a different reagent loading site and spontaneously moved to reaction site to dilute the resulting crude reaction mixture. Afterwards, the diluted droplet was transferred into the collection vial. The collection process was repeated 5x to minimize residue on the chip. A schematic of the on-chip process is shown in Figure 5-8.

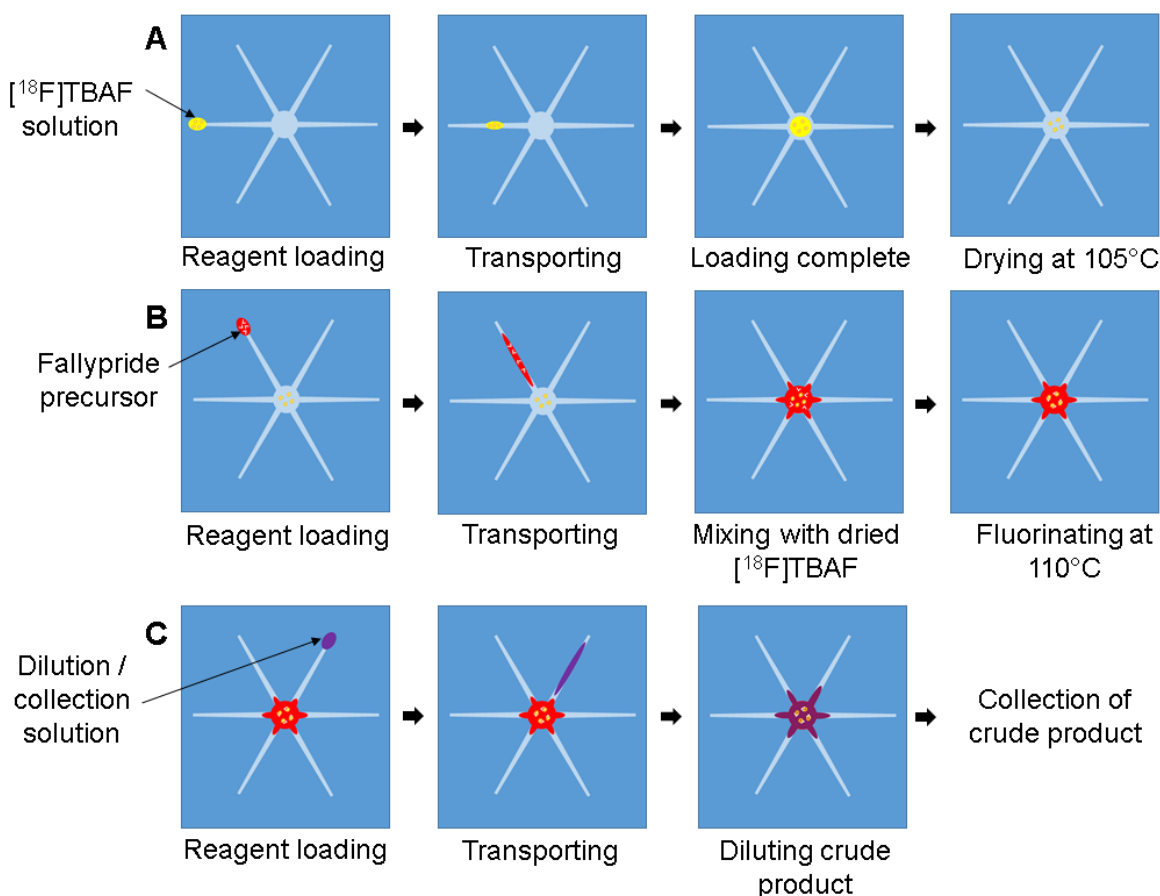


**Figure 5-8: Schematic of  $[^{18}\text{F}]$ fallypride synthesis on the passive microfluidic chip**

(A)  $[^{18}\text{F}]$ fluoride solution is loaded and dried. (B) Precursor solution is loaded and fluorination reaction is performed. (C) Collection solution is loaded to dilute the crude product, which is then collected. Note that each reagent is loaded from a dedicated dispenser and reagent pathway. The synthesis of  $[^{18}\text{F}]$ FDG is quite similar but there is an additional reaction step between steps B and C. After the fluorination reaction, the deprotection agent (NaOH) is added, transported to the center, and the room temperature hydrolysis reaction is performed.

### 5.2.5 Analytical methods

Performance of the chip-based reaction was assessed via measurements of radioactivity and radiochemical purity (RCP). Radioactivity was measured with a calibrated dose calibrator (CRC-25R, Capintec, Florham Park, NJ, USA) at various times throughout the synthesis process (including starting radioactivity on the chip after loading of  $[^{18}\text{F}]$ fluoride stock solution). Radioactivity recovery was calculated as the activity of the collected crude product divided by the starting radioactivity, corrected for decay. Collection efficiency was calculated as the activity

of the collected crude product divided by the activity on chip after synthesis, corrected for radioactive decay. To gain further insights into the synthesis process, residual activity on the chip was measured after collection of the crude product. We report this as a fraction of the activity on chip just prior to the collection step, corrected for radioactive decay. Similarly, the residual activity in the collection system was measured and expressed as a fraction of the activity on chip just prior to collection, corrected for radioactive decay. In manual syntheses, the residual activity on the pipette tips used for collection was measured in a dose calibrator. In automated syntheses, the residual activity in the collection tubing was determined by measuring the activity of the cleaning solution (1:1 v/v MeOH/water, 1 mL) in a dose calibrator.

RCP of the crude compound collected from the chip was determined via radio thin layer chromatography (radio-TLC). A 1  $\mu$ L droplet was spotted on a silica TLC plate (JT4449-2, J.T. Baker, Center Valley, PA, USA) with a micropipette. The TLC plate was developed in an appropriate mobile phase and then analyzed with a scanner (MiniGITA star, Raytest, Straubenhardt, Germany).

For [ $^{18}$ F]fallypride, the TLC mobile phase was 60% MeCN in 25 mM  $\text{NH}_4\text{HCO}_2$  with 1% TEA (v/v). In the resulting TLC chromatogram, two peaks are identified: unreacted [ $^{18}$ F]fluoride ( $R_f=0.0$ ) and [ $^{18}$ F]Fallypride ( $R_f=0.9$ ). RCP was calculated as the area under the [ $^{18}$ F]fallypride peak divided by the area under both peaks. Fluorination efficiency (conversion of [ $^{18}$ F]fluoride to product) was the same as RCP. The decay-corrected crude radiochemical yield (crude RCY) of [ $^{18}$ F]fallypride was defined as the radioactivity recovery times the RCP.

In a few experiments, we also performed radio-HPLC purification of the crude [ $^{18}$ F]fallypride mixture and analysis of the purified and formulated [ $^{18}$ F]fallypride using a Smartline HPLC system (Knauer, Berlin, Germany) equipped with a degasser (Model 5050), pump (Model 1000), a UV (254nm) detector (Eckert & Ziegler, Berlin, Germany) and a gamma-

radiation detector and counter (B-FC- 4100 and BFC-1000; Bioscan, Inc., Poway, CA, USA). Separation was performed using a C18 column (Kinetex, 250 x 4.6 mm, 5  $\mu$ m, Phenomenex, Torrance, CA, USA). The mobile phase was 60% MeCN in 25 mM  $\text{NH}_4\text{HCO}_2$  with 1% TEA (v/v) and flow rate was 1.5 mL/min. The retention time of fallypride was 4.5 min. The crude  $^{18}\text{F}$ fallypride mixture collected from the chip was manually injected into the HPLC system, and the  $^{18}\text{F}$ fallypride fraction ( $\sim 2$  mL) was collected. Chromatograms were collected using a GinaStar analog-to-digital converter (raytest USA, Inc., Wilmington, NC, USA) and GinaStar software (raytest USA, Inc.) running on a PC. The chromatogram of crude  $^{18}\text{F}$ fallypride had two peaks,  $^{18}\text{F}$ fluoride ( $t_R = 1.6$  min) and  $^{18}\text{F}$ fallypride ( $t_R = 4.4$  min) (e.g., Figure 5-9).

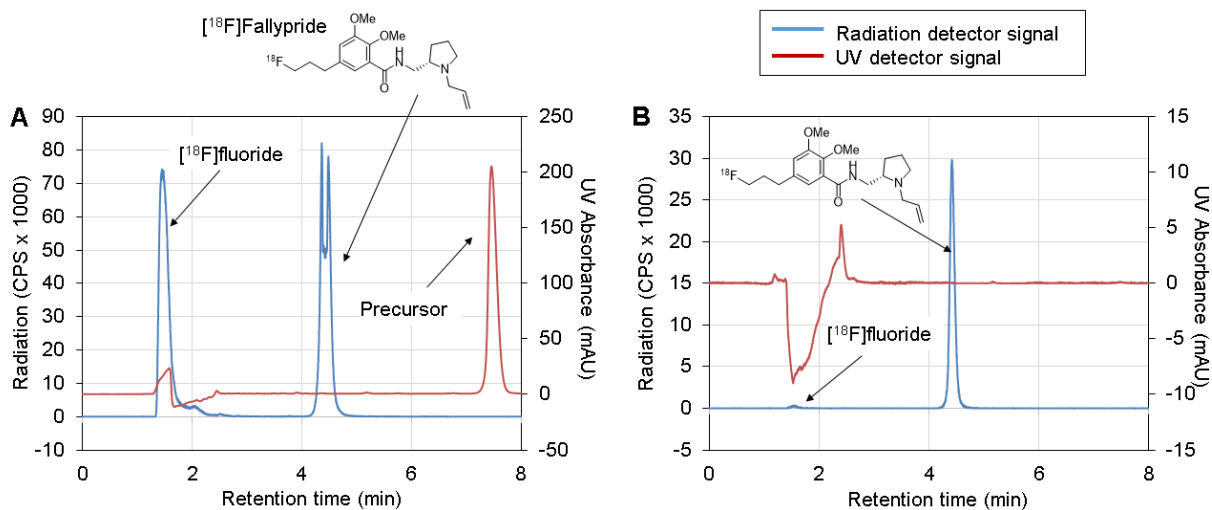


**Figure 5-9: Examples of radio-HPLC chromatograms of  $^{18}\text{F}$ fallypride synthesis on the microfluidic reaction chip**

(A) Analysis of crude product. Note that the apparent double peak of  $^{18}\text{F}$ Fallypride is an artifact due to saturation of the radiation detector. (B) Analysis of formulated product. The RCP was 99%.

Finally, we also used the technique of Cerenkov imaging [144] to visualize the distribution of radioactivity on the microfluidic chip after different steps. To obtain an image, a glass microscope slide (1mm thick) was placed on top of the chemical reaction chip prior to placing it in the imaging chamber. The Cerenkov imaging setup was described previously. [145]

Exposure time was set to 300 s. In addition to performing image corrections (dark mask, flat mask and median mask) described previously, we also performed a background subtraction and a decay correction (to the starting time of the first image). For purposes of analysis, regions of interest (ROIs) were drawn. The background correction used an ROI drawn in an area of the chip not exposed to radioactive solutions; the background level was the average pixel value in this region. Other ROIs analyzed include the total chip, the reaction region, and the reagent pathways. For each experiment trial, images were taken after the evaporation step, the fluorination step and the collection step.

### 5.2.6 Micro PET/CT imaging protocol

For *in vivo* imaging, the synthesis was started by preparing a 5x more concentrated [ $^{18}\text{F}$ ]fluoride stock solution consisting of 100  $\mu\text{L}$  [ $^{18}\text{F}$ ]fluoride/[ $^{18}\text{O}$ ]H $_2\text{O}$  (i.e. 1850 MBq, 50 mCi) and 5  $\mu\text{L}$  TBAHCO $_3$  solution (75 mM). A 2  $\mu\text{L}$  droplet (~37 MBq; ~1 mCi) was used for the synthesis. The collected (diluted) crude [ $^{18}\text{F}$ ]fallypride product from the chip was purified via analytical-scale HPLC (identical conditions as for analysis described above). The product fraction was dried by evaporation of solvent in an oil bath at 110°C for 8 min with nitrogen flow, and then redissolved in PBS. The amount of PBS was adjusted to ensure 2.6- 3.0 MBq (~70– 80  $\mu\text{Ci}$ ) of the tracer in 200  $\mu\text{L}$  PBS for one mouse injection. The formulated [ $^{18}\text{F}$ ]fallypride was analyzed via radio-HPLC to confirm purity and determine molar activity according to typical procedures [55]. Isolated RCY was calculated as activity of formulated [ $^{18}\text{F}$ ]fallypride divided by the starting activity.

The *in vivo* imaging study was conducted with a 10 week-old female C57Bl/6J mice (Jackson Laboratory, Bar Harbor, ME) in accordance with UCLA Animal Research Committee approved protocols and guidelines. For static PET imaging, the mouse was pre-warmed, anesthetized (2% isoflurane in oxygen), and injected via tail vein with ~2.6 MBq (~70  $\mu\text{Ci}$ ) [ $^{18}\text{F}$ ]Fallypride, followed by 60 min uptake period under anesthesia and a 10 min static PET

acquisition (G8 PET/CT, Sofie Biosciences, Culver City, CA, USA) with an energy window of 150-650 keV. Images were reconstructed using maximum-likelihood expectation maximization as recommended by the vendor, corrected for CT-based photon attenuation, detector normalization and radionuclide decay (scatter correction was not applied), and converted to units of percent injected dose per gram (%ID/g). PET scans were followed by a 50 sec CT scan for anatomical co-registration and attenuation correction with a 50 kVp, 200  $\mu$ A X-ray source and reconstructed using a Feldkamp algorithm. PET/CT images were analyzed using AMIDE version 1.0.5. [146]

## **5.3 Results and Discussion**

### **5.3.1 Development of fabrication method**

To prepare surfaces with patterned wettability, Ghosh et al. [141] deposited a mixture of hydrophobic fluoroacrylic copolymer (PMC), TiO<sub>2</sub> nanoparticles and EtOH onto a substrate, and then used UV irradiation to activate the TiO<sub>2</sub> to catalyze the local destruction of PMC. Because it has been shown the TiO<sub>2</sub> nanoparticles can catalyze a variety of chemical and radiochemical reactions [142], they could therefore potentially interfere with the reactions we wanted to perform on the chip, and thus we avoided the use of nanoparticles. Instead, the patterned surface was prepared by dry-etching of a Teflon coating on a silicon substrate.

Contact angle measurements (Table 5-1), made using DI water droplets, showed that the patterned regions (i.e. uncovered silicon surface) were very hydrophilic ( $\theta=7\pm 3^\circ$ , n=3), while the remaining Teflon regions were very hydrophobic ( $\theta=122\pm 1^\circ$ , n=3). Importantly, the hydrophobic layer maintained its integrity and adhesion to the substrate throughout the full patterning process.

**Table 5-1: Contact angle measurements of a droplet of DI water (~2  $\mu$ L) on the microfluidic chip at different stages during the fabrication process**

Treatment	Contact angle ( $^{\circ}$ ) (n=3)
Initial Si wafer	$41 \pm 4$
Hydrophobic region before patterning	$122 \pm 2$
Hydrophilic region (after acetone wash)	$57 \pm 10$
Hydrophilic region (after Piranha clean)	$7 \pm 3$

### 5.3.2 Feasibility studies and characterization

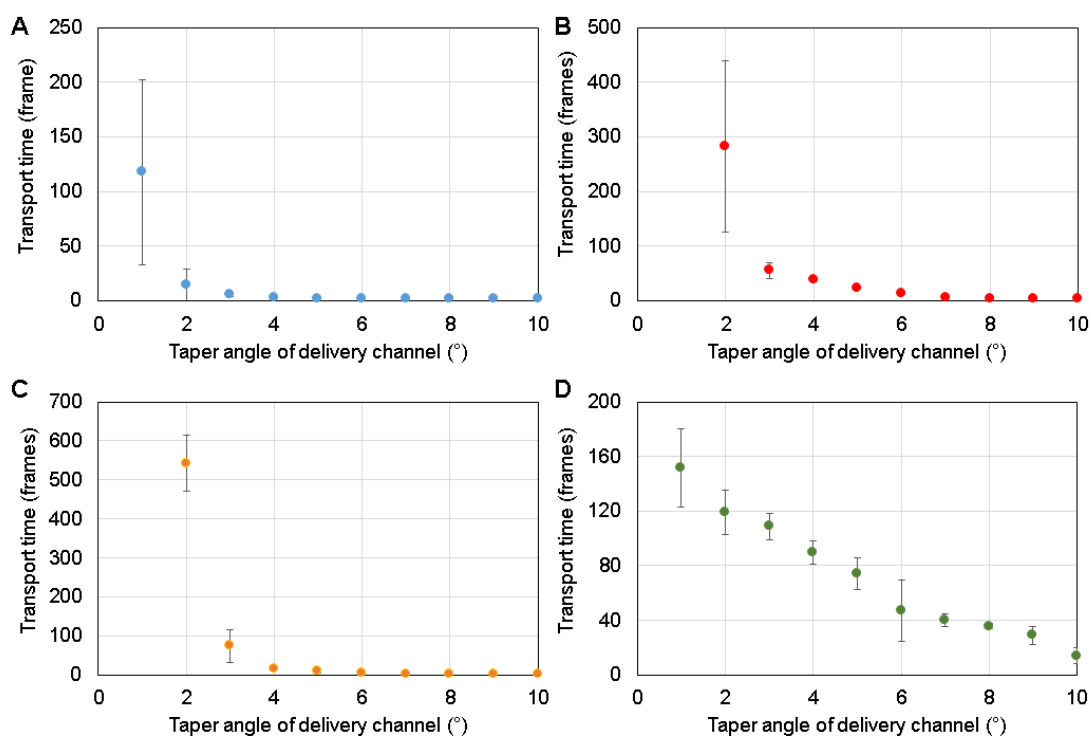


**Figure 5-10: Moving rate of different solvents as a function of taper angle of the reagent delivery pathway**

(A) 1  $\mu$ L droplet of DI water (n=4). (B) 1  $\mu$ L droplet of MeOH (n=4). (C) 1  $\mu$ L droplet of MeCN (n=4 for 1-5 $^{\circ}$ ; n=2 for 6-10 $^{\circ}$ ). (D) 1  $\mu$ L droplet of DMSO (n=3). Note that if the time to reach the reaction site exceeded 1000 frames, the transport speed was considered to be zero and the data was omitted from the graph (i.e. 1 $^{\circ}$  taper angle for MeOH and MeCN). All solvents were deposited via non-contact dispensers (INKX0514300A for DI water, MeOH and MeCN; INKX0514100A for DMSO).

First, we assessed whether the passive transport mechanism was compatible with the various solvents and solvent mixtures used in the desired reactions. The simple chip was fabricated to study the behavior of droplets of solvents as a function of taper angle (Figure 5-3). We found that all solvents (DI water, MeOH, MeCN, DMSO) could be spontaneously transported for taper angles of 4° or larger (Figure 5-10). To provide a safety margin, we used an angle of 5° for subsequent experiments.

We then designed the chemical reaction chip in Figure 5-1A, consisting of a 3mm diameter hydrophilic reaction zone and six radially-oriented reagent droplet transport 'channels'. We observed that the droplets behaved differently depending on the type of solvent and the volume. For example, some droplets moved to the central reaction zone and remained confined to this zone, while others would wet the reaction zone and then 'overflow' along the radial channels. We suspect that surface tension and density (i.e. gravity) may play a role in determining this behavior. We empirically explored the behavior of different droplet volumes of each solvent on the 6-inlet chip (Figure 5-4) to determine the maximum volume that could be loaded while avoiding the overflow issue. The maximum volumes for DI water, MeOH, MeCN and DMSO were 1, 1, 1, and less than 0.5  $\mu\text{L}$ , respectively. Thus, we adjusted reagent concentrations so the desired absolute amount of reagents could be efficiently loaded without exceeding the maximum droplet volume. To determine a suitable dilution solution for product collection, different combinations of MeOH and DI water were tested after performing mock syntheses. For [ $^{18}\text{F}$ ]fallypride, a ratio of 9:1 (v/v) was used. These ratios exhibited sufficient mobility to reach the reaction zone, yet avoided overflow of the reaction site (when 1  $\mu\text{L}$  was loaded).

### 5.3.3 Mock radiosynthesis

Next, we performed a mock synthesis of [ $^{18}\text{F}$ ]fallypride replacing [ $^{18}\text{F}$ ]fluoride solution with  $\text{TBAHCO}_3$  solution and precursor solution with just the solvent. Diluted food dyes were added in each solution. A series of photographs of the whole process is shown in Figure 5-11. Movements of different droplets were fast and smooth. Evaporations proceeded smoothly without bubbling or bursting of droplets. Surprisingly, 2  $\mu\text{L}$  droplets of mock precursor solution remained confined to the reaction site, even though such volume of MeCN caused 'overflow', perhaps due to the presence of dried salts ( $\text{TBAHCO}_3$ ) and food dye from the evaporation step, or altered surface properties. The collection process seemed effective, with no visible residue apparent at the reaction site after collection.

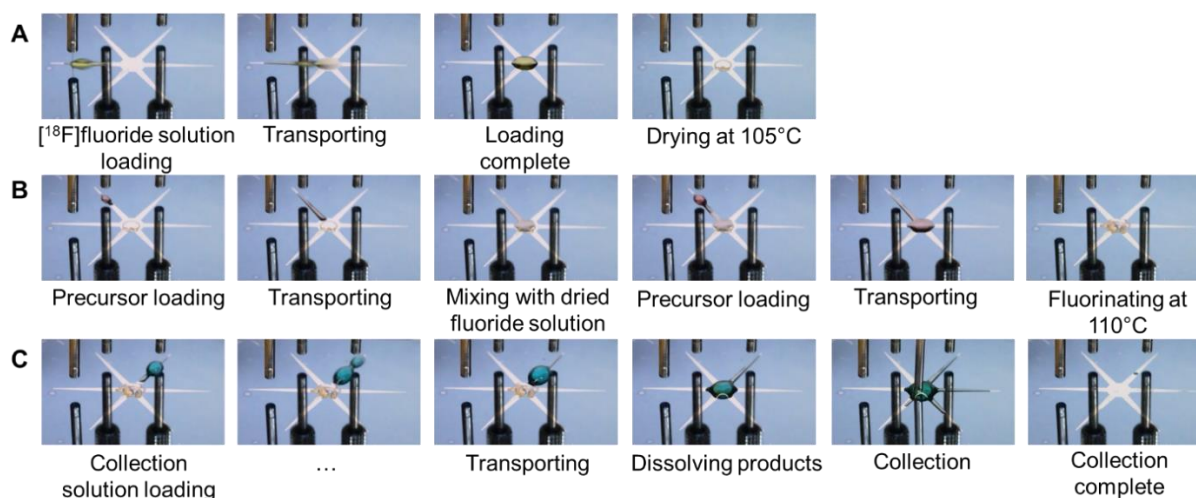


**Figure 5-11: Sequence of photographs of the microfluidic chip during the mock synthesis of [ $^{18}\text{F}$ ]fallypride**

(A) A DI water droplet (2 $\mu\text{L}$ , dyed yellow) containing  $\text{TBAHCO}_3$  (77mM) was loaded, spontaneously transported to the reaction site, and then the chip was heated to 105°C to remove the solvent. (B) Next, two droplets of a 1:1 v/v mixture of MeCN and thexyl alcohol (1 $\mu\text{L}$ , dyed red) were loaded from a separate inlet and transported to the reaction site in sequence, after which the droplet was heated to 110°C to simulate fluorination reaction. Note that loading in two separate portions instead of a single larger droplet helped to prevent over-flowing of the reaction site. (C) Next, two droplets of collection solution (9:1 v/v MeOH/water) (5  $\mu\text{L}$  each, dyed blue) were loaded from a third inlet and transported to the center to dilute the reaction mixture. Finally the collection tubing was lowered and the droplet was collected into a vial with the aid of vacuum. Very little residue was apparent on the chip after collection.

### 5.3.4 Multi-step radiosyntheses

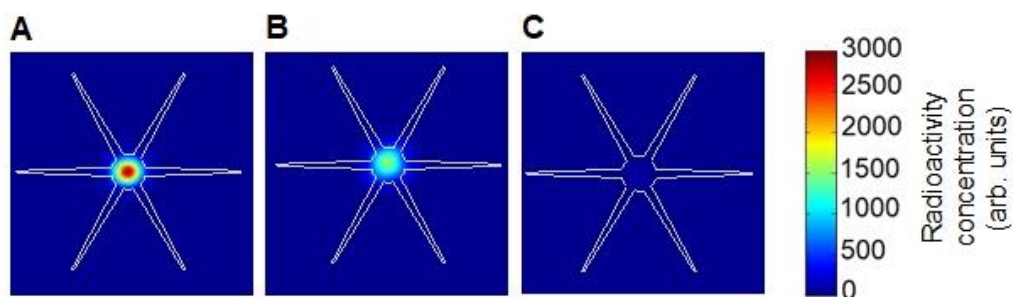


**Figure 5-12: Distribution of radioactivity visualized using Cerenkov imaging after different steps of radiosyntheses.** (A) after [ $^{18}\text{F}$ ]fluoride drying step; (B) after fluorination reaction; (C) residual radioactivity on chip after collection of product.

Subsequently, we attempted the radiosyntheses of [ $^{18}\text{F}$ ]fallypride. Cerenkov images, showing distribution of radioactivity on the chip at different stages of the syntheses, are shown in Figure 5-12. Images after the [ $^{18}\text{F}$ ]fluoride drying process showed all the radioactivity confined to the reaction zone, as did images after the fluorination reaction, and images after the collection process showed very little activity remained on the chip. The amount of radioactivity on the whole chip as determined by Cerenkov imaging correlated well with radioactivity measurements made via dose calibrator (data not shown).

Initially, reactions were performed with manual pipetting of reagents to the reagent loading sites and manual collection of the crude product via pipette. Then, fully automated synthesis was performed on the chip, including automated dispensing of reagents and automated collection of the crude product.

**Table 5-2: Performance of [<sup>18</sup>F]fallypride synthesis using manual or automated reagent loading and product collection**

All measurements were repeated n=4 times. Starting radioactivity was 7.4 MBq (0.2 mCi). Fluorination efficiency, radioactivity recovery, crude RCY, and isolated RCY are expressed with respect to starting [<sup>18</sup>F]fluoride activity, while collection efficiency and residual activities are expressed with respect to activity on chip just prior to the collection step.

Parameter	Manual synthesis	Automated synthesis
Fluorination efficiency (%)	74 ± 8	76 ± 4
Radioactivity recovery (%)	79 ± 4	84 ± 4
Collection efficiency (%)	90 ± 4	93 ± 2
Synthesis time (min)	25 ± 3	20 ± 1
Crude RCY (%)	59 ± 9	64 ± 6
Isolated RCY (%)	N/A	46 ± 4
Residual activity on chip (%)	12 ± 3	5 ± 2
Residual activity on collection tip/tubing (%)	2 ± 1	2 ± 0

The performance of [<sup>18</sup>F]fallypride synthesis is summarized in Table 5-2. With manual operations, the fluorination efficiency was 74 ± 8 % (n=4), collection efficiency was 90 ± 4 % (n=4), and the crude RCY was 59 ± 9% (n=4). Analysis of radioactivity measurements during the synthesis on passive chips showed negligible losses (-3 ± 1%, n=4, relative to the starting radioactivity) during drying of [<sup>18</sup>F]fluoride, but slightly higher losses of 15 ± 2% (n=4) during fluorination and 9 ± 4% (n=4) residual activity on chip and pipette tips after collection. Note that the negative evaporation loss is likely due to measurement error in the dose calibrator. The crude RCY was slightly lower than we previously reported for the droplet-based synthesis using EWOD chips, i.e. 84 ± 7% (n=6). [50] The reported fluorination and collection efficiencies on EWOD were 90 ± 9 % (n=6) and 94 ± 3 % (n=6), respectively, suggesting the current platform and reaction conditions give slightly lower fluorination efficiency. We plan to perform further optimization of conditions and investigation of additional substrate materials in the future. The synthesis time (up to the end of the collection process) for [<sup>18</sup>F]fallypride was ~25 min.

Automated loading and collection provided a marginal increase in the crude RCY of [ $^{18}\text{F}$ ]fallypride to  $64 \pm 6\%$  ( $n=4$ ). This increase can be explained by the improved radioactivity recovery ( $84 \pm 4\%$ ;  $n=4$  compared to  $79 \pm 4\%$ ;  $n=4$  for manual operation), which was due to lower residual activity on chip and collection tubing ( $7 \pm 2\%$ ;  $n=4$  of the activity on chip before the collection step, compared to  $14 \pm 3\%$ ;  $n=4$  for the manual setup). The isolated RCY was  $46 \pm 4\%$  ( $n=4$ ). Typically, in macroscale synthesis, about 5-10% of the radioactivity of the crude product can be lost during purification and formulation. Here we lost about 28% of the activity, suggesting that significant improvements can still be made, perhaps in injection of the small volume of collected product into the HPLC system. The synthesis time was reduced to ~20 min (~12 min for drying and fluorination steps and ~8 min for collection) due to elimination of manual steps. This time is slightly shorter than reported for EWOD-based synthesis (i.e., ~31 min for [ $^{18}\text{F}$ ]fallypride). [50] The synthesis time is also somewhat shorter than macroscale processes (~29 min for [ $^{18}\text{F}$ ]fallypride). [55,147] The total time of purification and formulation (~13 min) is shorter than macroscale processes as well (20 min). [147] It should be pointed out that the formulation step was not yet optimized; it is expected that this process could be performed more quickly by using a cartridge based method rather than evaporation. The time for collection can possibly be further condensed by optimizing the speed of the product droplet collection process.

### 5.3.5 Scaling up the amount of radioactivity

The starting activity of [ $^{18}\text{F}$ ]fallypride was minimized in preliminary experiments for safety reasons to ~7.4 MBq (~0.2 mCi) by loading a 2  $\mu\text{L}$  droplet (radioactivity concentration ~0.1 mCi/ $\mu\text{L}$ ). Though sufficient radioactivity was recovered for small animal imaging, it will be desirable in the future to scale this up to enable tracer production for multiple animal studies or for clinical doses. One way to scale up activity is by pre-concentrating the [ $^{18}\text{F}$ ]fluoride solution

from the cyclotron using a miniaturized anion exchange cartridge as described in chapter 3.

Another approach is to repeatedly load droplets of [<sup>18</sup>F]fluoride solution before drying.

**Table 5-3: Performance of [<sup>18</sup>F]fallypride synthesis with scaled-up starting radioactivity**

Addition of [<sup>18</sup>F]fluoride/[<sup>18</sup>O]H<sub>2</sub>O solutions was followed in all cases by the same amount of TBAHCO<sub>3</sub> solution (2 μL, 3.6 mM). All experiments were performed n=1 times.

Parameter	Trial 1	Trial 2	Trial 3	Trial 4
[ <sup>18</sup> F]fluoride/[ <sup>18</sup> O]H <sub>2</sub> O solution volume (μL)	2	4	6	8
Starting radioactivity (MBq)	9	15	21	23
Radioactivity recovery (%)	83	72	76	79
Fluorination efficiency (%)	70	76	57	63
Crude RCY (%)	58	55	43	50

Preliminary experiments were conducted to test the feasibility of the latter approach with manual loading and collecting (see Table 5-3). To ensure the same ratio of precursor to TBAHCO<sub>3</sub> in the fluorination reaction, multiple 2 μL droplets of [<sup>18</sup>F]fluoride/[<sup>18</sup>O]H<sub>2</sub>O solution (i.e. no TBAHCO<sub>3</sub>) were first loaded, followed by a single 2 μL droplet of TBAHCO<sub>3</sub> solution (3.6 mM). The mixture was dried at 105°C for 1 min. In a preliminary experiment, loading of 2, 4, or 8 μL of [<sup>18</sup>F]fluoride/[<sup>18</sup>O]H<sub>2</sub>O solution resulted in crude RCYs was 58% (n=1), 54% (n=1), and 50% (n=1). This apparent reduction in crude RCY as a function of [<sup>18</sup>F]fluoride/[<sup>18</sup>O]H<sub>2</sub>O volume could be a mixing issue as it may become increasingly difficult to dissolve the increasing amount of residue in the precursor solution droplet prior to fluorination. Instead of loading a large volume and drying it once, each droplet of [<sup>18</sup>F]fluoride/[<sup>18</sup>O]H<sub>2</sub>O could be dried after loading, perhaps limiting the lateral extent of the initial residue. For the 8 μL case, the starting activity was 2.34 MBq (~ 0.63 mCi).

### 5.3.6 Preclinical imaging

Using [<sup>18</sup>F]fallypride synthesized automatically on the chip, in vivo small-animal PET/CT imaging was performed after purification (purity > 99%) and reformulation. Separation via radio-HPLC revealed no additional radioactive impurities. Molar activity was 185 GBq/μmol (~5.0

Ci/ $\mu$ mol) at the end of synthesis. The biodistribution, showing high uptake of [ $^{18}$ F]fallypride in the striatum (Figure 5-13), was similar to literature reports. [148]

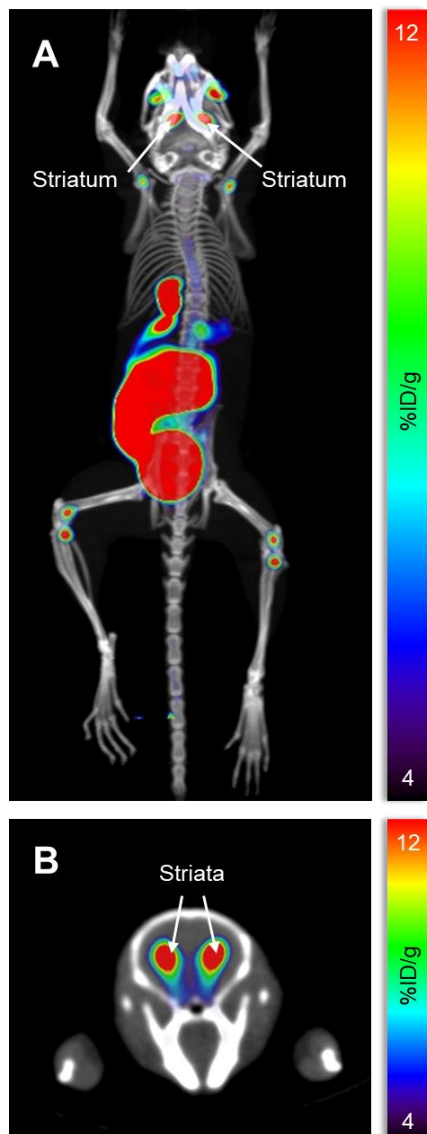


**Figure 5-13: Small-animal PET/CT images from the static scan after 60 min uptake of [ $^{18}$ F]Fallypride**

(A) Maximum intensity projection (MIP) image of whole mouse; (B) Transverse slice highlighting uptake in striata in the brain.

## 5.4 Conclusion

An automated microfluidic platform for droplet-based reactions was developed based on passive droplet transport using patterned wettability. A new approach to fabricating such patterned surfaces was developed and implemented on silicon substrates. After optimization and characterization were performed to determine optimal taper angle of the pathways and optimal droplet volumes for various solvents, multi-step chemical reactions (including evaporative drying, fluorination and deprotection steps) were performed to synthesize [ $^{18}\text{F}$ ]fallypride. As a demonstration of the ability to produce useful amounts of these tracers, a batch of [ $^{18}\text{F}$ ]fallypride was prepared, purified, formulated, and used for preclinical imaging.

Cerenkov imaging revealed the distribution of radioactivity after various synthesis steps. As desired, the majority of radioactivity was confined in the reaction site during fluoride drying and reaction steps, and minimal residual radioactivity remained on chip after the collection step. More detailed analysis of Cerenkov images may be helpful in further optimization of aspects of the on-chip synthesis such as droplet mixing and redissolution of dried residues.

Though synthesis performance was slightly lower than on EWOD chips, the cost of the passive chips is significantly lower due to the very simple fabrication process. Furthermore, the overall system for connecting reagent sources and collecting the crude product is significantly less complicated. Synthesis times were also shorter than on EWOD chips, potentially enabling the production of more batches of tracers in one day.

By combining with a [ $^{18}\text{F}$ ]fluoride concentrator (presented in chapter 3), or sequentially loading [ $^{18}\text{F}$ ]fluoride droplets, the system can be scaled up to higher amounts of radioactivity. Other than PET imaging, our automated platform has the potential to be applied for small scale chemical reactions or assays as well.

## 6 Chapter 6: Combined radionuclide concentration and PET tracer synthesis

### 6.1 Introduction

For more than a decade, there has been interest in microreactors for preparation of radiolabeled probes for positron emission tomography (PET). By performing radiochemical reactions in microliter scale, the substantial cost of tracer production can be greatly reduced through lower consumption of expensive reagents (e.g. precursor) and small system footprint that can reduce amount of needed shielding or can enable many synthesizers to be installed in a single hot cell. Furthermore, yields can be increased due to the higher concentration of radionuclide, rapid mixing of reagents, fast heat transfer and short evaporation times. [149]

Several prototypes of microreactors leveraging those advantages have been reported for preclinical tracer production [42,45,50,150,151] but only a few systems were shown to produce doses of both sufficient quantity and quality for clinical use. For example, Lebedev *et al.* reported a batch-type microfluidic reactor (volume 50  $\mu\text{L}$ ) and showed rapid reaction times and high yields for several  $^{18}\text{F}$ -labeled tracers. [65,152] A concentrator subsystem was incorporated to increase the amount of activity that could be loaded into the 50  $\mu\text{L}$  reactor, and production of [ $^{18}\text{F}$ ]fallypride for clinical imaging was demonstrated. Volume reduction not only reduced the amount of expensive reagents used but also reduced times needed for heating, evaporations, etc. Another microfluidic system (NanoTek, Advion, Inc.) is based on reagents flowing through a pre-heated capillary. Zheng *et al.* and Liang *et al.* demonstrated the successful syntheses of [ $^{18}\text{F}$ ]FMISO and [ $^{18}\text{F}$ ]T807, respectively, for clinical use. [99,153] This “flow-through” reactor design allows scaling of reaction volumes to adjust the batch size (e.g. changing the volume of radionuclide solution scales the amount of activity), enabling production of small batches for optimization or large batches for clinical doses. However, the large scale reactions (required for

producing clinical doses) use similar volumes as conventional systems, generally minimizing reagent savings. [153]

Our group has been developing droplet-based platforms for the synthesis of PET tracers based on electro-wetting on dielectric (EWOD) [46,48–50] or passive droplet transport [64]. These technologies enable reaction volumes to be scaled down to the microliter range (and reagent masses to the 10s of microgram level). The small reaction volume is also advantageous for increasing molar activity, enabling high molar activity even from relatively small batches, something that is not possible with conventional synthesizers [63], and enabling high molar activity in isotopic exchange reactions [154]. Furthermore, by removing bulky reagent delivery systems, system size is drastically reduced, enabling safe operation with only small amounts of lead shielding [48] or potentially enabling multiple systems to be operated within a single hot-cell.

While earlier radiochemistry performed in these droplet platforms was limited to 10s to 100s of MBq [0.27 mCi to 2.7mCi] due to the small chip volume, our lab recently developed a fully-automated standalone [<sup>18</sup>F]fluoride concentrator, relying on a miniaturized strong anion exchange (SAX) cartridge (presented in chapter 3), that can increase the radionuclide concentration by reducing the initial volume (1-5 mL) down to an output volume of 12.4 $\mu$ L. [131]

In this chapter, we leverage this technology to enable increased activity to be loaded into the micro-droplet synthesizer. We describe design and development of an integrated system (Figure 6-1) comprising the concentrator and passive transport-based microreactor, characterize the radionuclide concentration process, optimize the radionuclide transfer into the microreactor, and demonstrate the successful droplet-based synthesis of [<sup>18</sup>F]Fallypride using concentrated [<sup>18</sup>F]fluoride. The synthesis is demonstrated with starting activities up to 41 GBq [1.1 Ci] of activity and we explore the synthesis performance as a function of activity level.

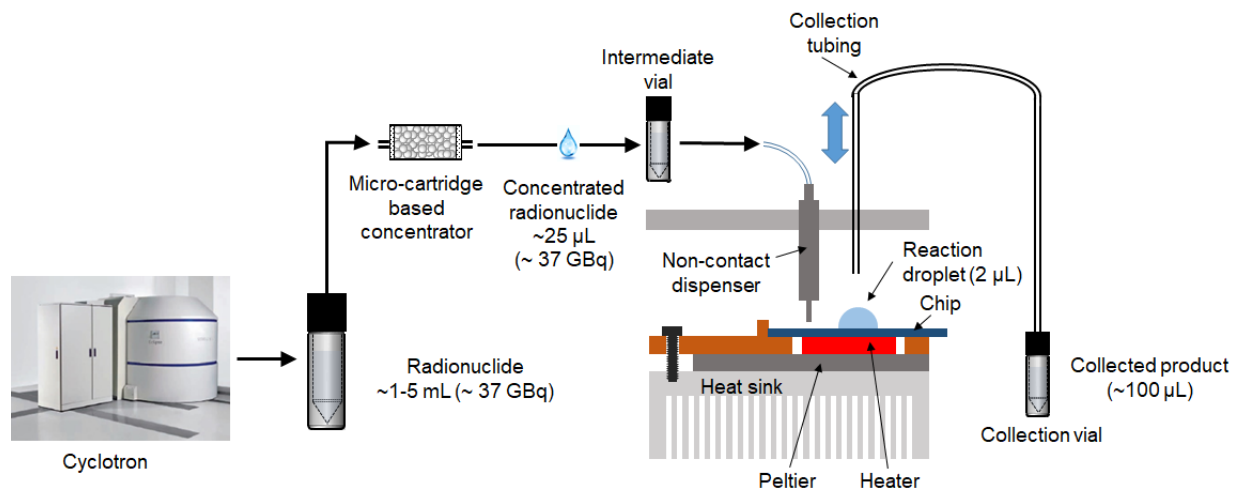


**Figure 6-1: Tracer production scheme using the integrated radionuclide concentrator and microfluidic radiosynthesizer**

Radionuclide (e.g. [ $^{18}\text{F}$ ]fluoride) is produced in a cyclotron (1-5mL) and is concentrated down to 25 $\mu\text{L}$  and then transferred to the droplet-based microfluidic system to perform the radiosynthesis.

## 6.2 Materials and Methods

### 6.2.1 Materials

Anhydrous methanol (MeOH, 99.8%), ethanol (EtOH, 99.5%), anhydrous acetonitrile (MeCN, 99.8%), 2,3-dimethyl-2-butanol (hexyl alcohol, 98%), ammonium formate ( $\text{NH}_4\text{HCO}_2$ , 97%) and trimethylamine (TEA, 99%) sodium hydroxide (NaOH, 1N) were purchased from Sigma-Aldrich. Tetrabutylammonium bicarbonate ( $\text{TBAHCO}_3$ , 75mM), tosyl fallypride (fallypride precursor, >90%) and fallypride (reference standard for [ $^{18}\text{F}$ ]fallypride, >95%) were purchased from ABX Advanced Biochemical Compounds (Radeberg, Germany). DI water was obtained from a Milli-Q water purification system (EMD Millipore Corporation, Berlin, Germany). No-carrier-added [ $^{18}\text{F}$ ]fluoride in [ $^{18}\text{O}$ ]H $_2\text{O}$  was obtained from the UCLA Ahmanson Biomedical Cyclotron Facility.

## 6.2.2 Apparatus

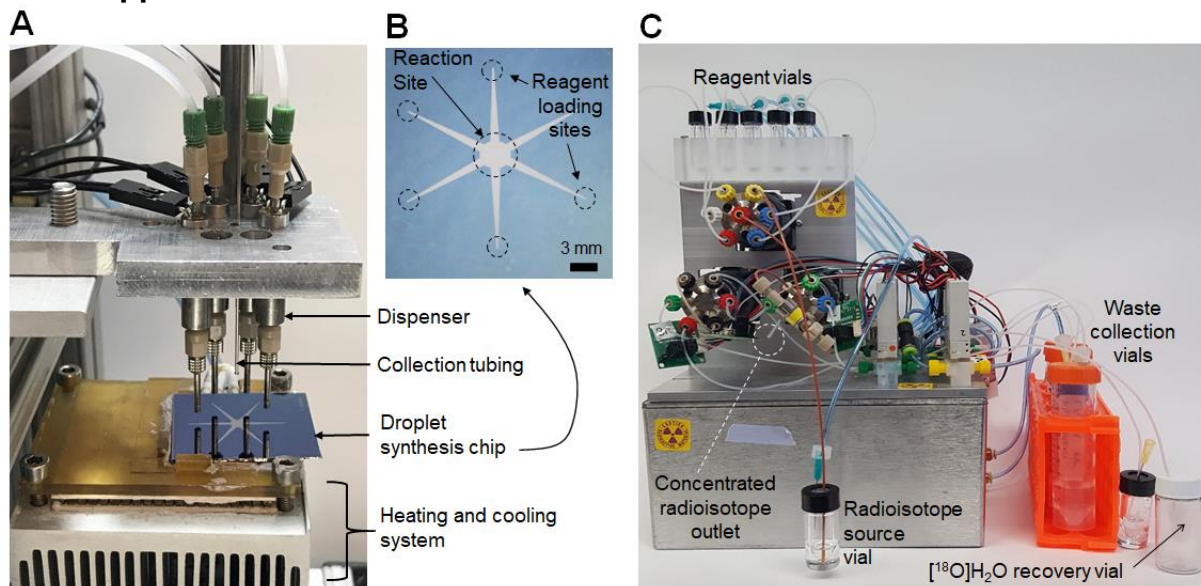


**Figure 6-2: Photographs of subcomponents used in the integration platform**

(A) Photograph of the microfluidic radiosynthesis platform. (B) Photograph of the microfluidic chip. (C) Photograph of the radionuclide concentrator.

An integrated system was developed comprising an automated radionuclide concentrator (Figure 6-2C) coupled to an automated micro-droplet synthesis platform (Figure 6-2A). A detailed report of the design and operation of the [<sup>18</sup>F]fluoride concentrator, operated here in the “direct loading” configuration, was recently published [131] and also presented in chapter 3. Briefly, the system relies on a miniature strong anion exchange (SAX) cartridge. The [<sup>18</sup>F]fluoride in [<sup>18</sup>O]H<sub>2</sub>O from the cyclotron is passed through this cartridge to trap the [<sup>18</sup>F]fluoride, while the [<sup>18</sup>O]H<sub>2</sub>O is collected in a waste vial. The trapped [<sup>18</sup>F]fluoride is then released into a small volume of eluent solution.

Upstream of the concentrator, we incorporated a simple module for strong cation exchange (SCX) cartridge filtration of the initial [<sup>18</sup>F]fluoride solution to eliminate contaminants and small particles that could potentially interfere with trapping on the micro-cartridge. The core of SCX filtration module (Figure 6-3) is a 7-port, 6-position rotary stream selection valve

("filtration selection valve", Titan HT 715-005, IDEX Health and Science). Connected to three inputs of this valve are three septum-capped glass v-vials (3mL, W986277NG, Wheaton, Millville, NJ, USA) for supplying [<sup>18</sup>F]fluoride and two rinses of DI water (each 0.5 mL). The remaining three inputs of the stream selection valve are not used. The vials are each connected to the valve via an ETFE dip tube (0.02" ID, 1/16" OD ETFE tubing; 1516L; IDEX), and are also connected to a regulated inert gas source or vented to atmosphere via 3-way valves (V1-V3) (S070B-5DG, SMC). Inert gas pressure was provided from an electronic pressure regulator (ITV0010-2BL, SMC Corporation, Japan) connected to a nitrogen source. The output of the stream selection valve is connected to an SCX cartridge and then to a collection vial (3mL v-vial; Wheaton) via 0.02" ID, 1/16" OD ETFE tubing (1516L, IDEX). Two strong cation exchange cartridges were explored; Oasis MCX plus short cartridges (225mg, 186003516, Waters), and Maxi-Clean cartridges (600mg, 21902, Alltech). The collection vial is also connected via a 3-way valve (LVM105R, SMC Corporation, Japan) to atmosphere or the regulated inert gas supply. Finally a dip tube from the collection vial is connected to the fluoride input port of the [<sup>18</sup>F]fluoride concentrator via 0.02" ID, 1/16" OD ETFE tubing (1516L, IDEX).

The use of the SCX filtration module required a slight modification of the [<sup>18</sup>F]fluoride trapping procedure. Initially the reagent selection valve of the SCX filtration module is set to the [<sup>18</sup>F]fluoride vial, and V4 is set to vent the collection vial of the module. V1 is connected to pressure (20 psi) pushing [<sup>18</sup>F]fluoride through the SCX cartridge into the SCX module collection vial. Immediately after, the reagent select valve is switched to connect to the first water rinse vial and V2 is connected to pressure (20 psi) to deliver 0.5 mL of DI water through the SCX cartridge to recover residual [<sup>18</sup>F]fluoride. The radionuclide concentrator is then configured in "trapping" mode, the reagent selection valve of the SCX filtration module is changed to an unused (plugged) position (to prevent pressure leakage from the SCX module collection vial),

and V4 is switched to connect to pressure (20 psi) to drive the mixture of filtered [ $^{18}\text{F}$ ]fluoride and DI water rinse to the concentrator. When complete, V4 of the SCX filtration module is switched to vent the collection vial, the reagent select valve is connected to the second water rinse vial, and V2 is connected to pressure (20 psi) to flush the 0.5 mL of DI water through the SCX cartridge and into the collection vial. Finally, the reagent selection vial of the SCX filtration module is switched to an unused (plugged) position, and V4 is connected to pressure (20 psi) to drive the water to the radionuclide concentrator. Operation of the concentrator module then proceeds as described in section 6.2.4 and in more detail in chapter 3.

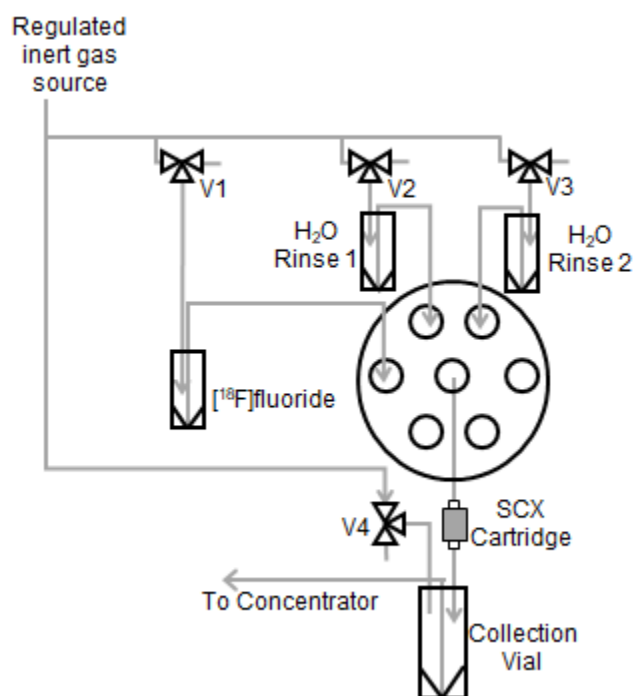


**Figure 6-3: Schematic of the SCX filtration module**

The design and operation of the microfluidic chips and microdroplet reaction system were previously published [64] and is described in chapter 5. Each microfluidic chip (25.0 x 27.5 mm<sup>2</sup>) comprises a hydrophobic Teflon-coated silicon surface with a circular hydrophilic (silicon) reaction zone in the center (3 mm diameter), and six tapered hydrophilic pathways for reagent

transport from reagent loading sites to reaction zone (Figure 6-2B). The chip is affixed atop a heater for temperature control. Reagents are delivered by non-contact liquid dispensers to the reagent loading sites. The crude product is collected from the reaction zone into an evacuated V-vial via a metal collection tubing inserted into the droplet.

The design and evaluation of the interface between the concentrator and droplet synthesis platform is described in detail below. To prepare for each high activity run, [ $^{18}\text{F}$ ]fluoride solution is loaded in the source vial, reagents needed for elution and reaction are loaded in the corresponding V-vials in the concentrator and droplet synthesizer, and a clean V-vial is installed in the droplet synthesizer for product collection.

### **6.2.3 Micro-cartridge fabrication**

The micro-cartridges for the radionuclide concentrator were fabricated by a different method than our previous report in chapter 3. Due to the high cost and limited re-usability of commercially-packed cartridges (with  $\sim 4$   $\mu\text{L}$  bed volume and  $\sim 2$  mg of resin), we opted to pack the resin ourselves into short segments of tubing. Doing so allowed convenient exploration of different resin types, resin masses, and cartridge geometries. Cartridges were packed with one of several different resins: Bio-Rad AG-MP1 (200-400 mesh size; Bio Rad, Hercules, CA, USA), resin from Sep-Pak Plus QMA Light Cartridges (37-55  $\mu\text{m}$  particle size; Waters Corporation, Milford, MA, USA), or resin from Oasis MAX Plus short cartridges (30  $\mu\text{m}$  particle size; Waters Corporation). Throughout this chapter, resin type will be referred to by the cartridge name from which they are extracted (e.g. Bio-Rad AG-MP1, Sep-Pak QMA, and Oasis MAX). All resin types rely on quaternary ammonium functionality for trapping anionic species. Different resin masses ranging from 2-7mg were explored.

Resin was packed into ETFE tubing with 1/16" outer diameter (OD) and different inner diameter (ID): 0.02" (1516L; IDEX Health and Sciences, Wallingford, CT, USA), 0.03" (1528L;

IDEX) or 0.04" (1517L; IDEX). Loose resin was weighed on a balance (Excellence Plus, Mettler Toledo, Columbus, OH, USA) and placed within a 0.2 mL PCR tube (Fisherbrand, Fisher Scientific, Pittsburg, PA, USA). Tubing with desired inner diameter was cut to a length of 11 cm. A small polyethylene frit (1/8" thick, 20 micron pore size) was punched out of a larger disk (FT20751P, UCT, Inc., Bristol, PA USA) and was inserted into the tubing segment. Depending on tubing inner diameter (0.02", 0.03" or 0.04"), the frit was cut with a 0.5mm (504528, World Precision Instruments, Sarasota, FL, USA), 0.70mm (504529, World Precision Instruments), or 1.0mm (504646, World Precision Instruments) biopsy punch. Once the frit was inserted into the tubing, it was pushed down 4cm using the needle clearing rod from a spinal needle (Quincke Spinal Needle, BD Biosciences, San Jose, CA, USA) and secured within the tubing by pinching the tube to plastically deform the tube near the frit. The deformation was performed on the side of the frit closest to the opening in which the frit was loaded. Next, the same end of the tubing was connected to vacuum (-12 psi). For the Bio-Rad AG-MP1 and Sep-Pak QMA resins, slurries were made by adding 0.2mL of MeOH into the PCR tube with the measured resin. For Oasis MAX resin, a slurry was made with 0.2mL of DI water. Compared to DI water, the MeOH slurry was loaded into the cartridge tubing more smoothly with less fluidic resistance; however, for the Oasis MAX resin, there was no difference between solvents. Next, the other end of the tubing was inserted into the bottom of the PCR tube to aspirate the slurry into the tubing. The frit served to trap the resin beads within the tubing. The PCR tube was then refilled with 0.2mL of the same solvent and aspiration repeated. Rinsing of the PCR tubing was performed a total of 2 times after the initial slurry loading. For cartridges packed with MeOH slurries, the cartridge was rinsed an additional time using 0.2mL DI water. After complete loading and rinsing, a second frit was punched, placed into the tubing, and is pushed right up to the resin bed. Finally, the tubing near this second frit was pinched to secure the frit and resin bed in place.

After cartridge fabrication cartridge packing was assessed by flowing DI water through cartridges and measuring the flow rate. A sample reservoir (Falcon 15 mL conical tube, BD Biosciences, San Jose, CA, USA), flow sensor (SLI-2000, Sensirion Westlake Village, CA, USA), a cartridge to be tested, and a waste reservoir (Falcon 15 mL conical tube, BD Biosciences, San Jose, CA, USA) were connected in series with tubing (0.03" ID 1/16" OD ; 1528L, IDEX). 3mL of DI water was loaded into the sample reservoir. The sample reservoir was pressurized to 20 psi with a manual pressure regulator (ARX21-N01, SMC Corporation, Japan) connected to a nitrogen source. Flow rates of DI water through the cartridge was recorded (at 74 ms intervals) until the 3mL in the sample reservoir was depleted. An average flow rate and standard deviation was determined by averaging the last 500 samples taken. This was performed to compare different cartridge geometries (i.e. was the flow rate sufficiently fast to trap the radionuclide in a reasonable time), and to monitor the cartridge-to-cartridge variation.

#### **6.2.4 Optimization and evaluation of concentrator performance**

We anticipated eluting the trapped [ $^{18}\text{F}$ ]fluoride with tetrabutylammonium bicarbonate ( $\text{TBAHCO}_3$ ), the phase transfer catalyst we used in our previous work synthesizing [ $^{18}\text{F}$ ]fallypride in micro-droplets. [64] To avoid introducing additional types of anions during elution, which could affect the downstream synthesis, we performed preconditioning with the same bicarbonate anion, choosing 1M potassium bicarbonate ( $\text{KHCO}_3$ ) as the preconditioning solution.

In order to develop a preconditioning protocol, we fabricated cartridges using 0.03" ID tubing filled with 3mg of either Bio-Rad AG-MP1, Sep-Pak QMA resin, or Oasis MAX resin. Examining first the Bio-Rad AG-MP1 cartridges, we first flowed 0.5mL of preconditioning solution through the cartridge at 20 psi. Next, the cartridge was rinsed with DI water of different volumes. (The cartridge was left wetted after the rinse; no air drying was implemented.) Finally,

we performed trapping of [<sup>18</sup>F]fluoride on the cartridge to determine the impact of rinsing volume (Table 6-1). All solutions were flowed through the cartridge in the same direction. If a rinse volume of 8.0 or 10. mL was used, trapping on the cartridge was quantitative. Lower amounts of rinse solution (4.0 or 6.0 mL) resulted in significantly worse trapping (i.e. 75% or 90%, respectively), perhaps due to small amounts of residual preconditioning solution that compete with [<sup>18</sup>F]fluoride for binding. We elected to use 10mL of DI water for the rinse after preconditioning for the Bio-Rad AG-MP1 resin. We tried the same conditions with the other resins and found the trapping to be quantitative as well (Table 6-1). The optimal preconditioning protocol for all cartridges was determined to be rinsing with 0.5mL of KHCO<sub>3</sub> followed by 10 mL of deionized (DI) water. Resin remained hydrated after the preconditioning step and was not air dried before use. Note that the preconditioning step can be performed during setup (prior to the introduction of the radionuclide) and thus the time needed does not adversely impact the overall radiochemical yield.

**Table 6-1: Trapping efficiency of [<sup>18</sup>F]fluoride in cartridges with 3mg of varying resin as a function of volume of DI water rinse used during preconditioning**

Unless otherwise noted, data points represent n=1.

	Resin type					
	Bio-Rad AG-MP1				Sep-Pak QMA	Oasis MAX
<b>Water rinse volume (mL)</b>	4.0	6.0	8.0	10.	10.	10.
<b>Trapping Efficiency (%)</b>	75	90	99	99	99.8 ± 0.3 (n = 2)	99

The input source vial was loaded with [<sup>18</sup>F]fluoride in [<sup>18</sup>O]H<sub>2</sub>O from the cyclotron, diluted with DI water if needed to ensure the volume was in the range 0.5-1.0 mL. These starting solutions contained activities ranging from 0.011 – 41 GBq [0.3 mCi – 1.1 Ci]. For most experiments, [<sup>18</sup>F]fluoride was first pushed through an SCX filtration module prior to trapping on

the SAX cartridge (as described above). Following SCX filtration, trapping was performed by the radionuclide concentrator by flowing this solution at 20 psi through the pre-conditioned micro-cartridge. Water was collected in the [ $^{18}\text{O}$ ]H $_2$ O recovery vial. After the initial trapping of [ $^{18}\text{F}$ ]fluoride was completed, 0.5mL of DI water was passed through the system and cartridge to the [ $^{18}\text{O}$ ]H $_2$ O recovery vial to recover any residual [ $^{18}\text{F}$ ]fluoride.

Elution efficiency was tested as a function of eluent composition and eluent volume. Three different elution compositions of TBAHCO $_3$  were tested: 3.8mM, 10.mM, and 25mM. The performance for different eluent concentrations was explored in order to find the best tradeoff between the amount of TBAHCO $_3$  needed for the elution versus the amount needed for the downstream droplet synthesis. In these experiments, a total of 6 elutions were performed (6.2  $\mu$ L of eluent per elution), with elution efficiency measured after each pair of elutions (i.e., elutions 1 and 2 together, elutions 3 and 4 together, etc.).

To characterize trapping and elution efficiency, various radioactivity measurements were made with a calibrated dose calibrator (CRC-25 PET, Capintec, Inc., Ramsey, NJ). For the purposes of calculations, all radioactivity measurements were decay-corrected to a common time point. Measurements were made of the activity in the [ $^{18}\text{F}$ ]fluoride source vial before trapping ( $A_{0\text{source}}$ ), activity in the source vial after trapping ( $A_{\text{source}}$ ), activity in the [ $^{18}\text{O}$ ]H $_2$ O recovery vial after trapping ( $A_{\text{waste}}$ ), and the collected activity after elution ( $A_{\text{collect}}$ ). The activity on the cartridge after trapping ( $A_{\text{cartridge}}$ ) was determined indirectly (i.e. calculated as  $A_{0\text{source}} - (A_{\text{waste}} + A_{\text{source}})$ ) to minimize radiation exposure. This method also proved to be significantly more accurate than directly measuring the cartridge in the dose calibrator, presumably due the differing geometry of the cartridge compared to the vials, which can affect dose calibrator measurements. Trapping efficiency (%) was computed as  $A_{\text{cartridge}} / (A_{0\text{source}} - A_{\text{source}})$ . Elution efficiency (%) was calculated as  $A_{\text{collect}} / (A_{\text{cartridge}})$ . Recovery efficiency (%), defined as the

amount of activity recovered following elution relative to starting activity, was calculated as trapping efficiency x elution efficiency. Starting activity was defined as  $A_{0_{\text{source}}} - A_{\text{source}}$  which can be approximated as  $A_{0_{\text{source}}}$  since we found  $A_{\text{source}} < \sim 0.1\%$  of  $A_{0_{\text{source}}}$ .

### **6.2.5 Interface between concentrator and droplet synthesizer**

In chapter 5, we showed that multiple 2  $\mu\text{L}$  droplets of the initial [ $^{18}\text{F}$ ]fluoride solution could be sequentially loaded onto the synthesis chip, each one spontaneously moving to the reaction site. Though synthesis scale of [ $^{18}\text{F}$ ]fallypride was modestly increased in this manner (up to 4x more activity, i.e. 8  $\mu\text{L}$  loaded), we observed a reduction in reaction efficiency as activity increased. We suspect that after drying of the larger radionuclide volumes, the residue was spread over a larger surface area of the chip, making it difficult to efficiently redissolve into the precursor solution for the subsequent reaction. Because the concentrator output volume presented in this chapter ( $\sim 25$   $\mu\text{L}$  after optimization) was significantly greater than 8  $\mu\text{L}$ , we suspected even larger impact on reaction efficiency.

We thus compared several methods of loading and drying larger volumes of [ $^{18}\text{F}$ ]fluoride onto the reaction chip, and used Cerenkov luminescence imaging (CLI; further described below) to visualize the distribution of activity on the chip after drying.

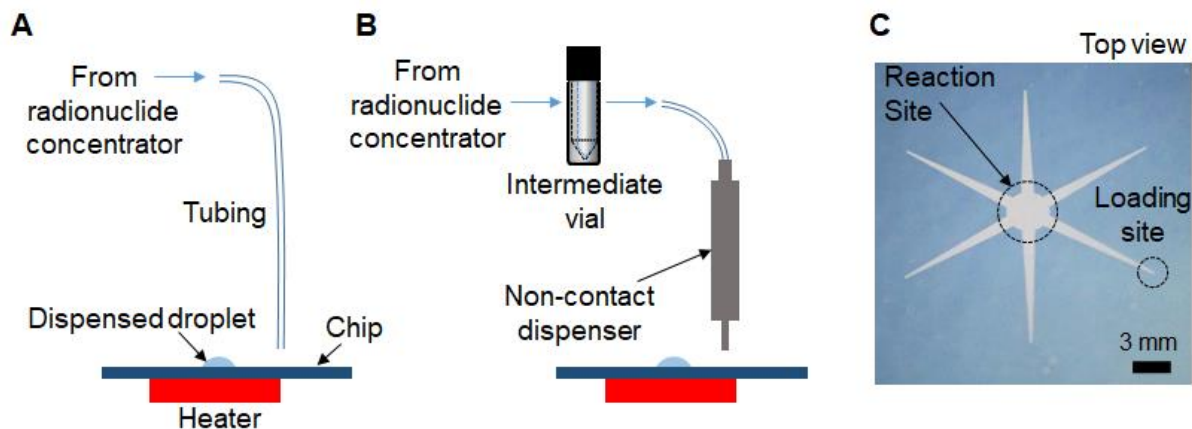


**Figure 6-4: Two different designs of the interface between the radionuclide concentrator and the droplet-based radiochemistry chip**

(A) Concentrated activity is directly dispensed onto the reaction chip. (B) Concentrated activity is first transferred to an intermediate vial (to merge the liquid from individual elution steps into a single liquid plug), and then transfer the contents to the chip as a series of small droplets using a piezoelectric dispenser. (C) Top view of the reaction chip showing both the reaction site and the reagent loading site (highlighted by dotted lines).

In the “direct” method (Figure 6-4A), the concentrator output tubing (ETFE, 0.01” ID, 1/16” OD; 1529L; IDEX) was mounted such that the outlet terminated just above the loading site of the chip. Each ~6  $\mu$ L eluent plug was delivered to the chip immediately after it passed through the cartridge and the resulting droplet was spontaneously transported to the reaction zone. After two eluent plus were loaded onto the chip, the droplets were dried. The elution process could then be repeated to load more eluent onto the chip.

In the “dispenser” method (Figure 6-4B), the eluent plugs from the concentrator were first transferred via ETFE tubing (0.02” ID, 1/16” OD; 1516L; IDEX) to an intermediate vial, and then the combined volume of concentrated [ $^{18}$ F]fluoride solution was connected to the input of a piezoelectric reagent dispenser (INKX0514300A, Lee Company, Westbrook, CT, USA) in the droplet synthesis platform via ETFE tubing (0.01” ID, 1/16” OD; 1529L; IDEX). The intermediate vial was then pressurized (7.5 psi) and concentrated [ $^{18}$ F]fluoride was delivered to the reagent loading site as a series of smaller droplets. We also explored the development of a specialized

droplet merging chip as an alternative to the intermediate vial. In this chip, air gaps between eluent plugs are removed through a porous PTFE membrane (see Appendix Section 8.1.3). However, the intermediate vial method was ultimately used due to simplicity of operation and higher reliability. Detailed fluidic connections for each droplet merging technique to the dispenser can be seen in Appendix Figure 8-1.

## 6.2.6 [ $^{18}\text{F}$ ]fallypride synthesis on chip

### 6.2.6.1 Optimization of synthesis conditions

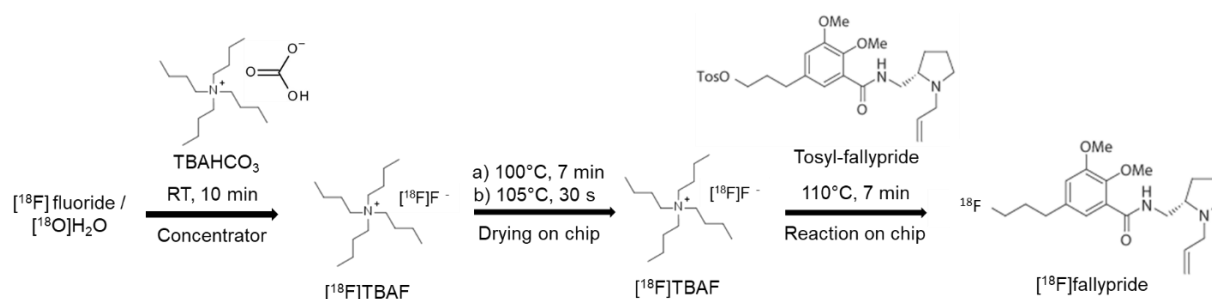


**Figure 6-5: Microdroplet synthesis of [ $^{18}\text{F}$ ]fallypride**

The synthesis conditions of [ $^{18}\text{F}$ ]fallypride (Figure 6-5) were adapted from our previous work (described in chapter 5) synthesizing this compound with the droplet radiosynthesis setup. To facilitate the integration with the upstream [ $^{18}\text{F}$ ]fluoride concentrator, further optimization of the synthesis protocol was performed due to the higher salt amount (TBAHCO $_3$ ) required for efficiently eluting [ $^{18}\text{F}$ ]fluoride from the micro-cartridge. Different [ $^{18}\text{F}$ ]fluoride/TBAHCO $_3$  stock solutions were prepared by mixing [ $^{18}\text{F}$ ]fluoride/[ $^{18}\text{O}$ ]H $_2$ O (11~22 MBq [0.3-0.6 mCi]) with different amounts of 75 mM TBAHCO $_3$  solution to produce final concentrations in the range 0.51 – 71 mM. For each, a 12.4  $\mu\text{L}$  droplet of [ $^{18}\text{F}$ ]fluoride/TBAHCO $_3$  solution was manually loaded on the reaction site of the chip and dried at 105°C for 1 min. Then, a droplet of precursor solution (77 mM, tosyl fallypride dissolved in a 1:1 (v:v) mixture of MeCN and thexyl alcohol) was loaded and moved to the reaction site automatically, and the

chip was heated at 110°C for 7 min to perform the fluorination step. Different volumes (2-8  $\mu\text{L}$ ) of precursor solution were tested. Afterwards, twenty 1  $\mu\text{L}$  droplets of collection solution (9:1 (v:v) mixture of MeOH and DI water) were sequentially deposited at a different reagent loading site and spontaneously moved to the reaction site to dilute the resulting crude reaction mixture. After automatically lowering the collection tubing into the droplet, the diluted droplet was then transferred into the collection vial via negative pressure. The collection process was repeated 4x to maximize recovery of the crude product.

#### **6.2.6.2 *Synthesis using integrated platform***

For synthesis performed with the integrated systems, up to 41 GBq [1.1 Ci] of activity was loaded in the source vial and concentrated into  $\sim 25$   $\mu\text{L}$  (i.e. 4 elution steps) comprised of 25 mM TBAHCO<sub>3</sub> (12.4  $\mu\text{L}$ ) and DI water (12.4  $\mu\text{L}$ ). The concentrated activity was loaded on the loading site of the chip as a series of  $\sim 0.5$   $\mu\text{L}$  droplets. During the loading process, each droplet spontaneously moved toward the reaction site. The chip was heated to 100 °C and the interval between droplets adjusted (to about 4 s) such that each droplet dried soon after reaching the reaction site. The full amount of concentrated activity could be delivered in  $\sim 3$  min. To ensure efficient delivery of activity to the chip, the concentrator fluid paths (minus the SAX cartridge) were further rinsed with a total of 25  $\mu\text{L}$  of DI water (i.e. 4 elution steps) and delivered to the chip and dried in the same fashion. After  $\sim 3$  min additional time for loading and drying the rinse solution, the chip was heated an extra 30s at 105 °C. Next, eight 1  $\mu\text{L}$  droplets of fallypride precursor solution were then loaded sequentially on the chip, and the fluorination was performed at 110°C for 7 min. Afterwards, the crude product was collected via  $\sim 80$   $\mu\text{L}$  of collection solution into the collection vial as described above.

For [ $^{18}\text{F}$ ]fallypride synthesis of GBq level, we waited several hours for the activity to first decay before taking detailed measurements. To prevent radiolysis during this time, the crude [ $^{18}\text{F}$ ]fallypride was collected into a vial pre-loaded with 2 mL of EtOH.

### 6.2.7 Evaluation of synthesis performance

Performance of the on-chip [ $^{18}\text{F}$ ]fallypride synthesis was assessed via measurements of radioactivity and fluorination efficiency (conversion of [ $^{18}\text{F}$ ]fluoride to product). Radioactivity was measured with a calibrated dose calibrator (CRC-25R, Capintec) at various times throughout the synthesis process. Radioactivity recovery was calculated as the collected crude product divided by the starting radioactivity, corrected for decay. Fluorination efficiency of the collected crude product was determined via radio thin layer chromatography (radio-TLC). A 1  $\mu\text{L}$  droplet of crude product was spotted on a silica TLC plate (JT4449-2, J.T. Baker, Center Valley, PA, USA) with a micropipette. The TLC plate was developed in the mobile phase (60% MeCN in 25 mM  $\text{NH}_4\text{HCO}_2$  with 1% TEA (v/v)) and then analyzed with a scanner (MiniGITA star, Raytest, Straubenhardt, Germany). In the resulting TLC chromatogram, two peaks were identified: unreacted [ $^{18}\text{F}$ ]fluoride ( $R_f=0.0$ ) and [ $^{18}\text{F}$ ]fallypride ( $R_f=0.9$ ). Fluorination efficiency was calculated as the area under the [ $^{18}\text{F}$ ]fallypride peak divided by the area under both peaks. The decay-corrected crude radiochemical yield (crude RCY) of [ $^{18}\text{F}$ ]fallypride was defined as the radioactivity recovery times the fluorination efficiency.

Cerenkov Luminescence Imaging (CLI) [145] was utilized to visualize the distribution of radioactivity on the chip after drying the [ $^{18}\text{F}$ ]fluoride solution as previously described in chapter 5. Briefly, to obtain an image, a glass microscope slide (1mm thick) was placed on top of the chip prior to placing it in the light-tight imaging chamber. An image was then collected (exposure time 300 s) and then image corrections and background subtraction were applied.

### **6.2.8 Purification, formulation, and quality control testing**

For some batches of [<sup>18</sup>F]Fallypride produced at the 15 MBq [0.41 mCi] and 1 GBq [27 mCi] scale, we also performed radio-HPLC purification of the crude product, and analysis of the pure product, both using an analytical scale Smartline HPLC system (Knauer, Berlin, Germany) equipped with a degasser (Model 5050), pump (Model 1000), a 200 µL injection loop, a UV (254nm) detector (Eckert & Ziegler, Berlin, Germany) and a gamma-radiation detector and counter (B-FC- 4100 and BFC-1000; Bioscan, Inc., Poway, CA, USA). Separation was performed using a C18 column (Kinetex, 250 x 4.6 mm, 5 µm, Phenomenex, Torrance, CA, USA). The mobile phase was 60% MeCN in 25 mM NH<sub>4</sub>HCO<sub>2</sub> with 1% TEA (v/v) and flow rate was 1.5 mL/min. The retention time of fallypride was 4.5 min. Chromatograms were collected using a GinaStar analog-to-digital converter (raytest USA, Inc., Wilmington, NC, USA) and GinaStar software (raytest USA, Inc.) running on a PC. Based on the chromatograms, molar activity of [<sup>18</sup>F]fallypride was calculated as described previously. [63]

For purification, the crude [<sup>18</sup>F]fallypride mixture collected from the chip (80 µL) was diluted with 90 µL mobile phase and manually injected into the HPLC system, and the pure [<sup>18</sup>F]fallypride fraction (~2 mL) was collected through a selector valve (Cheminert, Valco Instrument Co. Inc.) based on the gamma detector signal.

## **6.3 Results and Discussion**

### **6.3.1 [<sup>18</sup>F]fluoride concentrator cartridge optimization**

First, due to the change in cartridge fabrication, we performed optimization of the cartridge design and [<sup>18</sup>F]fluoride concentration process. Initially, we compared flow rates (of DI water) through the different cartridge designs (resin type, resin mass, tubing inner diameter). The results are tabulated in Table 6-2. We consider flow rates ≥ 0.5mL/min to be acceptable, which ensures trapping of [<sup>18</sup>F]fluoride can be completed in a short time. We also found that flow rates in this range gave reliable, repeatable elution compared to cartridges with slow flow rates. For

the Bio-Rad AG-MP1 resin, both 2 mg and 3 mg cartridges had suitable flow rates. For the Sep-Pak QMA resin, cartridges with sufficient flow included 3mg resin in 0.03” ID tubing and 5 mg resin in 0.04” ID tubing. Lastly, flow rates were adequate for all tested Oasis MAX cartridges (3 mg or 5 mg in 0.03” ID tubing and 7 mg in 0.04” ID tubing).

**Table 6-2: Flow rates of water (driven at 20 psi) through different SAX cartridges (resin type and mass)**

Resin Type	Bio-Rad AG-MP1			Sep-Pak QMA				Oasis MAX		
<b>Resin Mass (mg)</b>	2	3	4	3	5	5	7	3	5	7
<b>Tubing inner diameter (inch)</b>	0.03	0.03	0.03	0.03	0.03	0.04	0.04	0.03	0.03	0.04
<b>Flow Rate (mL/min)</b>	0.92 ± 0.11 (n=3)	0.84 ± 0.06 (n=4)	0.47 ± 0.04 (n=3)	0.68 ± 0.11 (n=4)	0.28 ± 0.11 (n = 2)	0.56 ± 0.08 (n = 2)	0.23 ± 0.07 (n = 2)	0.70 ± 0.03 (n = 2)	0.50 ± 0.04 (n = 2)	0.92 ± 0.08 (n = 2)

It should be noted that these resin masses are all equal to or higher than literature reports where efficient trapping of up to 110 GBq [3Ci] [<sup>18</sup>F]fluoride was achieved using 2 mg of various SAX resins [45,65].

### 6.3.2 Optimization of [<sup>18</sup>F]fluoride concentration process

**Table 6-3: Effect of resin type on trapping and elution performance (for 3 mg cartridges)**

Values are presented as average ± standard deviation, calculated from the indicated number of repeats (n). Each of the 6 eluent plugs (E1, E2,...E6) contains 6.2 μL of 25mM TBAHCO<sub>3</sub>. Eluted percentages are relative to activity that is initially trapped on the cartridge. All measurements are decay corrected.

	Resin type		
	Sep-Pak QMA	AG-MP1	Oasis MAX
Number of repeats (n)	2	2	1
Trapping efficiency (%)	99.4 ± 0.8	96± 4	99
Partial elution efficiency (E1+E2) (%)	92 ± 5	21± 3	65
Partial elution efficiency (E3+E4) (%)	6 ± 4	68± 6	34
Partial elution efficiency (E5+E6) (%)	0.9 ± 0.4	12± 8	3
Overall elution efficiency (E1 to E4) (%)	98± 1	89 ± 9	100
Overall elution efficiency (E1 to E6) (%)	98.9 ± 0.2	101 ± 1	103

Trapping and elution performance was first compared between the 3 resin types, using cartridges containing 3 mg of resin (Table 6-3). Eluent composition was arbitrarily chosen to be 25mM TBAHCO<sub>3</sub> as a starting point. Trapping of fluoride was high for all resins: 99.4 ± 0.8% (n = 2) for the Sep-Pak QMA resin, 96 ± 4% (n = 2) for the Bio-Rad AG-MP1 resin, and 99% for the Oasis MAX resin. However, differences were observed among elution efficiencies. Sep-Pak QMA cartridges released 92 ± 5% (n = 2) of the activity in the first two elutions, while the Bio-Rad AG-MP1 and Oasis MAX cartridges released only 21 ± 3% (n = 2) and 65% (n = 1), respectively. After four elution steps, all cartridges had high cumulative elution efficiencies, i.e. 98 ± 1% (n=2) and 100% (n=1) for the Sep-Pak QMA and Oasis MCX resins, respectively, and 89 ± 9% (n=2) for the Bio-Rad AG-MP1 resin. Due to the high elution efficiency using minimal

eluent volume (only 2 elution steps) using the Sep-Pak QMA resin, further experiments focused on this resin.

In order to explore if eluent concentration could be decreased to reduce the amount of TBAHCO<sub>3</sub> that enters the downstream reaction, we explored the effect of eluent concentration (Table 6-4) using the 3 mg Sep-Pak QMA cartridges. Consistent with the previous experiment, trapping of [<sup>18</sup>F]fluoride was nearly quantitative for all trials (≥93%). Increasing concentration of TBAHCO<sub>3</sub> was found to increase the amount of activity eluted, especially in the first two elution steps. For 3.8 mM TBAHCO<sub>3</sub>, the efficiency was only 5 ± 1% (n=3) in the first 2 elutions and only reached 64 ± 4 (n=3) after 6 elution steps. In the case of 10 mM TBAHCO<sub>3</sub>, elution efficiency after 2 steps was also low (17 ± 9, n=3), but increased to ~89% (n=3) after 4 elution steps. For additional repeats of 25 mM TBAHCO<sub>3</sub>, we again observed reliable and high recovery (95 ± 2%; n=4) within the first two elution steps (12.4 μL). We hypothesized that the missing ~5% of activity had likely been released from the cartridge but was lost as residual liquid left behind in the system. We explored using eluting with two plugs of 25mM TBAHCO<sub>3</sub> followed by two plugs of DI water (12.4 μL; to rinse this residual activity to the concentrator outlet), and found that all of the activity (100. ± 1%, n=3) was recovered. Because this approach resulted in a total salt amount lower than using 4 elutions of 10 mM eluent, we focused on this approach for further experiments.

**Table 6-4: Effect of eluent concentration on trapping and elution performance (for 3 mg Sep-Pak QMA cartridges)**

Values are presented as average  $\pm$  standard deviation, from the indicated number of repeats (n). Each elution plug was 6.2 $\mu$ L. Eluted percentages are relative to activity that is trapped on the cartridge. All measurements are decay corrected.

\* In the final column, eluent plugs 1 and 2 were 25 mM TBAHCO<sub>3</sub>, eluent plugs 3 and 4 were DI water. No further elution steps were performed.

	TBAHCO <sub>3</sub> concentration (mM)			
	3.8	10.	25	25*
<b>Number of repeats (n)</b>	3	3	4	3
<b>Trapping efficiency (%)</b>	99.8 $\pm$ 0.4	99.8 $\pm$ 0.2	93 $\pm$ 5	99.6 $\pm$ 0.3
<b>Elution 1+2 efficiency (%)</b>	5 $\pm$ 1	17 $\pm$ 9	95 $\pm$ 2	94 $\pm$ 3
<b>Elution 3+4 efficiency (%)</b>	18 $\pm$ 1	72 $\pm$ 3	2.9 $\pm$ 0.4	5 $\pm$ 1
<b>Elution 5+6 efficiency (%)</b>	41 $\pm$ 3	12 $\pm$ 7	0.8 $\pm$ 0.3	N/A
<b>Elutions 1 to 6 efficiency (%)</b>	64 $\pm$ 4	101 $\pm$ 1	99 $\pm$ 2	100. $\pm$ 1

### 6.3.3 Optimization of [<sup>18</sup>F]fallypride synthesis conditions

First, the effect of TBAHCO<sub>3</sub> amount on fluorination efficiency of [<sup>18</sup>F]fallypride was investigated (Table 6-5). Across all conditions, the radioactivity recovery was relatively constant (85-93%), but the fluorination efficiency varied significantly, with a maximum value (99% conversion; 90% crude RCY) for a concentration of 10 mM. With higher concentration, we observed the formation of a radioactive side-product, perhaps due to the base-sensitivity of the precursor. With lower concentration, we did not observe the side product, but the conversion decreased.

**Table 6-5: Effect of different TBAHCO<sub>3</sub> concentrations (mixed with [<sup>18</sup>F]fluoride source) on the performance of the droplet synthesis of [<sup>18</sup>F]fallypride (n=1)**

In each case, the volume of this initial solution was 12.4 μL. After drying, the fluorination was performed by adding 2 μL of precursor solution (77 mM; in a mixture of MeCN and hexyl alcohol (1:1, v/v)). All reported efficiencies and yields are decay-corrected.

	Concentration of TBAHCO <sub>3</sub> (mM)					
	71	25	10.	3.6	1.2	0.51
Radioactivity recovery (%)	88	86	91	93	85	86
Fluorination efficiency (%)	12	65	99	47	32	39
Crude radiochemical yield (%)	11	56	90.	44	27	33
Residual on chip (%)	5	10.	5	4	4	3

However, as described above, the elution efficiency of the micro-cartridge with two elutions (12.4 μL) of 10 mM TBAHCO<sub>3</sub> was very low (17 ± 9%, n=2). Thus even with an optimal synthesis, the overall performance (concentrator efficiency and synthesis efficiency) would be expected to be very low (~17% x 90% = 15%). Comparing instead the elution procedure with 12.4 μL of 25 mM TBAHCO<sub>3</sub> followed by 12.4 μL of DI water, the concentrator efficiency was much higher (100. ± 1%, n=3). Even with the reduced synthesis efficiency with 25 mM TBAHCO<sub>3</sub> (65% conversion; 56% crude RCY), the overall performance would be expected to be good (~100% x 56% = 56%).

**Table 6-6: Optimization of precursor volume for [<sup>18</sup>F]fallypride synthesis**

Concentration of TBAHCO<sub>3</sub> solution for all reactions was 25 mM. Precursor concentration was 77 mM in a mixture of MeCN and thexyl alcohol (1:1, v/v) for all reactions. Note: all reported efficiencies and yields are decay-corrected.

	Precursor volume (μL)		
	2 (n=2)	4	8
Radioactivity recovery (%)	88 ± 2	93	92
Fluorination efficiency (%)	65 ± 0	98	99
Crude radiochemical yield (%)	57 ± 1	91	92
Residual on chip (%)	10 ± 1	3	6

Using the condition of 25 mM TBAHCO<sub>3</sub> mixed with the [<sup>18</sup>F]fluoride solution (12.4 μL), we then studied the effect of the amount of precursor (Table 6-6). Increasing the volume of precursor solution (77 mM) was found to increase the fluorination efficiency and crude RCY. Increasing from 2 μL to 4 μL resulted in a significant improvement (from 57 ± 1%, n=2 to 91%, n = 1) in crude RCY. Little difference was observed upon further increasing the precursor solution volume from 4 μL to 8 μL, but we elected to use the higher amount to provide a safety factor. One factor to consider is whether the DI water rinse during the radionuclide concentration phase was important, as this resulted in only a modest increase in activity recovered from the concentrator (94 ± 3%, n=3 to 100. ± 1%, n=3), but took additional time for elution (~1min) and drying (~1.5 min). Radioactive decay during this added time is less than the gains from the rinsing step and thus the rinsing step has an overall benefit on process efficiency.

### 6.3.4 Performance of transfer method between systems

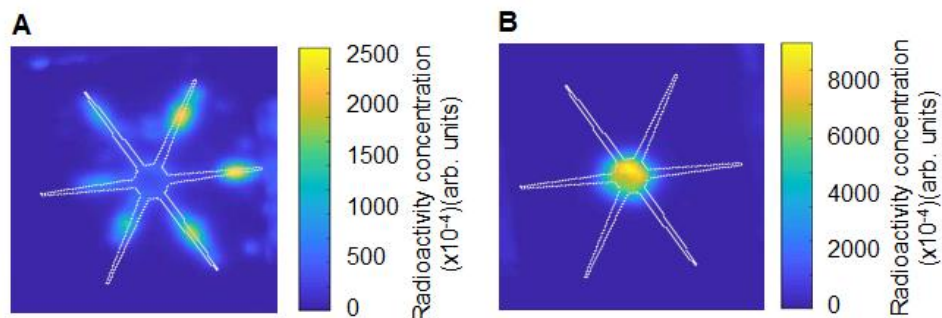


**Figure 6-6: Distribution of radioactivity on the chip after evaporation following initial [<sup>18</sup>F]fluoride loading and drying, visualized using Cerenkov imaging**

(A) Concentrated [<sup>18</sup>F]TBAF (12.4  $\mu$ L) + water rinse of the cartridge (12.4  $\mu$ L) were loaded via the “aliquotting” method as a series of small droplets ( $\sim$ 0.5  $\mu$ L) that were dried as they arrived at the reaction site; (B) Concentrated [<sup>18</sup>F]TBAF loaded all at once (12.4  $\mu$ L total) and then dried followed by water rinse of the cartridge (12.4  $\mu$ L) loaded all at once and dried. The white line indicates the boundary of the hydrophilic pattern on the chip.

First the “direct” loading method was tested. The output volume of two elutions (12.4  $\mu$ L) from the concentrator was loaded on the microfluidic chip as two sequential 6.2  $\mu$ L droplets and dried. The micro-cartridge was then rinsed with two 6.2 $\mu$ L DI water plugs and this rinse volume was also loaded onto the chip and dried. In this direct loading method, however, the droplet did not remain confined to the reaction zone and spread out along all of the reagent delivery paths. Indeed, CLI imaging of the chip after drying confirmed that radioactivity was distributed across all hydrophilic areas of the chip after the [<sup>18</sup>F]fluoride drying process (Figure 6-6A). This is undesirable as much of the dried [<sup>18</sup>F]TBAF complex would not be dissolved into the precursor droplet loaded for the subsequent fluorination step. The problem was likely due to the mismatch between the volume (12.4  $\mu$ L) output from the concentrator and the capacity of the chip (2  $\mu$ L). Next, the “dispenser” loading method was evaluated. The concentrator output was connected to the dispenser through an intermediate vial, which first collected the full volume of concentrated activity from the 2 eluent plugs and 2 DI water plugs (total 25  $\mu$ L), and then delivered this

volume to the reagent loading site via the dispenser as a series of ~0.5  $\mu\text{L}$  droplets while the chip was heated at 100°C. We observed that only 48% of the eluted activity was found to be loaded on the chip – an additional 26% and 20% of the eluted radioactivity were found as residual activity in the dispenser and intermediate vial, respectively. To recover the radioactivity left in the dispenser and the intermediate vial, another 4 plugs of DI water (25  $\mu\text{L}$  total) were rinsed through the concentrator (without passing through the cartridge), into the intermediate vial, and then dispensed as a series of ~0.5  $\mu\text{L}$  droplets and dried in the same manner as described above. With this modification, a total of 96% of the eluted radioactivity was loaded onto the chip, with only 4% of eluted radioactivity found as residual activity in other parts of the system (Table 6-7). In stark contrast to the above method where the full volume was loaded, the CLI image taken after the droplet-by-droplet loading and drying step confirmed that all of the radioactivity was confined within the reaction zone (Figure 6-6B), suggesting that it would be efficiently solvated when the precursor solution was added.

**Table 6-7: Activity loss in various locations within the integrated system during [ $^{18}\text{F}$ ]fluoride transfer and dispensing.**

Each measurement is relative to amount of activity trapped on the cartridge.

	Distribution of radioactivity after elution	
	Without the 2nd DI water rinse	With the 2nd DI water rinse
Activity left in the dispenser (%)	25.6	3.1
Activity loaded on the chip (%)	48.2	95.9
Activity left in the intermediate vial (%)	20.1	0.5
Activity left in the tubing and frit (%)	1.5	0.5

### 6.3.5 Low activity [ $^{18}\text{F}$ ]fallypride synthesis

Using the optimal [ $^{18}\text{F}$ ]fluoride concentration and transfer method, [ $^{18}\text{F}$ ]fallypride synthesis was initially performed on the integrated system with low overall starting activity to verify the functionality of the system and assess its performance (Table 6-8). Starting with 11 – 170 MBq [0.3 – 4.5 mCi] of [ $^{18}\text{F}$ ]fluoride solution, the trapping efficiency of the micro-cartridge

was consistent at  $100 \pm 0 \%$  ( $n = 6$ ), followed by high elution of trapped activity ( $91 \pm 7 \%$ ;  $n = 6$ ) from the cartridge. The concentration process followed by the “dispenser” transfer method as described above resulted in  $89 \pm 7 \%$  ( $n = 6$ ) of overall starting activity loaded onto the chip. The fluorination efficiency was  $89 \pm 5 \%$  ( $n = 6$ ) and the overall radioactivity recovery was  $81 \pm 9 \%$  ( $n = 6$ ), resulting in an overall crude RCY of  $72 \pm 8 \%$  ( $n = 6$ ). After collection of the crude product, only  $7 \pm 3 \%$  ( $n = 6$ ) of the initially-loaded radioactivity remained stuck to the chip. The crude RCY was slightly higher than we previously reported for the droplet-based synthesis using passive transport chips with low starting activity (in chapter 5), i.e.  $64 \pm 6\%$  ( $n=4$ ). The previously reported fluorination efficiency and radioactivity recovery were  $76 \pm 4 \%$  ( $n=4$ ) and  $84 \pm 4 \%$  ( $n=4$ ), respectively, suggesting that the current synthesis protocol with increased salt concentration and optimized precursor volume resulted in substantial improvement in fluorination efficiency. The integrated system had slightly lower radioactivity recovery due to the ~6% activity loss from the concentration step.

**Table 6-8: Detailed performance of integrated process of radionuclide concentration and droplet synthesis of [<sup>18</sup>F]fallypride**

All reported losses, efficiencies, and yields are decay-corrected. Values are presented as average ± standard deviation, computed from n=6 repeats. Except where otherwise indicated, losses and recovery efficiencies are computed with respect to the starting activity.

<b>Radionuclide Concentration Steps</b>	
Starting activity (MBq [mCi])	11-170 [0.3 - 4.5]
Trapping efficiency (%)	100 ± 0
Elution efficiency (%) (relative to trapped activity)	91 ± 7
Waste vial (%)	0 ± 0
Activity on cartridge after elution (%)	6 ± 6
Activity on chip after elution (%)	89 ± 7
Activity in the intermediate vial after dispensing (%)	2 ± 1
<b>Droplet Radiosynthesis Steps</b>	
Fluorination efficiency (%)	89 ± 5
Residual activity on chip after collection (%)	7 ± 3
<b>Integrated Synthesis Performance</b>	
Overall radioactivity recovery (%)	81 ± 9
Overall crude RCY (%)	72 ± 8

### 6.3.6 High activity [<sup>18</sup>F]fallypride synthesis

Next, syntheses were performed starting with higher activities (ranging from 3.7 GBq to 41 GBq [0.10 Ci to 1.1 Ci]). While the synthesis was successful at all scales, we observed the crude RCY to decrease from 65 % to 25 % as the overall starting activity increased (Figure 6-7A). To better understand the effect, we looked at the performance of different factors individually. In the radionuclide concentration module, the elution efficiency of [<sup>18</sup>F]fluoride was high and consistent (96 ± 4%, n=11) across all experimental runs, but the overall performance was adversely impacted by the trapping efficiency, which decreased from ~94% to ~63% as the starting activity was increased (Figure 6-7B). The decreased trapping performance of the micro-cartridge suggests the capacity of the cartridge was insufficient to trap all of the [<sup>18</sup>F]fluoride.

This was surprising as several reports have indicated trapping of high amounts of [<sup>18</sup>F]fluoride (up to 110 GBq [3 Ci]) using cartridges packed with only ~2 mg of resin. [45,65] After some investigation, we discovered there may be impurities in our source of [<sup>18</sup>F]fluoride that reduce the trapping efficiency far below the capacity as measured by spiking KF solutions with [<sup>18</sup>F]fluoride (See Appendix, Sections 8.2-8.4). Further studies, such as investigation of cartridges with higher resin mass, could potentially improve the trapping performance at high activity levels.

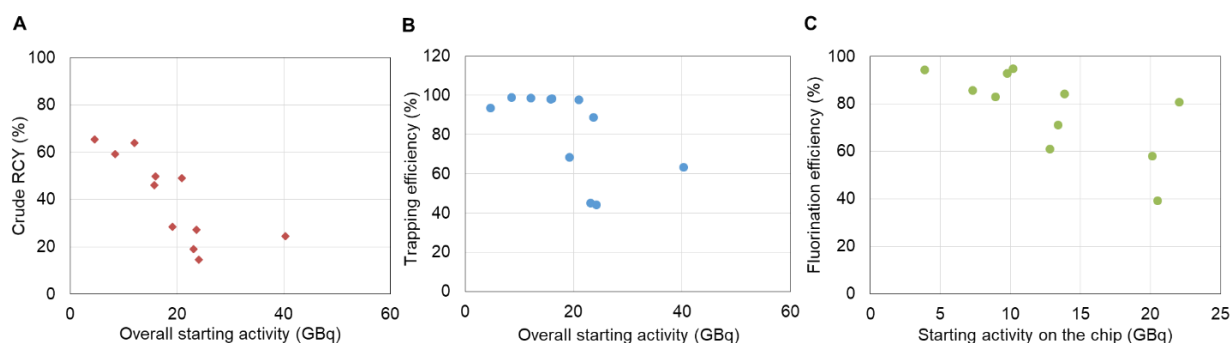


**Figure 6-7: Performance of synthesis on integrated system at higher activity levels (3.7 – 41 GBq [0.10 – 1.1 Ci])**

(A) Overall crude RCY (including radionuclide concentration and crude synthesis) as a function of starting activity. (B) Trapping efficiency within the cartridge as a function of starting activity. The elution efficiency remained consistent ( $96 \pm 4\%$ ,  $n=11$ ) across all experimental runs and is not shown here. (C) Fluorination efficiency as a function of concentrated activity loaded onto the chip.

Looking at the performance of the droplet synthesis process, we observed that the fluorination efficiency decreased from around 90% to 40% as the amount of starting activity on the chip increased (Figure 6-7C). One potential explanation is that the reaction conditions may move out of the optimal range as the precursor to fluoride ratio decreased due to increased starting activity. Based on the molar activity of [<sup>18</sup>F]fluoride at EOB previously reported as 740 GBq/ $\mu$ mol (20 Ci/ $\mu$ mol) [63], the molar ratio of precursor to fluoride at low starting activity (11 to 170 MBq) ranged from 41000 to 2700 while the ratio of that at high starting activity (3.7 to 41 GBq [0.1 to 1Ci]) ranged from only 100 to 11. Potentially at the higher activity levels the reduced

excess of precursor adversely impacts the yield during the short fluorination reaction. Further studies at high activity scales, e.g. using different amounts of precursor, could help to determine whether this is a factor. The decrease in fluorination efficiency when using high activities might also be due to radiolysis during the fluorination step. At the beginning of the reaction, the activity concentration in the reaction droplet is quite high, ranging from 460 to 5100 GBq/mL [13 to 140Ci/mL] (assuming 8  $\mu$ L precursor solution is added) and is increasing somewhat during the fluorination reaction as the reaction solvent partially evaporates. Although EtOH was preloaded in the collection vial to prevent radiolysis after the collection step (by dilution and because EtOH acts as a radical scavenger), some radiofluorinated impurities were observed in the HPLC chromatograms of the crude products when starting activity was higher than 8.0 GBq [0.22Ci] (Figure 6-8) and the number and quantity of radioactive impurities increased with increased starting activity. In contrast, the HPLC chromatogram from a batch starting with 0.20 GBq [5.4 mCi] of activity showed only two peaks, [ $^{18}$ F]fluoride and [ $^{18}$ F]fallypride. Further studies would be needed to confirm exactly when radiolysis is happening, which would guide potential methods to reduce it such as addition of radical scavengers at other stages of the synthesis, or attempting to change the droplet geometry (i.e. make it flatter) to reduce radiolysis by geometric effects. [54] Another potential approach could be to divide the activity into a few smaller batches (e.g., < 8 GBq [0.22Ci], where no radiolysis was evident in chromatograms), performing several smaller-scale syntheses in parallel, and then combining the batches in the presence of a radiolysis quenching agent. At <8 GBq [0.22Ci] activity level, the crude RCY was still ~60 %, not far from the value 72 % at low activities, potentially enabling overall conversion of 60 % for much larger batch sizes.

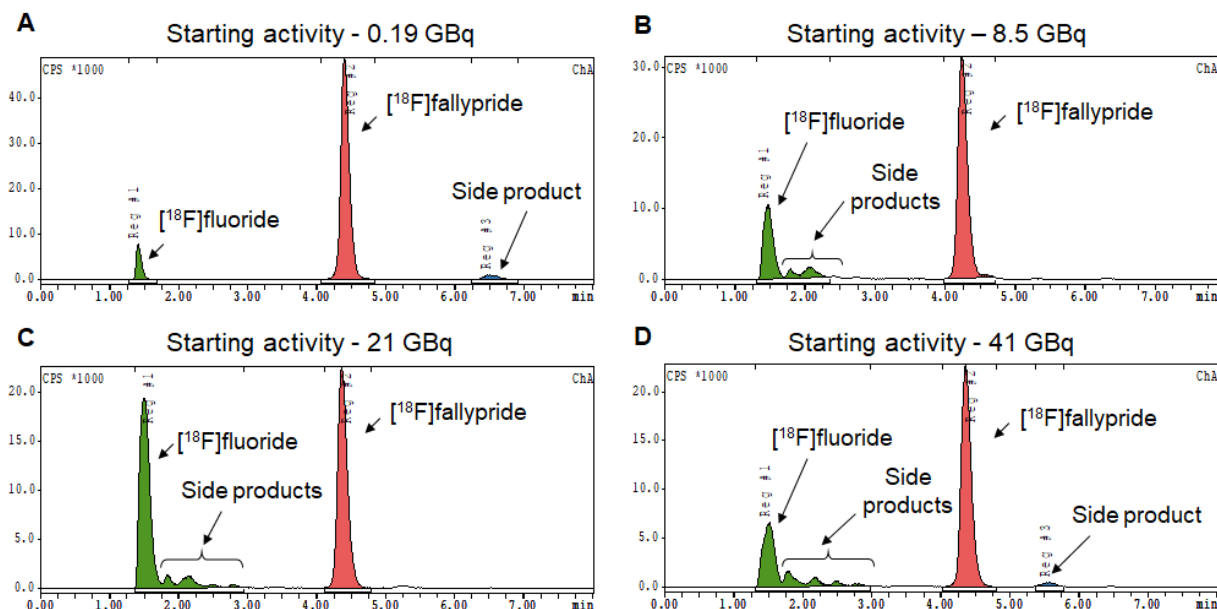


**Figure 6-8: Examples of HPLC purification (crude) chromatograms of syntheses**  
 Starting activities of (A) 0.19 GBq [5.1 mCi], (B) 8.5 GBq [230 mCi], (C) 21 GBq [570 mCi], and (D) 41 GBq [1.1 Ci] were explored.

Even though the crude RCY was only 25% with 41 GBq [1.1Ci] starting activity, a total of 7.2 GBq [0.19 Ci]  $[^{18}\text{F}]$ fallypride product (not decay corrected) was produced after 35 min synthesis, 5 min purification via analytical-scale HPLC, and 10 min formulation. The resulting amount of  $[^{18}\text{F}]$ fallypride could easily supply multiple human doses (each needing  $\sim 0.37$  GBq [10 mCi] at the time of injection), even if they were scheduled throughout the day (i.e. product loss due to radioactive decay).

The overall crude synthesis took  $\sim 35$  min. This is 15 min longer than our previously reported microdroplet synthesis method (chapter 5), due to the extra time needed for concentration of  $[^{18}\text{F}]$ fluoride ( $\sim 10$  min) and transfer, loading, and drying of the  $[^{18}\text{F}]$ fluoride onto the chip ( $\sim 7$  min), compared to only  $\sim 1$  min in our previous synthesis method. However, the previous method was limited to using only  $\sim 74$  MBq [2 mCi] of activity (2  $\mu\text{L}$ ; assuming 37 GBq/mL [1Ci/mL]), and scaling up by the methods reported therein would have required

sequential loading and drying of 1000  $\mu\text{L}$  to load 37 GBq [1Ci] of activity, a process that would have taken  $\sim$ 170 min.

The molar activity (81-270 GBq/ $\mu\text{mol}$  [2.2 – 7.3 Ci/ $\mu\text{mol}$ ] , at the end of formulation) of all experimental runs carried out on the integrated system was up to 5 times higher than previously reported molar activities for [ $^{18}\text{F}$ ]fallypride synthesis in the macroscale (15 – 78 GBq/ $\mu\text{mol}$  [0.4 – 2.1 Ci/ $\mu\text{mol}$ ]). [55] Although molar activity ranging from 140 – 192 GBq/ $\mu\text{mol}$  [3.8 – 5.2 Ci/ $\mu\text{mol}$ ] was reported by Moon et al, relative high starting activity (8.1 – 26 GBq [0.22 – 0.70 Ci]) was needed. [155] Using our platform, we achieved similar molar activity but only required 3.7 GBq (0.1 Ci) of starting activity.

## 6.4 Conclusion and Future Work

In this chapter we successfully integrated an automated [ $^{18}\text{F}$ ]fluoride concentrator with a microfluidic droplet-based radiosynthesis platform. We presented a thorough characterization and optimization of the concentration parameters, the transfer of concentrated [ $^{18}\text{F}$ ]fluoride between the two components, and the synthesis of [ $^{18}\text{F}$ ]fallypride as a model compound. Integration of the two platforms followed by complete automation of the overall process enabled fast, safe, reliable, and high-yielding radiosynthesis of [ $^{18}\text{F}$ ]fallypride of clinical quality. Repeatable and reliable concentration of [ $^{18}\text{F}$ ]fluoride followed by radiosynthesis of [ $^{18}\text{F}$ ]fallypride was performed 17 times with starting activities ranging from 11MBq – 41GBq [0.3 mCi – 1.1 Ci]. Complete concentration and synthesis could be performed in 35 min. For “low activity” syntheses starting with 11-170 MBq [0.3 – 4.6 mCi], fluorination efficiency and crude RCY were  $89 \pm 5\%$  ( $n = 6$ ) and  $72 \pm 8\%$  ( $n = 6$ ), respectively. As starting activity was increased (4.5 – 41 GBq [0.12 – 1.1 Ci]), the overall crude RCY dropped significantly, primarily due to the a decreasing in the trapping efficiency of [ $^{18}\text{F}$ ]fluoride during the concentration process, which can likely be addressed through further cartridge optimization. We also observed some reduction in

fluorination efficiency as the starting activity was increased, potentially due to mismatched stoichiometry or radiolysis effects at higher activities. Future studies will further investigate these factors and potential solutions.

This study shows that despite a small reaction volume (2-8  $\mu\text{L}$  here), it is possible to load significant quantities of the radionuclide into microdroplet reactors. In this study, starting activity were scaled up to 41 GBq [1.1 Ci], limited only by the capacity of our cyclotron facility. We also found the chips to be compatible with the high activity levels and no disruption to the droplet-based processes was observed.

This integrated platform enables production of clinical grade PET tracers in large quantities to enable imaging of several patients or imaging over several radionuclide half-lives (e.g. 4-5 half-lives). Production is reliable and can be completed in a short time enabling ease of use within research facilities and radiopharmacies. We are currently exploring the synthesis of additional  $^{18}\text{F}$ -labeled tracers (e.g. [ $^{18}\text{F}$ ]FDOPA, [ $^{18}\text{F}$ ]FET, etc.) and molecules labeled with different isotopes. In fact, with small modifications of the concentrator module (as seen in chapter 4), we believe that tracers labelled with different radionuclides, such as gallium-68, could also be synthesized at clinically-relevant scales using the integrated platform.

In addition to exploring factors that affect fluorination efficiency at higher starting activities, additional future work will be to also explore optimization of trapping and elution efficiency during concentration with high starting activities. Lastly, we will also perform a full set of clinical quality control tests on several batches of formulated [ $^{18}\text{F}$ ]fallypride to verify that the synthesized tracer is ready for clinical use.

## 7 Future outlook

In chapter 1 I presented the advantages of applying microfluidic technologies for the production of PET tracers. As a recap, these advantages include reduced physical size of synthesis equipment reducing required radiation shielding, better control of reaction parameters such as heating and cooling, increased molar activity of produced tracers, and reduced reagent consumption allowing for decreased production costs. Most importantly, microfluidic technologies can enable decentralized PET tracer production in a cost effective manner by reducing equipment and infrastructure costs and allowing for the production of varying amounts of tracer depending on tracer needs for that day. Comparatively, macroscale production methods are optimized for clinical production of large amounts of tracers which makes scaling down difficult to do in a cost-effective manner. Several groups including our own have focused on building microfluidic versions of the equipment commonly used for production of PET tracers. Chapters 2-6 of this dissertation are focused on describing some of these new microfluidic systems. In chapter 2 of this dissertation, I presented a microfluidic system for concentrating and formulating PET tracers following HPLC purification. In chapter 3 and 4 of this dissertation, I described the design and fabrication of an automated radionuclide concentration platform for the concentration of both [ $^{18}\text{F}$ ]fluoride and [ $^{68}\text{Ga}$ ]Ga $^{3+}$ . In chapter 5, I presented a microfluidic radiosynthesizer using simple to fabricate, simple to use, inexpensive substrates. Lastly, in chapter 6, I described our efforts to combine the radionuclide concentrator and the microfluidic radiosynthesizer to perform integrated synthesis of [ $^{18}\text{F}$ ]fallypride with high starting amounts of [ $^{18}\text{F}$ ]fluoride.

Despite the new systems described in this dissertation, there are still steps in tracer production that could benefit from the development of microfluidic technologies. One step that requires the most attention is in purification of PET tracers. Currently, the gold standard, is

HPLC purification. These HPLC systems, however, are expensive, may have long operation times further reducing product yields due to radioactive decay, and may require relatively large reagent volumes. We believe that microfluidic capillary electrophoresis could be a viable technique for purifying PET tracers, eventually serving as a replacement for HPLC systems. Colleagues in our lab are currently exploring the feasibility of this idea by first testing the use of microfluidic capillary electrophoresis for separation of analytes in nano-liter volumes to assist in PET tracer quality control and then scaling up this separation method for purification of PET tracers.

In addition to exploring new microfluidic technologies for tracer production, there is also an equally important need to work on integrating all of these systems together to allow for an automated, reliable, and efficient system that is capable of producing tracers ready for direct injection into subjects. This dissertation presents the integration of the radionuclide concentrator and microfluidic radiosynthesizer, however, there are still steps in the synthesis process that need to be integrated into the automated workflow. For example, the radiosynthesizer needs interfacing with downstream purification techniques such as HPLC (or possibly capillary electrophoresis in the near future). Furthermore, this purification technique then needs proper interfacing to the concentrator and reformulator platform to prepare the purified tracer for injection. Lastly, an automated method to extract a tiny sample of the final formulated product for QC is also needed. Fellow colleagues of my lab are currently working on techniques for integrating these independent synthesis steps. We envision in the near future demonstration of completely automated PET tracer synthesis from radionuclide concentration to tracer reformulation and quality control testing. We believe that this fully automated microfluidic PET tracer production platform will revolutionize the field of PET imaging by providing researchers

and clinicians with tools to be able to produce tracers on demand in quantities that are cost effective and meet daily tracer needs.

## 8 Appendix

### 8.1 Droplet merging methods at interface of radionuclide concentrator and droplet synthesizer

#### 8.1.1 Overview

Since the concentrated activity is eluted from the micro-cartridge as a series of 6.2 $\mu$ L plugs, the plugs are separated by air gaps. The initial plugs contain most of the concentrated activity, while lower amounts of activity are contained in later plugs. We were concerned that these gaps between plugs could impede efficient transfer to the downstream piezoelectric dispenser and/or adversely affect the dispenser performance. We therefore explored two methods to remove these air gaps; one involved the use of an intermediate vial and the other relied on the use of a microfluidic droplet merging chip.

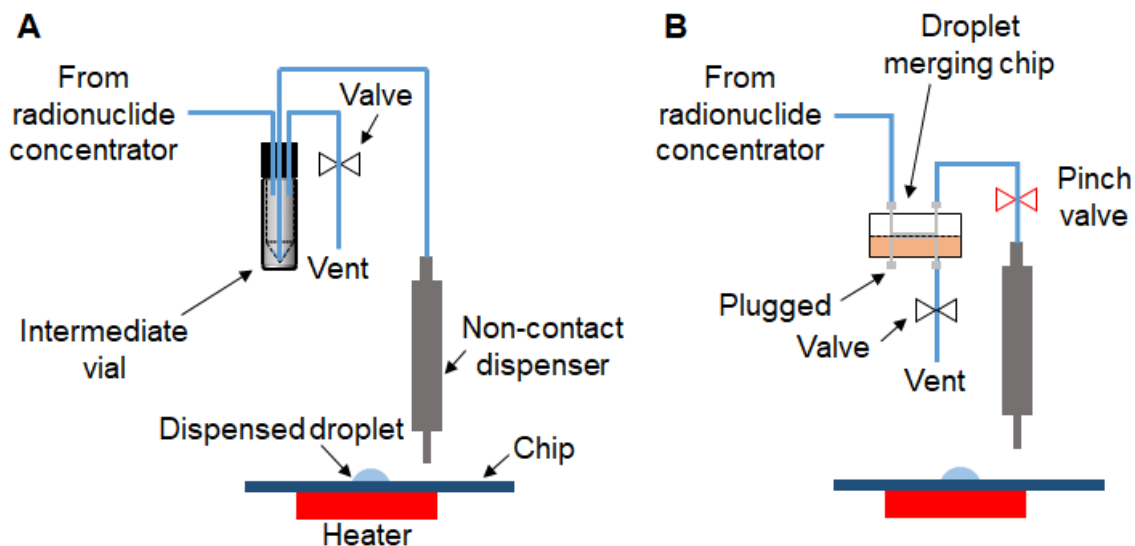


**Figure 8-1: Illustration of droplet merging methods used between the radionuclide concentrator and downstream dispenser**

(A) Intermediate vial setup. (B) Droplet merging chip setup.

### 8.1.2 Intermediate vial approach

One approach to combine the sequential eluent plugs was to first collect them in a small intermediate vial, and then transfer the contents of the vial as a contiguous liquid plug to the reagent dispenser of the droplet-based synthesizer (Figure 8-1A).

The intermediate vial was comprised of a 250 $\mu$ L glass insert (5181-1270, Agilent, Santa Clara, CA, USA) positioned within a septum-capped 1mL v-vial (W986284NG, Wheaton, Millville, NJ, USA). The 1mL v-vial was sealed with a PTFE-faced silicone liner that allows for tubing to be inserted into the vial. The output of the concentrator was connected to the headspace of this vial via ETFE tubing (0.02" ID, 1/16" OD; 1516L; IDEX). An ETFE dip tube (0.01" ID, 1/16" OD; 1529L; IDEX) was inserted to the bottom of the intermediate vial and connected to the piezoelectric dispenser of the droplet synthesis platform. The end of the dip tube was cut at an angle to minimize dead volume at the bottom of the vial during fluid transfer. The dispenser was positioned ~ 5mm above the radionuclide loading site of the reaction chip. To allow venting of the vial, we also inserted a needle (1" long, 25 gauge; 305125; BD Biosciences, San Jose, CA, USA) and connected this the common port of an electronic 3-way valve (LVM105R, SMC Corporation, Japan) via 1/8" OD polyurethane tubing (TIUB01, SMC Corporation, Japan). One output of the valve was plugged and the other was vented to atmosphere.

During elution from the concentrator, this valve is vented to allow trapped air to escape from the intermediate vial. After completion of elution, this valve is closed (switched to the plugged output), and inert gas of the desired dispensing pressure is supplied by the concentrator to drive the vial contents toward the dispenser.

### 8.1.3 Microfluidic chip approach

To avoid potential losses due to splashing from the intermediate vial approach, we also explored the development of a microfluidic droplet merging chip to remove the air gaps (Figure 8-1B).

#### 8.1.3.1 Chip design and operation

The chip (Figure 8-2) is comprised of three layers. The top layer (“fluid layer”) was fabricated out of polyether ether ketone (PEEK) and has a fluid channel machined into it (1.6 mm wide, 0.63 mm deep, 30.3 mm long) along with two threaded inlet and outlet ports which can be interfaced to standard ¼-28 fittings. The middle layer is a Teflon membrane with small (0.22µm) pores which serves as a gas-permeable membrane allowing air in between droplets to pass through to the other side while preventing the passage of aqueous liquids. The bottom layer (“vent layer”) was machined out of acrylic and contains a channel matching the fluid layer (except depth was increased to 2.0 mm). The three layers were clamped together by eight M3 machine screws to form a liquid-tight seal.

Connections to and from the droplet merging chip are shown in Figure 8-2D. The output of the [<sup>18</sup>F]fluoride concentrator is connected to the fluid inlet port of the chip via ETFE tubing (0.01” ID, 1/16” OD; 1529L, IDEX). The fluid outlet port of the chip is connected via silicone tubing (1/32”ID, 1/16”OD; 05-14, Automate Scientific, Berkeley CA, USA) to a piezoelectric dispenser positioned in the synthesis platform. The dispenser was positioned ~ 5mm above the radionuclide loading site of the reaction chip (Figure 6-4). Near the outlet of the droplet merging chip, the silicone tubing passed through a pinch valve (ASCO251866, ASCO Valves, Florham Park, NJ, USA). A pinch valve was chosen here due to the negligible dead volume compared to other valve types. In the vent layer, one vent port is plugged while the other vent port is connected to the common port of a 3-way valve (LVM105R, SMC Corporation, Japan) to enable switching between vented or plugged states.

During operation, the pinch valve is initially closed, and the vent layer is vented to atmosphere. The first liquid plug from the concentrator enters the chip (as trapped air escapes through the vent layer) but cannot travel to the outlet port. The elution process of the [ $^{18}\text{F}$ ]fluoride concentrator proceeds normally. As each plug is eluted, the eluent enters the fluid channel of the droplet merging chip and merges with the existing liquid as air in the air gap is pushed through the membrane layer. After all of the elution steps are complete and the elution plugs are merged, the pinch valve is opened and the vent outlet is plugged using the 3-way valve. Pressure is applied from the concentrator to push the merged eluent plug toward the reagent dispenser of the reactor chip.

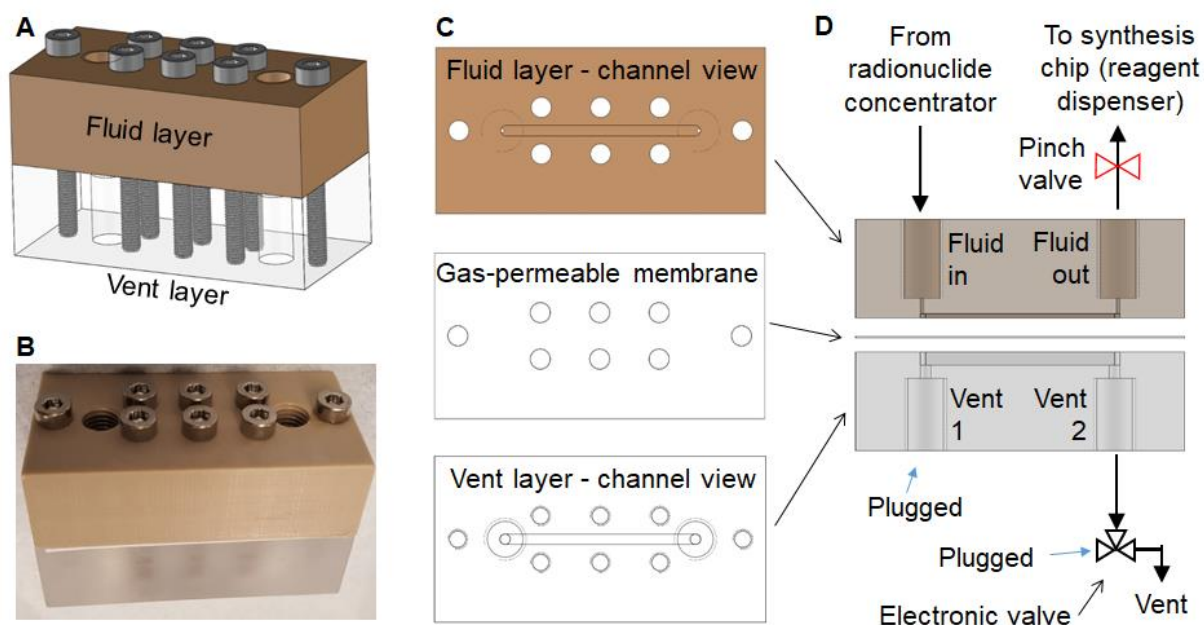


**Figure 8-2: Droplet merging chip**

(A) Structure of assembled chip. (B) Photograph of assembled chip. (C) Bottom view of fluid layer, top view of membrane layer, and top view of vent layer, showing channel, inlet and outlet ports, and holes for securing screws. (D) Side view showing the three layers (with securing screws omitted for clarity) and connections of the chip to upstream radionuclide concentrator and downstream radiosynthesis platform.

### **8.1.3.2 Chip performance**

We characterized the residual activity (dead volume) of the droplet merging chip as a function of the number of elution plugs. A mock eluent solution was made containing [<sup>18</sup>F]fluoride at a known concentration and plugs of this mock eluent solution (each 6.2 μL) were loaded into the droplet merging chip and merged using the procedure described above. The merged plug was collected in a small vial, and the recovered activity measured. Following each experiment, the chip was disassembled and cleaned to remove the possibility of carryover activity into subsequent experiments. The results are shown in Figure 8-3. When only one elution plug was passed through the chip, only 70 ± 6% (n = 3) of the activity was recovered. As the number of elution plugs was increased, the total amount of activity that was recovered increased. For 3 or 4 elution plugs, the activity recovery was high, i.e. 92.1 ± 5.1% (n=3) and 94.2 ± 1.9 (n=3), respectively.

It should be noted that these experiments were performed using plugs of uniform activity concentration. In real operation of the [<sup>18</sup>F]fluoride concentrator, later plugs would be more dilute and the loss of activity may in fact be lower than measured in these experiments.

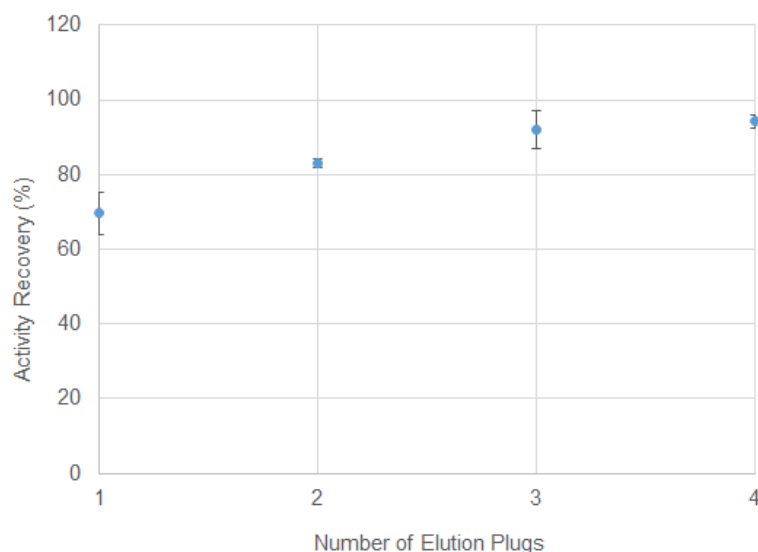


**Figure 8-3: Activity recovery from the droplet merging chip as a function of number of eluent plugs (each 6.2  $\mu\text{L}$ ) loaded into the chip**

Each data point represents an average of 3 repeats with error bars representing standard deviation.

Ultimately, we found the performance of the droplet merging chip to be comparable to the intermediate vial, and thus opted to use the intermediate vial. The complicated operation (compared to the vial) and susceptibility for membrane breakthrough (if fluid pressure is too high or if fluid has too high an organic solvent content) reduce its practicality.

## 8.2 Simulating higher activity levels in [ $^{18}\text{F}$ ]fluoride concentrator

When performing trap and elute experiments, we saw some limitations with the 3mg cartridge at higher activity levels, and therefore performed experimentation to explore what factors may be influencing trapping capacity in our cartridges.

### 8.2.1 KF spiking

To simulate high starting activities (i.e., 37 GBq [1Ci]), we tried performing trapping experiments with low amounts of [ $^{18}\text{F}$ ]fluoride spiked into a potassium fluoride (KF) solution. Estimating the molar activity of [ $^{18}\text{F}$ ]fluoride from our cyclotron to be 740 GBq/ $\mu\text{mol}$  [20Ci/ $\mu\text{mol}$ ] (based on prior measurements), the total amount of fluoride ion (both F-18 and F-19 forms)

expected for 37 GBq [1 Ci] should be 0.05  $\mu\text{mol}$ . Mock solutions were prepared using different concentrations of KF (1.0 mL volume) chosen from 50 – 5000  $\mu\text{M}$ , which were expected to correspond to simulated activity ranges of 37 GBq [1Ci] to 3.7 TBq [100Ci]. These solutions were spiked with 50  $\mu\text{L}$  of [ $^{18}\text{F}$ ]fluoride (15 - 37MBq [0.4 – 1 mCi]), an amount of activity sufficient for accurate activity measurements, but contributing negligible fluorine ion compared to the KF content. The measured trapping efficiency for each of these solutions is shown in Figure 8-4.

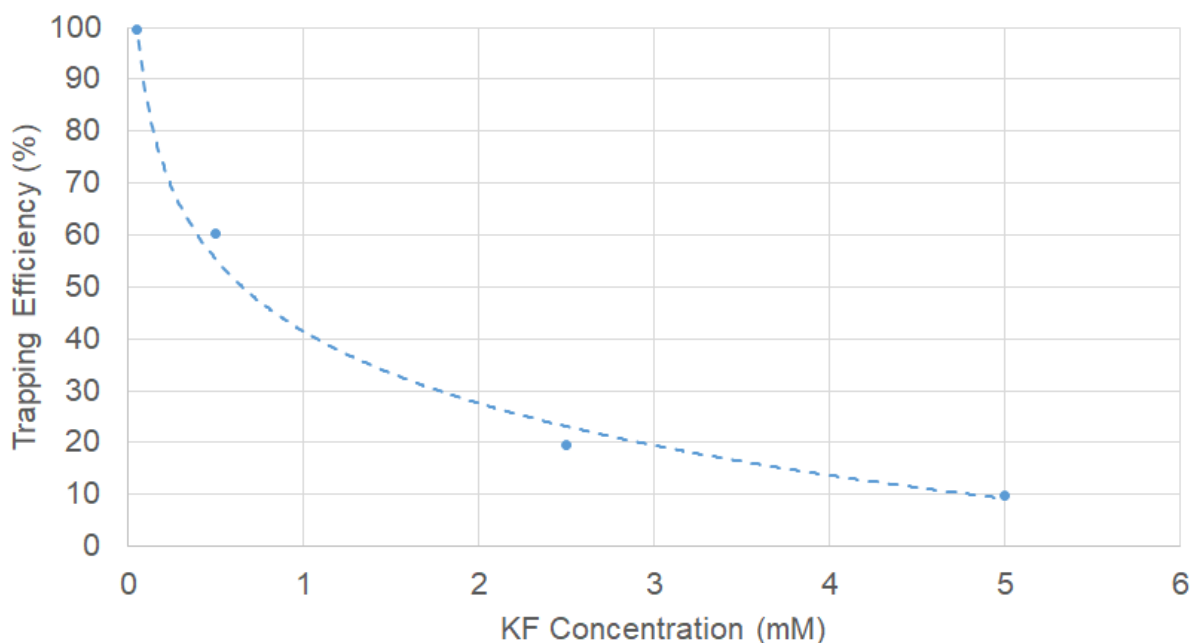


**Figure 8-4: Trapping efficiency of a solution containing 1.0 mL KF of various concentrations spiked with a small amount of [ $^{18}\text{F}$ ]fluoride**

All trapping experiments were performed with micro-cartridges packed with 3 mg of Sep-Pak QMA resin. Each condition was tried once ( $n=1$ ). Dotted line represents a logarithmic fit and has an  $R^2 = 0.9922$ .

Trapping efficiency of the mock 37 GBq [1 Ci] sample (i.e. 50  $\mu\text{M}$  KF) was 100% suggesting the cartridge should be able to trap 37Gbq [1Ci] of radioactivity, but the trapping was observed to fall off rapidly as the amount of KF increased. For example, at a mock activity level

of 740 GBq [20 Ci] (i.e., 1 mM KF), we can interpolate the measurements and estimate a trapping efficiency of ~40%.

### **8.2.2 Decayed, bombarded [<sup>18</sup>O]H<sub>2</sub>O spiking**

We performed additional experiments using decayed, bombarded [<sup>18</sup>O]H<sub>2</sub>O to evaluate whether the KF spiking measurements would be predictive of actual performance. We took 1.0 mL of decayed bombarded [<sup>18</sup>O]H<sub>2</sub>O (taken from a bombardment when the activity at end of bombardment was ~37 Gbq [1.0 Ci]). Though the [<sup>18</sup>F]fluoride had decayed, the total fluoride content was not expected to have significantly changed since the amount of [<sup>19</sup>F]fluoride right after bombardment far exceeds the amount of [<sup>18</sup>F]fluoride produced. We spiked in a small amount of activity (~19 MBq [0.5 mCi]) and performed a trapping experiment. Surprisingly, the trapping efficiency was found to be only 42%.

While we believe this experiment to be predictive of the results using 37 GBq [1 Ci] of freshly produced [<sup>18</sup>F]fluoride, this result suggested that KF solution is not a good substitute for performing mock experiments. Furthermore, it suggests that there may be a high concentration of a competing species (e.g. anion, metals) present in bombarded [<sup>18</sup>O]H<sub>2</sub>O that may also be interacting with the cartridge and limiting the capacity available for trapping fluoride.

Further study is needed to determine the impurities and how they may be hindering trapping. As mentioned earlier, other groups have reported efficient trapping of up to 110 GBq [3 Ci] using cartridges with only 2 mg of resin. (Our cartridges used 3 mg of resin.)

In the next section (Section 8.3), we explore whether larger resin mass can improve the trapping capacity, and in the subsequent section, we explore the use of SCX cartridges to filter the bombarded [<sup>18</sup>O]H<sub>2</sub>O to try to remove interfering species.

### 8.3 Performance of higher resin mass in [<sup>18</sup>F]fluoride concentrator

To attempt to increase trapping capacity, we explored cartridges packed with higher resin masses, i.e. 5mg of either Sep-Pak QMA or Oasis MAX resin. Due to limited supply of high levels of [<sup>18</sup>F]fluoride or corresponding amounts of bombarded [<sup>18</sup>O]H<sub>2</sub>O, we performed initial experiments with low amounts of activity spiked into a 1 mM KF solution (as described above). This KF concentration (corresponding to 740 GBq [20 Ci]) was chosen because the trapping efficiency in spiking experiments was ~40%, which matched the trapping efficiency in spiking experiments using 1.0 mL of decayed [<sup>18</sup>O]H<sub>2</sub>O from 37 GBq [1 Ci] bombardment. We are aware that the low trapping efficiency from the bombarded [<sup>18</sup>O]H<sub>2</sub>O spiking experiments may not entirely be due anion contamination, but, nonetheless, this experiment could still give us some insight on the trapping capacity of cartridges with larger resin amounts.

Detailed trapping and elution behavior can be seen in Table 8-1. Compared to 42% trapping for the 3mg Sep-Pak QMA cartridge reported above, trapping efficiency was 71± 1% (n = 2) for 5 mg Sep-Pak QMA cartridges and 68± 5% (n = 2) for 5 mg Oasis MAX cartridges. For 7 mg of Oasis MAX resin (packed in larger tubing as described in Section 6.2.3), trapping efficiency increased to 84% (n = 1), indicating that more resin mass can indeed improve the trapping.

One drawback of the larger resin mass is decreased elution efficiency. For the 5 mg cartridges, even after four elution steps, the elution efficiencies were 78± 1% (n = 2) and 78± 1% (n = 2) for Sep-Pak QMA and Oasis MAX resin, respectively. For the 7 mg Oasis MAX cartridge, elution efficiency was only 47% (n=1) after four elution steps. Comparing the overall recovery efficiency (i.e. trapping efficiency x elution efficiency (4 elutions)), the 5 mg Sep-Pak QMA cartridges performed the best (55.5 ± 0.4%, n = 2) compared to 5mg Oasis MAX (53 ± 4%, n = 2), and 7mg Oasis MAX (39%, n = 1).

**Table 8-1: Trapping and elution performance of a [<sup>18</sup>F]fluoride solution spiked with 1mM KF using cartridges with increased resin mass**

Values represent average ± standard deviation, calculated from the indicated number of repeats (n).

	Resin type		
	Sep-Pak QMA	Oasis MAX	Oasis MAX
<b>Cartridge Mass (mg)</b>	5	5	7
<b>Tubing ID (inch)</b>	0.03	0.03	0.04
<b>Number of repeats (n)</b>	2	2	1
<b>Trapping efficiency (%)</b>	71 ± 1	68 ± 5	84
<b>Elution 1+2 Efficiency (%)</b>	30 ± 2	27± 1	11
<b>Elution 3+4 Efficiency (%)</b>	49 ± 1	50.3 ± 0.3	36
<b>Elution 5+6 Efficiency (%)</b>	19.3 ± 0.1	21 ± 3	39
<b>Elution efficiency (4 elutions) (%)</b>	78 ± 1	78± 1	47
<b>Recovery Efficiency (4 elutions) (%)</b>	55.5 ± 0.4	53 ± 4	39
<b>Elution efficiency (6 elutions) (%)</b>	98 ± 1	98± 3	86

## 8.4 SCX filtration upstream of [<sup>18</sup>F]fluoride concentrator

### 8.4.1 [<sup>18</sup>F]fluoride filtering testing

We explored whether passing the [<sup>18</sup>F]fluoride/[<sup>18</sup>O]H<sub>2</sub>O solution through an SCX cartridge helped to improve the trapping efficiency of the downstream concentrator module. We hypothesized that SCX cartridges may filter out some competing contaminants and/or particles that may be interfering with the [<sup>18</sup>F]fluoride trapping efficiency. Two different SCX cartridges were explored: Oasis MCX Plus short cartridges (225mg, 186003516, Waters, Milford, MA, USA) and Maxi-Clean cartridges (600mg, 21902, Alltech Associates Inc. Deerfield, IL, USA). Before use, SCX cartridges were first preconditioned via manufacturer recommendations.

Alltech Maxi-clean cartridges were preconditioned with 10mL of DI water while Oasis MCX cartridges were conditioned with 5mL of MeOH followed by 5mL of DI water.

1.0 mL of decayed bombarded [ $^{18}\text{O}$ ]H $_2$ O (1mL; original activity of  $\sim 37$  GBq [ $\sim 1$  Ci]), was manually passed through a SCX cartridge via syringe, and then spiked with 50  $\mu\text{L}$  of [ $^{18}\text{F}$ ]fluoride (15 - 37MBq [0.4 – 1 mCi]). The spiked solution was then used as the source solution for the radionuclide concentrator and the trapping efficiency was measured. For this experiment, we used preconditioned 3 mg or 5 mg micro-cartridges packed with Sep-Pak QMA resin. The results are listed in Table 8-2. For the 3mg Sep-Pak QMA cartridges, SCX filtration (will Alltech Maxi-Clean cartridge) resulted in a dramatic increase in trapping efficiency from 42% (n = 1) to  $78 \pm 4\%$  (n = 2). The trapping efficiency was even higher ( $92 \pm 1\%$ , n=2) when the Oasis MCX cartridge was used for the SCX filtration step. For the 5mg cartridges, this effect was less significant. Trapping efficiency increased from  $81 \pm 4\%$  (n = 3) to  $96 \pm 2\%$  (n = 4) after SCX filtration using the Alltech Maxi-Clean cartridge. Oasis MCX cartridges in conjunction with the 5mg Sep-Pak QMA cartridges were not tested. Interestingly, after SCX filtration, higher trapping efficiency could be obtained with 3 mg cartridges, compared to trapping efficiency of 5 mg cartridges if SCX filtration was not performed. We elected to use the 3 mg Sep-Pak QMA cartridges in conjunction with SCX filtration (Oasis MCX cartridge) for the majority of experiments in this chapter. Surprisingly, during the synthesis of [ $^{18}\text{F}$ ]fallypride following SCX filtration, certain runs using high starting activity (i.e. 23-24GBq [620-650 mCi]) resulted in trapping efficiency of only 44-45%. These result suggest that maybe other factors need to be considered to ensure high trapping at high starting activities. Future studies are needed to determine if higher resin masses, in conjunction with the SCX module, could consistently achieve high trapping efficiencies, as well as high elution efficiency with low eluent volume.

**Table 8-2: Trapping performance of [<sup>18</sup>F]fluoride spiked into a solution of decayed [<sup>18</sup>O]H<sub>2</sub>O that was filtered through an SCX cartridge or not filtered**

Not filtered trials were indicated as “None” for SCX cartridge type. The micro-SAX cartridges were all packed with Sep-Pak QMA resin.

<b>SCX cartridge type</b>	None	Alltech Maxi- Clean	Oasis MCX	None	Alltech Maxi- Clean
<b>Micro-SAX cartridge resin mass (mg)</b>	3	3	3	5	5
<b>Trapping Efficiency (%)</b>	42 (n = 1)	78 ± 4 (n=2)	92 ± 1 (n=2)	81 ± 4 (n=3)	96 ± 2 (n=4)

## 9 References

1. Phelps ME. Positron emission tomography provides molecular imaging of biological processes. *Proc Natl Acad Sci*. 2000;97:9226–33.
2. Jacobs A, Voges J, Reszka R, Grossmann A, Kracht L, Kaestle C, et al. Positron Emission Tomography of Vector-Mediated Gene Expression in Gene Therapy for Gliomas. *Lancet*. 2001;358:727–9.
3. Herschman HR, MacLaren D, Iyer M, Namavari M, Bobinski KP, Green L, et al. Seeing Is Believing: Non-Invasive, Quantitative and Repetitive Imaging of Reporter Gene Expression in Living Animals, Using Positron Emission Tomography. *J Neurosci Res*. 2000;59:699–705.
4. Greco M. Axillary Lymph Node Staging in Breast Cancer by 2-Fluoro- 2-deoxy-D-glucose–Positron Emission Tomography: Clinical Evaluation and Alternative Management. *J Natl Cancer Inst*. 2001;93:630–5.
5. Ciernik F, Dizendorf E, Baumert B, Reiner B, Burger C, Davis B, et al. Radiation Treatment Planning with an Integrated Positron Emission and Computer Tomography (PET/CT): A Feasibility Study. *Int J Radiat Oncol Biol Phys*. 2003;57:853–63.
6. Erdi Y, Rosenzweig K, Erdi A, Macapinlac H, Hu Y-C, Braban L, et al. Radiotherapy treatment planning for patients with non-small cell lung cancer using positron emission tomography (PET). *Radiother Oncol*. 2002;62:51–60.
7. Yagle K, Eary J, Tait J, Grierson J, Link J, Lewellen B, et al. Evaluation of <sup>18</sup>F-Annexin V as a PET Imaging Agent in an Animal Model of Apoptosis. *J Nucl Med*. 2005;46:658–66.
8. Sorger D, Patt M, Kumar Piyush, Wiebe L, Barthel H, Seese A, et al. [<sup>18</sup>F]Fluoroazomycin-arabinofuranoside (18FAZA) and [<sup>18</sup>F]Fluoromisonidazole (18FMISO): A comparative study of their selective uptake in hypoxic cells and PET imaging in experimental rat tumors. *Nucl Med Biol*. 2003;30:317–26.
9. Yuan H, Schroeder T, Bowsher J, Hedlund L, Wong T, Dewhirst M. Intertumoral Differences in Hypoxia Selectivity of the PET imaging agent <sup>64</sup>Cu(II)-Diacetyl-Bis(N4-methylthiosemicarbazone). *J Nucl Med*. 2006;47:989–98.
10. Seddon BM, Workman P. The role of functional and molecular imaging in cancer drug discovery and development. *Br J Radiol*. 2003;76:S128–38.
11. Rudin M, Weissleder R. Molecular Imaging in Drug Discovery and Development. *Nat Rev Drug Discov*. 2003;2:123–31.
12. Langer O, Karch R, Muller U, Debrozemy G, Abraham A, Zeitlinger M, et al. Combined PET and Microdialysis for In Vivo Assessment of Intracellular Drug Pharmacokinetics in Humans. *J Nucl Med*. 2005;46:1835–41.

13. Aboagye EO, Price PM, Jones T. In vivo pharmacokinetics and pharmacodynamics in drug development using positron-emission tomography. *Drug Discov Today*. 2001;6:293–302.
14. Lasne M-C, Perrio C, Rouden J, Barré L, Roeda D, Dolle F, et al. Chemistry of  $\beta$  +-Emitting Compounds Based on Fluorine-18. In: Krause W, editor. *Contrast Agents II* [Internet]. Berlin, Heidelberg: Springer Berlin Heidelberg; 2002 [cited 2011 Jul 18]. p. 201–58. Available from: <http://www.springerlink.com/content/mxd2n549krd665ax/>
15. Chen K, Conti PS. Target-specific delivery of peptide-based probes for PET imaging. *Adv Drug Deliv Rev*. 2010;62:1005–22.
16. Wadas TJ, Wong EH, Weisman GR, Anderson CJ. Coordinating Radiometals of Copper, Gallium, Indium, Yttrium, and Zirconium for PET and SPECT Imaging of Disease [Internet]. 2010 [cited 2019 Feb 5]. Available from: <https://pubs.acs.org/doi/abs/10.1021/cr900325h>
17. Schuster DM, Nanni C, Fanti S. PET Tracers Beyond FDG in Prostate Cancer. *Semin Nucl Med*. 2016;46:507–21.
18. Lopci E, Nanni C, Castellucci P, Montini GC, Allegri V, Rubello D, et al. Imaging with non-FDG PET tracers: outlook for current clinical applications. *Insights Imaging*. 2010;1:373–85.
19. Tsai W-TK, Wu AM. Aligning physics and physiology: Engineering antibodies for radionuclide delivery. *J Label Compd Radiopharm* [Internet]. [cited 2018 Jun 18];0. Available from: <https://onlinelibrary.wiley.com/doi/abs/10.1002/jlcr.3622>
20. Wester HJ, Schottelius M. Fluorine-18 Labeling of Peptides and Proteins. In: Schubiger PA, Lehmann L, Friebe M, editors. *PET Chem*. Springer Berlin Heidelberg; 2007. p. 79–111.
21. Richter S, Wuest F. 18F-Labeled Peptides: The Future Is Bright. *Molecules*. 2014;19:20536–56.
22. Tang G, Zeng W, Yu M, Kabalka G. Facile synthesis of N-succinimidyl 4-[18F]fluorobenzoate ([18F]SFB) for protein labeling. *J Label Compd Radiopharm*. 2008;51:68–71.
23. Glaser M, Årstad E, Luthra SK, Robins EG. Two-step radiosynthesis of [18F]N-succinimidyl-4-fluorobenzoate ([18F]SFB). *J Label Compd Radiopharm*. 2009;52:327–330.
24. Glaser M, Robins EG. ‘Click labelling’ in PET radiochemistry. *J Label Compd Radiopharm*. 2009;52:407–14.
25. Velikyan I. 68Ga-Based Radiopharmaceuticals: Production and Application Relationship. *Molecules*. 2015;20:12913–43.
26. Zettlitz KA, Tavaré R, Knowles SM, Steward KK, Timmerman JM, Wu AM. ImmunoPET of Malignant and Normal B Cells with 89Zr- and 124I-Labeled Obinutuzumab Antibody Fragments Reveals Differential CD20 Internalization In Vivo. *Clin Cancer Res*. 2017;23:7242–52.

27. Zettlitz KA, Tavaré R, Tsai W-TK, Yamada RE, Ha NS, Collins J, et al.  $^{18}\text{F}$ -labeled anti-human CD20 cys-diabody for same-day immunoPET in a model of aggressive B cell lymphoma in human CD20 transgenic mice. *Eur J Nucl Med Mol Imaging* [Internet]. 2018 [cited 2018 Nov 25]; Available from: <https://doi.org/10.1007/s00259-018-4214-x>
28. Song IH, Lee TS, Park YS, Lee JS, Lee BC, Moon BS, et al. Immuno-PET Imaging and Radioimmunotherapy of  $^{64}\text{Cu}$ -/ $^{177}\text{Lu}$ -Labeled Anti-EGFR Antibody in Esophageal Squamous Cell Carcinoma Model. *J Nucl Med*. 2016;57:1105–11.
29. Kassis AI. Therapeutic Radionuclides: Biophysical and Radiobiologic Principles. *Semin Nucl Med*. 2008;38:358–66.
30. Le Bars D. Fluorine-18 and medical imaging: Radiopharmaceuticals for positron emission tomography. *J Fluor Chem*. 2006;127:1488–93.
31. Keng PY, Esterby M, van Dam RM. Emerging Technologies for Decentralized Production of PET Tracers. In: Hsieh C-H, editor. *Positron Emiss Tomogr - Curr Clin Res Asp*. Rijeka, Croatia: InTech; 2012. p. 153–82.
32. Collins J, Waldmann CM, Drake C, Slavik R, Ha NS, Sergeev M, et al. Production of diverse PET probes with limited resources: 24  $^{18}\text{F}$ -labeled compounds prepared with a single radiosynthesizer. *Proc Natl Acad Sci*. 2017;114:11309–11314.
33. He P, Haswell SJ, Pamme N, Archibald SJ. Advances in processes for PET radiotracer synthesis: separation of  $^{18}\text{F}$ fluoride from enriched  $^{18}\text{O}$ water. *Appl Radiat Isot*. 2014;91:64–70.
34. Banister S, Roeda D, Dolle F, Kassiou M. Fluorine-18 Chemistry for PET: A Concise Introduction. *Curr Radiopharm*. 2010;3:68–80.
35. Mukherjee J, Yang Z-Y, Das MK, Brown T. Fluorinated benzamide neuroleptics -- III. Development of (S)-N-[(1-allyl-2-pyrrolidiny)methyl]-5-(3- $^{18}\text{F}$ fluoropropyl)-2,3-dimethoxybenzamide as an improved dopamine D-2 receptor tracer. *Nucl Med Biol*. 1995;22:283–96.
36. Ha NS, Sadeghi S, van Dam RM. Recent Progress toward Microfluidic Quality Control Testing of Radiopharmaceuticals. *Micromachines*. 2017;8:337.
37. Whitesides GM. The origins and the future of microfluidics. *Nature*. 2006;442:368–73.
38. Rensch C, Jackson A, Lindner S, Salvamoser R, Samper V, Riese S, et al. Microfluidics: A Groundbreaking Technology for PET Tracer Production? *Molecules*. 2013;18:7930–56.
39. Miller PW, deMello AJ, Gee AD. Application of Microfluidics to the Ultra-Rapid Preparation of Fluorine-18 Labelled Compounds. *Curr Radiopharm*. 2010;3:254–62.
40. Watts P, Pascali G, Salvadori PA. Positron Emission Tomography Radiosynthesis in Microreactors. *J Flow Chem*. 2012;2:37–42.

41. McMullen JP, Jensen KF. Integrated Microreactors for Reaction Automation: New Approaches to Reaction Development. *Annu Rev Anal Chem.* 2010;3:19–42.
42. Gillies JM, Prenant C, Chimon GN, Smethurst GJ, Perrie W, Hamblett I, et al. Microfluidic reactor for the radiosynthesis of PET radiotracers. *Appl Radiat Isot.* 2006;64:325–32.
43. Steel CJ, O'Brien AT, Luthra SK, Brady F. Automated PET radiosyntheses using microfluidic devices. *J Label Compd Radiopharm.* 2007;50:308–11.
44. Arima V, Pascali G, Lade O, Kretschmer HR, Bernsdorf I, Hammond V, et al. Radiochemistry on chip: towards dose-on-demand synthesis of PET radiopharmaceuticals. *Lab Chip.* 2013;13:2328–36.
45. Elizarov AM, van Dam RM, Shin YS, Kolb HC, Padgett HC, Stout D, et al. Design and Optimization of Coin-Shaped Microreactor Chips for PET Radiopharmaceutical Synthesis. *J Nucl Med.* 2010;51:282–7.
46. Keng PY, Chen S, Ding H, Sadeghi S, Shah GJ, Dooraghi A, et al. Micro-chemical synthesis of molecular probes on an electronic microfluidic device. *Proc Natl Acad Sci.* 2012;109:690–5.
47. Javed MR, Chen S, Kim H-K, Wei L, Czernin J, Kim C-J “CJ,” et al. Efficient Radiosynthesis of 3'-Deoxy-3'-18F-Fluorothymidine Using Electrowetting-on-Dielectric Digital Microfluidic Chip. *J Nucl Med.* 2014;55:321–8.
48. Keng PY, van Dam RM. Digital Microfluidics: A New Paradigm for Radiochemistry. *Mol Imaging.* 2015;14:579–94.
49. Javed MR, Chen S, Lei J, Collins J, Sergeev M, Kim H-K, et al. High yield and high specific activity synthesis of [18F]fallypride in a batch microfluidic reactor for micro-PET imaging. *Chem Commun.* 2014;50:1192–4.
50. Chen S, Javed MR, Kim H-K, Lei J, Lazari M, Shah GJ, et al. Radiolabelling diverse positron emission tomography (PET) tracers using a single digital microfluidic reactor chip. *Lab Chip.* 2014;14:902–10.
51. Keng PY, Sergeev M, van Dam RM. Advantages of Radiochemistry in Microliter Volumes. In: Kuge Y, Shiga T, Tamaki N, editors. *Perspect Nucl Med Mol Diagn Integr Ther* [Internet]. Springer Japan; 2016 [cited 2016 Apr 11]. p. 93–111. Available from: [http://link.springer.com/chapter/10.1007/978-4-431-55894-1\\_7](http://link.springer.com/chapter/10.1007/978-4-431-55894-1_7)
52. Fawdry RM. Radiolysis of 2-[18F]fluoro-2-deoxy-d-glucose (FDG) and the role of reductant stabilisers. *Appl Radiat Isot.* 2007;65:1193–201.
53. Búriová E, Macásek F, Melichar F, Kropáček M, Procházka L. Autoradiolysis of the 2-deoxy-2-[18F]fluoro-D-glucose radiopharmaceutical. *J Radioanal Nucl Chem.* 2005;264:595–602.

54. Rensch C, Waengler B, Yaroshenko A, Samper V, Baller M, Heumesser N, et al. Microfluidic reactor geometries for radiolysis reduction in radiopharmaceuticals. *Appl Radiat Isot Data Instrum Methods Use Agric Ind Med*. 2012;70:1691–7.
55. Lazari M, Collins J, Shen B, Farhoud M, Yeh D, Maraglia B, et al. Fully Automated Production of Diverse  $^{18}\text{F}$ -Labeled PET Tracers on the ELIXYS Multireactor Radiosynthesizer Without Hardware Modification. *J Nucl Med Technol*. 2014;42:203–10.
56. Hume SP, Gunn RN, Jones T. Pharmacological constraints associated with positron emission tomographic scanning of small laboratory animals. *Eur J Nucl Med Mol Imaging*. 1998;25:173–6.
57. Jagoda EM, Vaquero JJ, Seidel J, Green MV, Eckelman WC. Experiment assessment of mass effects in the rat: implications for small animal PET imaging. *Nucl Med Biol*. 2004;31:771–9.
58. Kung M-P, Kung HF. Mass effect of injected dose in small rodent imaging by SPECT and PET. *Nucl Med Biol*. 2005;32:673–8.
59. Solin O, Bergman J, Haaparanta M, Reissell A. Production of  $^{18}\text{F}$  from water targets. Specific radioactivity and anionic contaminants. *Int J Rad Appl Instrum [A]*. 1988;39:1065–71.
60. Satyamurthy N, Amarasekera B, Alvord CW, Barrio JR, Phelps ME. Tantalum  $[^{18}\text{O}]\text{Water}$  Target for the Production of  $[^{18}\text{F}]\text{Fluoride}$  with High Reactivity for the Preparation of 2-Deoxy-2- $[^{18}\text{F}]\text{Fluoro-D-Glucose}$ . *Mol Imaging Biol*. 2002;4:65–70.
61. Füchtner F, Preusche S, Mäding P, Zessin J, Steinbach J. Factors affecting the specific activity of  $[^{18}\text{F}]\text{fluoride}$  from a  $[^{18}\text{O}]\text{water}$  target. *Nukl Nucl Med*. 2008;47:116–9.
62. Sadeghi S, Ding H, Shah GJ, Chen S, Keng PY, Kim C-J “CJ,” et al. On Chip Droplet Characterization: A Practical, High-Sensitivity Measurement of Droplet Impedance in Digital Microfluidics. *Anal Chem*. 2012;84:1915–23.
63. Sergeev M, Lazari M, Morgia F, Collins J, Javed MR, Sergeeva O, et al. Performing radiosynthesis in microvolumes to maximize molar activity of tracers for positron emission tomography. *Commun Chem*. 2018;1:10.
64. Wang J, Chao PH, Hanet S, Dam RM van. Performing multi-step chemical reactions in microliter-sized droplets by leveraging a simple passive transport mechanism. *Lab Chip*. 2017;17:4342–55.
65. Lebedev A, Miraghaie R, Kotta K, Ball CE, Zhang J, Buchsbaum MS, et al. Batch-reactor microfluidic device: first human use of a microfluidically produced PET radiotracer. *Lab Chip [Internet]*. 2012 [cited 2012 Nov 7]; Available from: <http://pubs.rsc.org/en/content/articlelanding/2012/lc/c2lc40853h>

66. Diehl K-H, Hull R, Morton D, Pfister R, Rabemampianina Y, Smith D, et al. A Good Practice Guide to the Administration of Substances and Removal of Blood, Including Routes and Volumes. *Joural Appl Toxicol*. 2001;21:15–23.
67. Vu NT, Yu ZTF, Comin-Anduix B, Søndergaard JN, Silverman RW, Chang CYN, et al. A  $\beta$ -Camera Integrated with a Microfluidic Chip for Radioassays Based on Real-Time Imaging of Glycolysis in Small Cell Populations. *J Nucl Med*. 2011;52:815–21.
68. Serdons K, Verbruggen A, Bormans G. The Presence of Ethanol in Radiopharmaceutical Injections. *J Nucl Med*. 2008;49:2071–2071.
69. ICH Expert Working Group. Impurities: Guideline for Residual Solvents Q3C(R5). 1997.
70. Eckert & Ziegler Eurotope GmbH. Modular-Lab PharmTracer [Internet]. 2013 [cited 2013 Feb 3]. Available from: <http://www.ezag.com/home/products/radiopharma/radiosynthesis-technology/modular-lab-pharmtracer.html>
71. Trasis. All-in-One PET Tracer Synthesizer [Internet]. [cited 2017 May 7]. Available from: <http://www.trasis.com/products/allinone-universal-synthesizer>
72. Tseng W-Y, van Dam RM. Compact microfluidic device for rapid concentration of PET tracers. *Lab Chip*. 2014;14:2293.
73. Xu W, Wu LL, Li GP, Bachman M. A vapor-based microfluidic sample concentrator. *Proc Fourteenth Int Conf Miniaturized Syst Chem Life Sci*. Groningen, The Netherlands; 2010. p. 1208–10.
74. Solvas XC i, Turek V, Prodromakis T, Edel JB. Microfluidic evaporator for on-chip sample concentration. *Lab Chip*. 2012;12:4049–54.
75. Deadman B, Battilocchio C, Sliwinski E, Ley S. A prototype device for evaporation in batch and flow chemical processes. *Green Chem*. 2013;15:2050–5.
76. Sharma NR, Lukyanov A, Bardell RL, Seifried L, Shen M. Development of an evaporation-based microfluidic sample concentrator. In: Wang W, Vauchier C, editors. *Microfluid BioMEMS Med Microsyst VI* [Internet]. San Jose, CA, USA: SPIE; 2008 [cited 2010 Nov 19]. p. 68860R – 9. Available from: <http://link.aip.org/link/?PSI/6886/68860R/1>
77. Alkudhiri A, Darwish N, Nidal Hilal. Membrane distillation: A comprehensive review. *Desalination*. 2012;287:2–18.
78. Lazari M, Quinn KM, Claggett SB, Collins J, Shah GJ, Herman HE, et al. ELIXYS - a fully automated, three-reactor high-pressure radiosynthesizer for development and routine production of diverse PET tracers. *EJNMMI Res*. 2013;3:52.
79. Kiesewetter DO, Jacobson O, Lang L, Chen X. Automated radiochemical synthesis of [ $^{18}\text{F}$ ]FBEM: A thiol reactive synthon for radiofluorination of peptides and proteins. *Appl Radiat Isot*. 2011;69:410–4.

80. Meng D, Kim J, Kim C-J. A degassing plate with hydrophobic bubble capture and distributed venting for microfluidic devices. *J Micromechanics Microengineering*. 2006;16:419–24.
81. Meng D, Cubaud T, Ho C-M, Kim C-J “CJ.” A Methanol-Tolerant Gas-Venting Microchannel for a Microdirect Methanol Fuel Cell. *J Microelectromechanical Syst*. 2007;16:1403–10.
82. Kugel R. Raoult’s Law: Binary Liquid–Vapor Phase Diagrams A Simple Physical Chemistry Experiment. *J Chem Educ*. 1998;75:1125–9.
83. Wolfram Alpha LLC. WolframAlpha Computational Knowledge Engine [Internet]. Wolfram|Alpha. [cited 2016 Jan 14]. Available from: [www.wolframalpha.com](http://www.wolframalpha.com)
84. The “Golden Rule” for Solvent Removal [Internet]. Sigma-Aldrich Co; 2007. Available from: [https://www.sigmaaldrich.com/content/dam/sigma-aldrich/docs/Aldrich/General\\_Information/1/labwarenotes\\_v1\\_7.pdf](https://www.sigmaaldrich.com/content/dam/sigma-aldrich/docs/Aldrich/General_Information/1/labwarenotes_v1_7.pdf)
85. Hoegger R. Training Papers : Distillation with a Rotary Evaporator [Internet]. BÜCHI Labortechnik AG; 1998. Available from: <https://erowid.org/archive/rhodium/pdf/rotary.evaporator.pdf>
86. Ali K, Shah A-HA, Bilal S, Shah A-HA. Surface tensions and thermodynamic parameters of surface formation of aqueous salt solutions: III. Aqueous solution of KCl, KBr and KI. *Colloids Surf Physicochem Eng Asp*. 2009;337:194–9.
87. Xu L, Han G, Hu J, He Y, Pan J, Li Y, et al. Hydrophobic coating- and surface active solvent-mediated self-assembly of charged gold and silver nanoparticles at water–air and water–oil interfaces. *Phys Chem Chem Phys*. 2009;11:6490–7.
88. Professional Plastics. Thermal Properties of Plastic Materials [Internet]. Available from: <http://www.professionalplastics.com/professionalplastics/ThermalPropertiesofPlasticMaterials.pdf>
89. Trouve A, Minnich T. Thermal Properties Database. 2012.
90. Meranda D, Furter W. Elevation of the Boiling Point of Water by Salts at Saturation: Data and Correlation. *J Chem Eng Data*. 1977;22:315–7.
91. Radu CG, Shu CJ, Nair-Gill E, Shelly SM, Barrio JR, Satyamurthy N, et al. Molecular imaging of lymphoid organs and immune activation using positron emission tomography with a new 18F-labeled 2'-deoxycytidine analog. *Nat Med*. 2008;14:783–8.
92. Gebhardt P, Opfermann T, Saluz HP. Computer controlled 68Ga milking and concentration system. *Appl Radiat Isot*. 2010;68:1057–9.
93. Rensch C, Jackson A, Lindner S, Salvamoser R, Samper V, Riese S, et al. Microfluidics: A Groundbreaking Technology for PET Tracer Production? *Molecules*. 2013;18:7930–56.

94. Vallabhajosula S, Solnes L, Vallabhajosula B. A Broad Overview of Positron Emission Tomography Radiopharmaceuticals and Clinical Applications: What Is New? *Semin Nucl Med.* 2011;41:246–64.
95. Vallabhajosula S. 18F-Labeled Positron Emission Tomographic Radiopharmaceuticals in Oncology: An Overview of Radiochemistry and Mechanisms of Tumor Localization. *Semin Nucl Med.* 2007;37:400–19.
96. Vallabhajosula S. Positron Emission Tomography Radiopharmaceuticals for Imaging Brain Beta-Amyloid. *Semin Nucl Med.* 2011;41:283–99.
97. Kumar P, Bacchu V, Wiebe LI. The Chemistry and Radiochemistry of Hypoxia-Specific, Radiohalogenated Nitroaromatic Imaging Probes. *Semin Nucl Med.* 2015;45:112–35.
98. Pascali G, Watts P, Salvadori P. Microfluidics in radiopharmaceutical chemistry. *Nucl Med Biol.* 2013;40:776–87.
99. Liang SH, Yokell DL, Normandin MD, Rice PA, Jackson RN, Shoup TM, et al. First Human Use of a Radiopharmaceutical Prepared by Continuous-Flow Microfluidic Radiofluorination: Proof of Concept with the Tau Imaging Agent [18F]T807. *Mol Imaging.* 2014;13:1–5.
100. Hoover AJ, Lazari M, Ren H, Narayanam MK, Murphy JM, van Dam RM, et al. A Transmetalation Reaction Enables the Synthesis of [18F]5-Fluorouracil from [18F]Fluoride for Human PET Imaging. *Organometallics.* 2016;35:1008–14.
101. Lemaire CF, Aerts JJ, Voccia S, Libert LC, Mercier F, Goblet D, et al. Fast Production of Highly Reactive No-Carrier-Added [18F]Fluoride for the Labeling of Radiopharmaceuticals. *Angew Chem Int Ed.* 2010;49:3161–4.
102. Seo JW, Lee BS, Lee SJ, Oh SJ, Chi DY. Fast and Easy Drying Method for the Preparation of Activated [18F]Fluoride Using Polymer Cartridge. *Bull Korean Chem Soc.* 2011;32:71–6.
103. Iwata R, Pascali C, Terasaki K, Ishikawa Y, Furumoto S, Yanai K. Minimization of the amount of Kryptofix 222 - KHCO<sub>3</sub> for applications to microscale 18F-radiolabeling. *Appl Radiat Isot [Internet].* [cited 2017 Apr 20]; Available from: <http://www.sciencedirect.com/science/article/pii/S0969804316310193>
104. Iwata R, Pascali C, Terasaki K, Ishikawa Y, Furumoto S, Yanai K. Practical microscale one-pot radiosynthesis of 18F-labeled probes. *J Label Compd Radiopharm.* 2018;61:540–9.
105. Richarz R, Krapf P, Zarrad F, Urusova EA, Neumaier B, Zlatopolskiy BD. Neither azeotropic drying, nor base nor other additives: a minimalist approach to 18F-labeling. *Org Biomol Chem.* 2014;12:8094–9.
106. De Leonardis F, Pascali G, Salvadori PA, Watts P, Pamme N. On-chip pre-concentration and complexation of [18F]fluoride ions via regenerable anion exchange particles for

radiochemical synthesis of Positron Emission Tomography tracers. *J Chromatogr A*. 2011;1218:4714–9.

107. Salvador B, Luque A, Fernandez-Maza L, Corral A, Orta D, Fernández I, et al. Disposable PDMS Chip With Integrated [<sup>18</sup>F]Fluoride Pre-Concentration Cartridge for Radiopharmaceuticals. *J Microelectromechanical Syst*. 2017;26:1442–8.

108. Ismail R, Irribarren J, Javed MR, Machness A, van Dam M, Keng PY. Cationic imidazolium polymer monoliths for efficient solvent exchange, activation and fluorination on a continuous flow system. *RSC Adv*. 2014;4:25348–56.

109. Saiki H, Iwata R, Nakanishi H, Wong R, Ishikawa Y, Furumoto S, et al. Electrochemical concentration of no-carrier-added [<sup>18</sup>F]fluoride from [<sup>18</sup>O]water in a disposable microfluidic cell for radiosynthesis of <sup>18</sup>F-labeled radiopharmaceuticals. *Appl Radiat Isot*. 2010;68:1703–8.

110. Wong R, Iwata R, Saiki H, Furumoto S, Ishikawa Y, Ozeki E. Reactivity of electrochemically concentrated anhydrous [<sup>18</sup>F]fluoride for microfluidic radiosynthesis of <sup>18</sup>F-labeled compounds. *Appl Radiat Isot*. 2012;70:193–9.

111. Lee E, Hooker JM, Ritter T. Nickel-Mediated Oxidative Fluorination for PET with Aqueous [<sup>18</sup>F] Fluoride. *J Am Chem Soc*. 2012;134:17456–8.

112. Kamlet AS, Neumann CN, Lee E, Carlin SM, Moseley CK, Stephenson N, et al. Application of Palladium-Mediated <sup>18</sup>F-Fluorination to PET Radiotracer Development: Overcoming Hurdles to Translation. *PLoS ONE*. 2013;8:e59187.

113. Liu Z, Lin K-S, Bénard F, Pourghiasian M, Kiesewetter DO, Perrin DM, et al. One-step <sup>18</sup>F labeling of biomolecules using organotrifluoroborates. *Nat Protoc*. 2015;10:1423–32.

114. AG® MP-1M Anion Exchange Resins | Process Separations | Bio-Rad [Internet]. [cited 2017 Dec 4]. Available from: <http://www.bio-rad.com/en-ch/product/ag-mp-1m-anion-exchange-resins>

115. Holland JP, Sheh Y, Lewis JS. Standardized methods for the production of high specific-activity zirconium-89. *Nucl Med Biol*. 2009;36:729–39.

116. Lin M, Mukhopadhyay U, Waligorski GJ, Balatoni JA, González-Lepera C. Semi-automated production of <sup>89</sup>Zr-oxalate/<sup>89</sup>Zr-chloride and the potential of <sup>89</sup>Zr-chloride in radiopharmaceutical compounding. *Appl Radiat Isot*. 2016;107:317–22.

117. Zeng D, Desai AV, Ranganathan D, Wheeler TD, Kenis PJA, Reichert DE. Microfluidic radiolabeling of biomolecules with PET radiometals. *Nucl Med Biol*. 2013;40:42–51.

118. Wright BD, Whittenberg J, Desai A, DiFelice C, Kenis PJA, Lapi SE, et al. Microfluidic Preparation of a <sup>89</sup>Zr-Labeled Trastuzumab Single-Patient Dose. *J Nucl Med*. 2016;57:747–52.

119. Causey P, Stephenson K, Valliant J. A microfluidic approach to the preparation of radiometal-based probes. *J Nucl Med*. 2009;50:148–148.

120. Fani M, Andre JP, Maecke HR. 68Ga-PET: a powerful generator-based alternative to cyclotron-based PET radiopharmaceuticals. *Contrast Media Mol Imaging*. 2008;3:67–77.
121. Velikyan I. Prospective of 68Ga-Radiopharmaceutical Development. *Theranostics*. 2013;4:47–80.
122. Eiber M, Fendler WP, Rowe SP, Calais J, Hofman MS, Maurer T, et al. Prostate-Specific Membrane Antigen Ligands for Imaging and Therapy. *J Nucl Med Off Publ Soc Nucl Med*. 2017;58:67S-76S.
123. Schwarzenboeck SM, Rauscher I, Bluemel C, Fendler WP, Rowe SP, Pomper MG, et al. PSMA Ligands for PET Imaging of Prostate Cancer. *J Nucl Med Off Publ Soc Nucl Med*. 2017;58:1545–52.
124. Velikyan I. Chapter 17 - Radionuclides for Imaging and Therapy in Oncology. In: Chen X, Wong S, editors. *Cancer Theranostics* [Internet]. Oxford: Academic Press; 2014 [cited 2019 Feb 21]. p. 285–325. Available from: <http://www.sciencedirect.com/science/article/pii/B9780124077225000177>
125. Vorster M, Maes A, Wiele C van de, Sathekge M. Gallium-68 PET: A Powerful Generator-based Alternative to Infection and Inflammation Imaging. *Semin Nucl Med*. 2016;46:436–47.
126. Waldmann CM, Stuparu AD, van Dam RM, Slavik R. The Search for an Alternative to [68Ga]Ga-DOTA-TATE in Neuroendocrine Tumor Theranostics: Current State of 18F-labeled Somatostatin Analog Development. 2019;9:12.
127. Wheeler TD, Zeng D, Desai AV, Önal B, Reichert DE, Kenis PJA. Microfluidic labeling of biomolecules with radiometals for use in nuclear medicine. *Lab Chip*. 2010;10:3387–96.
128. Zhernosekov KP, Filosofov DV, Baum RP, Aschoff P, Bihl H, Razbash AA, et al. Processing of Generator-Produced 68Ga for Medical Application. *J Nucl Med*. 2007;48:1741–8.
129. Eppard E, Wuttke M, Nicodemus PL, Rosch F. Ethanol-Based Post-processing of Generator-Derived 68Ga Toward Kit-Type Preparation of 68Ga-Radiopharmaceuticals. *J Nucl Med*. 2014;55:1023–8.
130. Mueller D, Klette I, Baum RP, Gottschaldt M, Schultz MK, Breeman WAP. Simplified NaCl Based 68Ga Concentration and Labeling Procedure for Rapid Synthesis of 68Ga Radiopharmaceuticals in High Radiochemical Purity. *Bioconjug Chem*. 2012;23:1712–7.
131. Chao PH, Lazari M, Hanet S, Narayanam MK, Murphy JM, van Dam RM. Automated concentration of [18F]fluoride into microliter volumes. *Appl Radiat Isot*. 2018;141:138–48.
132. Pascali G, Matesic L. How Far Are We from Dose On Demand of Short-Lived Radiopharmaceuticals? In: Kuge Y, Shiga T, Tamaki N, editors. *Perspect Nucl Med Mol Diagn Integr Ther* [Internet]. Springer Japan; 2016 [cited 2016 Sep 26]. p. 79–92. Available from: [http://link.springer.com/chapter/10.1007/978-4-431-55894-1\\_6](http://link.springer.com/chapter/10.1007/978-4-431-55894-1_6)

133. Darhuber AA, Troian SM. Principles of Microfluidic Actuation by Modulation of Surface Stresses. *Annu Rev Fluid Mech.* 2005;37:425–55.
134. Xing S, S. Harake R, Pan T. Droplet-driven transports on superhydrophobic-patterned surface microfluidics. *Lab Chip.* 2011;11:3642–8.
135. Yeh S-I, Fang W-F, Sheen H-J, Yang J-T. Droplets coalescence and mixing with identical and distinct surface tension on a wettability gradient surface. *Microfluid Nanofluidics.* 2013;14:785–95.
136. Liu C, Sun J, Li J, Xiang C, Che L, Wang Z, et al. Long-range spontaneous droplet self-pulsion on wettability gradient surfaces. *Sci Rep.* 2017;7:7552.
137. Ng V-V, Sellier M, Nock V. Marangoni-induced actuation of miscible liquid droplets on an incline. *Int J Multiph Flow.* 2016;82:27–34.
138. Dangla R, Kayi SC, Baroud CN. Droplet microfluidics driven by gradients of confinement. *Proc Natl Acad Sci.* 2013;110:853–8.
139. Hong J, Park JK, Koo B, Kang KH, Suh YK. Drop transport between two non-parallel plates via AC electrowetting-driven oscillation. *Sens Actuators B Chem.* 2013;188:637–43.
140. Luo C, Heng X, Xiang M. Behavior of a Liquid Drop between Two Nonparallel Plates. *Langmuir.* 2014;30:8373–80.
141. Ghosh A, Ganguly R, Schutzius TM, Megaridis CM. Wettability patterning for high-rate, pumpless fluid transport on open, non-planar microfluidic platforms. *Lab Chip.* 2014;14:1538–50.
142. Sergeev ME, Morgia F, Lazari M, Wang C, van Dam RM. Titania-Catalyzed Radiofluorination of Tosylated Precursors in Highly Aqueous Medium. *J Am Chem Soc.* 2015;137:5686–94.
143. Cho C-C, Wallace RM, Files-Sesler LA. Patterning and etching of amorphous teflon films. *J Electron Mater.* 1994;23:827–30.
144. Cho JS, Taschereau R, Olma S, Liu K, Chen Y-C, Shen CK-F, et al. Cerenkov radiation imaging as a method for quantitative measurements of beta particles in a microfluidic chip. *Phys Med Biol.* 2009;54:6757–6771.
145. Dooraghi AA, Keng PY, Chen S, Javed MR, Kim C-J “CJ,” Chatziioannou AF, et al. Optimization of microfluidic PET tracer synthesis with Cerenkov imaging. *Analyst.* 2013;138:5654–64.
146. Loening AM, Gambhir SS. AMIDE: a free software tool for multimodality medical image analysis. *Mol Imaging.* 2003;2:131–7.

147. Lu S, Giamis AM, Pike VW. Synthesis of [ $^{18}\text{F}$ ]fallypride in a micro-reactor: rapid optimization and multiple-production in small doses for micro-PET studies. *Curr Radiopharm.* 2009;2:1–13.
148. Mukherjee J, Constantinescu CC, Hoang AT, Jerjian T, Majji D, Pan M-L. Dopamine D3 receptor binding of 18F-fallypride: Evaluation using in vitro and in vivo PET imaging studies. *Synapse.* 2015;69:577–91.
149. Elizarov AM. Microreactors for radiopharmaceutical synthesis. *Lab Chip.* 2009;9:1326–33.
150. Pascali G, Mazzone G, Saccomanni G, Manera C, Salvadori PA. Microfluidic approach for fast labeling optimization and dose-on-demand implementation. *Nucl Med Biol.* 2010;37:547–55.
151. Zhang X, Liu F, Knapp K-A, Nickels ML, Manning HC, Bellan LM. A simple microfluidic platform for rapid and efficient production of the radiotracer [ $^{18}\text{F}$ ]fallypride. *Lab Chip.* 2018;18:1369–77.
152. Bejot R, Elizarov AM, Ball E, Zhang J, Miraghaie R, Kolb HC, et al. Batch-mode microfluidic radiosynthesis of N-succinimidyl-4- $^{18}\text{F}$ fluorobenzoate for protein labelling. *J Label Compd Radiopharm.* 2011;54:117–22.
153. Zheng M-Q, Collier L, Bois F, Kelada OJ, Hammond K, Ropchan J, et al. Synthesis of [ $^{18}\text{F}$ ]FMISO in a flow-through microfluidic reactor: Development and clinical application. *Nucl Med Biol.* 2015;42:578–84.
154. Lisova K, Sergeev M, Evans-Axelsson S, Stuparu AD, Beykan S, Collins J, et al. Microscale radiosynthesis, preclinical imaging and dosimetry study of [ $^{18}\text{F}$ ]AMBF3-TATE: A potential PET tracer for clinical imaging of somatostatin receptors. *Nucl Med Biol.* 2018;61:36–44.
155. Seok Moon B, Hyung Park J, Jin Lee H, Sun Kim J, Sup Kil H, Se Lee B, et al. Highly efficient production of [ $^{18}\text{F}$ ]fallypride using small amounts of base concentration. *Appl Radiat Isot.* 2010;68:2279–84.